Mechanistic studies of solar fuel generation at electrode surfaces

Khezar Saeed

March 2022

Supervisor: Prof. Alexander Cowan

Thesis submitted to The University of Liverpool in partial fulfilment of the degree of Doctor in Philosophy

Abstract

Mechanistic studies of solar fuel generation at electrode surfaces

Khezar Saeed

Solar fuel generation addresses the inherent intermittency of solar energy and can be part of the global solution to tackling climate change. The idea involves harnessing solar energy to drive chemical reactions to produce high energy density fuels. Thus, when the Sun is not shining, the sustainably produced fuels can be converted to energy to meet demands. Key to the future wide-scale adoption of this process is the development of efficient solar fuel generation devices from cheaper, more stable and abundant materials. Mechanistic studies on both state-of-the-art (and expensive) materials as well as the cheaper, less efficient alternatives can provide vital information on both efficient catalytic process and causes of inefficiencies in cheaper materials. This mechanistic understanding can be used to inform the design of improved materials in the future. *In situ* vibrational spectroscopy can provide direct chemical information on the identity of surface intermediates, making it a powerful tool in mechanistic studies. Unfortunately, almost all solar fuel reactions occur at heterogeneous interfaces and the spectroscopic response is often dominated by the inactive bulk of these materials. Surface-sensitive vibrational spectroscopies are inherently blind to the majority of the bulk response, thus selectively providing mechanistic information from the catalytically active interface. This thesis explores the development of several surface-sensitive spectroscopic experiments for studying photo- and electrocatalytic water splitting materials to produce hydrogen and oxygen as the solar fuels. Electrochemical shell-isolated nanoparticle-enhanced Raman spectroscopy is used to detect surface intermediates at state-of-the-art hydrous iridium oxide electrodes. *In situ* vibrational sum frequency generation is applied to studying the interfacial water structure at hematite and TiO_2 electrode surfaces under water oxidation conditions. Finally, photoinduced absorption and electric field-induced second harmonic generation spectroscopy are used to follow slow surface hole kinetics and understand the impact of surface trap states on interfacial electric fields.

List of Publications

The following papers have been published in peer-reviewed journal articles over the course of this PhD:

- A. M. Gardner, K. H. Saeed and A. J. Cowan, Vibrational sum-frequency generation spectroscopy of electrode surfaces: Studying the mechanisms of sustainable fuel generation and utilisation, *Phys. Chem. Chem. Phys.*, 2019, **21**, 12067–12086.
- K. H. Saeed, M. Forster, J. F. Li, L. J. Hardwick and A. J. Cowan, Water oxidation intermediates on iridium oxide electrodes probed by *in situ* electrochemical SHINERS, *Chem. Commun.*, 2020, **56**, 1129–1132.
- V. L. Piercy, K. H. Saeed, A. W. Prentice, G. Neri, C. Li, A. M. Gardner, Y. Bai, R. S. Sprick, I. V. Sazanovich, A. I. Cooper, M. J. Rosseinsky, M. A. Zwijnenburg and A. J. Cowan, Time-Resolved Raman Spectroscopy of Polaron Formation in a Polymer Photocatalyst, *J. Phys. Chem. Lett.*, 2021, **12**, 10899–10905.

Acknowledgements

I am incredibly grateful to the many people who have helped and supported me over this PhD.

First and foremost, I would like to express my deepest gratitude to my supervisor Alex. Thank you for the endless support, advice and patience. Thank you for assembling such an amazing group of people to share a lab with. And finally, thank you for the inspiration to do all the work in this thesis. It has been a pleasure working with you.

Thanks to Mark, Gaia and Adrian for being almost like second supervisors to me over the years. Always remember that "You are a star postdoc".

Thanks to everyone else in the Cowan group and the rest of the SIRE, past and present, for making the labs and offices such a pleasure to work in and being such a fun group of people out of work too.

Thanks to all the collaborators and colleagues who made all this work possible:

Prof. Laurence Hardwick & Prof. Jian-Feng Li and their groups for access to the Raman spectrometer, help with the SHINERS technique and giving me the opportunity to visit Xiamen University to learn the techniques.

Prof. Tim Veal and Dr Tom Featherstone for help with sputtering ITO samples

Prof. Matt Rosseinsky and his group for pulsed laser deposition of hematite

Prof. Ken Durose for access to the gold thermal evaporation equipment

The Imaging Centre at Liverpool (ICaL) and Dr Mark Forster for SEM imaging

Dr Paul Donaldson and the entire CLF team for all their help with the SFG experiments over the years.

Finally, a big thank you to all of my family, without whom none of this would be possible

List of Abbreviations

ABS	Acyrlonitrile butadiene styrene
ALD	Atomic layer deposition
APTMS	Aminopropyl trimethylsilane
ATR	Attenuated total reflectance
BBO	Beta barium borate
BG	Band gap
bpy	Bipyridine
CB	Conduction band
CCD	Charge coupled device
CISHG	Current-induced second harmonic generation
CLF	Central Laser Facility
CV	Cyclic voltammetry
CW	Continuous wave
DFG	Difference frequency generation
DFT	Density Functional Theory
ED	Electrodeposited
E_{DC}	Direct current electric field
EDL	Electrical double layer
EF	Fermi level energy
Efb	Flat band potential
EFISHG	Electric field induced second harmonic generation
EIS	Electrochemical impedance spectroscopy
ε_0	Vacuum permittivity
FFT	Fast Fourier transform
FID	Free induction decay
FTIR	Fourier transform infrared
FTO	Fluorine-doped tin oxide
GCE	Glassy carbon electrode
HD	Heterodyne detected
HER	Hydrogen evolution reaction
Im	Imaginary
IR	Infrared
ITO	Indium tin oxide
kb	Boltzmann constant
λ_D	Debye length
LED	Light emitting diode
LO	Local oscillator
LP	Long-pass
LSPR	Localised surface plasmon resonance
LSV	Linear sweep voltammogram
MIR	Mid-infrared
NHE	Normal hydrogen electrode
NI-DAQ	National Instruments Data Acquisition
NIR	Near-infrared
NR	Nonresonant

OCP	Open circuit potential
OD	Optical density
OER	Oxygen evolution reaction
OPA	Optical parametric amplifier
PCMW2D	Perturbation correlation moving window two dimensional
PCX	Planoconvex
PEC	Photoelectrochemical cell
PEEK	Polyether ether ketone
PEM	Proton exchange membrane
PIA	Photoinduced absorption
PLA	Polylactic acid
PLD	Pulsed laser deposition
PS	Phase-sensitive
PTFE	Polytetrafluoroethylene
PV	Photovoltaic
PZC	Point of zero charge
pzc	Potential of zero charge
R	Resonant
RHE	Reversible hydrogen electrode
SC	Spray-coated
SCL	Space charge layer
SCLJ	Semiconductor liquid junction
SEM	Scanning electron microscopy
SERRS	Surface enhanced resonance Raman spectroscopy
SERS	Surface enhanced Raman spectroscopy
SFG	Sum frequency generation
SHG	Second harmonic generation
SHIN(s)	Shell-isolated nanoparticle(s)
SHINERS	Shell-isolated nanoparticle-enhanced Raman spectroscopy
SP	Short-pass
SPR	Surface plasmon resonance
T	Temperature
t_0	Zero time delay
TAS	Transient absorption spectroscopy
TCO	Transparent conducting oxide
TEM	Transmission electron microscopy
UV	Ultraviolet
VB	Valence band
VIA	Voltage induced absorption
VIS	Visible
VSFG	Vibrational sum frequency generation
W_{SC}	Space charge layer width

Table of Contents

Chapter 1

Introduction

1.1. Solar fuel generation:

Developing secure and sustainable sources of energy is perhaps one of the greatest challenges facing humanity in the 21st Century. The problem is compounded by a combination of increasing energy demands due to economic and population growth, as well as a growing aversion to conventional fossil fuel-based resources. Available solar energy is more than sufficient for worldwide energy needs, with enough energy striking the Earth in ninety minutes to cover global annual consumption for one year.[1] However efficiently harvesting and storing this energy remain difficult problems. For example, current solar photovoltaic (PV) devices can efficiently convert sunlight into electrical energy and are forecast to meet a significant proportion of energy demands while the sun is shining,[2] but the intermittency of sunlight mean that there would be a deficit in energy at night and on cloudy days. In a grid-based energy infrastructure this deficit will ultimately need to be met by another energy source, limiting complete reliance on PV devices. Solar fuel generation is a process that uses energy from sunlight to drive the production of a high energy density fuel from abundant or waste resources. Thus, "harvesting" the fuel during daylight and using it when (and where) it is needed solves the problem of intermittency of sunlight.

The simplest solar fuel is hydrogen, which can be generated from the splitting of water using solar energy to yield H_2 and O_2:

$$2H_2O \rightarrow O_2 + 4H^+ + 4e^+ \qquad E^O = 1.23\ V\ vs\ RHE$$

Eq. 1.1

$$4H^+ + 4e^- \rightarrow 2H_2 \qquad E^O = 0\ V\ vs\ RHE$$

Eq. 1.2

$$2H_2O \rightarrow 2H_2 + O_2 \qquad E^O_{cell} = 1.23\ V$$

Eq. 1.3

Fuel cells can then be used to carry out the reverse reaction to generate electricity. Water splitting produces hydrogen as the solar fuel, but organic solar fuels can also be made by introducing a carbon source, such as carbon dioxide to the water splitting reaction.[3] Depending on their form, these organic solar fuels can either be used to directly generate electricity or further processed using established Fischer-Tropsch chemistry to generate conventional liquid fuels that can be used as drop-in substitutes in existing fossil fuel-based infrastructure.[4] Furthermore, by combining solar fuel generation with modern carbon capture methods, the process can also approach carbon neutrality.

There are numerous ways of generating fuels from sunlight, including combining solar PV with an electrolyser, where electricity generated by the PV panel is used drive a polymer electrolyte membrane (PEM) electrolyser.[5] Direct photocatalysts are another option, utilising solar energy to drive chemical reactions without the external circuit.[6] The focus in this project will be on photoelectrochemical cells (PECs), which combine the light absorption and catalytic reactions in a single device. A PEC is an electrochemical cell where at least one of the electrodes is a semiconductor material with a band gap which is responsive to at least a portion of the solar spectrum, allowing it to act as a photoelectrode. In all the cases shown in Figure 1, oxidising and reducing catalytic centres (or equivalents) are required and their catalytic mechanisms are often unknown.

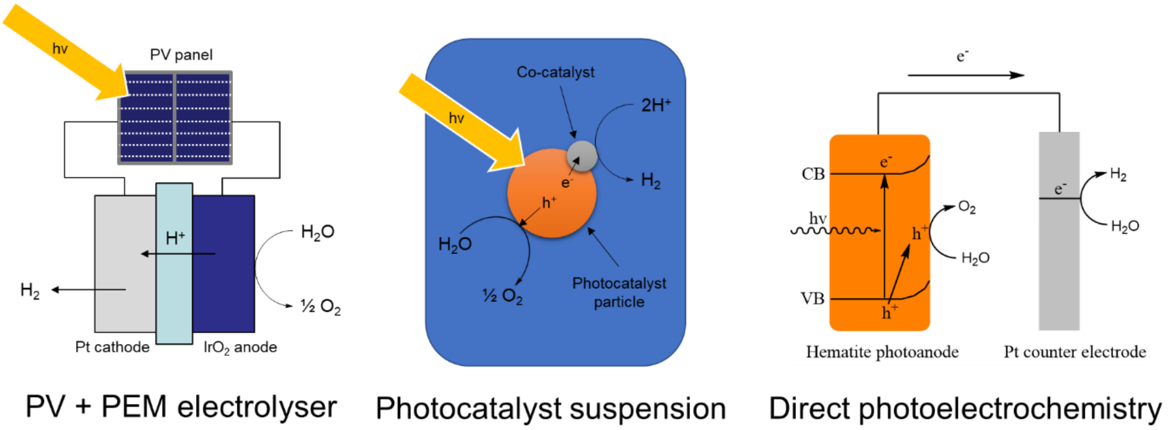

Figure 1: Diagram showing three routes for solar fuel generation with a PV panel coupled to a PEM electrolyser (left), a photocatalyst suspension (centre) and a photoelectrochemical cell (right).

1.2. Semiconductor photoelectrodes:

Many of the most promising routes to solar fuels rely on semiconductor materials. The key property of these materials can be described by the band model of electronic structure in solids. These properties will be summarised here based on various pieces of introductory literature.[7,8] Semiconductors contain a filled valence band and an empty conduction band. The difference between the valence (E_{vb}) and conduction bands (E_{cb}) energies is known as the bandgap (E_{bg}). The Fermi level energy (E_F), which can be thought of as the electrochemical potential, lies somewhere within this bandgap. For an intrinsic (undoped) semiconductor E_F lies close to halfway between E_{vb} and E_{cb}, though the addition of impurities, known as dopants, can shift the position of E_F. Electron donating dopants are known as n-type and shift E_F towards E_{cb}, while electron accepting dopants are known as p-type and shift E_F towards E_{vb}. In an electrochemical experiment the position of E_F in the semiconductor can be shifted up or down by applying a bias voltage using a potentiostat, just like in metal electrodes. However, unlike in metal electrodes, absorption of photons with energies greater than E_{bg} in the semiconductor can excite electrons from the valence band to the conduction band, leaving behind a mobile hole in the valence band. These photo-excited charge carriers can also be used to carry out redox reactions such as splitting water, enabling solar fuel generation.

Key to the action of semiconductor photoelectrodes is the interfacial electric field that enables efficient separation of charges. This can arise when immersing the semiconductor in an aqueous electrolyte, which leads to the formation of a semiconductor liquid junction (SCLJ). The difference in potential between E_F and the redox potential of the electrolyte is balanced by a transfer of electrons. Depending on the position of E_F relative to the potential of the electrolyte, this either causes a depletion or accumulation of electrons within the semiconductor. A special case arises when E_F matches the potential of the electrolyte, which is known as the flat band potential (E_{fb}). Otherwise, a net charge results over a small interfacial region in the semiconductor, known as the space charge layer. The presence of this space charge layer generates a linearly varying electric field between the semiconductor-electrolyte interface and the bulk of the semiconductor. As a result, the electrical potential varies parabolically over this space charge layer, represented by the bending of the valence and conduction bands in Figure 2. Here the bands bend upwards as the n-doped photoanode had an E_F above that of the electrolyte, which caused electrons to flow into the electrolyte, leaving a positive space charge layer. Bending in the opposite direction occurs when E_F is below that of the electrolyte.

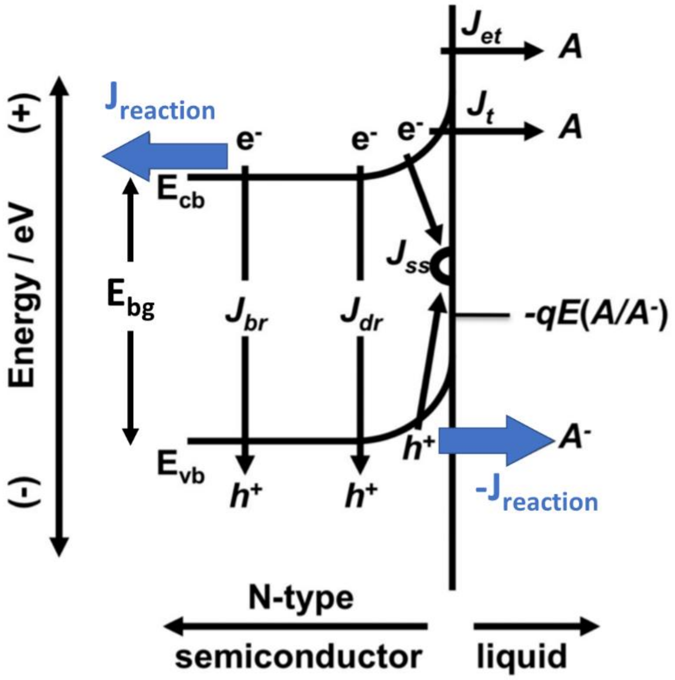

Figure 2: Diagram showing the current densities associated with various electron transfer pathways at an n-type photoanode immersed in an electrolyte, adapted with permission from a review article by Walter et al.[8] *The blue arrows represent the intended reaction pathways for a photoanode, where holes are transported to the surface to oxidise a solution species and the electrons are transported through the bulk to the back contact and transported through an external circuit to a counter electrode. The black arrows represent deleterious pathways, where* J_{br} *represents recombination in the bulk semiconductor,* J_{dr} *is recombination in the depletion region,* J_{ss} *is recombination due to defect surface states,* J_{et} *is the electron transfer current between the semiconductor and a redox species in the liquid and* J_t *corresponds to a flow of electrons due to quantum tunnelling close to the interface.*

The processes represented in Figure 2 describe the movement of charges after photoexcitation in an n-type photoanode. The simplest way for this excited system to return to equilibrium would be for the electron and hole to recombine, either radiatively (with the emission of a photon) or non-radiatively (where the energy is lost through thermal processes), both of which can be represented by the bulk recombination current (J_{br}). In order to carry out a redox reaction, a charge carrier must move to the surface to enable charge transfer with the electrolyte. This is often a bottleneck in many photocatalysts and photoelectrodes as the charge carrier mobility must be high enough to outcompete J_{br}. The space charge field plays an important role in helping separate these charges, which in this case takes the form of a depletion layer close to the interface. The upward band bending from the depletion region helps transport holes to the surface of the photoanode to carry out oxidation reactions, while the electrons can be transported through the electrical circuit to the counter electrode to carry out the reduction reaction. The favourable electric field gradients in the depletion region mean that any charge carriers generated close to this region are much less likely to recombine. Thus, recombination within the depletion region (J_{dr}) is typically much less than J_{br}, though this ratio can be significantly influenced by dopant concentrations, film thickness and nano-structuring.

This setup describes a photoanode optimised to transport holes to the surface to carry out oxidation reactions. However, sufficiently energetic electrons can overcome the upward band bending to transfer to solution species, described by J_{et}. Additionally, electrons close to the surface can also tunnel through this barrier, giving rise to J_t. Defects in the crystal structure at the surface of the semiconductor give rise to mid bandgap electronic states. These states may not have favourable energetics to oxidise or reduce species in solution, which can lead to trapped charges at the surface. Thus, these surface states can also act as centres for recombination, represented by J_{ss}.

The complexity of the water oxidation reaction makes it hard to find a material that satisfies all the requirements for an efficient photoelectrode. The semiconductor material needs to have a suitably sized band gap that is small enough to absorb a reasonable portion of solar radiation, but not too small as to result in thermalisation losses. The energies of the valence and conduction band edges must also overlap favourably with the reduction and oxidation potentials of the OER and HER. Valence band edges of some of the commonly studied semiconductors can be seen in Figure 3 from Grätzel's review of photoelectrochemical cells.[9] Once these criteria are satisfied, the photoelectrochemical cell will work, however it may not be efficient or cost-effective. For the material to reach commercial success it would also be desirable for it to be non-harmful, cheap, abundant and stable.

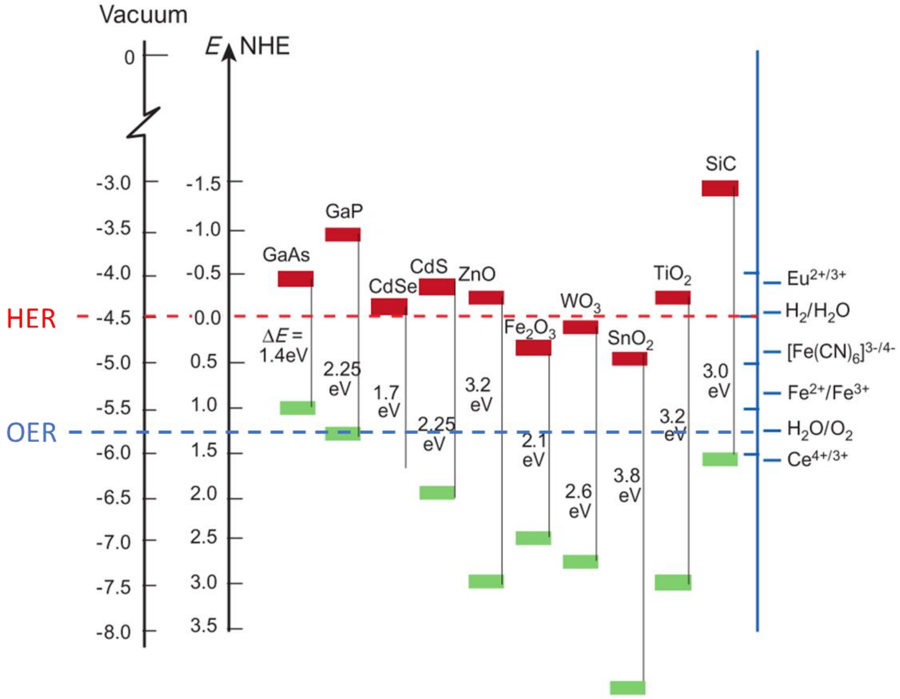

Figure 3: Band edge positions of common semiconductors in relation to some relevant redox potentials, including the hydrogen evolution reaction (HER) and oxygen evolution reaction (OER), involved in water splitting. Adapted with permission from Grätzel's 2001 review of photoelectrochemical cells.[9]

Semiconducting metal oxides, such as Fe_2O_3, TiO_2 and WO_3, show some promise as photoanodes as they have appropriate band gaps and are cheap, abundant and generally stable. E_{vb} lies well below the OER potential for all three materials, enabling them to act as photoanodes to oxidise water. To carry out the reduction reaction E_{cb} should lie sufficiently above the HER potential, which is not the case for Fe_2O_3 and WO_3 and not sufficiently above for TiO_2. These photoanodes can instead be combined with a metal counter electrode to carry out the corresponding reduction reaction and photoelectrochemically split water. A bias voltage is applied with a potentiostat to raise E_F in the metal above the HER potential, while simultaneously lowering it in the photoanode, enhancing charge carrier separation.

These competing recombination pathways make it difficult for the charge carriers to reach the appropriate interfaces, detrimentally affecting device performance. However, the kinetics of the interfacial redox reactions themselves can also represent a major challenge. Water splitting involves the transfer of 4 electrons and holes, the mechanism of which can vary drastically across different materials and experimental conditions. Inefficiencies in electron transfer, or the steps preceding electron transfer, between the electrode and species in solution manifest themselves as an overpotential. This overpotential is an additional potential difference beyond that based solely on the difference in thermodynamic potentials of the HER and OER. While the semiconductors discussed above can be thought of as OER catalysts, they generally have prohibitively high overpotentials. Co-catalysts are materials that can be added to the semiconductor surface that exhibit much lower overpotentials, which can drastically improve the OER kinetics. This lower overpotential is achieved by accessing alternative reaction pathways, the mechanisms of which are often unknown. Examples of active co-catalysts for the OER include iridium and cobalt oxides, which can, in the case of iridium oxide, lower the overpotential of hematite photoanodes by up to 300 mV.[10,11] While such co-catalysts can significantly improve device performance, their increased cost can be prohibitive for larger scale deployment.

Developing efficient catalysts for solar fuel generation can be accelerated with an improved understanding of the underlying mechanistic details. Studying the active, but prohibitively expensive, OER catalysts can provide insights into efficient mechanistic pathways. In particular, understanding the cause of inefficiencies in more abundant water oxidation catalysts can be used to guide improvements for future catalytic materials. As a common step in generating almost all solar fuels, understanding the mechanism of water oxidation is therefore especially important. A wide variety of methods can be used to investigate OER mechanisms at photoelectrode surfaces. Operando X-ray absorption spectroscopies have been used to identify band edges and energetics of important surface states.[12–15] Transient absorption spectroscopy can be used to monitor charge transfer dynamics.[16–20] Further insights into surface states and charge transfer mechanisms can also be gained by electrochemical impedance spectroscopy (EIS).[21,22] *In situ* vibrational spectroscopies in particular can directly access structural information of OER intermediates and will be explored in more detail below.

1.3. *In situ* vibrational spectroscopy at semiconductor photoelectrodes:

Several recent reports have spectroscopically determined the structure of key intermediates in the photoelectrochemical water splitting reaction on different materials using Fourier-Transform Infrared (FTIR) spectroscopy.[23] Frei *et al.* observed two surface intermediates thought to be involved in water oxidation on cobalt oxide nanoparticles using rapid-scan FTIR: a cobalt superoxide (at 1013 cm^{-1}) and a cobalt oxo species (at 840 cm^{-1}).[24] This time-resolved data showed that the two species display independent kinetics, suggesting two alternative catalytic sites exist on the Co_3O_4 surface. Time resolution in this experiment is achieved by rapidly recording a series of FTIR spectra during and after pulsed illumination of a suspension of Co_3O_4 nanoparticles. These nanoparticles are suspended in a solution containing an excess of photosensitiser and electron acceptor molecules. In this case a 300 ms laser pulse at 476 nm excites a $[Ru(bpy)_3]^{2+}$ photosensitiser complex in solution, which transfers an electron to a persulfate electron acceptor to form $[Ru(bpy)_3]^{3+}$. Collision of these oxidised $[Ru(bpy)_3]^{3+}$ complexes with cobalt oxide nanoparticles can initiate the water oxidation reaction by transfer of a hole, with four total electron/hole transfers required to complete the reaction. By recording FTIR spectra during and after illumination, the time evolution of surface intermediates at these catalytic nanoparticles can be followed. The superoxide, a three-electron intermediate, grows at a fast catalytic site and evolves oxygen within the 300 ms pulse, while the oxo species does not advance beyond a one-electron intermediate in the same time period. The proposed mechanism for the fast catalytic site, shown in Scheme 1 (a), involves two cobalt centres connected via bridging oxygen atoms. The proximity of the two centres allows for electronic coupling between adjacent Co(IV), increasing the oxidising strength of the species and providing a site to deprotonate water. Conversely, the slow site, Scheme 1 (b), lacks such a neighbouring group, making the O-O bond formation step much slower and no oxygen is released. Again, many intermediates are proposed in the mechanism but only the three-electron intermediate was observed spectroscopically. In such experiments the rate-limiting intermediates are more likely be detected as they will accumulate over time, while earlier (and later) intermediates will only be transiently present at the surface. Improving time-resolution and sensitivity in the measurements is required to get a full picture of the mechanism of water oxidation on metal oxides.

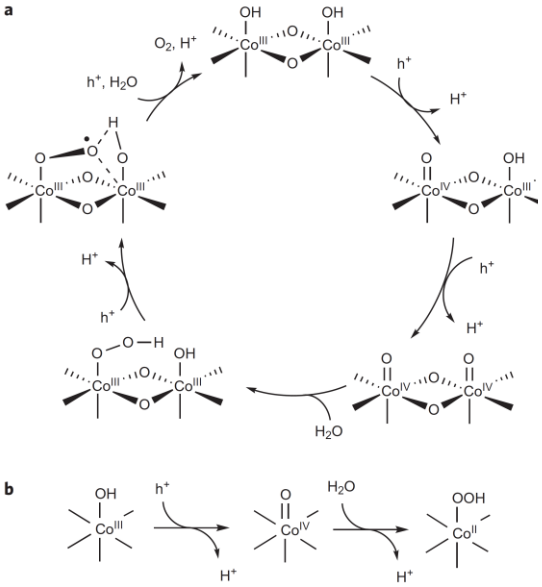

Scheme 1: Proposed mechanisms of water oxidation on cobalt oxide, involving (a) a fast catalytic centre that evolves oxygen and (b) a slower centre that does not evolve oxygen within a 300 ms pulse reproduced with permission from Frei et al.[24]

Some of the problems associated with identifying other intermediates in the above reports were due to interference from bulk water, especially the tumbling motion of water below 800 cm^{-1}. To avoid this interference, the researchers used D_2O as the solvent instead of H_2O to achieve greater transmission in the spectral region of interest. Another way of avoiding interference from bulk solvent signal is to probe through a small layer of solvent using attenuated total reflectance (ATR) IR spectroscopy. The infrared beam is reflected through an ATR prism, where each reflection produces an evanescent wave that propagates a short distance into the sample. The photoelectrode surface can be studied by minimising the distance between the metal oxide surface and the ATR prism to allow the evanescent wave to reach the surface. Using a D_2O-based electrolyte, as well as reducing the electrolyte path length between the electrode and the prism lowers the extraneous signal from the water, leading to an improved signal, especially below 800 cm^{-1}. The ATR-IR setup used by Zandi and Hamann for spectroelectrochemical study of thin film hematite electrodes is shown in Figure 4, using a 395 nm LED as the illumination source.[25] In this setup the infrared beam is reflected in the prism multiple times, increasing the size of the signal with each reflection.

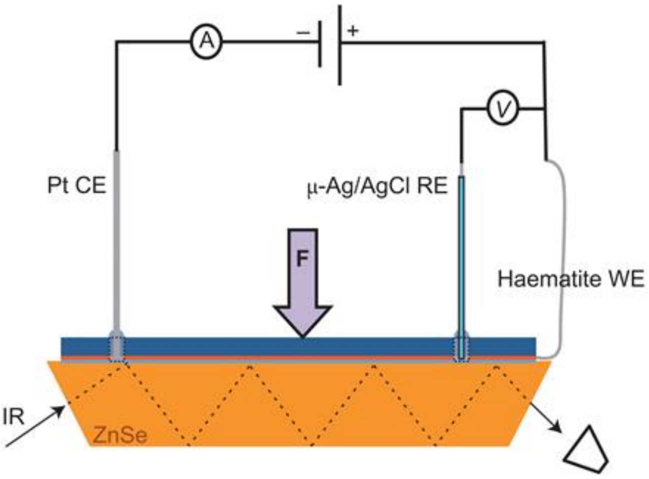

Figure 4: ATR-IR setup for photoelectrochemical measurements used by Zandi and Hamann (reproduced with permission),[25] *where the hematite working electrode is pressed up close to the ZnSe ATR prism with only a thin layer of D_2O-based electrolyte in the middle. Contact points for the working and counter electrodes are drilled through the hematite electrode to maintain the thin pathlength.*

Using this setup, a photoinduced vibrational band at 898 cm^{-1} assigned to an iron oxo species was observed, which is thought to be the first intermediate of water oxidation on hematite.[25] By monitoring the evolution of this peak under the working conditions of the cell, they propose the mechanism shown below in Scheme 2, which is analogous to the mechanism on cobalt oxide shown previously in Scheme 1.

$$\mathrm{R{-}Fe^{III}{-}OH \xrightarrow{h^+} R{-}Fe^{IV}{=}O + H^+}$$

$$\mathrm{R{-}Fe^{IV}{=}O + H_2O \xrightarrow{h^+} R{-}Fe^{III}{-}O{-}O{-}H + H^+}$$

$$\mathrm{R{-}Fe^{III}{-}O{-}O{-}H \xrightarrow{h^+} R{-}Fe^{III} + O_2 + H^+}$$

$$\mathrm{R{-}Fe^{III} + H_2O \xrightarrow{h^+} R{-}Fe^{III}{-}OH + H^+}$$

Scheme 2: Proposed mechanism for water oxidation at a hematite electrode from Zandi and Hamann.[25]

While the *in situ* vibrational techniques outlined above provide direct detection of some OER intermediates, the proposed mechanistic cycles require further detection of proposed intermediates to fully validate the mechanisms. This project will investigate the application of several alternative techniques for studying electrode interfaces with a focus on improved surface sensitivity to enable detection of low concentrations of transient surface intermediates. Chapter 2 will introduce a surface enhanced Raman technique, known as shell-isolated nanoparticle-enhanced Raman spectroscopy (SHINERS) and detail its application to the study of various electrode surfaces under OER conditions. Chapter 3 explores the use of a surface-selective nonlinear vibrational spectroscopy called sum frequency generation (SFG) spectroscopy and uses it to study interfacial water structure at photoelectrode surfaces. Finally, Chapter 4 investigates the application of photoinduced absorption (PIA) spectroscopy and electric field-induced second harmonic generation (EFISHG) spectroscopy to address charge carrier kinetics, surface trap states and interfacial electric fields. Almost all aspects of the project involved building new experimental setups within our lab that have not previously been applied to semiconductor OER catalysts within the literature. This necessitated development of new spectroelectrochemical cells, electrode geometries and custom ultrafast laser setups, all of which are detailed either in their respective Chapters or in the Appendices.

1.4. References:

1 IEA (2011), Solar Energy Perspectives, https://www.iea.org/reports/solar-energy-perspectives.

2 E. Dupont, R. Koppelaar and H. Jeanmart, *Appl. Energy*, 2020, **257**, 113968.

3 L. Lyu, F. Jin, H. Zhong, H. Chen and G. Yao, *RSC Adv.*, 2015, **5**, 31450–31453.

4 A. Y. Khodakov, W. Chu and P. Fongarland, *Chem. Rev.*, 2007, **107**, 1692–1744.

5 R. E. Clarke, S. Giddey, F. T. Ciacchi, S. P. S. Badwal, B. Paul and J. Andrews, *Int. J. Hydrogen Energy*, 2009, **34**, 2531–2542.

6 X. Chen, S. Shen, L. Guo and S. S. Mao, *Chem. Rev.*, 2010, **110**, 6503–6570.

7 L. M. Peter, in *Photocatalysis: Fundamentals and Perspectives*, 2016, pp. 1–28.

8 M. G. Walter, E. L. Warren, J. R. Mckone, S. W. Boettcher, Q. Mi, E. A. Santori and N. S. Lewis, *Chem. Rev.*, 2010, **110**, 6446–6473.

9 M. Grätzel, *Nature*, 2001, **414**, 338–344.

10 B. Klahr, S. Gimenez, F. Fabregat-Santiago, J. Bisquert and T. W. Hamann, *J. Am. Chem. Soc.*, 2012, **134**, 16693–16700.

11 L. Badia-Bou, E. Mas-Marza, P. Rodenas, E. M. Barea, F. Fabregat-Santiago, S. Gimenez, E. Peris and J. Bisquert, *J. Phys. Chem. C*, 2013, **117**, 3826–3833.

12 D. S. Ellis, A. Tsyganok, P. Ghigna, A. Minguzzi, A. Naldoni, V. Murzin, W. Caliebe and A. Rothschild, *Langmuir*, 2020, **36**, 11564–11572.

13 C. Pasquini, S. Liu, P. Chernev, D. Gonzalez-Flores, M. R. Mohammadi, P. Kubella, S. Jiang, S. Loos, K. Klingan, V. Sikolenko, S. Mebs, M. Haumann, P. Beyer, L. D'Amario, R. D. L. Smith, I. Zaharieva and H. Dau, *Anal. Bioanal. Chem.*, 2021, **413**, 5395–5408.

14 L. Li, J. Yang, H. Ali-Löytty, T. C. Weng, F. M. Toma, D. Sokaras, I. D. Sharp and A. Nilsson, *ACS Appl. Energy Mater.*, 2019, **2**, 1371–1379.

15 V. A. Saveleva, L. Wang, D. Teschner, T. Jones, A. S. Gago, K. A. Friedrich, S. Zafeiratos, R. Schlögl and E. R. Savinova, *J. Phys. Chem. Lett.*, 2018, **9**, 3154–3160.

16 J. Tang, J. R. Durrant and D. R. Klug, *J. Am. Chem. Soc.*, 2008, **130**, 13885–13891.

17 Z. Huang, Y. Lin, X. Xiang, W. Rodríguez-Córdoba, K. J. McDonald, K. S. Hagen, K.-S. Choi, B. S. Brunschwig, D. G. Musaev, C. L. Hill, D. Wang and T. Lian, *Energy Environ. Sci.*, 2012, **5**, 8923.

18 G. X. Pei, J. H. J. Wijten and B. M. Weckhuysen, *Phys. Chem. Chem. Phys.*, 2018, **20**, 9806–9811.

19 A. T. Paradzah, M. Diale, K. Maabong and T. P. J. Krüger, *Phys. B Condens. Matter*, 2017, **535**, 138–142.

20 M. Forster, D. W. F. Cheung, A. M. Gardner and A. J. Cowan, *J. Chem. Phys.*, 2020, **153**, 150901.

21 Gurudayal, L. M. Peter, L. H. Wong and F. F. Abdi, *ACS Appl. Mater. Interfaces*, 2017, **9**, 41265–41272.

22 B. Klahr and T. Hamann, *J. Phys. Chem. C*, 2014, **118**, 10393–10399.

23 M. Zhang and H. Frei, *Annu. Rev. Phys. Chem.*, 2017, **68**, 209–231.

24 M. Zhang, M. de Respinis and H. Frei, *Nat. Chem.*, 2014, **6**, 362–7.

25 O. Zandi and T. W. Hamann, *Nat. Chem.*, 2016, **8**, 778–783.

Chapter 2

In situ SHINERS of electrode surfaces

Parts of this chapter (Section 2.2.2) are published in “Water oxidation intermediates on iridium oxide electrodes probed by *in situ* electrochemical SHINERS” by K. H. Saeed, M. Forster, J. F. Li, L. J. Hardwick and A. J. Cowan, *Chem. Commun*., 2020, **56**, 1129-1132. All the experimental data shown was recorded and interpreted by myself with additional help from M. Forster, J.C. Dong, J. Wu and J. F. Li in the initial synthesis of the SHIN’s and the design of the spectroelectrochemical cell.

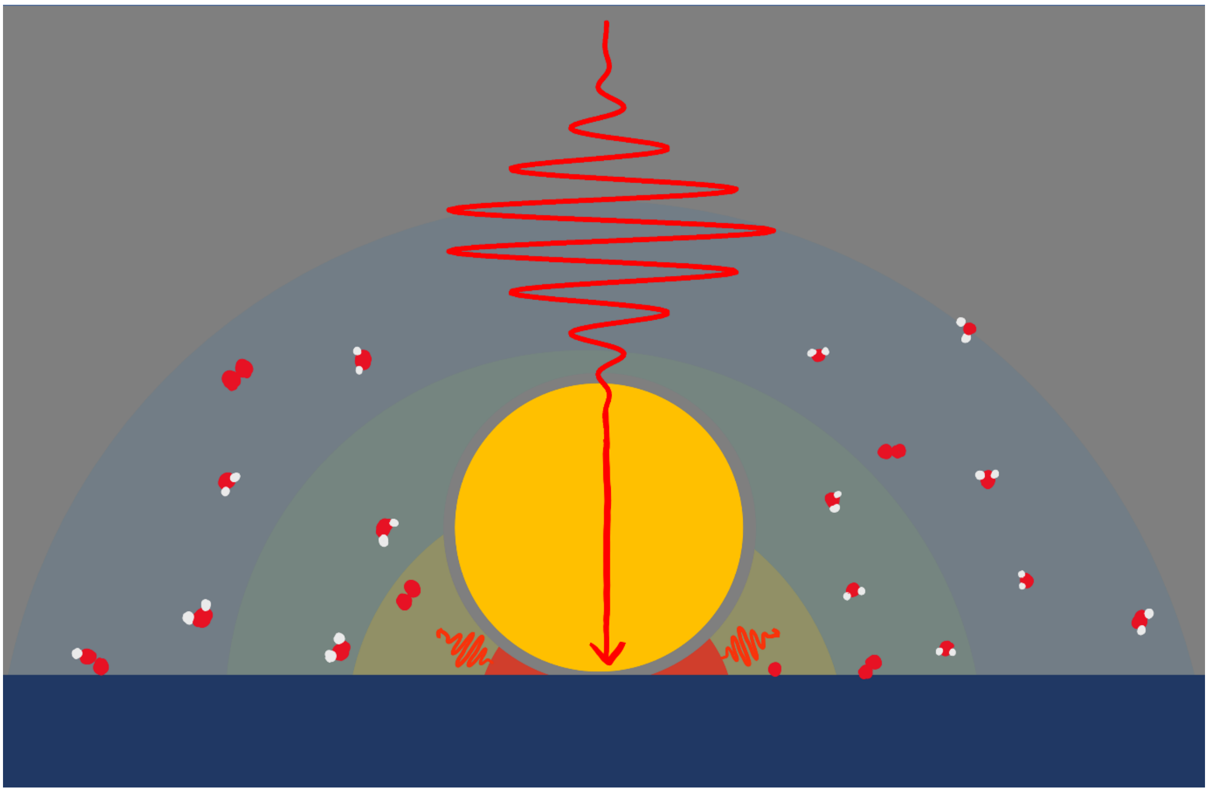

2.1. Introduction:

2.1.1. SHINERS background:

In situ Raman spectroscopy is an especially promising technique for studying the aqueous electrode surfaces involved in water splitting as many of the proposed intermediates for these reactions are expected to have vibrational modes below 1000 cm^{-1}. This spectroscopic region is much harder to probe experimentally using infrared spectroscopy (and by extension sum frequency generation spectroscopy, which will be discussed in the next Chapter) due to significant attenuation of IR light by water itself at this wavelength. By using visible light to probe vibrational modes, Raman spectroscopy overcomes this drawback as water has much greater transparency across the visible spectrum.

Raman spectroscopy relies on detecting inelastically scattered photons (Stokes or Anti-Stokes scattering from Figure 5), where the difference in energy between incident and scattered photons corresponds to the energy of a molecular vibration. In a typical Raman experiment most photons are scattered elastically (Rayleigh scattering), giving no structural information; in many cases only around 1 in 10^8 are inelastically scattered, resulting in an inherently weak Raman signal.[1] This weak signal can be enhanced by many orders of magnitude through localised surface plasmon resonances (LSPRs) on the roughened surfaces of some metals.[2] These plasmon resonances arise due to oscillations of electrons within the plasmonic material at the same frequency of the incident light. This provides a significant (and highly localised) enhancement to the electric field at the incident frequency, which in turn induces stronger oscillating dipoles within the material being probed (at the Raman scattered frequencies). The resulting electric field from the Raman scattered photons can then also be enhanced by the plasmon resonance, providing a further enhancement to the Raman signal.[3] Surface-enhanced Raman spectroscopy (SERS) makes use of these phenomena to gain surface-sensitive structural information since only species close to the plasmonic surface are enhanced enough to give an appreciable SERS signal. Using the surface plasmon resonance on gold and silver nanoparticles has even allowed the detection of single molecules at surfaces.[4,5] The processes discussed so far have also assumed that the incident photon is not resonant with any electronic transitions within the material, presented as virtual excited states in Figure 5. Resonance with real electronic excited states can also increase the Raman signal, giving rise to so-called resonance Raman spectroscopy. Resonance with charge transfer transitions between the analyte being studied and a SERS substrate can also provide a further mechanism for enhancement, known as surface-enhanced resonance Raman spectroscopy (SERRS).

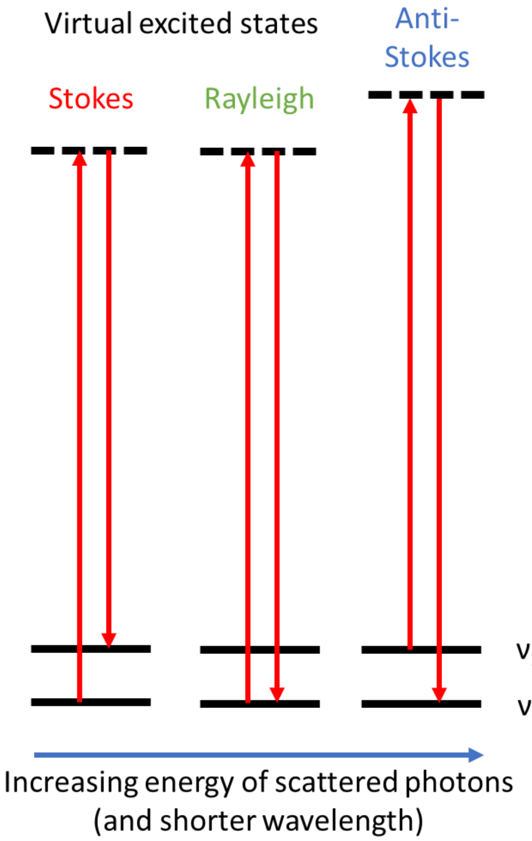

Figure 5: Energy level diagram highlighting the key transitions involved in the scattering processes related to Raman spectroscopy.

Shell-isolated nanoparticle-enhanced Raman spectroscopy (SHINERS) is a novel approach to SERS, where the enhancement is provided by nanoparticles encapsulated within an inert shell.[6] To create these shell-isolated nanoparticles (SHINs), the bare plasmonic nanoparticles (*e.g.* Au or Ag) were covered in a thin (around 2 nm) inert shell material, such as SiO_2 and Al_2O_3. SHINs with alternative shell materials, including TiO_2,[7] SnO_2,[8] MnO_2[9] and graphene[10] have since been synthesised, each with different chemical stability and surface enhancing properties. These SHINs can be dropped onto the surface of any sample, thus overcoming the constraints of traditional SERS, where only a limited number of SERS-active substrates are available. The inert shell eliminates concerns of the nanoparticles metal core affecting the (electro-) chemistry and is thin enough to still give enhancement to the Raman signal, greatly broadening the applicability of enhanced Raman spectroscopies. The relative ease of synthesis and broad applicability of SHINERS has been exploited in various fields in recent years, including heterogeneous catalysis,[7,11] bioanalysis,[12,13] food safety[6] and *in situ* electrochemistry.[14–29]

Figure 6 (from a review by Ding *et al.*)[30] shows simulated magnitudes of the Raman enhancement when 2 SHINs are in close proximity on metal and semiconductor surfaces. In both cases there is a substantial enhancement between the 2 nanoparticles (circled in white), but crucially for the *in situ* electrochemical experiments there is also a significant enhancement at the contact between the nanoparticle and the electrode surface (circled in red). Thus, any intermediates formed on the electrode surface close to the SHINs will experience a large enhancement in their Raman response. The experiments described in this chapter use a simple drop-casting method for depositing the SHINs where the distance between the nanoparticles on an electrode surface is not controlled, so the major contribution to the enhanced signal will come from regions highlighted in red circles in Figure 6. While molecules located in the gap between two nanoparticles (white circle in Figure 6) would experience the largest enhancement, there is no way in our electrochemical experiments to control the position of analytes to exploit the enhancement in this gap.

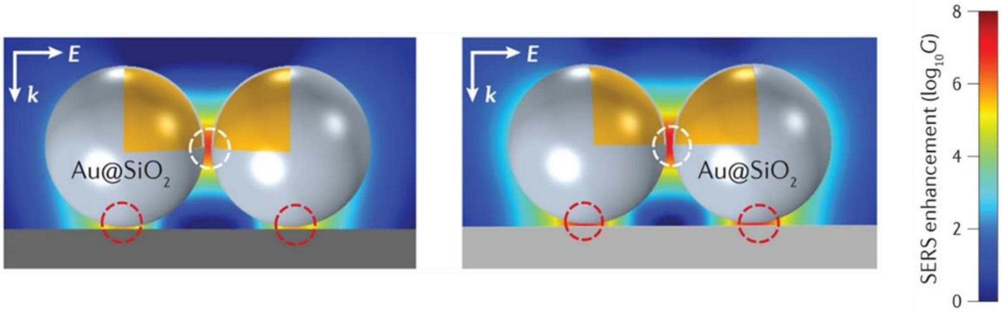

Figure 6: Representation of a shell-isolated gold nanoparticle at a semiconductor (left) and metal (right) electrode surface, highlighting the localised field enhancement close to the nanoparticle-surface interface in red, and the decay of this field further away from the nanoparticle (blue). Molecular vibrations within this red region will experience significant electric field enhancement, giving rise to a SHINER spectrum. This figure is adapted (with permission) from a review by Ding et al.[30]

The surface sensitivity of SHINERS is especially appealing for studying electrochemical systems as the important mechanistic processes necessarily occur at a surface (*i.e.* the electrode/electrolyte interface). To this end, many groups have exploited the surface-sensitivity of SHINERS to study electrochemical interfaces, which have been highlighted in several recent reviews.[23,31–33] Until now, many of the *in situ* electrochemical applications of SHINERS have been limited to the study of single-crystal surfaces. Part of this project will aim to extend the applications of the SHINERS technique to investigate state-of-the-art materials for water splitting, which often have nanostructured surfaces.

2.1.2. Iridium oxide SERS:

The high sensitivity and wide-ranging applications of the SHINERS technique are appealing for studying the semiconductor photoelectrodes introduced in Chapter 1. However, before studying the more-complicated photoelectrodes, a (dark) electrocatalytic system was chosen as a stepping-stone-type experiment in order to develop the experimental methodology for studying electrodes *in situ* using SHINERS. This initial work focused on studying iridium oxide (IrO_x) electrodes for water splitting since (i) IrO_x represents the leading, and arguably only viable oxygen evolution catalyst for use in PEM electrolysers and (ii) there is already established literature on mechanistic studies of IrO_x using conventional SERS[34,35] Therefore choosing to study the mechanism of water oxidation by IrO_x as a starting point allows us to both develop the *in situ* SHINERS technique with a literature source to corroborate results and also to further increase our understanding of this important catalyst. In particular it is anticipated that SHINERS may help address confusion regarding assignments of vibrational modes at <600 cm^{-1} which was complicated in the SERS studies due to the presence of the Au surface (and gold oxide modes), as there is no exposed gold in our SHINERS experiment.

Hydrated amorphous iridium oxides (IrO_x, typically synthesised electrochemically) have consistently been shown to be significantly more active than their Rutile crystalline analogues (IrO_2, grown by thermal oxidation).[35–37] Initially it was thought that the key to this activity was correlated with the detection of a reactive and electrophilic O^{1-} species only present in the hydrous IrO_x electrodes by X-ray absorption spectroscopy.[36,37] This reactive oxygen species was thought to be directly involved with the rate-determining O-O bond formation step. However later studies also found this same species in thermally grown IrO_2, instead citing the improved structural flexibility of the hydrated IrO_x structure as the reason for its improved performance.[38] Further studies under operating conditions could be used to address these mechanistic questions.

IrO_x electrodes are known to undergo two oxidation steps in a CV prior to the catalytic OER onset, where the first oxidation peak involves transformation of Ir^{3+} centres to Ir^{4+} and the second oxidation peak corresponds to Ir^{4+} to Ir^{5+}.[39] However, the charge related to the second oxidative step (*i.e.* the area under the second oxidation peak) is usually smaller than the first, suggesting a comparatively smaller proportion of the electrode is transformed into this Ir^{5+} state. Furthermore, the position of these redox couples shifts by more than 59 mV per pH unit (super-Nernstian), meaning that the second oxidation peak becomes almost discernible from the OER current at low pH values.[40] These partial oxidations enable charge accumulation within the IrO_x structure, which have been explored using *in situ* optical (electronic) evanescent wave spectroscopy.[41] These studies demonstrate the importance of understanding the different oxidation states within the IrO_x structure and the role of charge accumulation on water oxidation at these electrodes.

Various different mechanisms have been proposed for water oxidation at iridium oxide electrodes, which have been summarised in a recent review.[42] A brief summary of the vibrational spectroscopic findings will be presented here. Sivasankar *et al.* detected a surface hydroperoxide intermediate in the photoelectrochemical water oxidation reaction on IrO_2 nanoparticles using rapid-scan FTIR spectroscopy and a $[Ru(bpy)_3]^{2+}$ light sensitiser.[43] A band at 830 cm^{-1} appeared within 610 ms of a 1 second laser pulse at 476 nm, which is characteristic of an O-O bond stretch in a peroxide group. The same band disappears completely in the next measurement 1830 ms after the laser pulse, indicating that the intermediate has a lifetime of several hundred milliseconds at most. After confirming the assignment of an iridium hydroperoxide species using isotopic labelling, the partial mechanism shown in Scheme 3 was proposed. The detected hydroperoxide moiety is thought to be the product of nucleophilic attack of water on the iridium oxo species, forming an O-O bond.

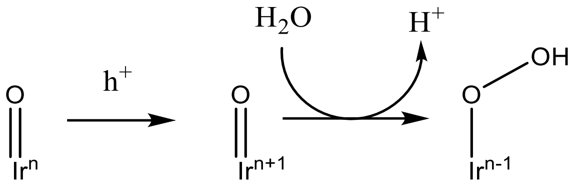

Scheme 3: Proposed mechanism of O-O bond formation on iridium oxide from Sivasankar et al.[43]

More recently Pavlovic *et al.* have investigated the electrochemical analogue to the above photochemical experiments, which should provide a better comparison to our proposed electrochemical SHINERS experiments. The potential-dependent evolution of the IrO_x thin films was followed using conventional Raman spectroscopy[35] and then later SERS on roughened gold electrodes.[34] In both cases similar changes are observed, in line with the changing oxidation state of the material (observed in bands assigned to bulk Raman modes), but crucially in the SERS experiments an additional band is observed at 771 cm^{-1} that is assigned to a surface iridium oxo mode, thought to be a catalytic intermediate in the electrochemical water oxidation reaction. The aim for these initial SHINERS experiments is then to attempt to replicate these findings, especially the detection of the surface intermediate, while ensuring there is no electroactive gold within the system by using SHINs.

2.2. Results and discussion:

2.2.1. SHINs testing:

The synthetic procedure for the SHINs is described in detail in Chapter 5.5, based on established protocols to generate ~ 50 nm diameter SHINs coated with a SiO_2 shell, the thickness of which can be controlled by varying the time of the silica coating step in the synthesis.[44] Control of the shell thickness is key for SHINERS, as thick shells limit the plasmonic enhancement experienced by the surface of interest, since the surface plasmon resonance of the gold nanoparticles only extends a few nm away from the nanoparticle.[6] The size of the nanoparticles determines the wavelength of the localised surface plasmon resonance (λ_{LSPR}). The exact dimensions of the nanoparticles and the shell thickness were measured by TEM in these previous studies and correlated to their optical properties.[6,44] Figure 7 shows λ_{LSPR} = 536 nm for the SHINs used throughout this project, consistent with SHINs ~ 50 nm in diameter. A redshift of 38 nm is observed when the SHINs are deposited on a surface compared to suspended in solution. The λ_{LSPR} of SHINs suspended in solution represents non-aggregated single SHINs, while the spectrum for SHINs deposited on a surface will contain contributions from multiple arrangements of nanoparticles (monomers, dimers *etc.*). λ_{LSPR} for these other arrangements of nanoparticles will redshift due to coupling effects when the distance between SHINs is on the order of several nm and the increased absorption at longer wavelengths represents these further aggregates when the SHINs are deposited on a surface.[45] The exact position of λ_{LSPR} will impact the choice of Raman laser wavelength; the optimum enhancement is expected when the Raman laser wavelength is slightly blue-shifted from λ_{LSPR}.[46] Initial experiments with a 532 nm Raman laser exhibited damage to the SHINs particles (see Section 2.2.4 for more details on damage to SHINs), so a 633 nm laser was used for all further Raman experiments here to avoid damaging the SHINs, while still overlapping with the LSPR of the SHINs.

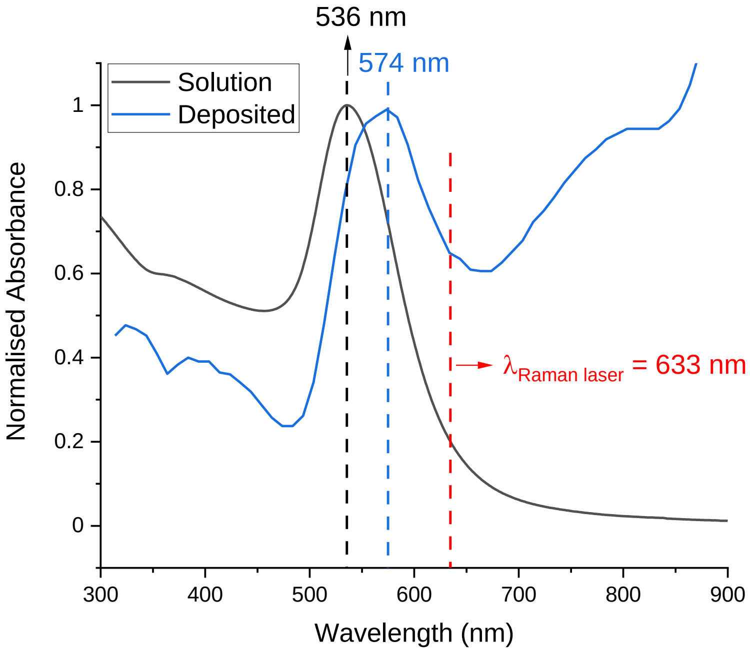

Figure 7: Transmission-mode UV-vis spectra of Au@SiO$_2$ SHINs suspended in aqueous solution (black) and dried on a microscope slide (blue), with the Raman laser wavelength highlighted at 633 nm.

Experimental evidence for the effect of shell thickness on Raman enhancement is shown in Figure 8. In this experiment the adsorption of pyridine on a gold surface is used to monitor the enhancement provided by the different shell thicknesses. Away from the SHINs particles there are no peaks observed for the pyridine ring breathing modes at 1013 and 1037 cm^{-1}. These bands only appear at these acquisition settings when there are SHINs present on the surface. The magnitude of the enhancement is greatest for the thinnest shell and the enhancement decreases with increasing shell thickness. This is consistent with the strongly distance-dependent decay of the LSPR field away from the surface, the thicker shell increases the distance between the plasmonic gold nanoparticle and the pyridine at the gold surface. As a result, the LSPR field experienced by the pyridine will be lower when a thicker shell is used, resulting in a lower Raman intensity.

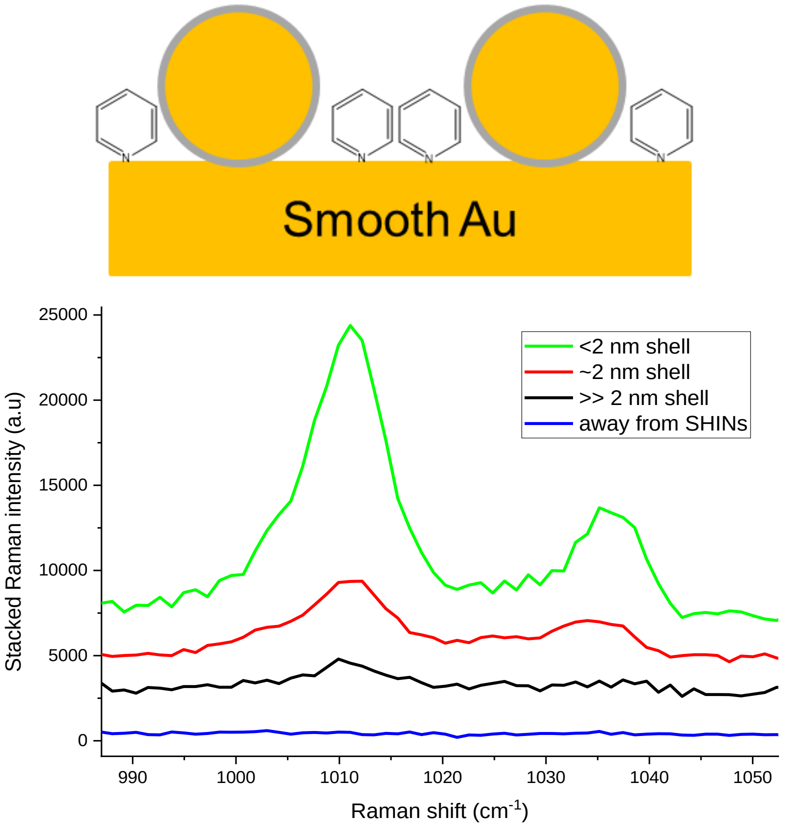

Figure 8: SHINs enhancement test. 2 µl of the SHINs suspension is dropped onto a clean gold wafer and allowed to dry in air. A drop of aqueous pyridine solution (10 mM) is sandwiched onto the gold wafer with a microscope slide cover slip and the Raman spectrum is recorded. The intensity of the ring breathing modes of pyridine adsorbed on a gold surface at 1012 and 1036 cm^{-1} are used as a test of the enhancement factor of the SHINs, where thinner shells give a larger enhancement.

However, if the shell is too thin it may contain pinholes that expose the underlying gold surface. Any molecules that adsorb to the exposed gold would produce an unwanted Raman signal that receives greater plasmon enhancement as they are even closer to the Au surface. This phenomenon can be used to test the SHINs for pinholes. As shown above, pyridine adsorbed on gold gives a strong Raman signal when enhanced. If pinhole-containing SHINs are dropped on a Si wafer (pyridine does not adsorb on Si), the pyridine can bind to the Au nanoparticle surface through the pinholes and the 1013 and 1037 cm^{-1} Raman modes can be observed. If the shell is complete, pyridine cannot bind and no such peaks will be observed. SHINs synthesis typically involves a coating step where the shell precursor is heated with the Au nanoparticles in solution. The pH of this solution, temperature and heating time all affect the thickness of the shell. Tuning these parameters allows SHINs with the appropriate shell thickness to be synthesised. The SHINs chosen for use in this study had a 2 nm shell as this strikes a good balance between inertness, enhancement and ease of synthesis though further improvements in signal size can be achieved using a thinner silica shell, at the cost of introducing more pinholes. Alternatively, larger Au cores can provide a greater electric field enhancement, however the synthetic procedures are more complex.[47]

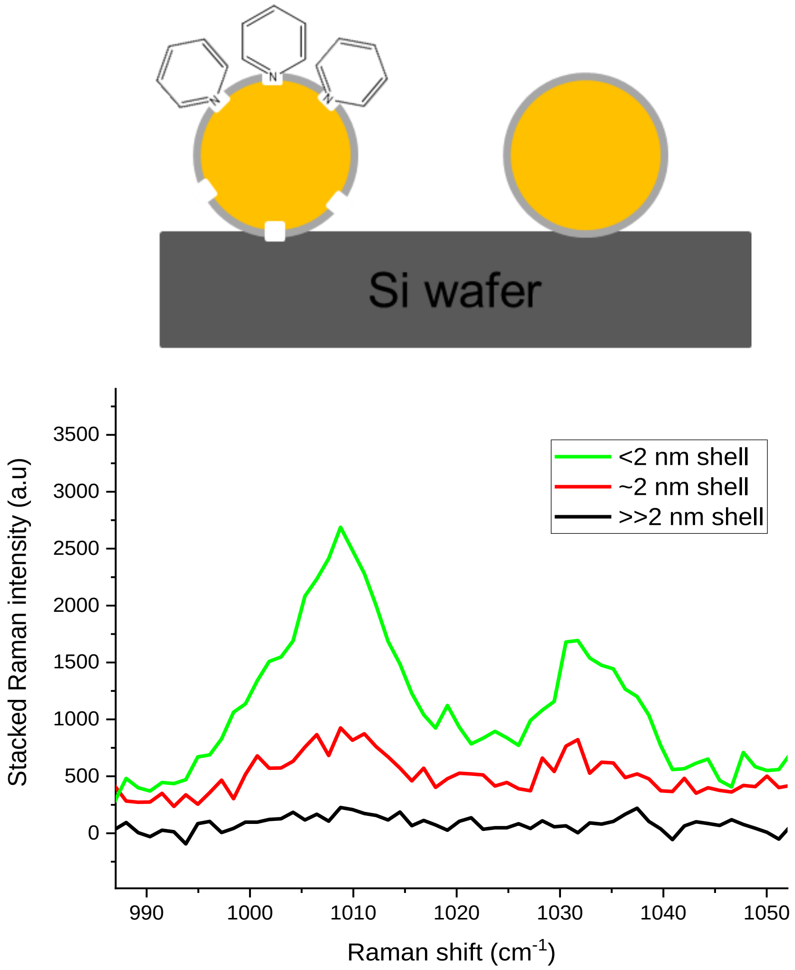

Figure 9: SHINs pinhole test. 2 µl of the SHINs suspension is dropped onto a clean silicon wafer and allowed to dry in air. A drop of aqueous pyridine solution (10 mM) is sandwiched onto the silicon wafer with a microscope slide cover slip and the Raman spectrum is recorded. Here the ring breathing modes of pyridine adsorbed on a gold surface can only be present if the pyridine can reach the gold surface of the SHINs, indicating the presence of pinholes in the SHINs.

Another key parameter in the application of SHINERS for studying surfaces is the distribution of the SHINs on the surface in question. The method of applying SHINs to surfaces that is used throughout this project was simply drop-casting, where an aqueous suspension of the SHINs is dropped onto a surface and left to dry. For the experiments shown in Figure 8 & Figure 9 the 633 nm Raman laser was focussed to a beam diameter of about 1.5 µm and the gold nanoparticles used are around 50 nm in diameter, so many SHIN particles could be present under the laser spot. Conventional drop-casting methods lead to the well-known coffee-stain effect due to faster solvent evaporation at the contact line of the drop, causing suspended particles to accumulate at these edges.[48] A significant amount of the SHINs end up in this ring where they can completely block the underlying surface. This not only reduces the area for doing experiments but also reduces the density of SHINs in the remaining areas within the ring. Figure 10 shows a Raman intensity map of the ring breathing modes of pyridine adsorbed on a gold wafer near the edge of dried SHINs drop. It is clear that the ring edges give almost no signal, but there is also spatial variation in the Raman enhancement within the ring. Attempts to overcome this problem of distribution by drying in an ethanol vapour are detailed in Appendix A, though this technique was not used for further experiments as it also introduced contaminants to the surface. Instead, a quick Raman intensity map (at much lower spatial resolution than Figure 10 to speed up acquisition) was carried out prior to potential-dependent experiments to highlight spots within the ring that provide good enhancement that could be used for the full experiments.

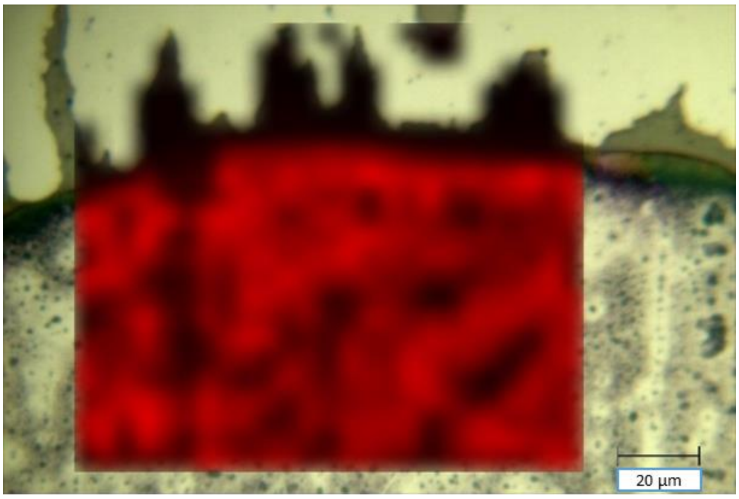

Figure 10: Raman intensity map of pyridine ring breathing mode at 1015 cm^{-1} around a drop of SHINs on a gold surface. Colour represents a peak-to-baseline value in counts, with the scale from 2000 counts (black) to 145000 counts (red). Unshaded areas within the square map area represent a peak-to-baseline value of less than 2000 counts.

2.2.2. *In situ* SHINERS on IrO_x:

IrO_x films were electrodeposited onto glassy carbon disk electrodes from a K_2IrCl_6 salt solution following the procedure laid out by Mallouk *et al.,*[49] the full synthetic procedure can be found in Chapter 5.1. The expected electrochemical response[49] for an IrO_x film is observed in Figure 11, showing the two oxidation peaks (around 0.5 and 1.0 V vs Ag/Ag^+), corresponding to oxidation of the Ir centres (discussed in more detail below) before the onset of a catalytic OER current above 1.2 V vs Ag/Ag^+. Cyclic voltammetry is also a common technique for identifying electrochemical activity from the gold particles. Even small quantities of exposed electroactive gold within the system can exhibit the characteristic redox features, including a small oxidative peak and a large, sharp reduction peak in the voltammogram. The absence of both additional peaks within the voltammograms of the system containing the SHINs in Figure 11 indicates that there is no electroactive gold within this system, so the electrochemical response can be attributed to the IrO_x surface. This also suggests that the dynamic spectroscopic response of the system during an electrochemical measurement will most likely be dominated by the changing IrO_x surface.

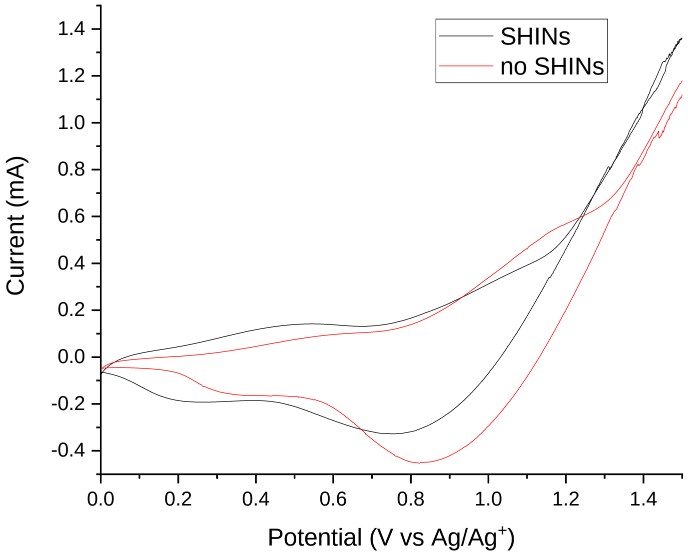

Figure 11: Comparative CVs of the IrO_x/GCE system with and without SHINs drop-cast on the surface, scanned at 50 mV s^{-1} in 1 M $NaClO_4$ in the spectroelectrochemical cell used for Raman. Potential values are slightly shifted due to the use of a Ag wire pseudo-reference electrode, but no additional features are present. The uniform nature of this shift across all redox features and OER onset indicates it is purely a result of the pseudo-reference electrode.

The use of a silver wire pseudo-reference electrode does introduce some uncertainty in the potential values. Ag/AgCl electrode is commonly used as a reference electrode for aqueous systems and would offer a more stable reference potential, however it would introduce the possibility of chloride ions contaminating the system which could also be oxidised under the experimental conditions. For this reason, a silver wire pseudo-reference electrode was used for the *in situ* experiments, with the understanding that all spectra can be directly correlated to the current response within that specific experiment.

A simple drop-casting procedure from an aqueous suspension, combined with rapid Raman peak intensity mapping was used to investigate the electrochemical water oxidation on an electrodeposited iridium oxide surface. By using a commercially available glassy carbon disk electrode as the substrate, we avoid complications from having a SERS active substrate and the electrode can be easily mounted into existing cells within the lab. A key feature of these cells is the ability to control the distance between the front window and the electrode surface. A distance of ~50 µm was found to be optimal for these experiments providing a balance between sufficient electrolyte pathlengths and minimising the effect of bubbles on the Raman signal (see Chapter 5.8. for full details on the experimental SHINERS setup and how this distance was controlled). Figure 12 demonstrates the enhancement provided by the SHINs particles in studying the IrO_x surface. Clear enhancement of the broad and overlapping Ir-O-Ir twisting modes (assignments are discussed in more detail below) is observed in the spectrum containing SHINs particles and the spectrum of the SHINs particles on a bare glassy carbon surface shows that no new peaks are introduced by the SHINs themselves within the spectral region of interest. The aim of these experiments was to identify some of the theorised water splitting intermediates, such as iridium oxo, peroxo or superoxo moieties. The previous SERS study mentioned above had already identified the iridium oxo mode (Ir=O stretch at 771 cm^{-1}) on a thin IrO_x film on a roughened gold surface. However, the signal in such experiments was complicated by the presence of an underlying electroactive gold surface that included significant spectral changes within this same region. Here using SHINERS we aim to corroborate this result while precluding any assignments to a gold surface since the particles are encased within an inert shell material.

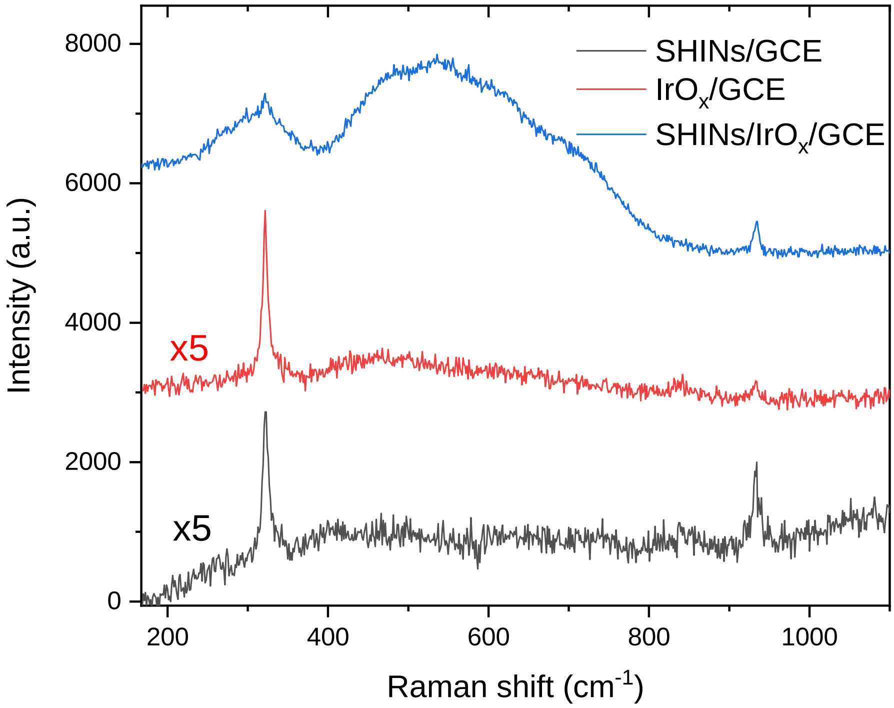

Figure 12: Stacked Raman spectra of the glassy carbon electrode system at 0.9 V (vs Ag/Ag$^+$) in 1 M NaClO$_4$, with the main IrO$_x$ feature (broad band between 400 and 800 cm^{-1}) being significantly enhanced in the presence of the SHINs. The sharp bands at 321 and 933 cm^{-1} correspond to CaF$_2$ (window material) and ClO$_4^-$ (electrolyte) modes respectively.

The pH stability of the SHINs also limits the choice of electrolyte for these experiments. Breakdown of the silica shell can occur above pH 10.5,[50] leading to contamination of the surface. Typically OER catalysts are most stable and active at high pH, where the hydroxide ions in solution provide the conductivity. Initial experiments here used a supporting electrolyte of 1 M NaClO$_4$ at a neutral pH to ensure the SHINs were not damaged. Comparing experiments between pH 7 & pH 10 in Figure 13 show little evidence of damage to the SHINs (see section 2.2.4 below for more information on identifying damage to SHINs), while the spectrum at pH 10 shows a stronger band in the expected region for a known water oxidation intermediate (η, assignments are discussed further below). For this reason, further experiments and analysis were carried out at pH 10.

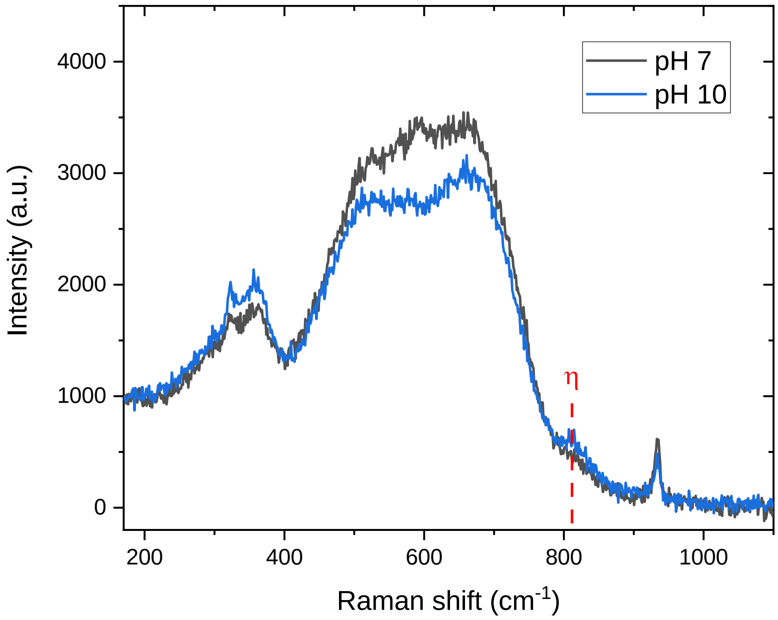

Figure 13: SHINER spectra of IrOx/GCE in 1 M $NaClO_4$ (pH 10 solution was adjusted by adding a small amount of NaOH) recorded at 1.8 V vs Ag/Ag^+. Both spectra show the presence of η at a similar wavenumber, however at higher pH a stronger Raman band for this species is measured.

Figure 14 shows the evolution of the SHINERS/IrO_x/GCE system during a linear sweep measurement. Several clear spectroscopic changes are observed that correlate well to the electrochemical response of the system. These have been assigned colours to match the 4 distinct regions of the voltammogram, starting with the response near the open circuit potential (region I), leading into the first oxidation of the material from mostly Ir^{3+} to Ir^{4+} (region II), to the second oxidation from mostly Ir^{4+} to Ir^{5+} (region III) and finally the catalytic OER regime (region IV). The transitions between these regions in the voltammograms are associated with the appearance of additional peaks in the SHINER spectra. Initially, the spectrum at open circuit potential is dominated by the bands labelled γ, δ and ε, with α and ζ only appearing after the first oxidation. Two further peaks, β and θ, develop only after the second oxidation. The labelling of the peaks α – η is used here to be consistent with the prior IrO_x SERS literature.[34,35] Based on this remarkable correlation with the electrochemical response, these specific bands can be assigned to the various Ir-O-Ir twisting and stretching vibrations at different oxidation states, as detailed in Table 1.

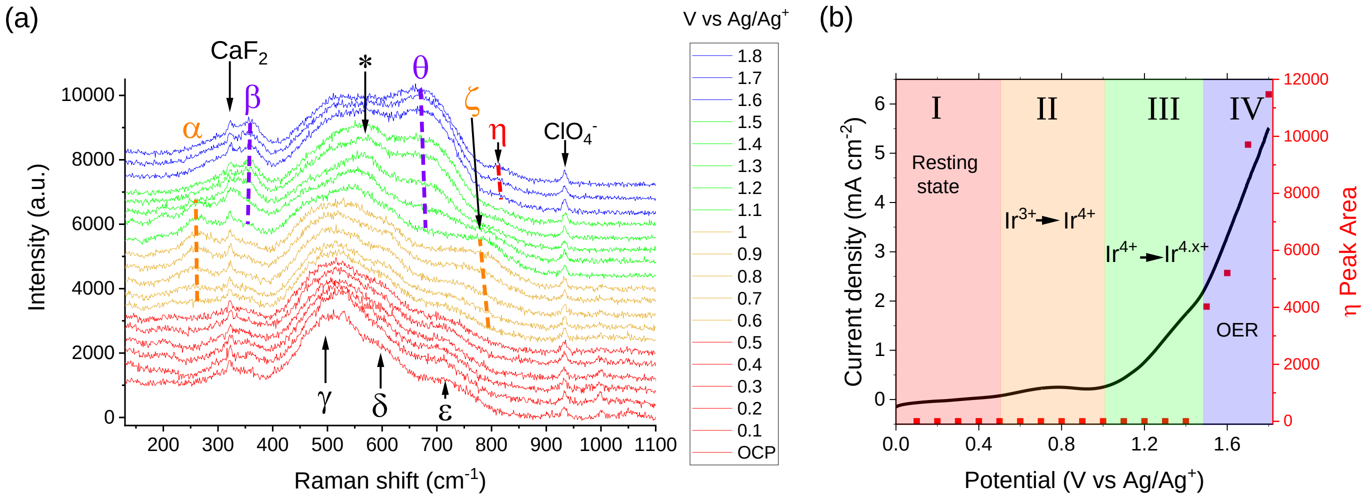

Figure 14: (a) Potential-dependent SHINER spectra (stacked) recorded during the (b) linear sweep voltammogram, overlaid with potential-dependence of the η peak area (full Lorentzian peak fittings can be found in Appendix A) of a SHINs/IrO_x/GCE system during a 5 mV s^{-1} linear sweep in 1 M $NaClO_4$ adjusted to pH 10 with NaOH.

Table 1: Approximate Raman peak positions and assignments of IrO_x/GCE system (Figure 14), based on previous literature reports.[34,35]

Label	Peak Position (cm^{-1})	Assignment	Species
α	262	Ir-O-Ir twist	Ir^{4+}
β	357	Ir-O-Ir twist	$Ir^{4.x+}$
γ	504	Ir-O-Ir stretch	Ir^{4+}
δ	608	Ir-O-Ir stretch	Ir^{3+}
ε	719	Ir-O-Ir stretch	Ir^{4+}
ζ	773	Ir-O-Ir stretch	Ir^{4+}
θ	672	Ir-O-Ir stretch	$Ir^{4.x+}$
η	813 in H_2O 817 in D_2O	Ir=O stretch	$Ir^{4.x+}$

α and ζ are proposed to be the Ir-O-Ir twisting and stretching modes of Ir^{4+} oxides, respectively, as they grow in during region II and decrease in intensity in region III, concomitant with the appearance of β and θ. The Ir^{4+} centres are expected to be further oxidised in region III, suggesting that β & θ correspond to vibrations of this “pre-catalytic” $Ir^{4.x+}$ species. The smooth transition between α & β is well-correlated with the second oxidation of the iridium centres, which could indicate that they correspond to the same vibration, blue-shifted due to the change in metal oxidation state. Similar weak modes have previously been observed in the Raman spectra of amorphous IrO_2, however there is no consensus on their origin.[51–54] Alternatively, two modes around these frequencies have been previously assigned to Ir-O-Ir twisting vibrations by Pavlovic *et al.*,[34] though no such potential dependence was observed in their spectra. The proximity to gold oxide bands that may have been formed in this past SERS study prevented detailed study of their potential-dependent behaviour. Using electrochemically inert SHINs we can preclude the formation of gold oxide, allowing us to tentatively assign these bands to the twisting Ir-O-Ir modes of Ir^{4+} and $Ir^{4.x+}$ centres. Similarly, the peaks labelled ζ and θ also correlate with the two oxidations observed in the voltammogram and are assigned to the Ir-O-Ir stretching modes of Ir^{4+} and $Ir^{4.x+}$ centres, respectively, on the basis of comparison to previous Raman studies,[34,35] though they are labelled independently of these reports to highlight their clear potential-dependence.

As observed in the literature,[35] the E_g peak of rutile IrO_2 at 563 cm^{-1} (labelled *) also appears transiently in region III, implying the presence of different phases of iridium oxide within the material. The transition from the hydrous IrO_x structure to rutile IrO_2 has been described as a deactivation pathway in anodic iridium oxide films.[35] It has been suggested that rutile formation is typically irreversible under the conditions used here and that the Rutile phase is less electrocatalytically active.[37] Interestingly, as we are carrying out experiments using confocal Raman microscopy, we are able to maintain study of a single region of the electrode throughout and we find that the formation of the rutile structure is not permanent and the spectrum after cycling back to OCP (Figure 15) largely resembles the initial spectrum, with no evidence of the Rutile IrO_2 E_g band remaining. Furthermore, certain features are significantly more intense on the reverse sweep, possibly due to the initially mixed valence surface being forced through the different individual oxidation states as the potential is scanned negatively.

These changes in relative intensity are not permanent and the spectrum by the end of the scan is decreasing in intensity, approaching the appearance of the initial spectrum.

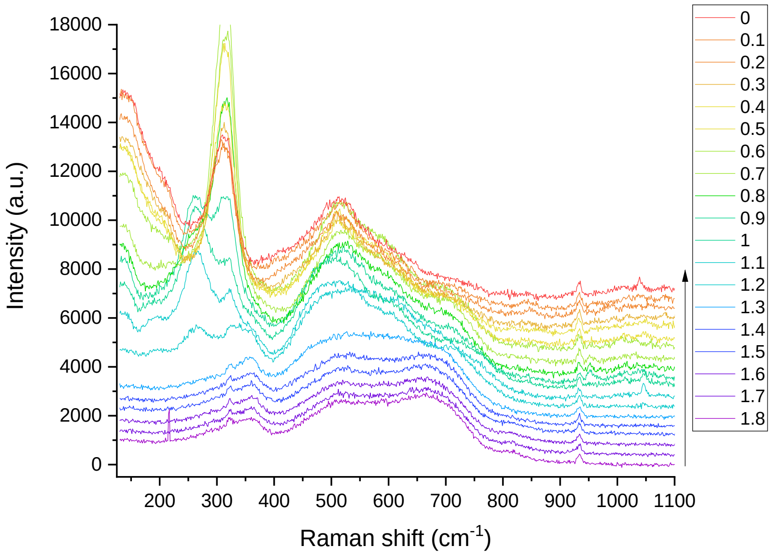

Figure 15: Reverse scan at 5 mV s^{-1} of dataset in Figure 14 in 1 M NaClO$_4$ adjusted to pH 10 with NaOH, arrow indicates scan direction.

Careful inspection of the Raman spectra in Figure 14 shows the formation of a new band, η, at 815 cm^{-1} at the most positive potentials studied (region IV) where the OER occurs. The development of this band is more apparent in the multi-Lorentzian peak fitting shown in Figure 16. To avoid unnecessary uncertainty the fitting is restricted to between 700 and 1000 cm^{-1}, due to the incredibly congested spectral region below 700 cm^{-1}, though an alternative data analysis procedure is explored for handling this congested region in the following section. It is striking that the potential-dependence of the peak area for this band directly correlates to the catalytic OER current, Figure 14 (b). η was previously assigned as the iridium-oxo intermediate by Pavlovic *et al.* at 771 cm^{-1} in their study, based on DFT modelling of iridium clusters. They predicted a vibrational mode at 829 cm^{-1} for the Ir=O stretch, though this mode can redshift significantly when a water molecule is placed nearby the cluster, hence the assignment of η at 771 cm^{-1} instead of 829 cm^{-1}. In these spectra, η is assigned as the peak at 813 cm^{-1}, based both on similarity in position to the theoretical value (between 771 and 829 cm^{-1}) and since it is only present when a catalytic water oxidation current is being drawn.

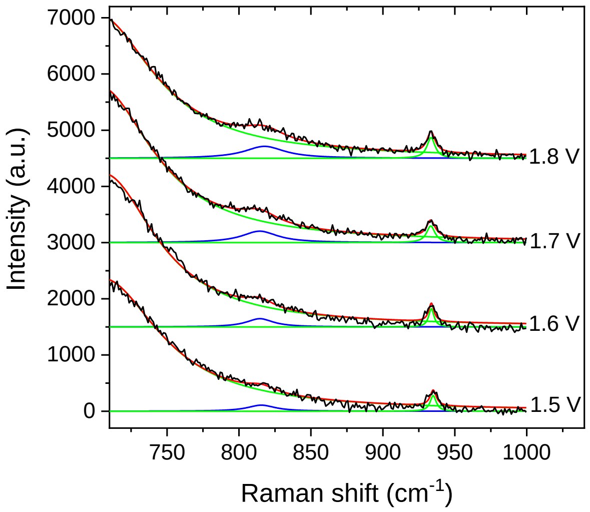

Figure 16: Multi-Lorentzian peak fits (red line) of potential-dependent SHINER spectra (black, raw data) of IrO_x/GCE surface during a 5 mV s^{-1} LSV in 1 M $NaClO_4$ adjusted to pH 10. The individual Lorentzian peaks are in green except for η shown in blue (ca. 815 cm^{-1}) and the peak width of η was fixed across all spectra.

To investigate the observed Raman bands further, in particular η, the experiments were repeated in a D_2O-based (1 M $NaClO_4$, pD = 10 adjusted using NaOD) electrolyte, Figure 17. It is notable that no significant change in peak positions is observed, thus, any of the vibrational modes observed in this region are not likely to be (protonated) hydroxides or peroxides. This is not entirely surprising as the only one of the proposed intermediates with a bond susceptible to such isotopic exchange experiments would be a peroxide intermediate (IrOOH), which was shown to be very short-lived by the rapid-scan FTIR experiments carried out by Sivasankar *et al.*[43] In their experiments this peroxide mode did not persist in spectra after 610 ms following initiation and also blue-shifted by 30 cm^{-1} upon deuteration. A minor shift is observed in the position of η in Figure 17 (around 4 cm^{-1}), though this is in-line with the assignment to an Ir=O stretch which is solvated by H_2O/D_2O.[34] Based on these criteria, this assignment to a high valence (4.x) iridium oxo mode is consistent with the mechanism proposed by previous literature, outlined in Scheme 4. The observed oxo mode is thought precede to the rate-limiting O-O bond formation step in the OER reaction, allowing such intermediates to accumulate to detectable concentrations within the timescale of these experiments (~20 seconds per spectrum).

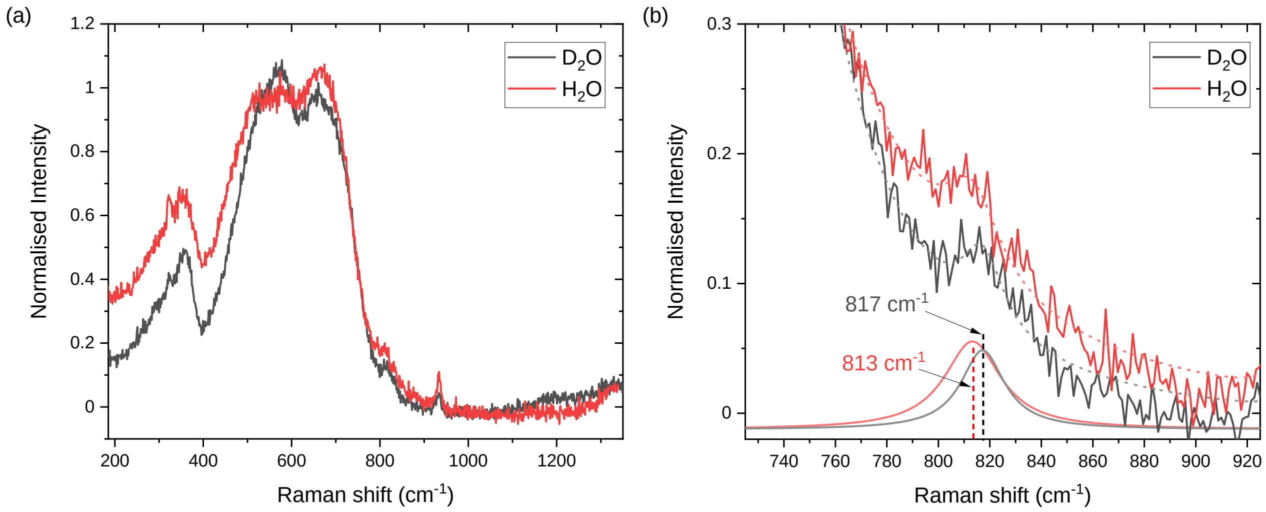

Figure 17: (a) Comparison of normalised SHINER spectra at 1.8 V vs Ag wire in H_2O and D_2O-based 1 M $NaClO_4$, adjusted to pH (or pD) 10. (b) Lorentzian peak fitting of η peak in both electrolyte systems (lighter red/black), including the experimental data (darker red/black) and the cumulative fit (dotted red/black). Note that that a similar multi-Lorentzian fitting procedure to Figure 16 was used here, but the additional peaks are omitted for clarity. Details of the peak fitting procedure and all fit peaks can be found in Appendix A.

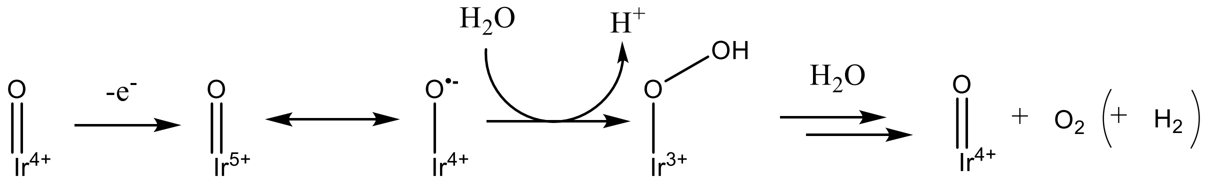

Scheme 4: Proposed mechanism for water oxidation at iridium centres based on the observed and predicted intermediates in the existing literature.[34,38,43,55,56]

The sensitivity of the SHINERS technique has enabled detection of surface intermediates on these IrO_x electrodes *in situ* during voltage-sweep measurements. This opens the door for future experiments to fully investigate the water oxidation mechanism on such electrodes, especially those only present transiently on the surface. While the remainder of this project will focus on applying this technique to the photoelectrode systems discussed in other chapters, there is significant potential for coupling this extremely sensitive spectroscopic technique to time-resolved potential-step or photo-initiated measurements on IrO_x electrodes in the hopes of detecting potentially short-lived intermediates such as the oxyl or peroxo species highlighted in Scheme 4. Another key advantage of the SHINERS technique is the relative ubiquity of microscopes alongside many modern Raman instruments. This is particularly pertinent to materials such as IrO_x as the inhomogeneity of the electrochemical response from such films, readily visualised by the electrochromic behaviour shown in Figure 18, has long been a topic of interest to the field. SHINERS experiments coupled with confocal microscopy offers the opportunity to map, in real-time, the changing chemistry of the electrode surface in unprecedented detail.

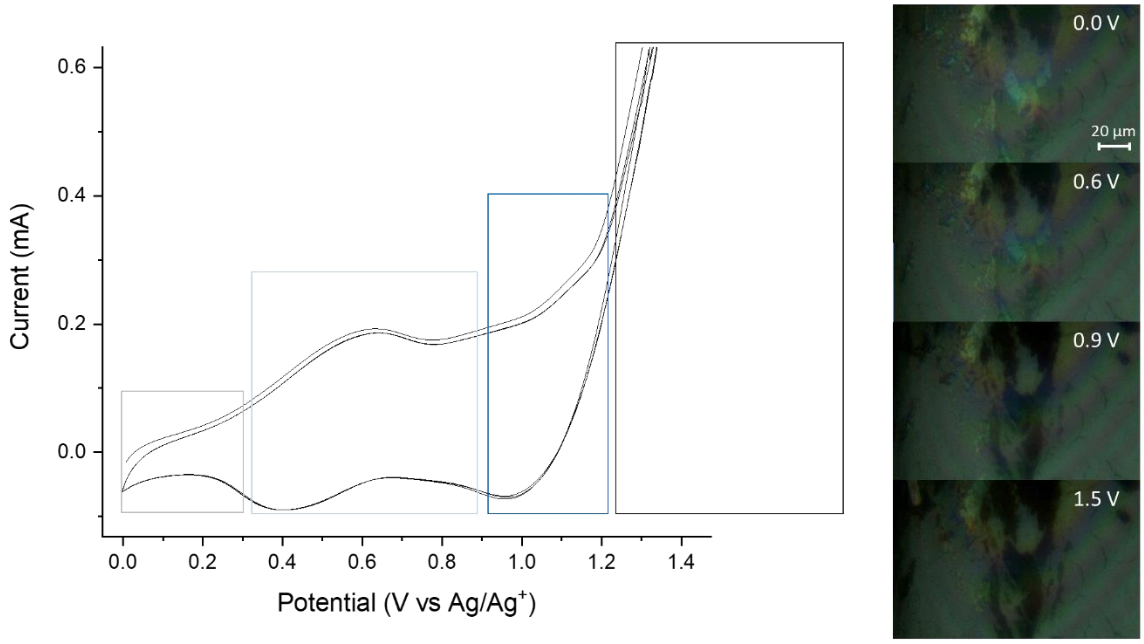

Figure 18: Electrochromic effect of IrO$_x$/GCE system displayed by optical microscope images of the electrode surface in the Raman microscope at the stated potentials (V vs Ag wire). Note that the Raman laser spot is focussed to a 1.5 µm spot at the centre of each image, where the colour change is most obvious. During cycling, the electroactive material changes from almost transparent in region I to a deep blue/black colour in region IV. Thus, depending on the proportion of electroactive material within the laser spot, the Raman spectrum can be significantly more intense at higher potentials. Often (as in Figure 14) some amount of electro-inactive material is present within the laser spot, giving a relatively large signal at lower potentials too. This phenomenon slightly complicates the comparison of peak positions at the low potential region across datasets; the assignments shown in Table 1 are taken from spectra held above 0.9 V to overcome this.

All of the above analysis involved significant peak fitting to deconvolute the many overlapped vibrational modes in the IrO$_x$ system. This necessarily involves some level of human bias in choosing how many peaks to fit, as well as the choice of bounds for the peak-fitting parameters. Development of a more automated data analysis procedure, with less human input would be beneficial to corroborate these results, as well as to speed up data analysis. Two-dimensional (2D) correlational analysis is a computational method of analysing dynamic spectral data and outputting correlation plots that highlight spectral components that change together (synchronously) or not (asynchronously). Typical *in situ* electrochemical SHINERS experiments carried out later in this project involved hundreds of spectra recorded during cyclic voltammetry, leading to large spectral datasets, also necessitating automated handling of data. The aim of this next section is to develop a rapid data analysis procedure for these *in situ* electrochemical SHINERS data to quickly identify overlapped spectral changes.

2.2.3. 2D correlational analysis of electrochemical SHINERS data:

The 2D correlational analysis used here is based on the method described by Noda,[57] which generalised his existing correlation analysis in 2D-IR spectra[58] to any dynamic set of spectra. The scheme allows correlational analysis on a given system that is monitored by any kind of spectroscopy, under any kind of perturbation. In this case, we employ a visible Raman probe and an electrochemical perturbation is applied to the system through the potentiostat, resulting in a set of time-varying dynamic spectra. The output consists of two different 2D plots with spectral frequencies across the x and y axes, allowing correlational analysis. As the name suggests, the synchronous output (exemplified in Figure 19) highlights synchronised changes at the two spectral frequencies, suggesting either a related origin or coupling. Conversely, the asynchronous output represents unsynchronised or sequential changes between the two spectral frequencies. The technique is especially powerful in identifying changes when there are multiple overlapping peaks present, providing a consistent method for data analysis that is free from human bias.

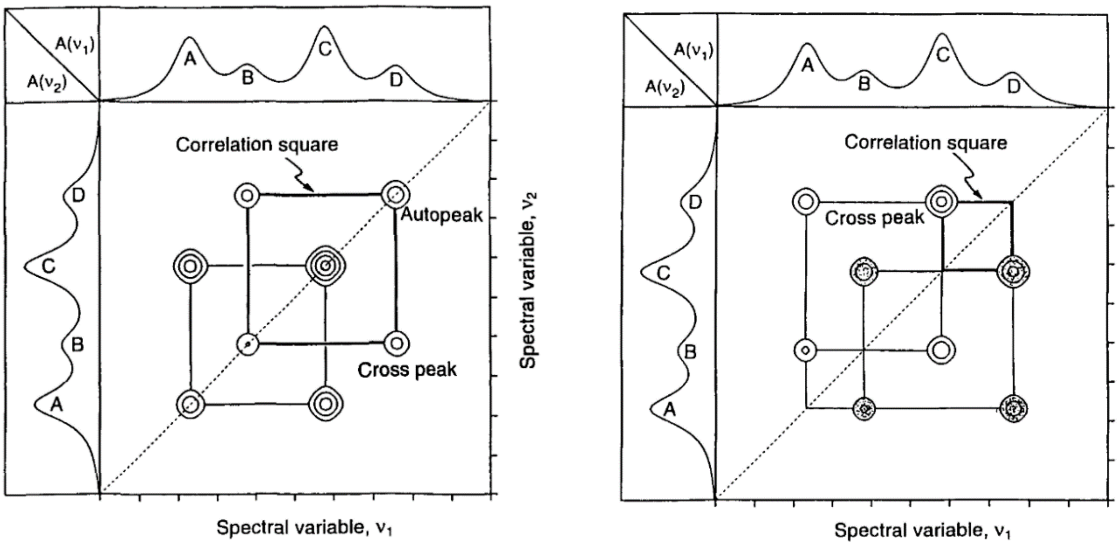

Figure 19: Examples of synchronous (left) and asynchronous (right) 2D correlation spectra, with the one-dimensional reference spectra included for each axis, from I. Noda in Appl. Spectrosc. 1993.[57]

Such correlation plots can contain a wealth of information; a brief description of how to read and understand these plots will be presented here, though further information including illustrative examples and accounting for frequency shifts can be found in other publications.[59–61] As seen from Figure 19, the synchronous output contains autopeaks on the diagonal, which are always positive and larger when there are larger changes in the data at that frequency. The presence of cross-peaks (off-diagonal) indicate synchronised changes between the two frequencies at that point. These can be positive when both peaks either increase or decrease, or negative, when one increases and the other decreases. The asynchronous output does not contain any autopeaks and cross-peaks only develop when the spectral intensities vary out of phase with each other, *i.e.* the changes are sequential. This is especially useful for allowing the distinction of overlapping peaks if they respond differently to the perturbation.

The mathematical approach is best described in Noda's original demonstration of the technique,[58] but will also be briefly summarised here, as applied to *in situ* electrochemical SHINERS . The input is a set of dynamic spectra, in this case this will be a set of difference spectra (compared to OCP) collected during a voltage sweep experiment (either LSV or CV). The first step is to collate all spectra into a two-dimensional array of intensity values, with Raman shift across the columns and spectrum number (*i.e.* the time-varying axis, which in this case is applied potential) across the rows. Other pre-treatment of data is carried out at this stage if necessary, including baseline-subtraction or cosmic ray removal. The dynamic spectrum ($\tilde{f}(v)$) is then calculated as a difference spectrum compared to the spectrum at OCP ($f_{OCP}(v)$).

$$\tilde{f}(v,t) = f(v,t) - f_{OCP}(v) \qquad \textit{Eq. 5.1.}$$

Then a fast-Fourier transform (FFT) algorithm is carried out at each Raman frequency over all spectra (*i.e.* the time varying axis), giving an array of complex Fourier frequencies ($\tilde{F}(\omega)$) at each Raman frequency (ν). Since the FFT is over the time-varying axis, this step essentially converts the dynamic spectra from the time domain into the frequency domain.

$$\tilde{f}(v,t) \xrightarrow{FFT} \tilde{F}(\omega) \qquad \textit{Eq. 5.2.}$$

The intensity in the correlation plot between any two Raman frequencies (ν_1 & ν_2) can then be obtained by multiplying $\tilde{F}(\omega)$ at ν_1 by the complex conjugate of the $\tilde{F}(\omega)$ at ν_2 and integrating over all Fourier frequencies.

$$\frac{1}{\pi T}\int_0^{\infty} \tilde{F}(\omega)_{v_1} \times \tilde{F}(\omega)^*_{v_2}\, d\omega \; = \; \phi(v_1,v_2) + i\psi(v_1,v_2) \qquad \textit{Eq. 5.3.}$$

The result of this integral is a complex quantity, where the real component (ϕ) corresponds to the synchronous correlation intensity and the imaginary component (ψ) is the asynchronous correlation intensity.

The main dataset for the iridium oxide SHINERS study from Figure 14 will now be used as an illustrative example of the utility of 2D correlational analysis. A home-made LabView programme was developed to carry out all of the above procedures, including baseline correction, cosmic ray removal and 2D correlational analysis. The programme takes the raw .txt file from the Raman spectrometer as an input and provides the synchronous and asynchronous correlation plots as outputs, as well as other optional additional functions such as inverse-FFT and moving-window 2D correlational analysis, which will be discussed later. All nineteen spectra from the aforementioned IrO_x SHINERS dataset were input into the programme, cosmic rays were removed, but no additional baseline correction was carried out. The synchronous and asynchronous correlation plots for this dataset are displayed in Figure 20. As seen from the overlaid 1-dimensional SHINER spectra, many of the IrO_x vibrational modes are overlapped between 400 & 800 cm^{-1}, producing a broad convoluted peak and making it hard to accurately monitor the dynamic response of each of the individual bands in this region. Analysis of the synchronous spectrum mainly highlights the changes of these broad bands as there is autopeak intensity across all of the Ir-O-Ir bands. The off-diagonal cross peaks also have some intensity across all of the Ir-O-Ir bands, largely reflecting the same pattern of intensities as observed in the autopeaks, with the dominant changes occurring around 320 and 500 cm^{-1}. More information can be gained from the asynchronous spectrum, which does contain some significant cross-peaks, especially at 320, 500 and 710 cm^{-1}. These peaks reflect the step changes in oxidation state from the electrochemical SHINERS experiment, highlighting the key Raman bands that change with each successive oxidation.

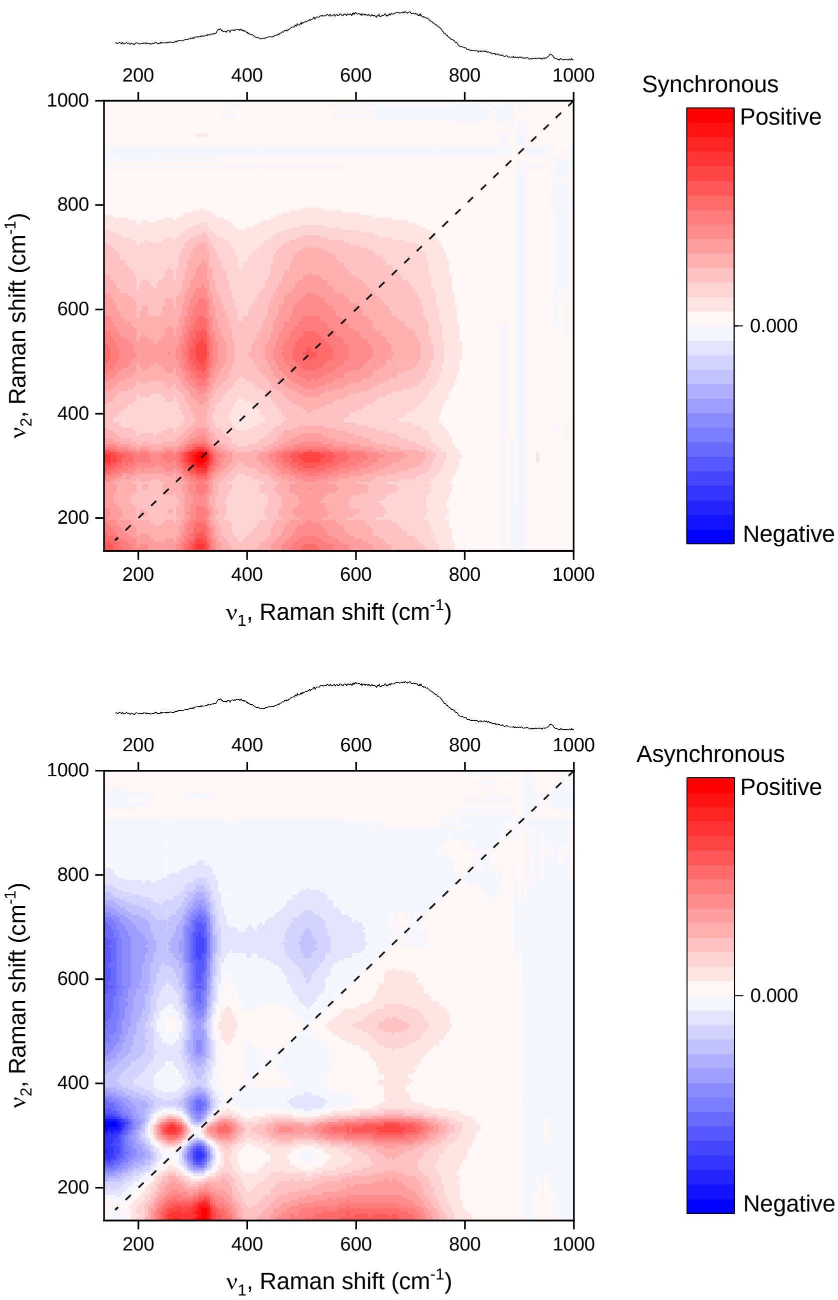

Figure 20: Synchronous (top) and asynchronous (bottom) 2D correlation plots for the IrO_x SHINERS dataset from Figure 14, a representative 1-dimensional Raman spectrum is displayed above each plot.

To aid visualisation, separate representative spectra of the synchronously and asynchronously changing components of the initial dataset can be extracted. This process involves separating the complex product in Eq. 5.3. and carrying out an inverse Fourier transform on both the real and imaginary components to get the representative synchronous and asynchronous spectra, respectively. This process was carried out for the IrO_x SHINERS dataset and the resulting spectra are shown in Figure

21. Many of the previously assigned bands from the above electrochemical SHINERS experiments turn out in these representative spectra, the peak labels for these bands are highlighted here. The output of the inverse FFT process is an array, which needs to be integrated over all spectra to extract the representative spectra. Any noise in the initial data, which undergoes successive FFT and inverse FFT algorithms, can manifest itself as artefacts in these representative spectra, especially after integrating over all spectra in the output array. The small sharp unlabelled peaks across the asynchronous spectrum below are likely a manifestation of this noise rather than real asynchronous changes. With larger datasets, adjacent averaging or smoothing of data could be employed to address the issues of noise, but in this case there were only 19 spectra available so further treatment was not carried out.

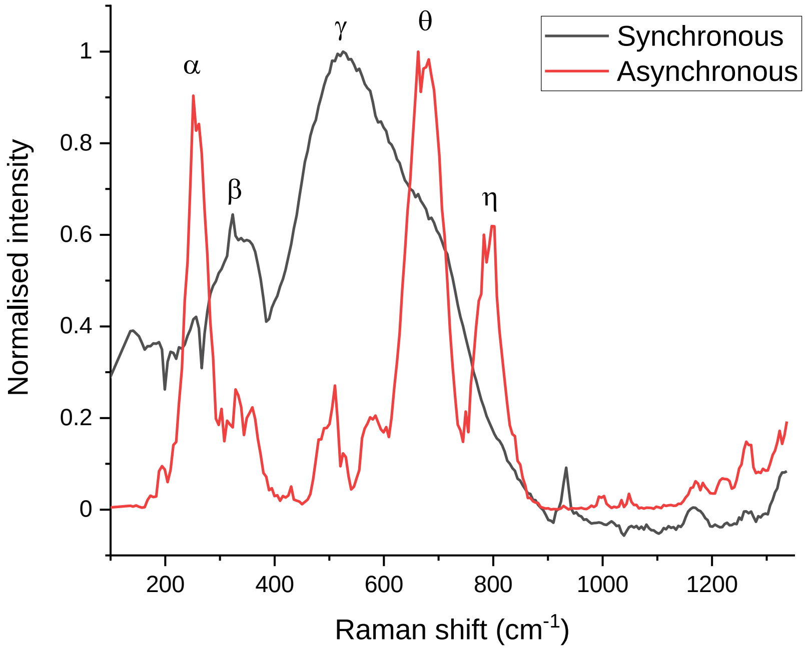

Figure 21: Representative synchronous and asynchronous spectra obtained from inverse-Fourier transforms of the 2D correlation plots in Figure 20, with the peak labels from the IrO_x vibrational modes from the SHINERS analysis above.

One of the drawbacks of the 2D correlation technique so far has been the lack of information across the time-varying axis, which in this case is the applied potential axis. This issue can be addressed with sufficiently large datasets using a technique known as perturbation-correlation moving-window two-dimensional (PCMW2D) analysis, which is described in detail by Morita el.[62] As a simplified explanation, the technique extends the inverse FFT method for extracting representative spectra across the entire time-varying axis. By dividing this axis into smaller windows and carrying out the inverse FFT algorithm on all windows, a more detailed picture of the dynamic response of the system can be built up over the time-varying axis. A minimum window of the three adjacent spectra is required to enable the technique, though greater window sizes can be used to address the aforementioned noise issues, at the expense of resolution in the perturbation dimension. This moving window functionality was added to the LabView programme and the result of this analysis on the IrO_x SHINERS dataset is shown in Figure 22. The key Raman bands relating to the newly oxidised IrO_x surface are readily apparent in the synchronous PCMW2D spectrum as the non-changing parts of the spectrum are not included. The asynchronous PCMW2D spectrum reflects the step-changes in the time-varying spectra, showing clear features at the first IrO_x oxidation (~0.8 V), the second IrO_x oxidation (~1.2 V) and then during the water oxidation region towards the final potentials. Due to the size of the moving window the first and last 2 spectra cannot be accurately accounted for using this technique so care should be taken when analysing these parts of the PCMW2D spectra.

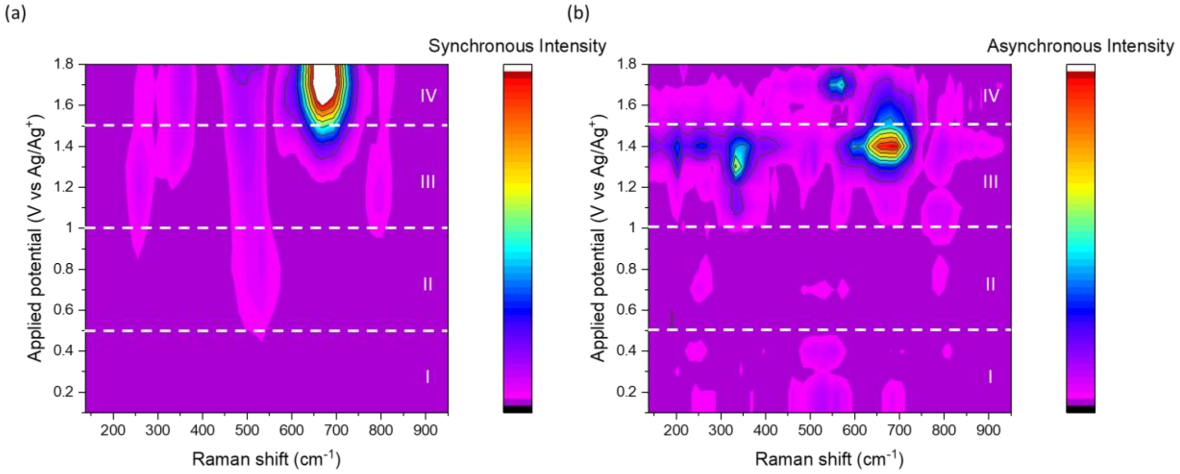

Figure 22: Synchronous (left) and asynchronous (right) PCMW2D correlation spectra of the IrO_x SHINERS system, with the dotted lines separating the 4 distinct regions (I-IV) in the voltammogram, where region I is the resting state of the catalyst, region II involves oxidation of Ir^{3+} to Ir^{4+}, region III is the oxidation of Ir^{4+} to $Ir^{4.x+}$ and region IV is the catalytic OER regime.

2.2.4. *In situ* SHINERS on photoelectrodes:

With the SHINERS technique having been successfully applied to the study of an electrode surface for water oxidation our attention now returns to the types of photoelectrodes introduced in Chapter 1. This section describes the initial work in investigating water oxidation mechanisms on the surfaces of TiO_2 and Fe_2O_3. Typically, the use of photoelectrodes necessitates a transparent electrode support, with fluorine doped tin oxide on glass being one of the most commonly used option. The prior electrochemical SHINERS experiments were carried out using commercial glassy carbon electrodes as the substrate, which could be mounted in existing cells with relative ease. Working with FTO/glass based electrodes introduces some additional challenges to the cell design for *in situ* experiments. The two most common sample orientations for Raman spectroscopy involve the laser either coming in from below or above the sample, while FTO/glass electrodes are typically employed with the sample oriented vertically. This is to ensure that a small part of the electrode can be left above the electrolyte level to allow a working electrode contact to be formed without short-circuiting the cell. One way of overcoming this is to use a fix a submersible contact to every electrode that will be studied. To achieve this, a wire is contacted to the surface using silver paint and once dry, the painted contact is completely covered in a chemically resistant epoxy to allow the whole contact to be submerged in electrolyte.

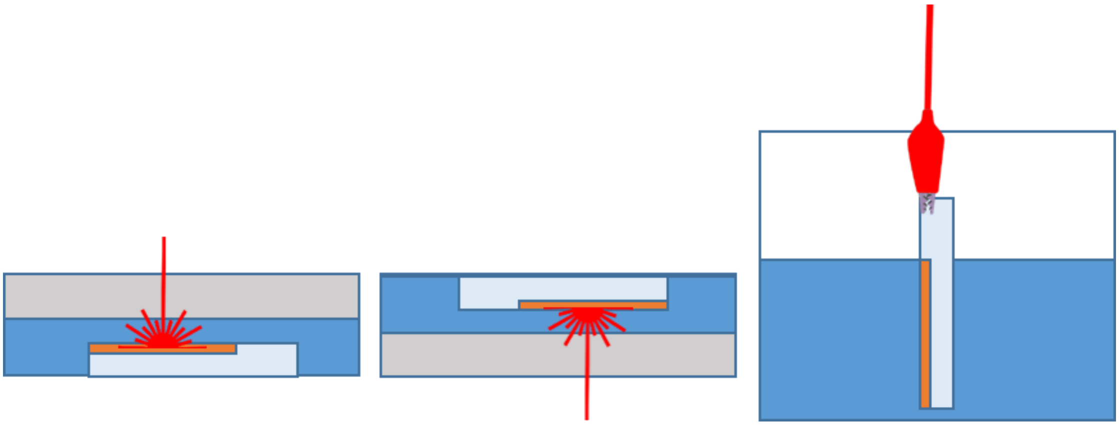

Figure 23: Common orientations for Raman spectroscopy of FTO/glass-based electrodes (left/middle) and conventional orientation for electrochemical measurements (right).

A further problem that arises with using the FTO/glass type electrodes is that only one face of the electrode is conductive. It was shown in the previous IrO_x work how important it is to control the distance between the front window of the cell and the electrode surface, with a typical working distance of ~ 50 µm found to be optimal for those experiments. Without careful cell design, the thickness of the protruding epoxy on the contact (typically several mm) for the working electrode on FTO/glass electrodes can limit the distance between the front window and the electrode surface. Furthermore, a key feature of the cell used for the IrO_x experiments was the ability to vary the electrolyte pathlength by screwing in or out the working electrode. This is also more difficult on the FTO/glass electrodes as the protruding epoxy contact makes it harder to rotate the electrode within the cell. To overcome this, a circular cell was designed (see Figure 24) with a small recessed front window, which allows space on all sides for the protruding epoxy. Furthermore, by keeping the front window smaller than the electrode, the same part of the electrode can be maintained within the aperture while the electrode is rotated. The wire for the working electrode contact is also fed through this same screw allowing free rotation without tangling the wire.

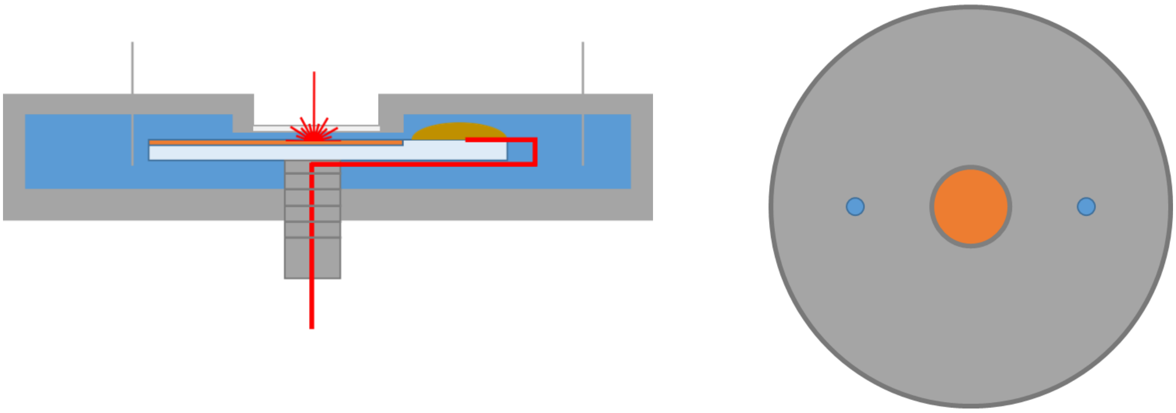

Figure 24: Diagrams showing cross-sectional (left) and top-down (right) views of the electrochemical cell developed for in situ SHINERS experiments on FTO/glass-based electrodes.

As an initial prototype, this new cell design was 3D-printed in nylon which provides good chemical stability to the electrolytes used for these SHINERS experiments (pH 6-11). In this prototype a microscope slide cover slip was cut to size and fixed (with epoxy) to the cell body to be used as a front window and the metal oxide/FTO/glass electrodes were glued to the 3D-printed hollow nylon screw with the working electrode contact wire fed through the cavity in the screw.

The very first SHINERS experiments on photoelectrodes in this project were carried out on thin and flat TiO_2 (~100 nm thickness) and Fe_2O_3 (25 nm thickness) electrodes on FTO substrates. The TiO_2 electrodes were prepared by spray coating, based on the procedure by Conde-Gallardo *et al.*,[63] while the pulsed-laser deposited (PLD) Sn-doped hematite surfaces were prepared by Prof. M. Rosseinsky's group. Full details of both synthetic procedures can be found in Chapter 5.3. Initial test LSVs for both electrodes are shown in Figure 25, showing that both electrodes produce a catalytic OER current that can be directly mapped to changes in the SHINER spectra. For both these samples, the weak adherence of the SHINs particles to the surface became a significant problem at higher OER current densities. Under such conditions the SHINs became dislodged from the surface, likely due to mechanical agitation from oxygen bubbles being formed on the surface. This was less of a problem in the studies on the electrodeposited IrO_x surfaces as they were significantly rougher (to the extent that this roughness could be observed in the optical microscope images), which likely provided alternative nucleation sites for bubbles away from the SHINs and/or aided adherence of the SHINs particles to the surface. As a result, these initial experiments on photoelectrodes were restricted to low OER current densities to avoid bubble formation entirely. This is detrimental as the concentration of surface intermediates for water oxidation would also likely be low under these conditions. In both cases the initial spectra are dominated by the bulk Raman modes of the respective crystalline structures (anatase for TiO_2 and α-Fe_2O_3 for hematite). The signal to noise ratio is low for these bulk modes due to the thin (< 100 nm) films, though this should make it easier to discriminate potential surface modes as the relative contribution of the surface to the signal (compared to the bulk) will be higher for thinner films.

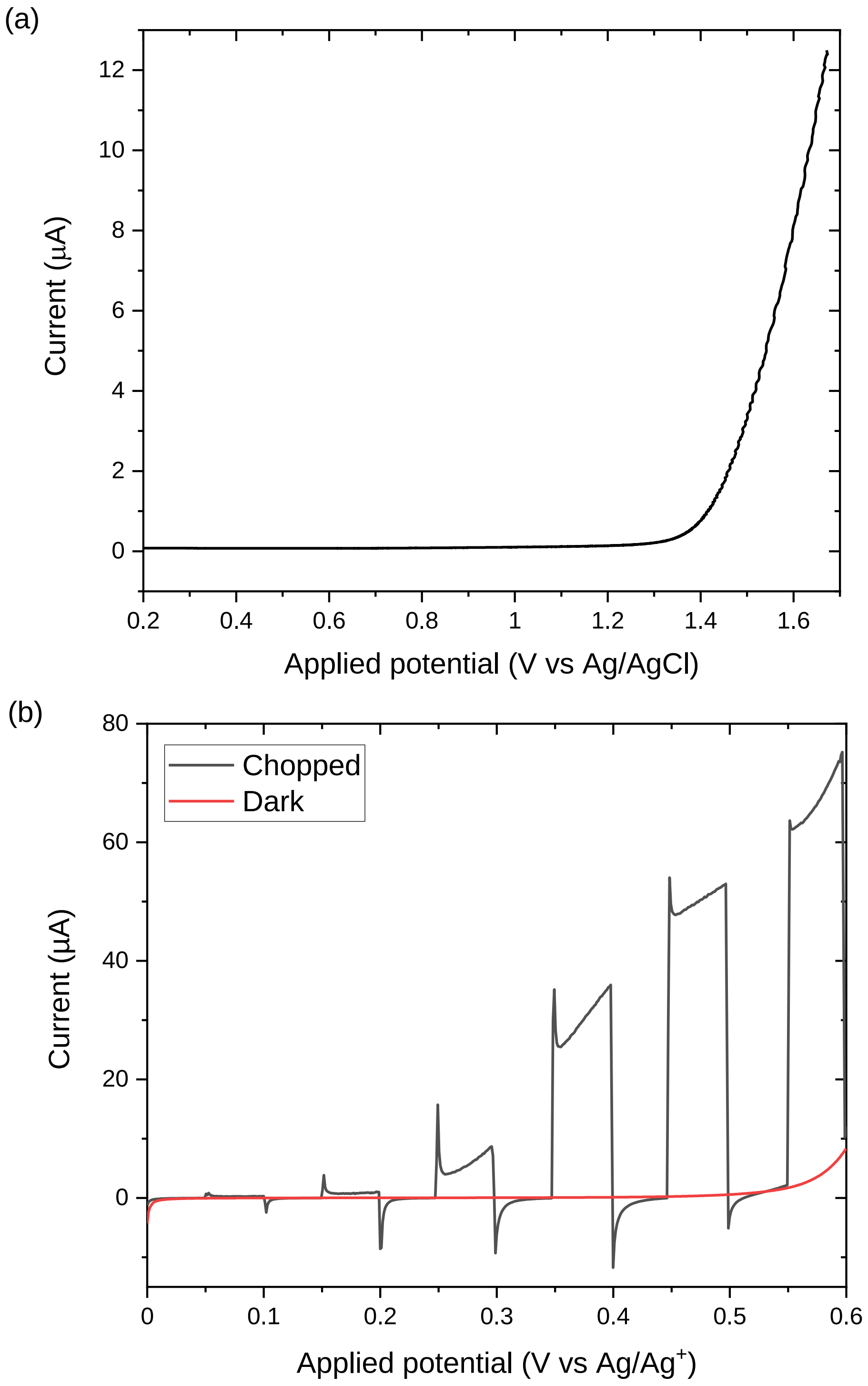

Figure 25: Linear sweep voltammograms at 100 mV s^{-1} for the SC-TiO2 (a) and PLD-Fe_2O_3 (b) electrodes. The TiO_2 experiments were carried out in 1 M NaCl electrolyte using an Ag/AgCl reference electrode, while the Fe_2O_3 experiments were carried out in 1 M NaOH using an Ag wire as a pseudoreference and the photocurrent performance under 365 nm LED illumination (~30 mW cm^{-2}) is also overlaid. There is a difference in these two sets of conditions as the TiO_2 experiment was carried out just before a SHINERS experiments in the Raman cell, so reflects the conditions used for SHINERS, while the Fe_2O_3 experiments were carried in a larger cell at a higher pH, closer to the optimal working conditions and enabled illumination as well.

The data shown in Figure 26 plotted as difference spectra compared to open circuit potential, do not contain any significant changes in the TiO_2 SHINER spectra that could be assigned to water splitting intermediates. A small peak appears in the difference spectrum at around 321 cm^{-1}, which is from the CaF_2 front window. A change in this band likely arises due to small changes in position of the cell over the long exposure times bringing the window closer to the focus of the Raman laser. There are also some minor potential dependent changes observed for the ClO_4^- electrolyte modes, which decrease around 600 and 900 cm^{-1} and increase at 933 cm^{-1}. A previous study on the adsorption of perchlorate on copper and silver surfaces assigned the sharp peak around 930 cm^{-1} to monodentate adsorption of ClO_4^-, while the broader peaks are attributed to free perchlorate species in solution (the Raman spectrum of solid sodium perchlorate is also included in the bottom of Figure 26 for comparison).[64] The observed trends would be consistent with free perchlorate anions in solution accumulating at the electrode surface as a positive bias is applied, resulting in a decrease in the proportion of free perchlorate in solution and increase in adsorbed perchlorate. Typically, vibrational modes of molecules close to or at an electrode surface display a shift in peak position as an electric field is applied, known as the vibrational Stark shift. No significant shift is seen for the symmetric stretch of perchlorate at 933 cm^{-1}, however this may be due to the relative orientation of the electric field, which is perpendicular to the surface, and the change in molecular polarisability of the vibration.

Similarly, the spectral response of a PLD-Fe_2O_3 electrode during an *in situ* SHINERS experiment is shown in Figure 27. In this experiment the acquisition times were much shorter (seconds rather than hours) compared to the TiO_2 data in Figure 26 to attain a similar level of signal-to-noise ratio. As a result, this experiment was carried during a 2 mV s^{-1} LSV, though no significant potential-dependent changes were observed here either.

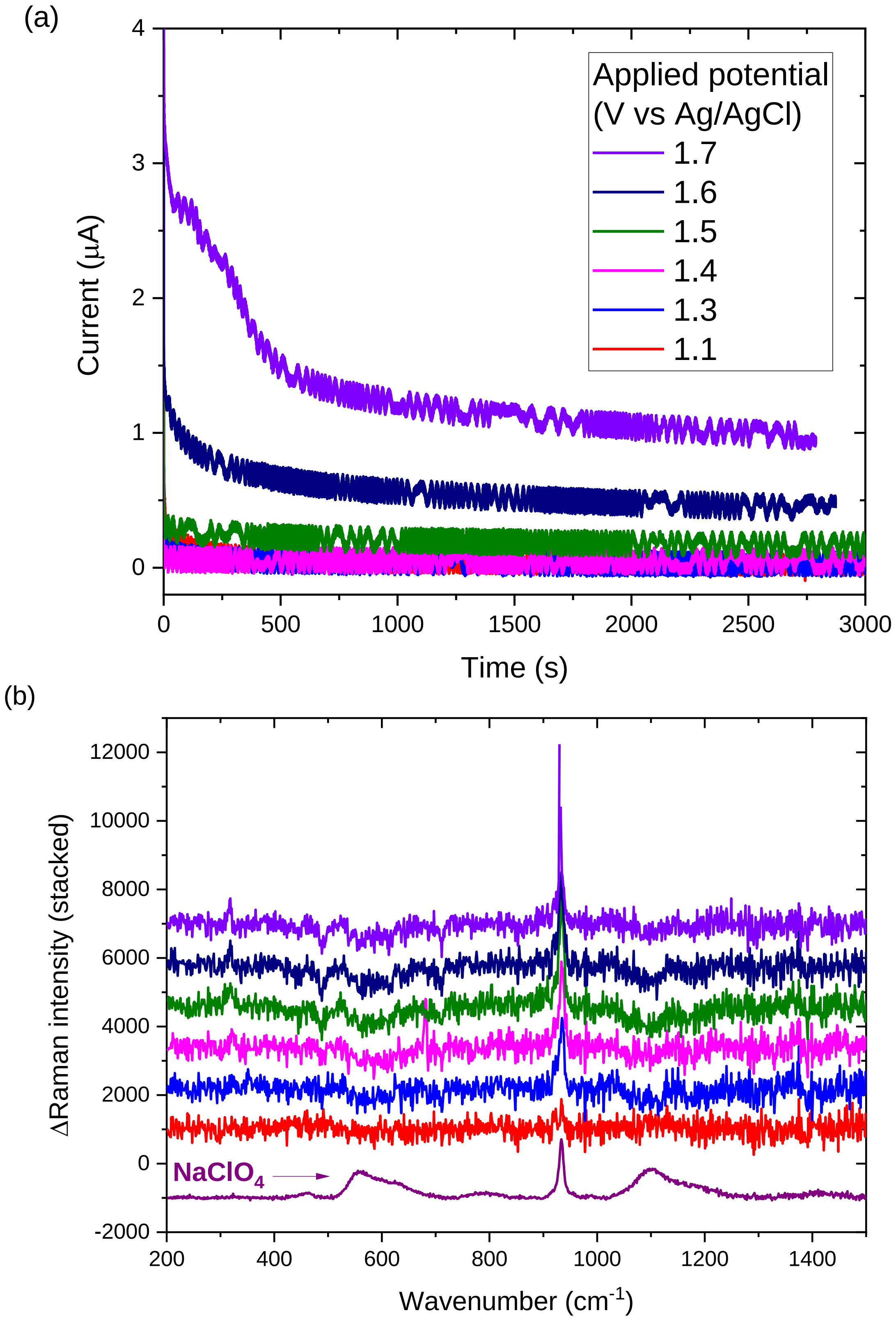

Figure 26: Electrochemical response (a) and in situ SHINERS spectra (b) of TiO_2/FTO electrode in 1 M $NaClO_4$ during potential-step experiments. All spectra are shown as a difference spectrum compared to the spectrum at OCP. A spectrum for solid sodium perchlorate overlaid at the bottom of (b) for comparison with some of the potential-dependent changes.

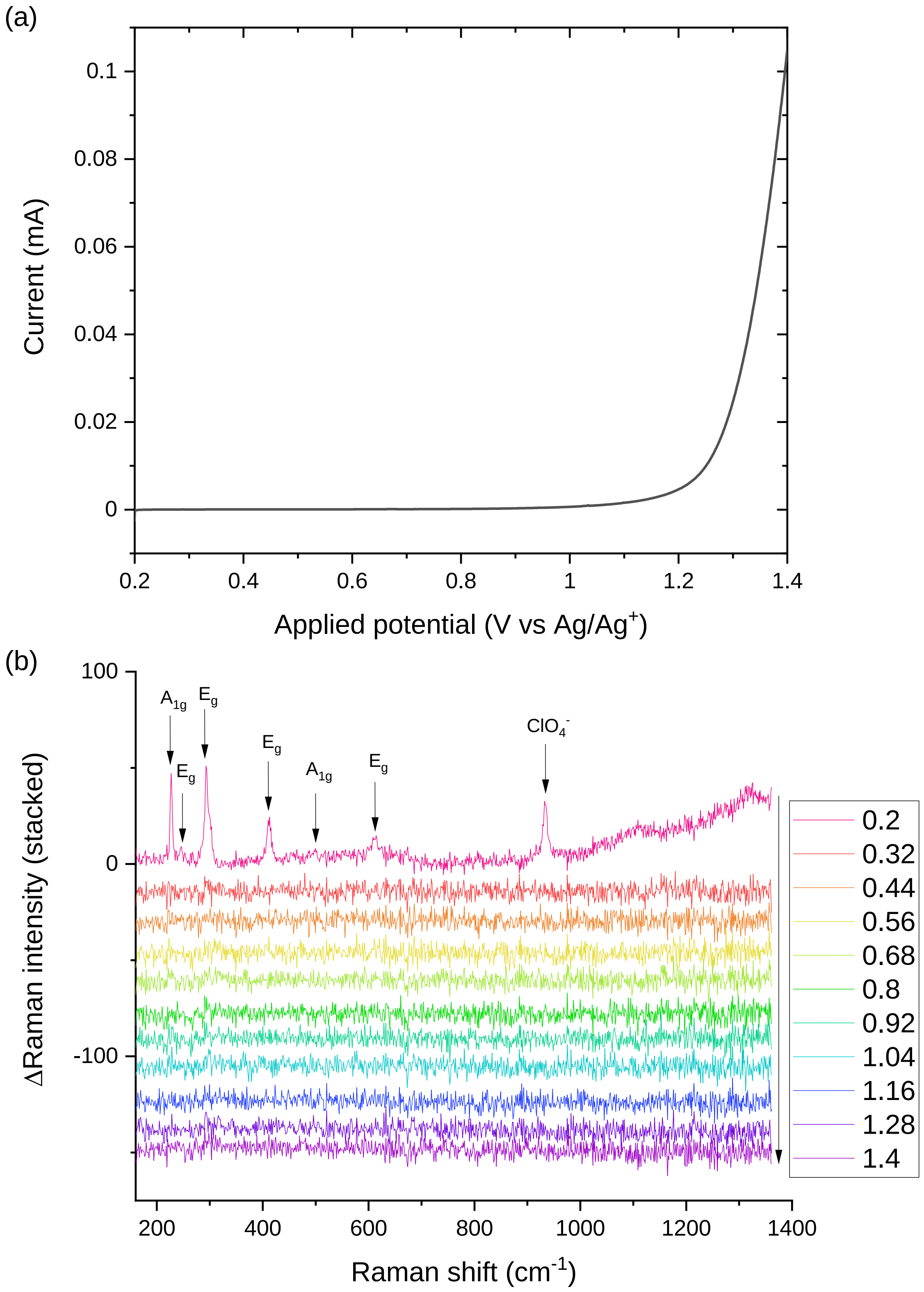

Figure 27: Electrochemical response (a) and in situ SHINER spectra (b) on a PLD hematite/FTO electrode in 1 M $NaClO_4$ during a 2 mVs^{-1} linear sweep voltammogram. Note all spectra after 0.2 V are plotted as a difference spectrum compared to 0.2 V.

With the thin planar electrodes not showing any significant potential-dependence, other, more nanostructured electrode materials were investigated. The planar surfaces from the PLD hematite electrodes are replaced with significantly thicker and rougher electrodeposited (ED) hematite electrodes. These were prepared following the procedure by Zandi *et al.*,[65] and the full synthetic procedure can be found in Chapter 5.4. The difference compared to the PLD-Fe_2O_3 is immediately apparent from the static, bulk Raman spectrum shown in Figure 28. The signal to noise ratio for the bulk Raman bands is significantly higher at the same acquisition settings as used previously due to the significantly thicker hematite layer. Furthermore, with the increased roughness, the SHINs adhere better to the surface and remain even under substantial OER currents. In this way similar current densities (based on geometric surface area) to the IrO_x system can be achieved, improving the chances of detecting small concentrations of water oxidation intermediates at the surface.

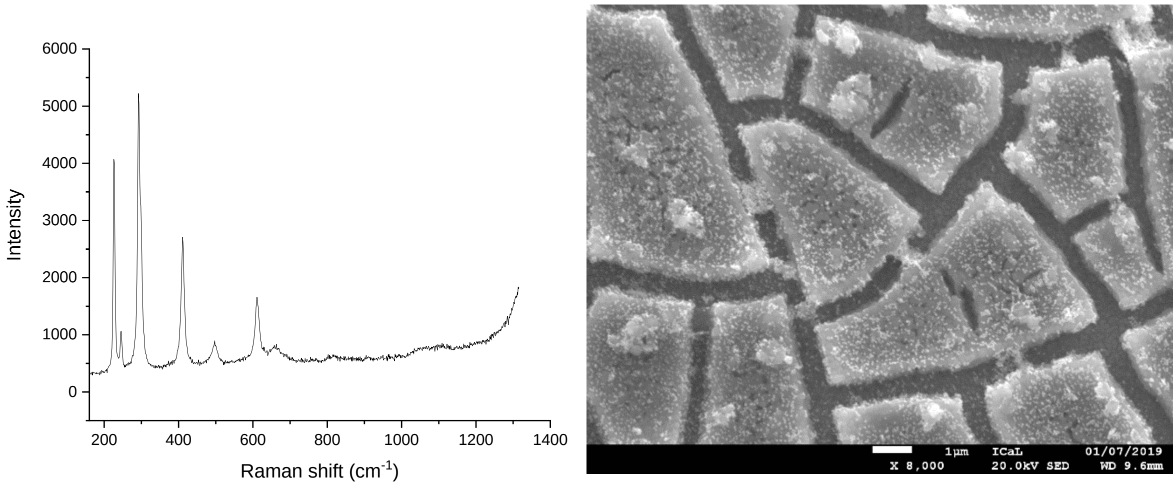

Figure 28: Static Raman spectrum of an electro-deposited hematite film (left) on FTO at the same exposure time, laser power and collection settings as Figure 27. SEM image of the same electrode (right) with SHINs drop-cast on the surface, highlighting the roughness of the surface on the scale of µm.

The photoelectrochemical performance of these ED-Fe_2O_3 is also superior to the PLD-Fe_2O_3 samples, demonstrated by the large photocurrents displayed in Figure 29. Larger current densities should be indicative of a higher concentration of surface water splitting intermediates, increasing the likelihood of detecting such intermediates in the *in situ* SHINERS experiments.

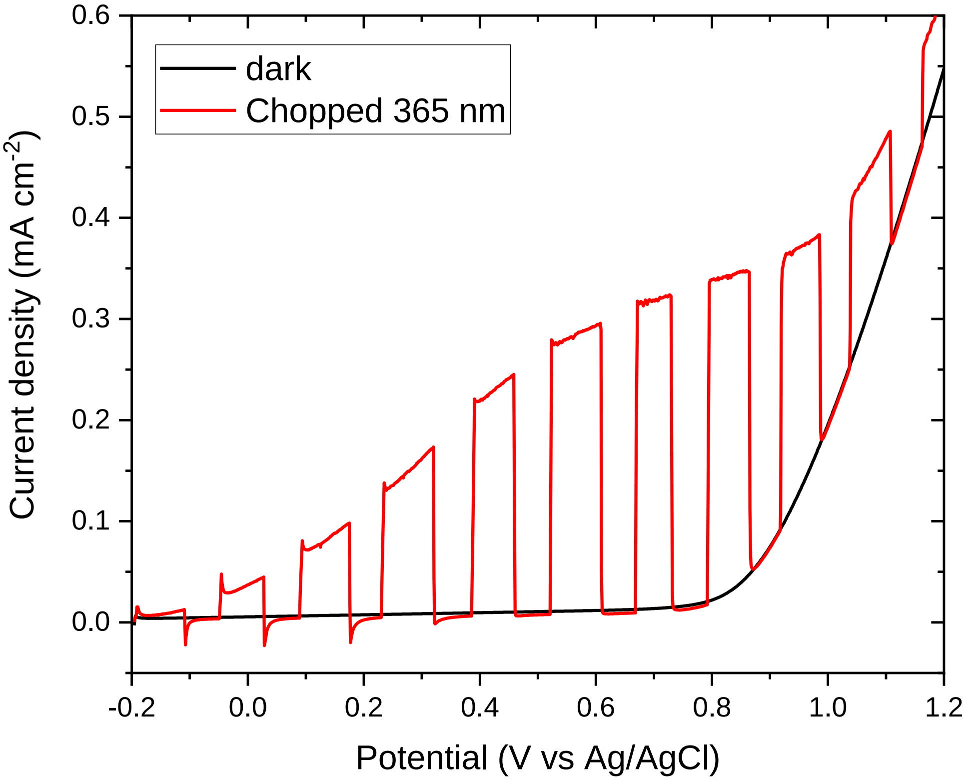

Figure 29: Chopped and dark LSVs at 10 mV s^{-1} of ED-Fe2O3 electrode used for in situ SHINERS experiments in 0.1 M NaOH. A 365 nm LED at 15 mW cm^{-2} was used for the chopped illumination.

So far, most experiments have attenuated the power of the 633 nm laser to 1-10% of the maximum power, as higher laser powers over very small beam areas (such as those used in a Raman microscope) can damage the material being studied. For example, anything above 10% laser power for more than several minutes on the glassy carbon electrodes would lead to visible scorch marks on the surface of the electrode. Furthermore, the SHINs are also susceptible to laser-induced damage as highlighted by Hartman *et al.*,[66] giving rise to many new Raman bands across the whole spectrum. This approach of using high laser powers was used to study hematite photoelectrodes at high current densities. It was found that the sample and SHINs were stable at the maximum powers at low applied potentials, but as the electrode was swept positive clear signs of laser-induced damage were observed after as short as 30 seconds of exposure, as seen in Figure 30. These signs of damage included the appearance of new bands, assigned to gold oxide formation (500-650 cm^{-1}) and to residual precursor materials from the SHINs synthesis, that did not disappear after the experiment, even after cycling to more negative potentials. These changes were only limited to the spot used for the electrochemical SHINERS experiments and moving to a new spot after the sample had returned to open circuit potential showed no such signs of damage. The laser-induced damage to SHINs particles also exposes the underlying gold, which can be observed in the electrochemical response of the system by the reduction peak of gold oxide in Figure 30. This demonstrates that damage to the surface is readily apparent in both the spectroscopy and the electrochemistry, making it obvious when the surface or SHINs are damaged. Careful use of higher laser powers could be exploited over shorter acquisition times to maximise the likelihood of detecting surface intermediates, as long as the spectroscopic or electrochemical signatures of damage are not observed. In doing so the dynamic response of the system during substantial OER currents can be monitored where the highest concentration of surface water splitting intermediates are expected.

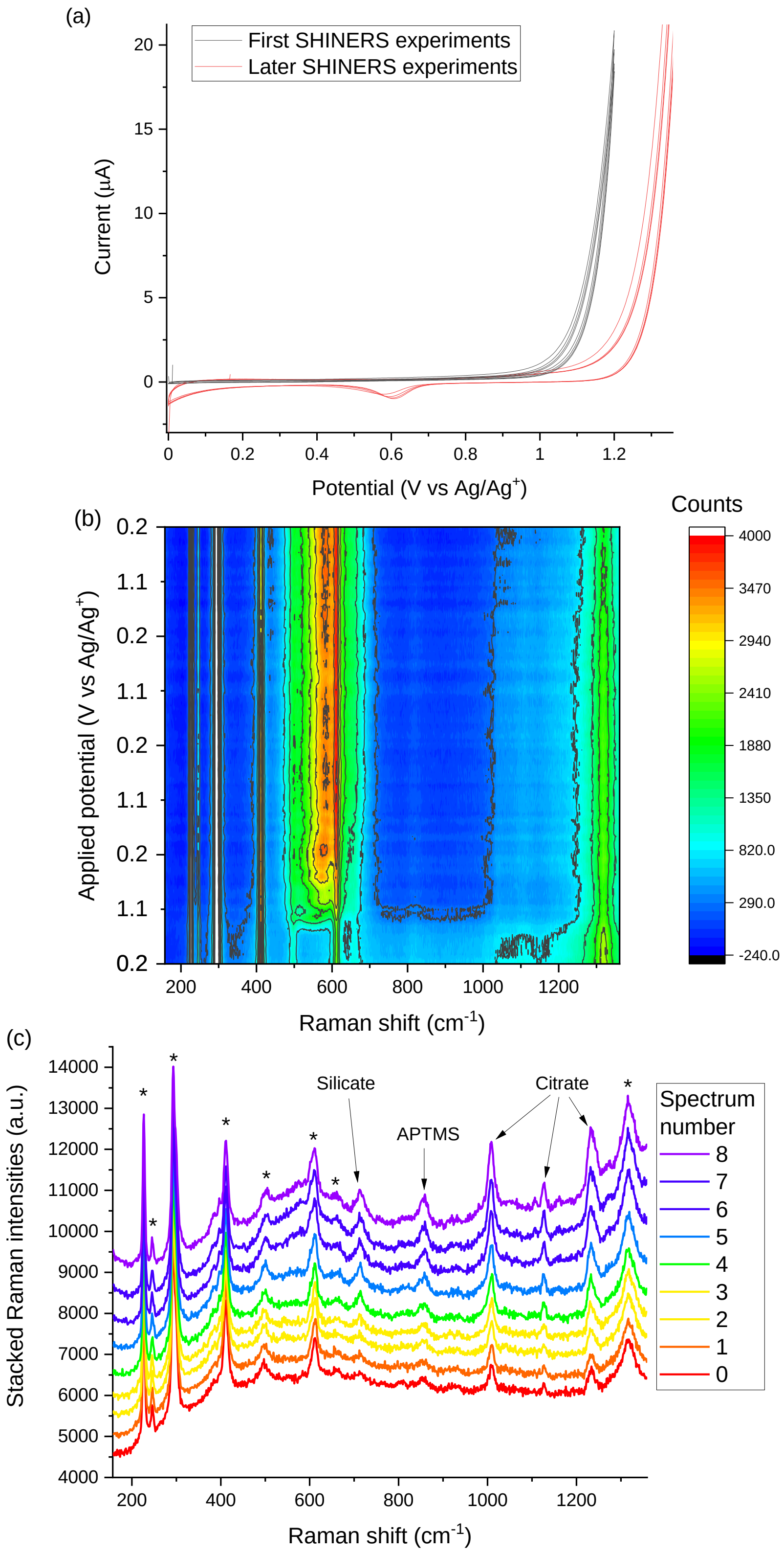

Figure 30: Cyclic voltammograms (2 mV s^{-1}) of electro-deposited hematite/FTO electrodes in 1 M $NaClO_4$ adjusted to pH 10 with NaOH before and after multiple high laser power SHINERS experiments (a). Laser-induced damage to the SHINs particles appears to have exposed the underlying gold as shown by the characteristic reduction peak of gold oxide ~ 0.6 V in the later experiments. In situ electrochemical SHINERS data for the same electrode showing the appearance of broad gold oxide Raman bands between 500 & 700 cm^{-1} after the sample is exposed to simultaneous high laser powers and large positive electrochemical bias (b). Stacked consecutive SHINER spectra of an ED-Fe_2O_3 electrode held at 1.1 V vs Ag/Ag$^+$ under high

*laser powers, showing the appearance of the same broad gold oxide band, as well as the growth of other contaminant bands assigned to residual precursor materials including sodium silicate, sodium citrate and APTMS (c), bands for crystalline α-Fe_2O_3 are signified with a *.*

Under these conditions, there are still no obvious and reproducible peaks for potential water splitting intermediates (such as oxo, superoxo or peroxo) which would be expected between 700 and 1200 cm-^{1} in Figure 31.[67,68] This suggests that either they are still below the detection limits for SHINERS or the vibrational modes for the intermediates are not Raman active.

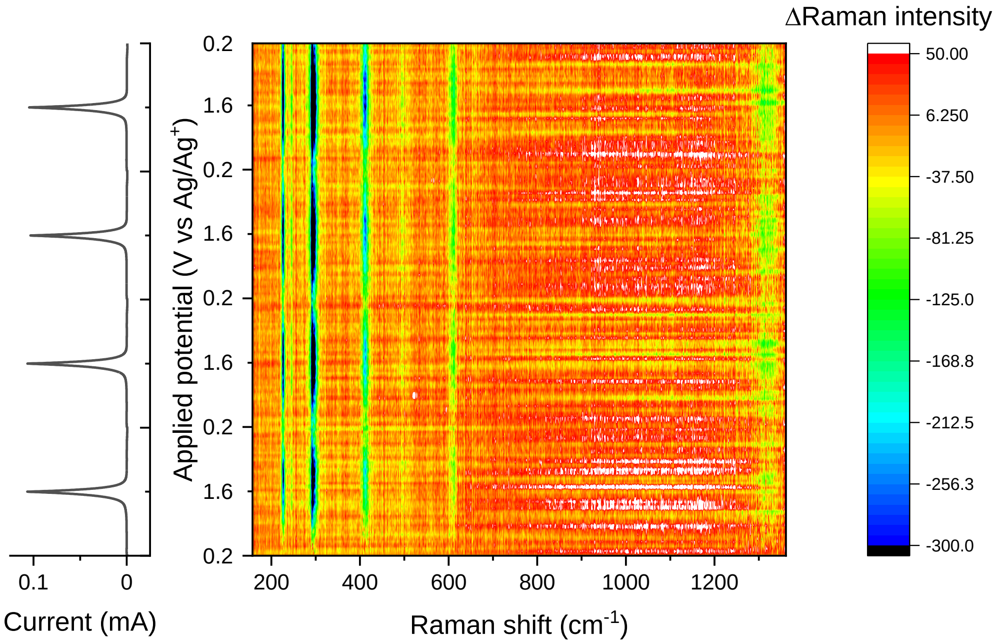

Figure 31: In situ electrochemical SHINER difference spectra compared to OCP of an ED-Fe_2O_3 film in 1 M $NaClO_4$ at 100% laser power at 633 nm, 5 mV s^{-1}, 4 CV cycles. Simultaneous current-voltage response is shown on the left.

Intriguingly, under the high laser power conditions the crystalline modes of the hematite also show a significant potential dependence in Figure 31. No potential dependence is observed on the same electrode in the same cell/electrolyte away from the SHINs particles. This clearly indicates that the effect requires the presence of the SHINs particles, suggesting it is an effect localised close to the surface. The shape of the potential dependence of the bulk Raman modes correlates well with the current voltage-response in the same experiments, as shown in Figure 32. If this response was simply due to optical absorbance changes in the hematite as the potential is cycled, the baseline in these Raman spectra would also be expected to show a similar potential-dependent change. Since no such change in the baseline is observed here this response is likely a real change in the crystalline hematite modes close to the surface. The peak positions do not show any significant shifts with applied potential, suggesting there are no significant structural changes that would change the bond strength. From Figure 31 it is unclear if all the crystalline Raman modes are changing in intensity in the same way, so the previously developed 2D correlational analysis was also carried out on this data.

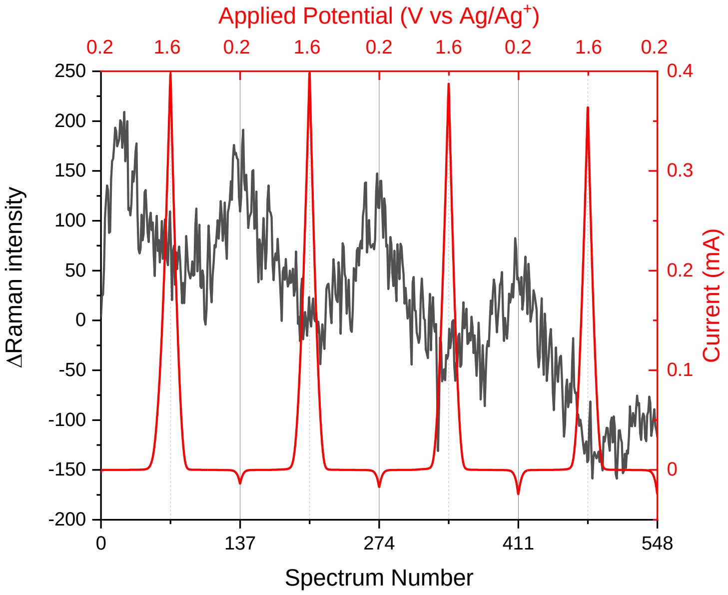

Figure 32: Potential-dependence of the largest crystalline Raman mode of hematite (E_g mode at 293 cm^{-1}) overlaid with the cyclic voltammograms from the in situ SHINERS experiment in Figure 31.

The aim of this correlational analysis is to identify if there is any difference in the potential-dependent response of the Raman bands of crystalline hematite, this could then indicate some surface structural changes during catalysis. The synchronous 2D plot in Figure 33 shows that all of the crystalline Raman bands of hematite have at least some positive cross-peak intensity with each other, indicating they are changing synchronously. There is some intensity across the asynchronous spectrum as well, however the signal to noise here is much lower, and the intensity in the cross-peaks is essentially at the same level as the noise in the background. This is made more apparent in the representative spectra shown in Figure 34, which was extracted using the same inverse FFT method described above for IrO_x in Figure 21.

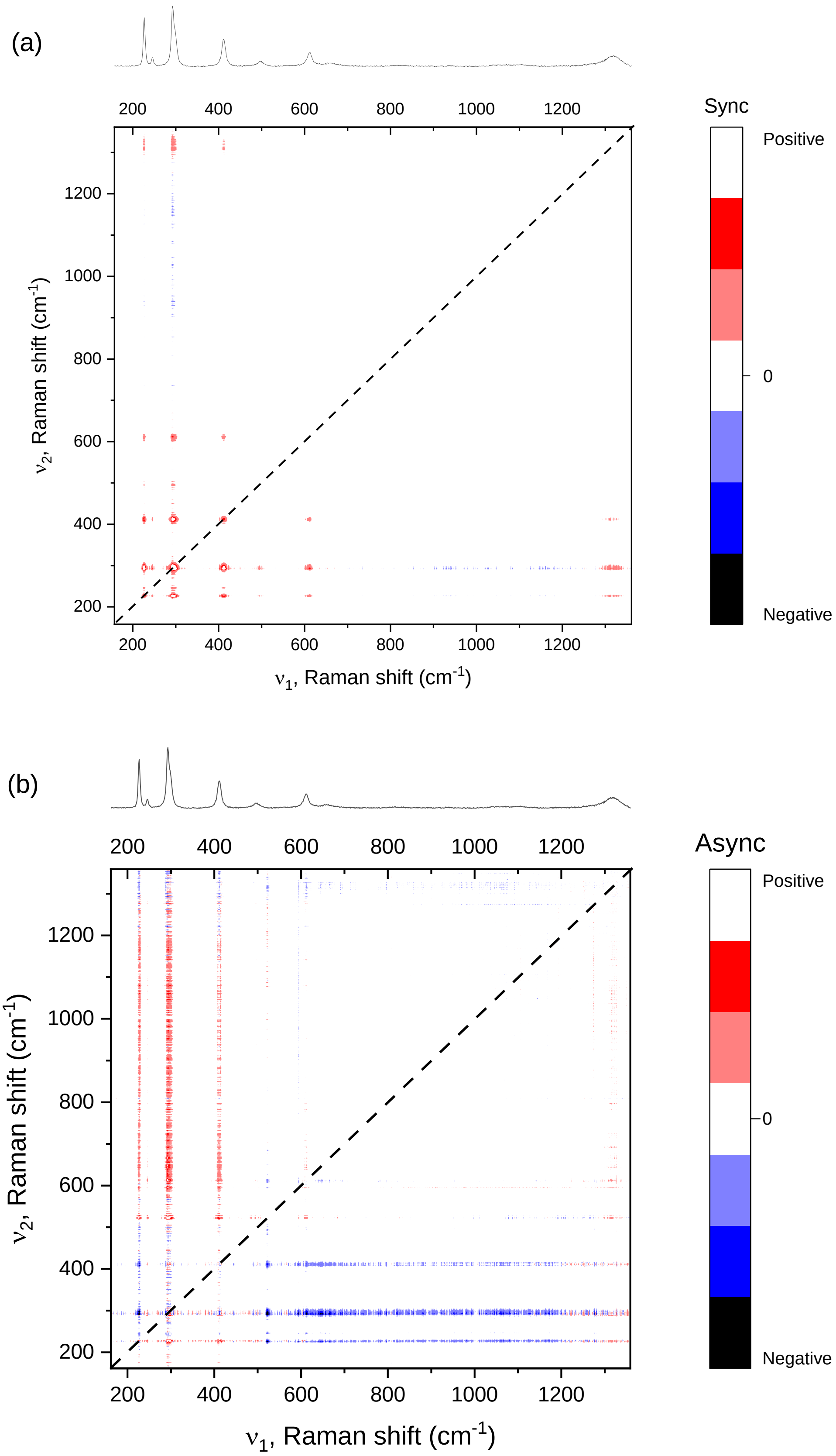

Figure 33: Synchronous (a) and asynchronous (b) 2D correlation plots for in situ SHINERS of ED-hematite electrodes during the in situ SHINERS experiment shown in Figure 31. Data was baseline corrected to a third order polynomial and then difference spectra to OCP were used as input for the 2D correlational analysis.

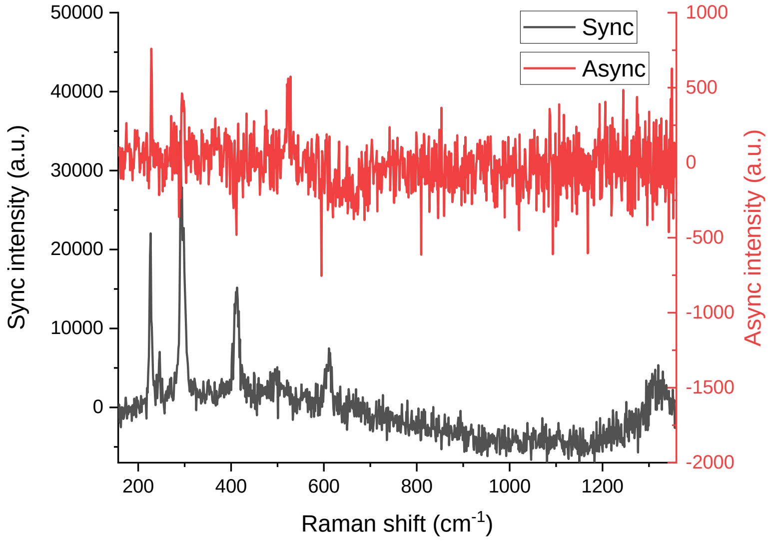

Figure 34: Representative synchronous and asynchronous spectra of the ED-Fe_2O_3 SHINERS experiment from Figure 31.

The data was then subject to the PCMW2D algorithm, using as small a window as possible (3 adjacent spectra) across the entire dataset of 220 spectra. The resulting synchronous and asynchronous spectra are displayed in Figure 35. As before, the synchronous spectrum indicates a clear potential dependence of all of the crystalline Raman modes. As 4 CV cycles are carried out for each experiment, only features present in all 4 cycles are likely real and no such modes can be seen in the asynchronous spectrum.

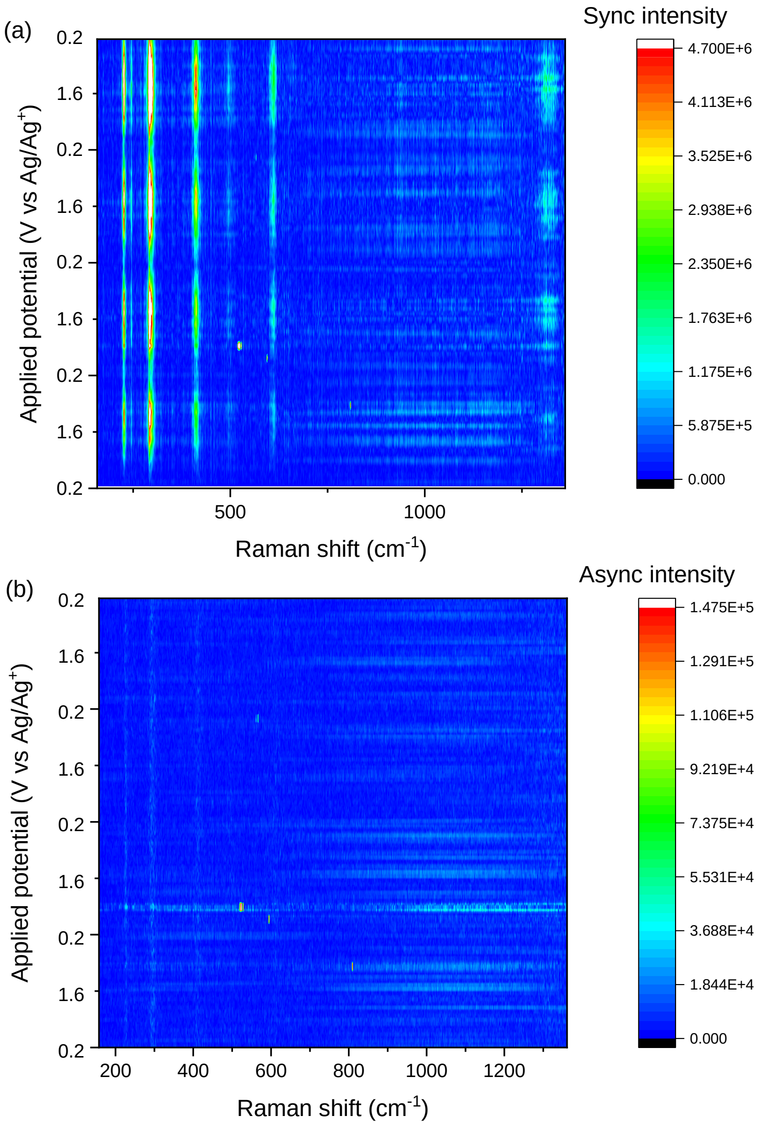

Figure 35: Synchronous (a) and asynchronous (b) PCMW2D of the ED-Fe_2O_3 SHINERS experiments from Figure 31.

This then returns us to the question of the nature of this potential dependence. The PCMW2D analysis has shown that all of the changes are synchronised, so all of the changes in the crystalline modes have a common origin. The changes are only observed at high laser powers and only on spots of the electrode containing SHINs. One possible explanation for this response could be related to potential-dependent changes in the plasmon resonance of gold nanoparticles, which has been observed previously on transparent electrodes.[69,70] There are several proposed mechanisms for this shift in plasmon resonance with potential, including depletion of free electrons in the outer layer the nanoparticle and changes in the dielectric constant of the medium surrounding the nanoparticle due to double layer charging. In this case, the silica shell electrically isolates the nanoparticle core from the electrode surface, so depletion of electrons from the nanoparticle will likely not be a factor. Instead, the double layer charging contribution could indeed be significant in these experiments. Such a shift in the position of the LSPR of the nanoparticles could explain the change in intensity without any shift in peak positions. However, regardless of the mechanism of the shift in plasmon resonance, a more positively charged electrode produced a redshift in the LSPR of the nanoparticles in this previous study.[70] As a result, an increase in the enhancement would be expected when using a 633 nm laser, as the LSPR maximum (λ_{LSPR} = 536 nm for the SHINs used here) would be shifted closer to the Raman laser wavelength with more positive potential. Instead, Figure 31 shows a decrease in signal of all the α-Fe_2O_3 modes with more positive potential, suggesting the potential-dependent shift in LSPR is not responsible for this effect.

This possible potential-dependence of λ_{LSPR} has not previously been investigated in detail for SHINs and could be an interesting area for future research. The previous investigations were carried out on uncoated gold nanoparticles, so transfer of electrons between the nanoparticle and the electrode surface could occur.[69,70] The resulting depletion of electrons in nanoparticles was listed as one of the possible causes of the observed redshift in λ_{LSPR}. The electrically insulating silica shell material around the SHINs used in this project will stop this electron transfer, likely leading to a different potential-dependent response. Experimentally, this effect could readily be investigated with *in situ* UV-VIS transmission studies of SHINs deposited on the same kind of transparent FTO/glass electrodes used above. Comparison of the response of gold nanoparticles with and without a silica shell could address whether this electron transfer is the main contributor to any observed shift in λ_{LSPR}.

The alternative explanation for the redshift of λ_{LSPR} with a positive applied potential was due to changes in the dielectric constant of the medium surrounding the nanoparticles.[70] This phenomenon is already acknowledged and used to explain the slight redshift in λ_{LSPR} when a silica shell is applied to the gold nanoparticles.[6] In an electrochemical system part of the surrounding medium is the electrolyte within the electrochemical double layer, and potential-dependent changes in the electrochemical double layer could be significant enough to affect the λ_{LSPR} of the SHINs. This contribution could also be addressed by *in situ* UV-VIS studies by changing the electrolyte composition. Both changes in the electrolyte concentration and the identity of the ionic species themselves can impact the double layer structure.[71] Thus, by varying the concentration and the size/valency of the electrolyte ions we could investigate the effect of double layer charging on λ_{LSPR}.

The *in situ* UV-VIS studies suggested above would need to be carried out on transparent electrodes. From the difference in the magnitude of enhancement at semiconductor *vs.* metal surfaces,[30] it is clear that the substrate itself has a big impact on the LSPR. This phenomenon arises due to hybridisation between the scattered electric field from the nanoparticles and the reflected electric field from the surface. Thus, To fully understand any such changes in λ_{LSPR} at hematite electrodes, the ideal substrate for the aforementioned *in situ* UV-VIS studies would be the hematite electrodes themselves, however there are several optical changes that occur in hematite between 500 & 600 nm[72,73] that would overlap with changes in λ_{LSPR}, complicating analysis. While it would be possible to synthesise larger SHINs (or SHINs with a different shape) to shift the LSPR away from these optical changes in hematite, this would also lead to an inherently weaker Raman signal as the Raman scattering cross section decreases at longer wavelengths.[74] Instead, these same ED-Fe_2O_3 electrodes will be revisited with another surface sensitive technique in Chapter 4, where *in situ* second harmonic generation spectroscopy will be carried out to address changes in local interfacial electric fields.

2.3. Conclusions and future work:

This chapter has introduced shell-isolated nanoparticle-enhanced Raman spectroscopy as a technique for studying electrode surfaces *in situ*. Initially the technique was used to investigate state-of-the-art IrO_x electrodes for dark electrochemical water splitting. This represents one of the first applications of the SHINERS technique to non-single crystal surfaces. The technique was used to identify catalytic surface intermediates as well as to monitor the changing oxidation state of the electrode surface in real-time, while addressing some of the complications from conventional SERS spectroscopy by not including any exposed gold in the system. The rapid acquisition times, combined with the sensitivity of the technique are incredibly appealing for studying many other electrochemical systems and the relative ease of drop-casting SHINs onto almost any surface further lowers the barrier to access. Time-resolved potential-step experiments with the sensitivity of the SHINERs technique are also an exciting next step, possibly enabling the detection of some of the previously undetected transient surface intermediates.

While the attempts at detecting intermediates on hematite and TiO_2 electrodes did not lead to any direct evidence of new catalytic intermediates, the techniques and analysis used along the way should hopefully be helpful when SHINERS are applied to other systems. Specifically, the power of the correlational analysis was demonstrated on the relatively small dataset from the IrO_x SHINERS data. The automated nature and indiscriminate method of analysis could very easily identify key bands related to catalytic intermediates in future experiments, especially if larger datasets are gathered.

2.4. References:

1 R. R. Jones, D. C. Hooper, L. Zhang, D. Wolverson and V. K. Valev, *Nanoscale Res. Lett.*, 2019, **14**, 231.

2 P. L. Stiles, J. A. Dieringer, N. C. Shah and R. P. Van Duyne, *Annu. Rev. Anal. Chem.*, 2008, **1**, 601–626.

3 S. Y. Ding, E. M. You, Z. Q. Tian and M. Moskovits, *Chem. Soc. Rev.*, 2017, **46**, 4042–4076.

4 S. Nie and S. R. Emory, *Science (80-.).*, 1997, **275**, 1102–1106.

5 K. Kneipp, Y. Wang, H. Kneipp, L. T. Perelman, I. Itzkan, R. R. Dasari and M. S. Feld, *Phys. Rev. Lett.*, 1997, **78**, 1667–1670.

6 J. F. Li, Y. F. Huang, Y. Ding, Z. L. Yang, S. B. Li, X. S. Zhou, F. R. Fan, W. Zhang, Z. Y. Zhou, D. Y. Wu, B. Ren, Z. L. Wang and Z. Q. Tian, *Nature*, 2010, **464**, 392–395.

7 T. Hartman and B. M. Weckhuysen, *Chem. - A Eur. J.*, 2018, **24**, 3733–3741.

8 A. Elci, O. Demirtas, I. M. Ozturk, A. Bek and E. Nalbant Esenturk, *J. Mater. Sci.*, 2018, **53**, 1–12.

9 X. D. Lin, V. Uzayisenga, J. F. Li, P. P. Fang, D. Y. Wu, B. Ren and Z. Q. Tian, *J. Raman Spectrosc.*, 2012, **43**, 40–45.

10 X. Bian, Z. L. Song, Y. Qian, W. Gao, Z. Q. Cheng, L. Chen, H. Liang, D. Ding, X. K. Nie, Z. Chen and W. Tan, *Sci. Rep.*, 2014, **4**, 29–32.

11 H. Zhang, C. Wang, H.-L. Sun, G. Fu, S. Chen, Y.-J. Zhang, B.-H. Chen, J. R. Anema, Z.-L. Yang, J.-F. Li and Z.-Q. Tian, *Nat. Commun.*, 2017, **8**, 15447.

12 L. Lin, X. Tian, S. Hong, P. Dai, Q. You, R. Wang, L. Feng, C. Xie, Z. Q. Tian and X. Chen, *Angew. Chemie - Int. Ed.*, 2013, **52**, 7266–7271.

13 D. Drescher, I. Zeise, H. Traub, P. Guttmann, S. Seifert, T. Büchner, N. Jakubowski, G. Schneider and J. Kneipp, *Adv. Funct. Mater.*, 2014, **24**, 3765–3775.

14 C. Y. Li, J. B. Le, Y. H. Wang, S. Chen, Z. L. Yang, J. F. Li, J. Cheng and Z. Q. Tian, *Nat. Mater.*, 2019, **18**, 697–701.

15 J. Dong, X. Zhang, V. Briega-Martos, X. Jin, J. Yang, S. Chen, Z.-L. Yang, D.-Y. Wu, J. M. Feliu, C. T. Williams, Z.-Q. Tian and J.-F. Li, *Nat. Energy*, 2018, 1–28.

16 M. M. Liang, Y. H. Wang, R. Shao, W. M. Yang, H. Zhang, H. Zhang, Z. L. Yang, J. F. Li and Z. Q. Tian, *Electrochem. commun.*, 2017, **81**, 38–42.

17 L. Cabo-Fernandez, D. Bresser, F. Braga, S. Passerini and L. J. Hardwick, *Batter. Supercaps*, 2019, **2**, 168–177.

18 G. Cabello, X. J. Chen, R. Panneerselvam and Z. Q. Tian, *J. Raman Spectrosc.*, 2016, **47**, 1207–1212.

19 J. Wang, J. C. Dong, J. Yang, Y. Wang, C. J. Zhang, M. M. Xu, B. W. Mao, J. L. Yao, J. F. Li and Z. Q. Tian, *Electrochem. commun.*, 2017, **78**, 16–20.

20 K. H. Saeed, M. Forster, J. F. Li, L. J. Hardwick and A. J. Cowan, *Chem. Commun.*, 2020, **56**, 1129–1132.

21 T. A. Galloway and L. J. Hardwick, *J. Phys. Chem. Lett.*, 2016, **7**, 2119–2124.

22 T. A. Galloway, J.-C. C. Dong, J.-F. F. Li, G. Attard and L. J. Hardwick, *Chem. Sci.*, 2019, **10**, 2956–2964.

23 Ji-Yang, J.-C. Dong, V. V. Kumar, J.-F. Li and Z.-Q. Tian, *Curr. Opin. Electrochem.*, 2017, **1**, 16–21.

24 J. F. Li, Y. J. Zhang, A. V. Rudnev, J. R. Anema, S. B. Li, W. J. Hong, P. Rajapandiyan, J. Lipkowski, T. Wandlowski and Z. Q. Tian, *J. Am. Chem. Soc.*, 2015, **137**, 2400–2408.

25 D. P. Butcher, S. P. Boulos, C. J. Murphy, R. C. Ambrosio and A. A. Gewirth, *J. Phys. Chem. C*, 2012, **116**, 5128–5140.

26 Y. F. Huang, C. Y. Li, I. Broadwell, J. F. Li, D. Y. Wu, B. Ren and Z. Q. Tian, *Electrochim. Acta*, 2011, **56**, 10652–10657.

27 A. J. Cowan and L. J. Hardwick, *Annu. Rev. Anal. Chem.*, 2019, **12**, 323–346.

28 N. Bodappa, M. Su, Y. Zhao, J.-B. B. Le, W.-M. M. Yang, P. Radjenovic, J.-C. C. Dong, J. Cheng, Z.-Q. Q. Tian and J.-F. F. Li, *J. Am. Chem. Soc.*, 2019, **141**, 12192–12196.

29 J. F. Li, S. Y. Ding, Z. L. Yang, M. L. Bai, J. R. Anema, X. Wang, A. Wang, D. Y. Wu, B. Ren, S. M. Hou, T. Wandlowski and Z. Q. Tian, *J. Am. Chem. Soc.*, 2011, **133**, 15922–15925.

30 S.-Y. Ding, J. Yi, J.-F. Li, B. Ren, D.-Y. Wu, R. Panneerselvam and Z.-Q. Tian, *Nat. Rev. Mater.*, 2016, **1**, 16021.

31 X.-D. Lin, J.-F. Li, Y.-F. Huang, X.-D. Tian, V. Uzayisenga, S.-B. Li, B. Ren and Z.-Q. Tian, *J. Electroanal. Chem.*, 2013, **688**, 5–11.

32 G. Barbillon, *Photonics*, 2021, **8**, 1–16.

33 A. J. Wain and M. A. O'connell, *Adv. Phys. X*, 2017, **2**, 188–209.

34 Z. Pavlovic, C. Ranjan, M. van Gastel and R. Schlögl, *Chem. Commun.*, 2017, **53**, 12414–12417.

35 Z. Pavlovic, C. Ranjan, Q. Gao, M. van Gastel and R. Schlögl, *ACS Catal.*, 2016, **6**, 8098–8105.

36 V. Pfeifer, T. E. Jones, S. Wrabetz, C. Massué, J. J. Velasco Vélez, R. Arrigo, M. Scherzer, S. Piccinin, M. Hävecker, A. Knop-Gericke and R. Schlögl, *Chem. Sci.*, 2016, **7**, 6791–6795.

37 V. Pfeifer, T. E. Jones, J. J. Velasco Vélez, R. Arrigo, S. Piccinin, M. Hävecker, A. Knop-Gericke and R. Schlögl, *Chem. Sci.*, 2017, **8**, 2143–2149.

38 V. A. Saveleva, L. Wang, D. Teschner, T. Jones, A. S. Gago, K. A. Friedrich, S. Zafeiratos, R. Schlögl and E. R. Savinova, *J. Phys. Chem. Lett.*, 2018, **9**, 3154–3160.

39 G. S. Nahor, P. Hapiot, P. Neta and A. Harriman, *J. Phys. Chem.*, 1991, **95**, 616–621.

40 P. Steegstra, M. Busch, I. Panas and E. Ahlberg, *J. Phys. Chem. C*, 2013, **117**, 20975–20981.

41 H. Ooka, A. Yamaguchi, T. Takashima, K. Hashimoto and R. Nakamura, *J. Phys. Chem. C*, 2017, **121**, 17873–17881.

42 T. Naito, T. Shinagawa, T. Nishimoto and K. Takanabe, *Inorg. Chem. Front.*, 2021, **8**, 2900–2917.

43 N. Sivasankar, W. W. Weare and H. Frei, *J. Am. Chem. Soc.*, 2011, **133**, 12976–12979.

44 J. F. Li, X. D. Tian, S. B. Li, J. R. Anema, Z. L. Yang, Y. Ding, Y. F. Wu, Y. M. Zeng, Q. Z. Chen, B. Ren, Z. L. Wang and Z. Q. Tian, *Nat. Protoc.*, 2013, **8**, 52–65.

45 S. K. Ghosh and T. Pal, *Chem. Rev.*, 2007, **107**, 4797–4862.

46 J. Zhao, J. A. Dieringer, X. Zhang, G. C. Schatz and R. P. Van Duyne, *J. Phys. Chem. C*, 2008, **112**, 19302–19310.

47 X. D. Tian, B. J. Liu, J. F. Li, Z. L. Yang, B. Ren and Z. Q. Tian, *J. Raman Spectrosc.*, 2013, **44**, 994–998.

48 R. D. Deegan, O. Bakajin, T. F. Dupont, G. Huber, S. R. Nagel and T. A. Witten, *Nature*, 1997, **389**, 827–829.

49 Y. Zhao, N. M. Vargas-barbosa, E. A. Hernandez-Pagan, T. E. Mallouk, E. A. Hernandez- and T. E. Mallouk, *Small*, 2011, **7**, 2087–2093.

50 S. H. Lee, I. Rusakova, D. M. Hoffman, A. J. Jacobson and T. R. Lee, *ACS Appl. Mater. Interfaces*, 2013, **5**, 2479–2484.

51 S. Thanawala, D. G. Georgiev, R. J. Baird and G. Auner, *Thin Solid Films*, 2007, **515**, 7059–7065.

52 A. Avila-García, G. Romero-Paredes and R. Peña-Sierra, *Progr. Abstr. B. - 2010 7th Int. Conf. Electr. Eng. Comput. Sci. Autom. Control. CCE 2010*, 2010, 537–540.

53 P. C. Liao, C. S. Chen, W. S. Ho, Y. S. Huang and K. K. Tiong, *Thin Solid Films*, 1997, **301**, 7–11.

54 S. Music, S. Popović, M. Maljković, Z. Skoko, K. Furić and A. Gajović, *Mater. Lett.*, 2003, **57**, 4509–4514.

55 Y. Mo, I. C. Stefan, W. Bin Cai, J. Dong, P. Carey and D. A. Scherson, *J. Phys. Chem. B*, 2002, **106**, 3681–3686.

56 H. G. Sanchez Casalongue, M. L. Ng, S. Kaya, D. Friebel, H. Ogasawara and A. Nilsson, *Angew. Chemie Int. Ed.*, 2014, **53**, 7169–7172.

57 I. Noda, *Appl. Spectrosc.*, 1993, **47**, 1329–1336.

58 I. Noda, *J. Am. Chem. Soc.*, 1989, **111**, 8116–8118.

59 I. Noda, *Vib. Spectrosc.*, 2012, **60**, 146–153.

60 M. A. Czarnecki, *Appl. Spectrosc.*, 1998, **52**, 1583–1590.

61 S. I. Morita, Y. F. Miura, M. Sugi and Y. Ozaki, *Chem. Phys. Lett.*, 2005, **402**, 251–257.

62 S. Morita, H. Shinzawa, I. Noda and Y. Ozaki, *Appl. Spectrosc.*, 2006, **60**, 398–406.

63 A. Conde-Gallardo, M. Guerrero, N. Castillo, A. B. Soto, R. Fragoso and J. G. Cabañas-Moreno, *Thin Solid Films*, 2005, **473**, 68–73.

64 A. . C. Sant'Ana, W. . A. Alves, R. H. . H. A. Santos, A. M. . M. D. Ferreira and M. L. A. Temperini, *Polyhedron*, 2003, **22**, 1673–1682.

65 O. Zandi, A. R. Schon, H. Hajibabaei and T. W. Hamann, *Chem. Mater.*, 2016, **28**, 765–771.

66 T. Hartman, C. S. Wondergem and B. M. Weckhuysen, *ChemPhysChem*, 2018, 2461–2467.

67 M. Zhang, M. de Respinis and H. Frei, *Nat. Chem.*, 2014, **6**, 362–7.

68 O. Zandi and T. W. Hamann, *Nat. Chem.*, 2016, **8**, 778–783.

69 H. Nishi, S. Hiroya and T. Tatsuma, *ACS Nano*, 2015, **9**, 6214–6221.

70 A. H. Ali and C. A. Foss, *J. Electrochem. Soc.*, 1999, **146**, 628–636.

71 A. J. Bard and L. R. Faulkner, *Electrochemical Method Fundamentals and Applications (Secon Edition)*, Wiley New York, 2001, vol. 2.

72 S. R. Pendlebury, X. Wang, F. Le Formal, M. Cornuz, A. Kafizas, S. D. Tilley, M. Grätzel and J. R. Durrant, *J. Am. Chem. Soc.*, 2014, **136**, 9854–9857.

73 M. Barroso, S. R. Pendlebury, A. J. Cowan and J. R. Durrant, *Chem. Sci.*, 2013, **4**, 2724.

74 D. A. Long, *The Raman effect: a unified treatment of the theory of Raman scattering by molecules. 2002*, Wiley, 2002, vol. 8.

Chapter 3

In situ sum frequency generation spectroscopy of photoelectrode surfaces

Parts of the introduction for this chapter are published in “Vibrational sum-frequency generation spectroscopy of electrode surfaces: Studying the mechanisms of sustainable fuel generation and utilisation” by A. M. Gardner, K. H. Saeed and A. J. Cowan, *Phys. Chem. Chem. Phys.*, 2019, **21**, 12067–12086, where the relevant section was written by myself. The data in this chapter was taken from several visits to the ULTRA-B experiment at the Central Laser Facility (Experiments 18130017 and 17330026), as such some of the data has previously been published online in the CLF Annual Reports (2017/18 & 2018/19)

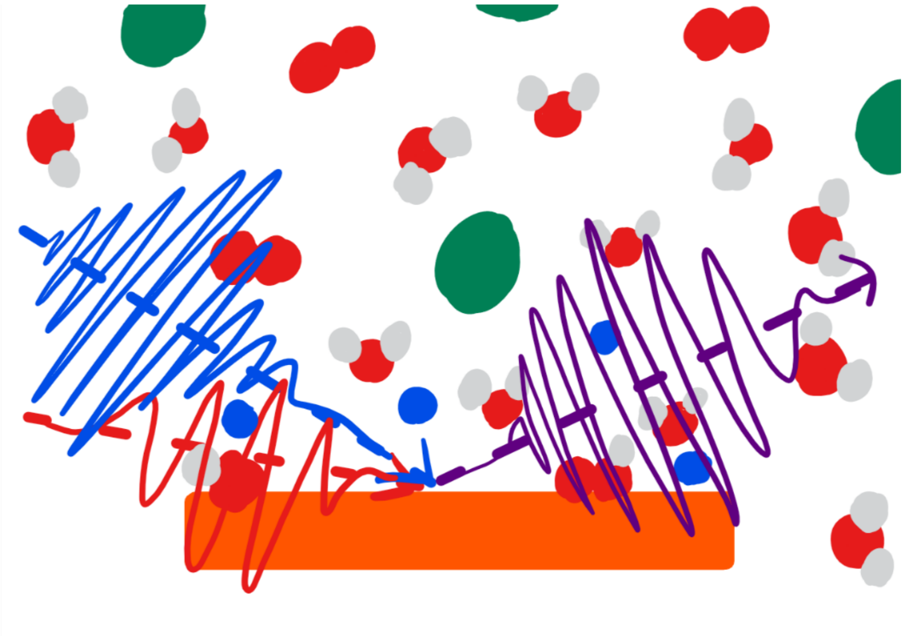

3.1. Introduction:

3.1.1. Importance of interfacial water structure:

The water structure at the electrode-electrolyte interface has the potential to play a profound role in controlling the OER mechanism and hence device performance but is largely understudied. The importance of bulk properties, such as pH,[1–3] are well-studied phenomena shown to have a drastic impact on the mechanism of water oxidation. However, the distinct physicochemical properties of a surface compared to the bulk can often lead to counterintuitive results, as in the case for determining the surface pH of water at the air/liquid interface.[4] Differences in the structure of water at the electrode/electrolyte interface compared to the bulk could have significant implications on both the energetics and kinetics of the water oxidation reaction. For example, it is known that the hydration structures around protons can control the mechanism of proton transfer,[5] which can then also influence the energetics of O-O bond formation.[6] The importance of water structure on OER kinetics and electrode stability was recently raised in a Perspective article by Grimaud *et al.*,[7] stating that they "believe that the next step in achieving enhanced electrocatalytic properties in solids lies within the structure of water in the vicinity of the active sites."

It is clear from above that a direct probe of interfacial water structure is needed to aid our understanding of and improve electrocatalytic materials. This chapter will introduce vibrational sum frequency generation (VSFG) spectroscopy and describe its application as a surface sensitive probe of interfacial water structure at photoelectrode surfaces. VSFG spectroscopy has been used to study water at charged interfaces for several decades; a summary of this research will be presented in Section 3.1.3. The remainder of this chapter will explore the development of an *in situ* electrochemical VSFG spectroscopy experiment to study changes in water structure during OER electrocatalysis, highlighting the many technical challenges and attempts to overcome them.

3.1.2. Vibrational sum frequency generation spectroscopy:

Infrared-visible sum frequency generation (SFG) spectroscopy is a form of vibrational spectroscopy that can give highly surface-sensitive structural information. Lambert *et al.* provide a useful, simplified introduction to the theory of SFG.[8] This review will focus on a summary of the key points in the simplified description of vibrational sum frequency generation (VSFG) spectroscopy. More rigorous derivations can be found elsewhere.[9]

Typically, the interaction of light with condensed phases is described by linear optical processes, such as absorption or transmission. Light propagating through a medium interacts with the valence electrons of the material, inducing electric dipoles. The sum of these dipoles, the bulk polarisability (**P**), can be described by Eq. 3.1. & 3.2.

$$\boldsymbol{P} = \varepsilon_0\left(\chi^{(1)}\boldsymbol{E} + \chi^{(2)}\boldsymbol{E}^{\boldsymbol{2}} + \chi^{(3)}\boldsymbol{E}^{\boldsymbol{3}} + \cdots\right) \qquad \text{Eq. 3.1.}$$

$$\boldsymbol{P} = \boldsymbol{P}^{(1)} + \boldsymbol{P}^{(2)} + \boldsymbol{P}^{(3)} + \cdots \qquad \text{Eq. 3.2.}$$

where ε_0 is the vacuum permittivity, **E** is the electric field and $\chi^{(1)}$, $\chi^{(2)}$ and $\chi^{(3)}$are the linear, 2nd and 3rd order susceptibilities, respectively. The $\chi^{(2)}$and $\chi^{(3)}$ terms are substantially smaller than $\chi^{(1)}$ and are neglected for linear optical processes. Second and third order effects are only seen with large electric fields, such as under pulsed laser irradiation.

IR-Vis SFG is a second-order process, where the surface is exposed to spatially and temporally overlapped visible and infrared pulses. Under these conditions, the electric field at the surface can be described by the sum of the two different laser frequencies:

$$\boldsymbol{E} = \boldsymbol{E}_1 cos(\omega_1 t) + \boldsymbol{E}_2 cos(\omega_2 t) \qquad \text{Eq. 3.3.}$$

The SFG field, as well as difference frequency generation (DFG) and second harmonic generation (SHG) fields, arise from the second order term when combining Eq. 3.1. and Eq. 3.3.

$$\boldsymbol{P}^{(2)} = \varepsilon_0 \chi^{(2)} (\boldsymbol{E}_1 \cos(\omega_1 t) + \boldsymbol{E}_2 \cos(\omega_2 t))^2 \qquad \textit{Eq. 3.4.}$$

Expansion of Eq. 3.4. gives the frequency dependence of the resulting fields:

$$\boldsymbol{P}^{(2)} = \varepsilon_0 \chi^{(2)} \left(\begin{array}{c} \boldsymbol{E}_1^2 + \boldsymbol{E}_2^2 + \boldsymbol{E}_1^2 cos(2\omega_1 t) + \boldsymbol{E}_2^2 cos(2\omega_2 t) + \frac{1}{2}\boldsymbol{E}_1\boldsymbol{E}_2 \cos(\omega_1 - \omega_2 t) \\ + \frac{1}{2}\boldsymbol{E}_1\boldsymbol{E}_2 \cos(\omega_1 + \omega_2 t) \end{array} \right) \qquad \textit{Eq. 3.5.}$$

The resulting fields shown in Eq. 3.5. include a frequency-independent field (red), fields oscillating at twice the frequency of the incident fields (green, SHG), at the difference of the two frequencies (blue, DFG) and the sum of the two frequencies (orange, SFG). In the dipole approximation, $\chi^{(2)} = 0$ in media with inversion symmetry, such as isotropic bulk material.[10] Another way of understanding this is that polarisation induced by **E** and **-E** would be the same:

$$\boldsymbol{P}^{(2)}(\boldsymbol{E}) = \boldsymbol{P}^{(2)}(-\boldsymbol{E}) \qquad \textit{Eq. 3.6.}$$

For centrosymmetric environments the bulk polarisation would be equivalent in both directions:

$$\boldsymbol{P}^{(2)}(\boldsymbol{E}) = -\boldsymbol{P}^{(2)}(-\boldsymbol{E}) \qquad \textit{Eq. 3.7.}$$

For both Eq. 3.6. & 3.7. to hold true, the induced bulk polarisation, $\boldsymbol{P}^{(2)}$ from Eq. 3.5., would have to be zero, therefore $\chi^{(2)} = 0$.

The inversion symmetry of the bulk is naturally broken at interfaces, so SFG signals can be selectively generated at surfaces. However, it should also be noted that although described here as interface-specific, $\chi^{(2)}$ can be greater than zero for materials with crystal structures that lack a centre of inversion, enabling SFG from their bulk as well as at interfaces. Such nonlinear optical materials are widely studied, make up many components of the laser systems used in this project and can also be exploited as alignment samples for the SFG experiment, as described in Appendix B.

The first VSFG spectrometers employed narrowband IR sources (<10 cm^{-1}),[11,12] recording spectra by scanning the frequency of the IR source. The spectrometers used in this project make use of femtosecond laser systems that enable generation of broadband IR light (>100 cm^{-1}) and will be described in more detail below. The broadband IR pulse generates a time-dependent IR polarisation that can interact with the visible pulse through an anti-stokes Raman process to generate the VSFG polarisation. A resonant SFG signal can be observed when the frequency of the IR pulse matches that of a vibrational mode for a surface species, otherwise, a wavelength independent non-resonant (NR) SFG signal is observed. It can be useful to think of a resonant VSFG process using a two-step model, as depicted in Figure 36a. (i) The IR pulse induces a net polarisation in molecules at the surface, which emits light at the corresponding resonant vibrational frequencies. (ii) This emitted light is upconverted by frequency mixing with the visible pulse to generate light at the sum of the infrared and visible frequencies. A non-resonant SFG signal is observed in cases when the IR frequency is not resonant with any molecular vibrations (Figure 36b). In this project broadband IR pulses with an approximately Gaussian profile are used. As a result, the nonresonant component of the VSFG spectrum follows the Gaussian shape of the incident IR profile (blue in Figure 36c), while the resonant component (red in Figure 36c) matches the frequencies of molecular vibrations. Both resonant and non-resonant transitions contribute to the detected VSFG signal, leading to the overall signal being a combination of both (black dotted line in Figure 36c). The depiction shown here is for the simplified case where there is no phase difference between the resonant and NR signals. In reality, a difference in phase between the resonant and NR leads to constructive/destructive interference between the two and can lead to negative and derivative-like peaks in the final spectrum.

The intensity of a surface VSFG signal stems from the second order nonlinear susceptibility, $\chi^{(2)}$, which is influenced by both the net (summed over all individual molecules) transition dipole moment and transition Raman polarisablity of the area being probed. Both of these net quantities approach zero in a completely disordered system due to cancellation from opposite orientations, conversely they would increase in an increasingly ordered system. Thus, the value of $\chi^{(2)}$ will be larger for ordered layers of molecules at a surface compared to disorderd interfacial molecules, which will influence both the resonant and nonresonant contributions to the signal.

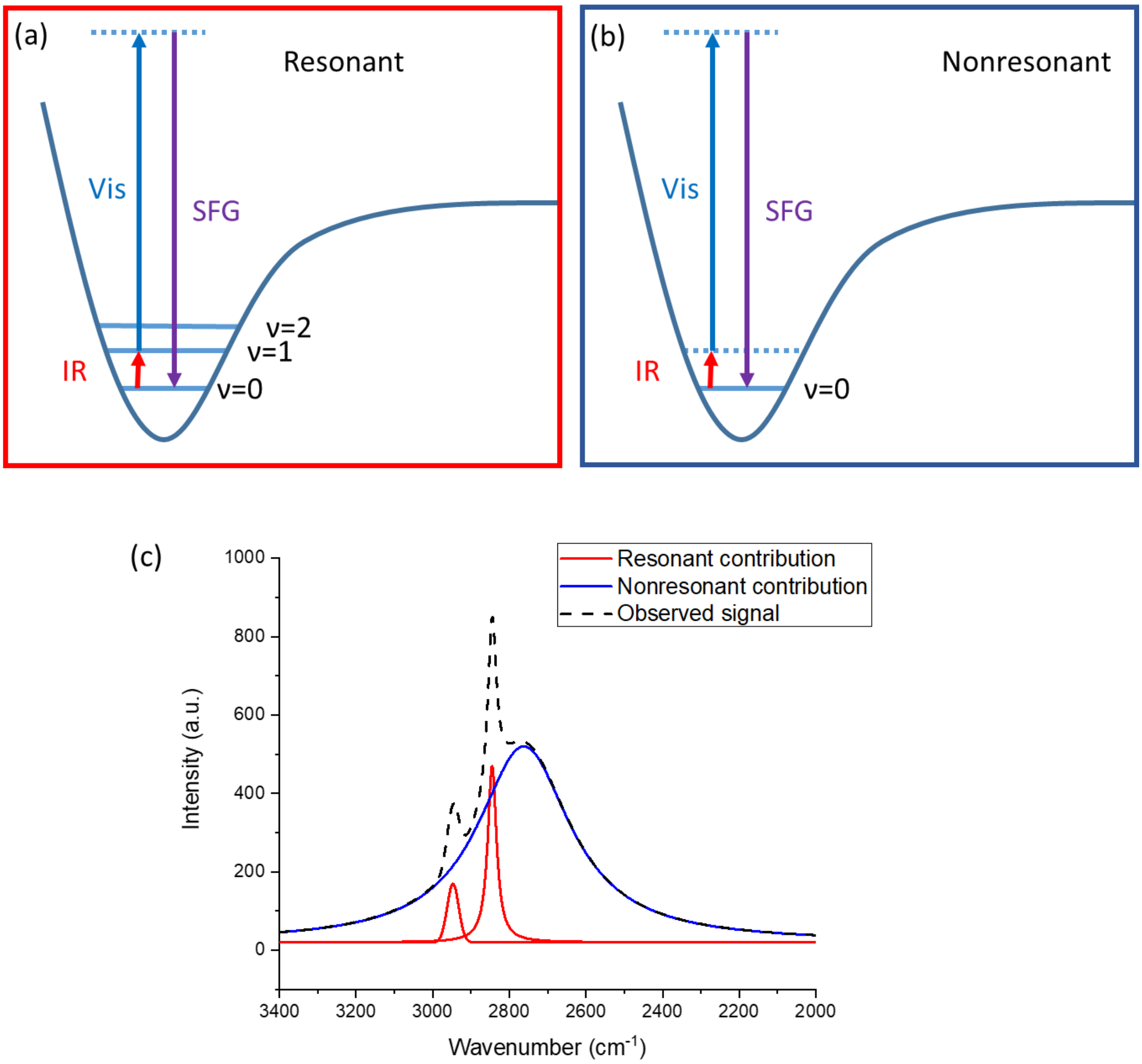

Figure 36: Schematic representations of energetic transitions for resonant (a) and non-resonant (b) SFG experiments, dotted lines represent virtual excited states. A simplified set of SFG spectra are shown in (c), assuming that there is no difference in phase between the resonant (red) and nonresonant (blue) contributions.

The intensity of the SFG signal can be described by Eq. 3.8.

$$I_{SFG}(\omega) \propto \left(\chi_R^{(2)} + \chi_{NR}^{(2)}\right)^2 \quad \text{Eq. 3.8.}$$

Where $\chi_R^{(2)}$ and $\chi_{NR}^{(2)}$ are the resonant and non-resonant 2nd order nonlinear susceptibilities, respectively. Separation of the resonant and nonresonant contributions to leave just the resonant spectrum would make it easier to understand the relevant spectral information. In linear spectroscopy, the presence of a background signal within the spectrum can sometimes be addressed by subtracting a suitable reference spectrum. However, in nonlinear SFG spectroscopy the expansion of Eq. 3.8. introduces a cross-term:

$$I_{SFG}(\omega) \propto {\chi_R^{(2)}}^2 + {\chi_{NR}^{(2)}}^2 + 2\chi_R^{(2)}\chi_{NR}^{(2)} \qquad \textit{Eq. 3.9.}$$

The presence of the (blue) cross term in Eq. 3.9. makes it impossible to separate the two contributions by simply subtracting a suitable reference spectrum, since any changes in the resonant contribution between the sample and reference would affect this cross term as well. Instead, an alternative approach can be used where the NR signal is significantly suppressed as discussed below.

Temporal overlap of the IR and visible pulses is key to both resonant and NR-SFG, as simultaneous vibrational and electronic excitations are required for an SFG signal. This is especially true for NR-SFG as it can be thought of as excitations to virtual excited states, which typically only persist for the duration of the sub-picosecond infrared laser pulse. Delaying the visible pulse outside of this timescale allows the transient nonresonant vibrational excitation to decay before the visible upconversion takes place, so minimal NR SFG signal is observed. This mechanism has been used for suppression of the NR-SFG signal by Lagutchev *et al.*[13] and relies on a time-asymmetric picosecond visible pulse. A sharp rise-time (<1 ps) to the visible pulse allows fine control of the temporal overlap, while a long (>1 ps) tail enables better sampling of longer-lived vibrational resonances. Fabry-Perot etalons were used in this project to convert the femtosecond outputs of the lasers to the required time-asymmetric picosecond pulse shapes.

The IR induced polarisation is described as the sum of the resonant (${P^{IR}}_R(t)$) and nonresonant (${P^{IR}}_{NR}(t)$) components:

$$P^{IR}(t) = P^{IR}{}_{R}(t) + P^{IR}{}_{NR}(t) \qquad \text{Eq. 3.10.}$$

$P^{IR}{}_{NR}(t)$ is very short-lived (< 200 fs), whereas $P^{IR}{}_{R}(t)$ can typically range from hundreds of femtoseconds to a few picoseconds as it is dependent on the lifetime of molecular vibrations. By delaying the visible pulse several hundred fs, the short-lived $P^{IR}{}_{NR}(t)$ responsible for the NR signal can decay, while the longer-lived $P^{IR}{}_{R}(t)$ is upconverted, giving a resonant SFG signal corresponding to these molecular vibrations, as shown in Figure 37. Thus, choosing an appropriate delay time for the visible laser pulse allows almost complete suppression of the NR SFG signal.

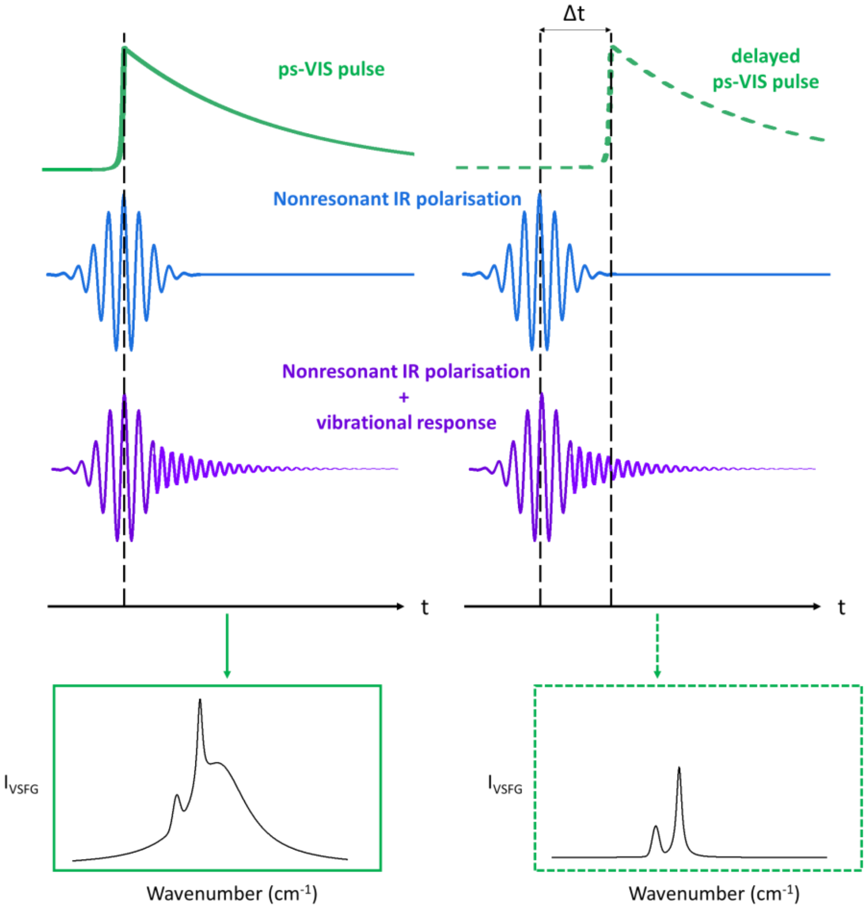

Figure 37: Schematic showing the temporal profiles of the polarisation induced by the femtosecond IR pulse & the time-asymmetric picosecond VIS pulse. When the IR pulse is vibrationally resonant with a surface mode the vibrational response can be seen as the free induction decay in purple. The left side shows how complete temporal overlap of the picosecond visible and femtosecond IR pulses leads to observance of a convoluted resonant and nonresonant response. The right side shows how adding short delay to the picosecond visible pulse (Δt) allows the transient nonresonant vibrational response (with the same Gaussian shape as the fs-IR pulse) to decay, leaving only the resonant vibrational response (shown here as the free induction decay) to be upconverted by the visible pulse.

Surface-sensitivity is an appealing feature of VSFG spectroscopy, especially for detecting small concentrations of surface species. Stiopkin *et al.* were able to demonstrate its sub-monolayer sensitivity at a gold surface, by monitoring the C-H stretching frequency of various surface coverages of octanol.[14] Previous research has also used SFG to probe electrochemical interfaces.[15] However, the SFG signal during *in situ* electrochemical measurements is further complicated by the presence of a charged electrode surface, which introduces an additional electrostatic field at the surface. This field extends further into the bulk electrolyte than just the interface, in a region known as the electrical double layer (EDL), depicted in Figure 38.[16]

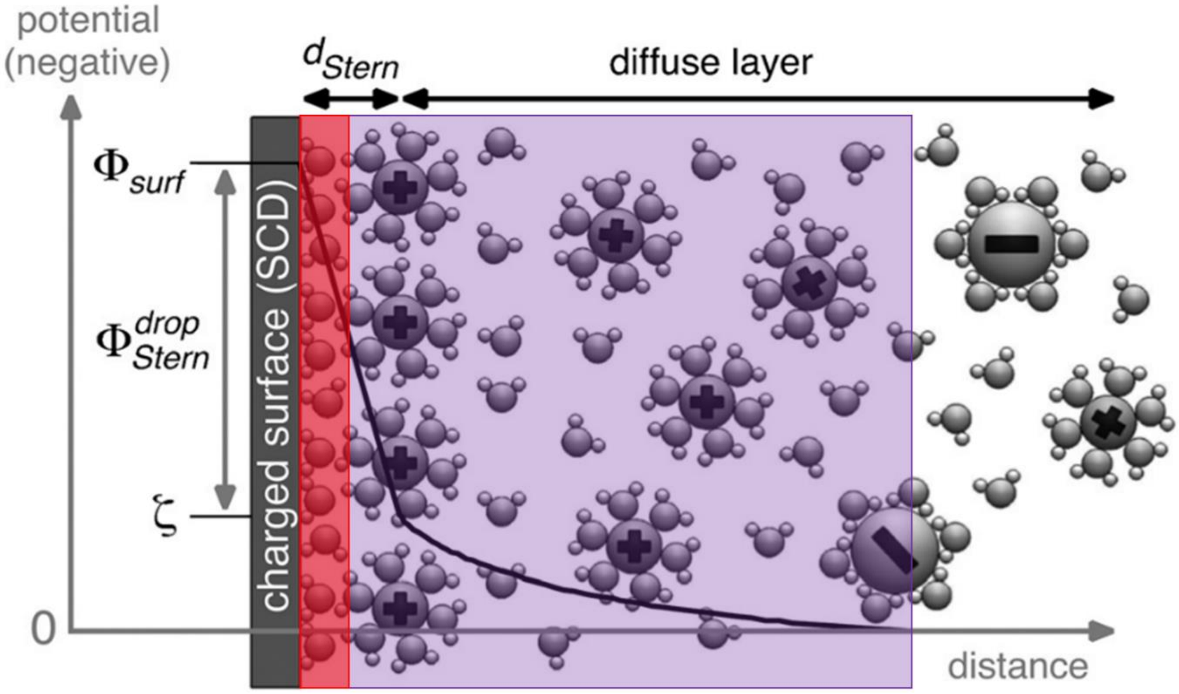

Figure 38: Diagram of the Gouy-Chapman-Stern model of the electrical double layer at a negatively charged solid/electrolyte interface, showing the ordering of water close to the surface as well as the potential drop over the diffuse layer (adapted with permission from Brown et al.*).*[16] *The red and purple areas correspond to the different areas probed by the corresponding terms in Eq.3.10.*

The resulting asymmetry of the double layer is expressed in the SFG polarisation by an additional term that depends on the DC field at the electrode (**E**$_{DC}$), which follows the third order susceptibility:

$$\boldsymbol{P}_{SFG} \propto \chi^{(2)}\boldsymbol{E}_{vis}\boldsymbol{E}_{IR} + \chi^{(3)}_{eff}\boldsymbol{E}_{vis}\boldsymbol{E}_{IR}\boldsymbol{E}_{DC} \quad \text{Eq. 3.10.}$$

What Eq. 3.10. suggests is that SFG signals at charged surfaces contain contributions from both the usual second order susceptibility term that arises from the surface/ordered water interface, as well as a third order susceptibility-dependent term that is generated from the diffuse region affected by $\boldsymbol{E}_{DC}$. The distance over which this $\boldsymbol{E}_{DC}$ term acts is highlighted in purple in Figure 38. This distance is related to a quantity known as the Debye length (λ_D), which describes the distance at which the field has dropped by a factor of 1/e. While this additional field interacts with the intrinsic third order susceptibility of this purple region, the purple term is labelled as the effective susceptibility in Eq. 3.10. as it also contains an additional contribution. The presence of a charged electrode surface interacts with the polar water molecules and induces an increased ordering of water molecules over λ_D. The resulting asymmetry of these water molecules, that would otherwise be considered bulk in the absence of $\boldsymbol{E}_{DC}$, will interact through both their second and third order susceptibilities.[17] Thus, for water the effective third order susceptibility can be summarised by:

$$\chi_{eff}^{(3)} = \chi^{(3)} + n_{H_2O}\left(\alpha_{H_2O}^{(2)}\right) \qquad \text{Eq. 3.11.}$$

Where α represents the orientationally averaged molecular hyperpolarisabilities and n_{H_2O} is the number of water molecules within the double layer.

The case for semiconductor photoelectrodes is further complicated since there is an additional electric field within the semiconductor over a region known as the space charge layer. This additional field breaks the inversion symmetry over a small region within the semiconductor close to the electrode/electrolyte interface. This will likely not lead to additional resonant changes in our experiments studying the stretching modes of water, but it could affect the nonresonant response. As a result, electrochemical VSFG spectroscopy at photoelectrodes can be sensitive to changes in molecular structure and/or interfacial electric fields that occur in the space charge layer within the electrode, at the electrode/electrolyte interface and over the electrochemical double layer, although analysis of spectra is complicated by these three contributing terms.

Rey & Dlott have previously modelled the potential dependence of the nonresonant VSFG signal in systems dominated by either a $\chi^{(2)}$ response or a $\chi^{(3)}$ response.[15] Such analysis will be relevant for interpreting potential-dependent VSFG spectra later in this chapter so will be expanded on here. The intensity of the observed SFG response is related to the square of both contributing nonlinear susceptibilities:

$$I_{SFG} \propto \left|\chi^2(E_{vis})(E_{IR}) + \chi^{(3)}_{eff}(E_{vis})(E_{IR})(E_{DC})\right|^2 \qquad \textit{Eq.3.12.}$$

Expansion of Eq. 3.12. gives:

$$\begin{aligned} I_{SFG} \propto\ & |\chi^2(E_{vis})(E_{IR})|^2 + 2\left(\chi^{(3)}_{eff}(E_{vis})(E_{IR})(E_{DC})\right)\left(\chi^{(2)}(E_{vis})(E_{IR})\right) \\ & + \left|\chi^{(3)}_{eff}(E_{vis})(E_{IR})(E_{DC})\right|^2 \end{aligned} \qquad \textit{Eq.3.13.}$$

In an electrochemical system E_{DC} is varied, so the last two terms in Eq. 3.13. will contribute to the changing VSFG signal with applied potential if there are no chemical/orientation changes at the interface. A changing signal that is dominated by the interfacial χ^2 term (orange in Eq. 3.13.) will have a linear dependence on E_{DC}. Conversely, a signal dominated by the χ^3 term (blue in Eq. 3.13.) will depend on $(E_{DC})^2$, so would show a quadratic potential dependence. Rey & Dlott simulated these linear and parabolic dependences during cyclic voltammograms in Figure 39 for the two extreme cases, where $\chi^2 \gg \chi^3$ results in a sawtooth pattern, while $\chi^3 \gg \chi^2$ results in a series of adjoining parabola. Any deviations from these expected behaviours could either be the results of changes in the interfacial structure (leading to a different value of χ^2) or overlapped vibrational resonances that also change with potential.

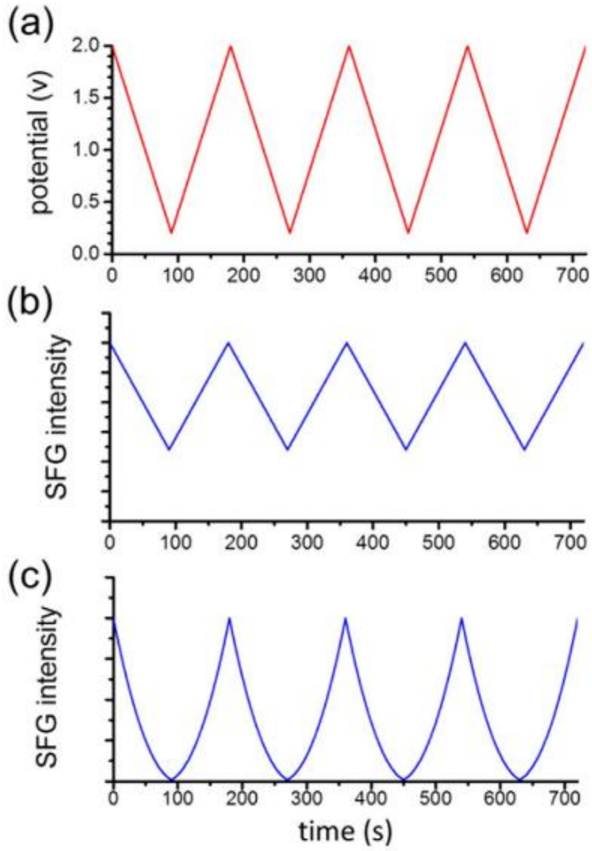

Figure 39: Computed nonresonant SFG intensities over 4 CV cycles at 5 mv s^{-1} *when* $\chi^{(2)}$ *is dominant (b) and when* $\chi^{(3)}$ *is dominant (c) reproduced with permission from Rey and Dlott, J. Electroanal. Chem., 2017.*[15]

3.1.3. VSFG of water at charged interfaces:

Charged solid/water interfaces are not just relevant to electrochemical water splitting but are naturally present when ionisable mineral surfaces come into contact with water. At such interfaces, an EDL will form at any pH away from the point of zero charge (PZC), leading to orientation of interfacial water molecules. VSFG spectroscopy has been used extensively to study the O-H stretch of water at a variety of such mineral interfaces,[18] including SiO_2,[19] Al_2O_3,[20,21] and CaF_2.[22,23] A typical VSFG spectrum for SiO_2/water interface is shown in Figure 40 from Ostroverkhov *et al.*,[24] depicting two broad resonant modes at ~ 3200 cm^{-1} and 3450 cm^{-1}. Due to the similarity to the ice/silica spectrum, the peak ~ 3200 cm^{-1} was initially assigned to the symmetric O-H stretch of water in an ordered H-bonding environment (“ice-like”), while the peak at 3450 cm^{-1} was assigned to O-H stretches in a more disordered H-bonding environment ("liquid-like") by Du *et al.*[25] In the same study, phase-sensitive measurements showed an inversion in the phase of the VSFG signal as the bulk pH was varied between 1.5 and 12.3, where the surface silanol groups are expected to be either fully protonated or deprotonated, respectively.[24] This was the first direct evidence of the flipping of water molecules due to opposite surface charges, to have the hydrogens either pointing away from a protonated surface or towards a deprotonated surface.

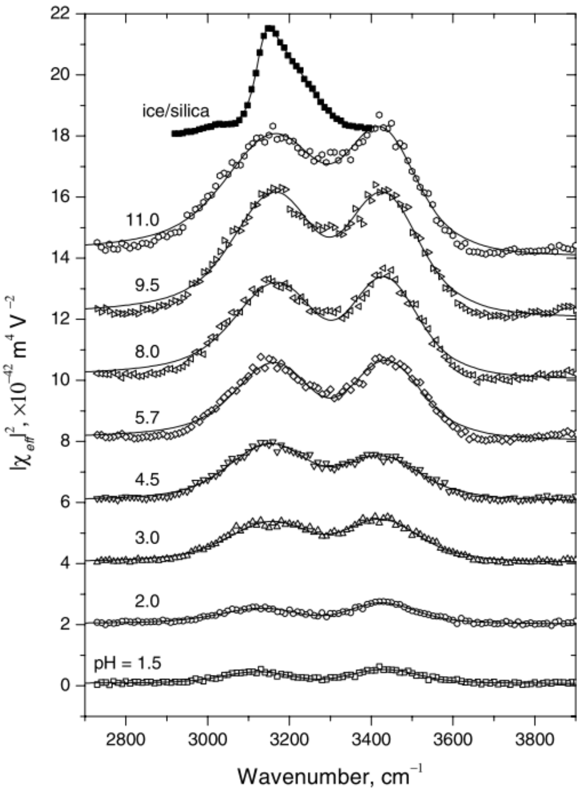

Figure 40: VSFG spectra of water/a-quartz (0001) interface at various bulk pH values (as well as ice/silica for comparison) in SSP polarisation of SFG, ''visible'' and IR respectively, reproduced with permission from Ostroverkhov et al.[24]

Furthermore, the magnitude of $\chi^{(2)}$ will be larger for a highly ordered layer of water molecules at a charged interface compared to a less ordered layer at an uncharged surface. This effect can be observed in the intensity of the VSFG signals in Figure 40 when taking into account that most SiO_2 surfaces typically have a PZC of less than 3.[26] The intensity of the VSFG signal increases with pH between pH 3 and 8, due to the more ordered layers of water expected at the more highly charged surfaces. The VSFG Intensity is relativley constant above pH 8, liklely due to the surface being fully deprotonated at these pH values so there are no further increases in the ordering of water close at the surface.

The assignment of this doublet structure to two different H-bonding environments has since been disputed by Sovago *et al.*,[27] who argue that the doublet peak structure arises instead from an intramolecular Fermi resonance. This Fermi resonance occurs when the usually weak (since the transition is both IR and Raman forbidden from the vibrational ground state) first overtone of the H-O-H bend vibration is resonant with the symmetric O-H stretch in liquid water, resulting in intramolecular coupling between the two modes.[28] They demonstrate that this coupling can be suppressed by gradual isotopic dilution of D_2O with H_2O, showing a smooth transition from two peaks to one, as seen in Figure 41 from Sovago *et al.*[29] This occurs as the H-O-D bending overtone is no longer resonant with either the O-D or O-H stretching vibrations in the mixed HOD species, leading to a single O-D stretch peak. Additional studies using this isotopic dilution technique and phase-sensitive VSFG spectroscopy have further confirmed this assignment to a Fermi resonance through intramolecular vibrational coupling.[30–32]

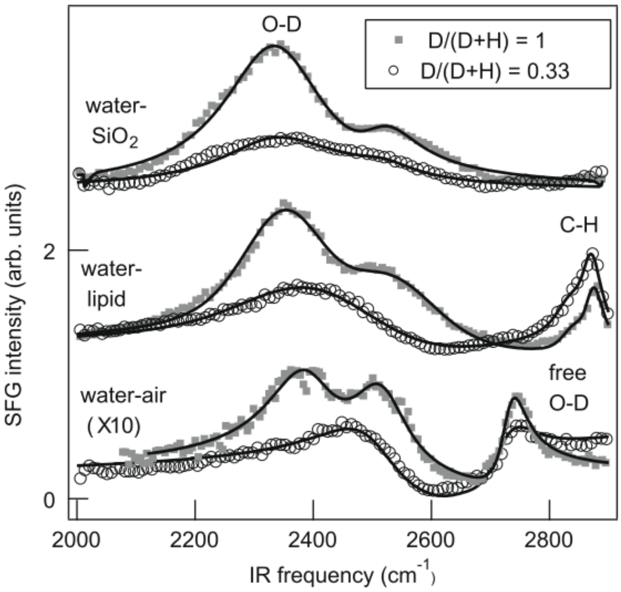

Figure 41: Offset VSFG spectra of the O-D stretch region at various D_2O interfaces (squares) and isotopically diluted (with H_2O) interfaces (open circles). The loss of the doublet structure upon isotopic dilution is due to suppression of intramolecular vibrational coupling. Figure adapted with permission from Sovago et al.[29]

The additional contribution of water molecules within the EDL to the interfacial water spectrum has been addressed by manipulating the ionic strength of the solutions,[33–38] which is known to change λ_D. By increasing the ionic strength, more of the oppositely charged (compared to the surface) ions in the electrolyte will accumulate near the surface, screening the surface charge and reducing λ_D. Urashima *et al.* used high ionic strengths to minimise λ_D and independently address the bound interfacial region using phase-sensitive (PS) VSFG spectroscopy in the O-H stretch region at the silica/water interface.[30] They found that the shape of the spectrum does not change above an ionic strength of 2 M, while there are significant differences as the ionic strength is reduced below 2 M. They suggest that the spectra above 2 M ionic strength are dominated by the response water molecules at the interface, due to the very short λ_D under these conditions. Thus, any difference at lower ionic strengths are assigned to contributions from water molecules across the EDL, and this contribution becomes larger as the ionic strength is decreased due to a longer λ_D. The PS-VSFG spectra for the low ionic strengths are always positive, indicating a net orientation of the water molecules with H pointed towards the silica. However, at high ionic strengths there is a small negative contribution to the O-H stretch signal around 3500 cm^{-1}, indicative of a small population of oppositely oriented water molecules (H towards bulk water) that are only present at the interface and reorient due to interactions with surface silanolates and bridging siloxanes. Isotopic dilution experiments with H_2O and D_2O mixtures significantly shift the spectra assigned to the EDL due to loss of vibrational coupling, but make almost no difference to the interfacial spectra. This suggests that the intramolecular O-H stretch vibrations of interfacial molecules are already vibrationally decoupled due to a different H-bonding environment at the surface and thus don’t show any change in coupling upon isotopic dilution.

Of relevance to semiconductor surfaces used in this project, Kataoka *et al.* have found a similar doublet structure in the O-H stretch region on TiO_2 surface.[39] The O-H stretch signal is strongest at high pH but reaches a minimum at pH 6 for TiO_2 compared to pH 2 for silica, due to the higher PZC of TiO_2. As a result, the signal also increases in intensity at pHs below the PZC as the protonated surface leads to ordering of interfacial water molecules in the opposite orientation, *i.e.* H pointing away from the surface. In the same study, they were then able to disrupt this orientation of water at low pH by adding phosphate ions to the solution, which are known to specifically adsorb onto the TiO_2 surface, leading to a much smaller intensity for the O-H stretch. This adds some additional complexity to the aforementioned studies using salt concentration to separate the interfacial and diffuse layer responses,[30] as they assumed that the salts did not strongly interact with the surface. Furthermore, this study was conducted on a thin film of TiO_2 deposited onto a silica substrate, so both the IR and VIS beams have to pass through an additional interface (SiO_2/TiO_2) before reaching the TiO_2/water interface. When studying such multi-layer oxide systems it becomes increasingly important to account for frequency-dependent Fresnel factors (especially in the IR) when trying to measure broad vibrational resonances such as the O-H stretch. These Fresnel factors arise due to the frequency-dependence of the refractive indices of the relevant interfaces. Backus *et al.* provide a useful framework for accounting for these in VSFG spectra in multi-layer systems.[40]

Most of the VSFG work so far has focussed on the doublet structure in the O-H (or O-D) stretch region discussed above, however other vibrational modes of water have also been studied, which could provide complementary information. A common feature in VSFG spectra of the air/water interface is a narrow band around 3700 $cm^{-1,}$ assigned to the O-H stretch of non-H-bonded water molecules, which occur due to the abrupt disruption of the H-bonding network at the air interface.[41,42] A similar mode has also been observed at various solid/water interfaces, assigned to surface hydroxyl groups that are not involved with H-bonding with the interfacial water.[21,43,44] The presence of this peak at solid surfaces not only provides information on the H-bonding structure at the interface, it can also be used to correlate to the hydrophobicity of the surface.[43]

The experiments mentioned above showed some ambiguity in assignment between the O-H stretch in non-H bonded water and the O-H stretch vibrations of surface hydroxyls. This uncertainty in assignment can be avoided altogether when studying the H-O-H bend vibration as this mode is only present in water molecules and not in surface hydroxyls. Historically, the much weaker intensity of the bending vibration has limited most VSFG experiments to studying the O-H stretch region, though over the last few years the H-O-H bending vibrational modes of water at charged interfaces have started to be investigated.[45–47] A further advantage of studying this bending region is that there are no longer any complications with Fermi resonances discussed above, since there are no resonances with overtones of other vibrational modes in water, as confirmed by unchanged spectra upon isotopic dilution.[45] As with the O-H stretch, the frequency of the bending mode is sensitive to the local H-bonding environment, with higher vibrational frequencies representing a stronger hydrogen bond.[45] Previous PS-VSFG experiments at the air/water interface determined that a significant bulk quadrupolar contribution dominated the water bending vibrational mode.[48] Typically, only considering electric dipoles is sufficient to assign most VSG spectra, but in this case the spectral data could not be fully understood purely using the dipole approximation. Subsequent PS-VSFG experiments at charged water interfaces found two different contributions to the H-O-H bend vibration, an interfacial dipolar component, centred at 1626 cm^{-1}, that flips sign at oppositely charged water interfaces and a bulk quadrupolar component, centred at 1656 cm^{-1}, that does not change sign.[47] This demonstrates the importance of phase-sensitive measurements to aid assignments in vibrational spectra of water, but also highlights the experimental difficulty of detecting such weak signals. In order to unambiguously detect such weak signals, new techniques had to be developed to reduce experimental noise sources. For example Moll *et al.* addressed the high frequency spectral noise in their measurements (due to interference from multiple reflections within the CCD pixels) by subtracting reference measurements that are 180° out of phase with each other.[47] In the case of studying such weak resonant signals, the usually weak quadrupolar effects can become significant and need to be accounted for in spectral assignments.

Water molecules in solution also show a low wavenumber mode due to hindered rotational modes known as librations. The strong H-bonding in water restricts its rotational motion, leading to these librational modes, which are typically observed between 300 & 900 cm^{-1}.[49] Probing this low wavenumber region with VSFG spectroscopy could potentially be useful in understanding the H-bonding environment and by extension the local water structure at interfaces. Tong *et al.* were able to experimentally detect a single librational mode at 834 cm^{-1}, after accounting for Fresnel reflections, in the VSFG spectrum of the air/water interface. This frequency is significantly blue-shifted (+ 165 cm^{-1}) away from the librational modes in bulk water, indicating a more "frustrated" rotation at the interface, likely due to a different H-bonding environment at the surface compared to the bulk. Due to experimental limitations it was not possible to probe frequencies below 650 cm^{-1}, so it is not clear whether there are additional lower frequency contributions. It is challenging to both produce significant powers of short-pulse IR light at such low frequencies and then to direct this light to a sample of interest. Such measurements will be even more challenging at solid/water interfaces due to significant IR absorption by both water and most substrates across this spectral region. These problems will need to be addressed if VSFG spectroscopy can be used to study possible OER reaction intermediates on electrode surfaces in this spectral region.

While the potential-dependence of interfacial water structure at semiconductor/water interfaces has not yet been reported, several groups have carried out *in situ* electrochemical VSFG experiments at metal/water interfaces in the O-H stretch region. Uosaki *et al.* have shown similar doublet structures at both gold and platinum electrodes that change with applied potential, reaching a minimum in intensity around the potential of zero charge, as seen in Figure 42.[50,51] Here, instead of changing the surface charge by manipulating bulk pH, the applied potential to the electrode controls the surface charge. Thus, the increase in amplitude of the O-H stretch vibration is explained by an increased ordering of interfacial water molecules as the electrode is either positively or negatively charged, with a flip in orientation of water molecules at the potential of zero charge. In their potential-dependent study at the Ag/water interface, Schultz *et al.* showed evidence of similar changes in the O-H stretch region relative to the potential of zero charge in both the interfacial region as well as in the EDL.[52]

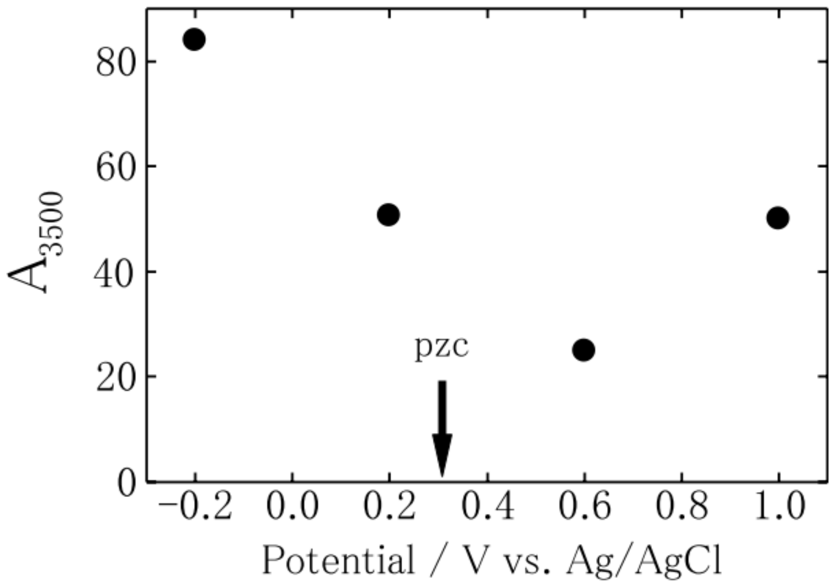

Figure 42: Potential dependent amplitude at 3500 cm^{-1} for the O-H stretch vibration in the VSFG spectrum of a gold electrode in 10 mM sulphuric acid reproduced with permission from Uosaki et al.[51] *Here the label pzc refers to the potential of zero charge.*

More recently, Dreier *et al.* have reported a method of recording potential-dependent VSFG spectra of water through a graphene electrode, demonstrating that a through-electrode geometry is possible, though they highlighted issues with reproducibility of the observed changes across samples, as well as the presence of water between the graphene layer and the window.[53] The difference in experimental geometry for this experiment is depicted in Figure 43c, as compared to some of the previous *in situ* electrochemical VSFG experiments by Uosaki *et al.* (Figure 43a)[50,51] and Schultz *et al.* (Figure 43b)[52]. In all three cases the IR and VIS beams are almost collinearly incident on the interface of interest and transmission through the aqueous electrolyte is either avoided (a & c) or minimised (b). Such characteristics will be used to inform the design of the *in situ* electrochemical VSFG experiments carried out in this project and these will be discussed in more detail in Section 3.2.1.

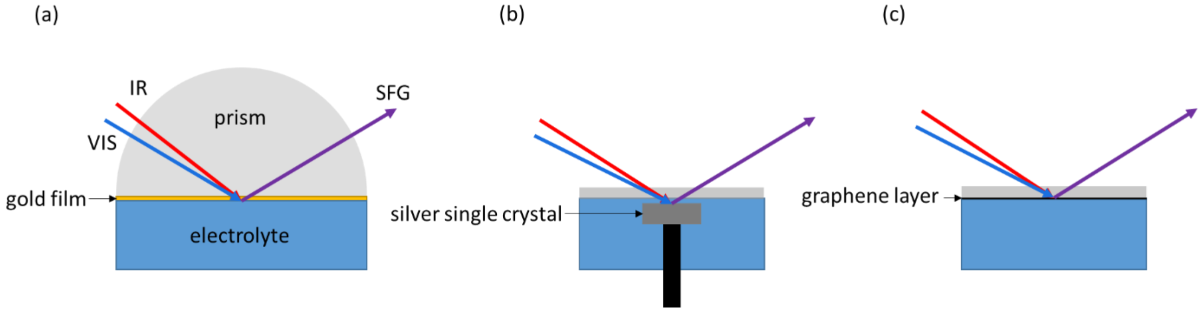

Figure 43: Examples of previously used experimental geometries for in situ electrochemical VSFG spectroscopy of water at electrode surfaces. Incident IR and VIS beams are shown by the red and blue arrows, respectively, while the reflected VSFG output is shown in purple. Reflected IR and VIS beams are omitted for clarity. The prism setup used in (a) by Uosaki et al. to study gold (and platinum) surfaces relied on internal reflection within the prism, with either a 10 nm Pt layer or a 25 nm Au layer.[50,51] *Schultz et al. used the setup in (b) where the silver single crystal electrode was held close to the window surface, such that the electrolyte pathlength was between 1 & 10 µm.*[52] *Dreier et al deposited a layer of graphene directly onto their* CaF_2 *window material and simply probed through this thin layer to record spectra of water/graphene interface.*[53]

3.2. Results and discussion:

3.2.1. Co-propagating through-electrode geometry:

A fundamental problem with doing surface spectroelectrochemistry in the infrared region is that most electrolytes will significantly attenuate the infrared light. Figure 44 shows the path length of aqueous electrolyte required to get an appreciable amount of IR light to the electrode surface (calculated using molar absorption coefficient data from Bertie *et al.*).[54] The maximum on the colour scale here is set to 6 µm as this is the thinnest commercially available Teflon spacer, which are typically used to control path length in IR cells. Thus, any region coloured white in Figure 44 would be accessible with a 6 µm path length. It is clear that several regions of the infrared spectrum, including around 3500 cm^{-1} and 1600 cm^{-1}, are essentially inaccessible, even at these short path lengths, due to strong absorptions from the stretch and bend vibrations of water. Furthermore, such short path lengths are detrimental to the electrochemical response as they will introduce severe mass transport limitations.

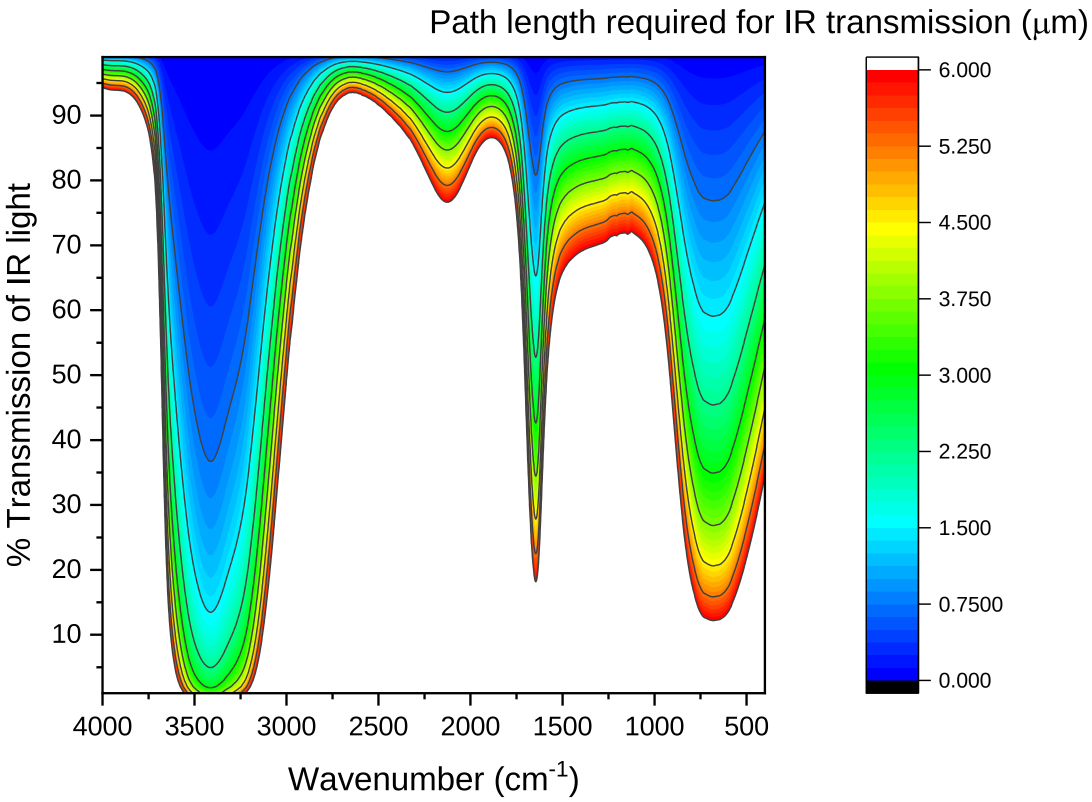

Figure 44: Path length of water required to get the stated transmission of infrared light, calculated using molar absorption coefficient data from Bertie et al.[54]

The problems of attenuation of IR light through electrolytes can be avoided altogether by probing through the back of transparent electrodes. Since VSFG spectroscopy is surface selective, the bulk vibrations between the back and the front of the electrode will not contribute to the detected signal. A slight complication is that transparent conducting oxides (TCOs) used in commercial optically transparent electrodes are usually not fully transparent to infrared light; a trade-off is made between transparency and conductivity. The main reason for this reduced transmission in the IR region is the plasma edge for the TCOs, where free carrier absorption takes place.[55] This type of absorption depends on the carrier concentration and the thickness of the TCO film. Commercial TCO-based electrodes, such as fluorine-doped tin oxide (FTO) and indium tin oxide (ITO) have a several hundred nanometre thick layer of TCO material, greatly reducing the infrared transparency of these materials. By selecting an appropriate infrared window material and a very thin TCO layer (<100 nm) the required optical properties could be achieved, with adequate electrical conductivity.

Several different transparent conducting materials were investigated for use as SFG substrates and their IR transmission can be found in Figure 45. Since the samples came from a variety of sources (full synthetic details of all samples can be found in Chapter 5), the glass substrates are not all the same thickness, which can significantly affect their transparency. The aim of this investigation is to identify a suitable TCO material and then move forward with depositing that material on an infrared transparent substrate (*e.g.* CaF_2) to avoid problems with IR absorption by the glass substrate. Thus, instead of overall transparency, the key information to be taken from Figure 45 is whether there are any substantial new features in the IR that cannot be explained by the substrate thickness. The spectrum of a microscope slide is included as reference sample for a "Glass" substrate. Commercially available "FTO/glass" and "ITO/glass" (from NSG-Pilkington) contain a thick TCO layer (>400 nm) which leads to their poor IR transmission alongside the use of a glass substrate, making them unsuitable for the VSFG experiments. Aluminium doped zinc oxide (AZO) is a promising material with potentially high transmission in the IR and appreciable conductivity when very thin layers are used.[56] Magnetron sputtered AZO (<100 nm) on glass samples were prepared by collaborators in the Veal group (University of Liverpool). Promisingly, such a thin layer of AZO shows a higher transmission than the "FTO/glass" and "ITO/glass" despite being on a much thicker (more than 3 times thicker) glass substrate.

However, the TCO material for this experimental setup must also be thermally stable to withstand the high temperatures required for the synthesis of active TiO_2 and α-Fe_2O_3 films. While initial investigations of AZO showed promising optical properties, upon annealing above 450 °C the materials became electrically insulating (electrical conductivity is required for the film to be used as an electrode). Both FTO and ITO are thermally stable up to the required temperatures but ITO was chosen for further studies due to its higher infrared transparency. Thin (<100 nm) magnetron sputtered samples of ITO on 2mm thick IR transparent windows (CaF_2 and SrF_2) were also prepared by the Veal group (University of Liverpool) and a 25 nm pulsed laser deposited layer of Sn-doped α-Fe_2O_3 was added by collaborators in the Rosseinsky group (University of Liverpool). These electrodes show >85% transmission across most of the mid-IR region, making them suitable for the VSFG experiments, with the SrF_2 samples even being suitable for studies below 1000 cm^{-1} where key water oxidation intermediates are expected.

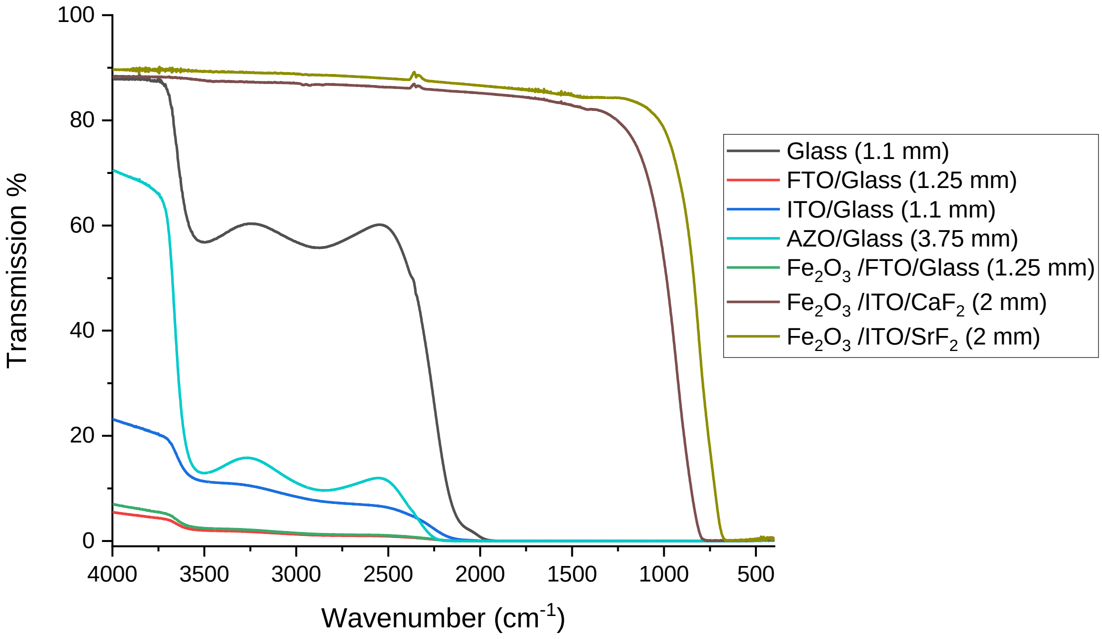

Figure 45: Infrared transmission of the various transparent conductive samples investigated taken on an FTIR spectrometer in transmission with an air background. Samples came from a variety of different sources so are not all on the same kind of substrate, the thickness of each substrate is given in brackets.

The exact design of the electrodes can be seen in Figure 46. The underlying ITO layer is sputtered into a circle with a diameter of around 1 cm in the centre of the IR transparent window (either CaF_2 or SrF_2). The substrate is then partially masked to leave most of the ITO exposed, upon which the electrode material is deposited. Several electrode materials were prepared over the course of this project, including the 25 nm PLD hematite layers prepared by the Rosseinsky group and spray-coated TiO_2 prepared in-house from a titanium isopropoxide precursor (based on the procedure by Conde-

Gallardo *et al.*[57], full experimental details can be found in Chapter 5.12.). A PTFE coated wire is contacted directly to the ITO layer and coated with epoxy to keep it isolated from the electrolyte when submerged. Later electrodes also featured a small circular spot of gold (prepared by thermal evaporation) towards the opposite side of the ITO relative to the wire contact. The role of this gold spot was to provide a reflective reference material to account for the MIR profile as well as to make alignment easier. By placing the gold spot opposite the wire contact, the sample can be easily aligned onto the gold spot, since the gold reflection is usually stronger and has a large nonresonant amplitude, and then the cell can simply be translated vertically to find a signal for the semiconductor/electrolyte interface. This gold spot was also covered in epoxy to ensure the layer did not delaminate from the surface due to poor adherence between gold and CaF_2. Typically thin (~5 nm) chromium layers are deposited between the gold layer and the substrate to aid adhesion in such multilayer device structures, however for our purposes this would add two additional interfaces (CaF_2/Cr and Cr/Au) that could contribute to (and further complicate) the VSFG response, especially as Cr diffusion can also lead to the formation of a Au/Cr alloy.[58] Thus, the gold was deposited directly onto the CaF_2 and the outer gold surface was completely coated in epoxy to keep it adhered, since this does not disrupt the interface of optical interest (CaF_2/Au).

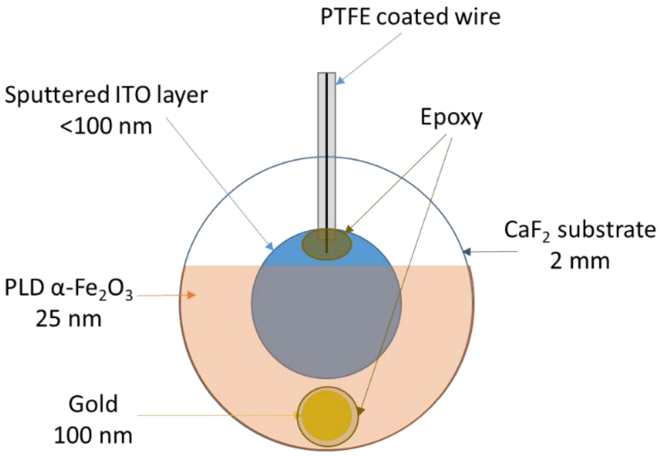

Figure 46: Diagram showing a face-on view of the hematite electrodes used for VSFG experiments

Since this experimental setup shines the infrared light through the working electrode, the electrolyte path length is no longer an issue, so a commercial infrared cell with a 1.7 mm spacer was used. The PTFE coated silver and platinum wires were passed through the flow inlet/outlet tubes to complete the electrochemical cell, the completed cell can be seen in Figure 47. Here it is important to use PTFE coated wires with a small non-isolated section at the tip to avoid short circuits with metal tubes of the cell. All VSFG experiments were carried out with the cell in a vertical orientation (*i.e.* with the PTFE wire contact pointing up) and the almost collinear IR and VIS beams at a 45° angle of incidence, detecting the VSFG response in reflection.

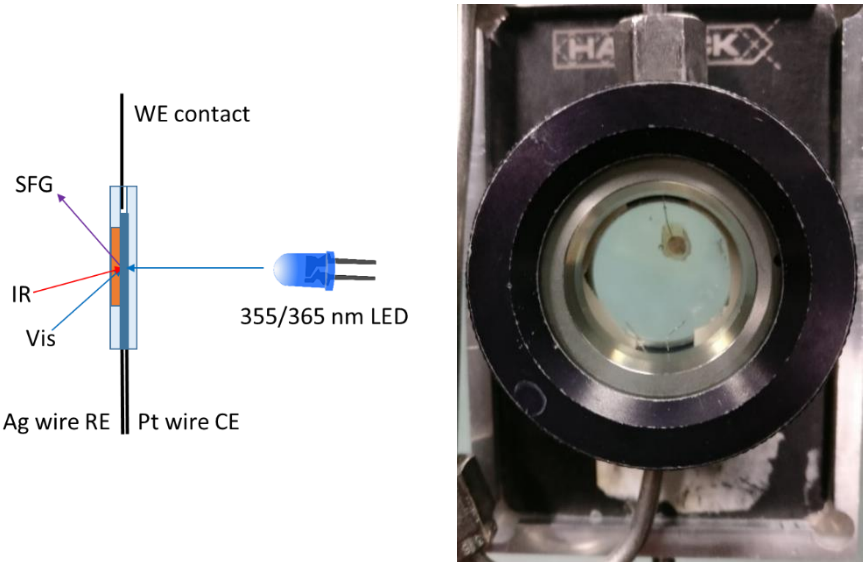

Figure 47: Experimental geometry (left) and spectroelectrochemical cell containing a $TiO_2/ITO/CaF_2$ electrode under water oxidation conditions (right) for the through-electrode setup.

The optical and photoelectrochemical response of the two main types of films studied are shown in Figure 48 & Figure 49, respectively. Both the hematite and TiO_2 samples contain the characteristic absorbance peaks for their respective materials, showing the bandgap transitions at around 590 nm (2.1 eV) for hematite and 360 nm (3.4 eV) for TiO_2.[57,59] The higher optical density of the TiO_2 sample stems from the significantly thicker film thickness (>100 nm) compared to the 25 nm thick PLD hematite electrodes. This difference in optical density is likely the cause of the difference in photocurrent seen in Figure 49, where the hematite films have a much smaller photocurrent. However, both films produce some activity, allowing further study with VSFG spectroscopy.

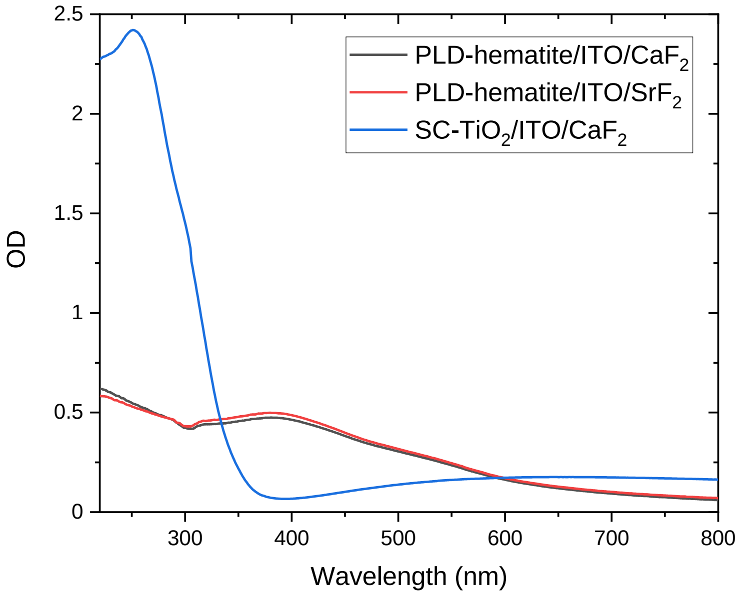

Figure 48: UV-VIS spectra of electrodes used for VSFG experiments with an air background. Note that the beam in the spectrometer was masked so that it would only probe the centre of the electrodes (i.e. only the part of the sample that contained the electrode material, TCO and substrate) for both the sample and air reference measurements.

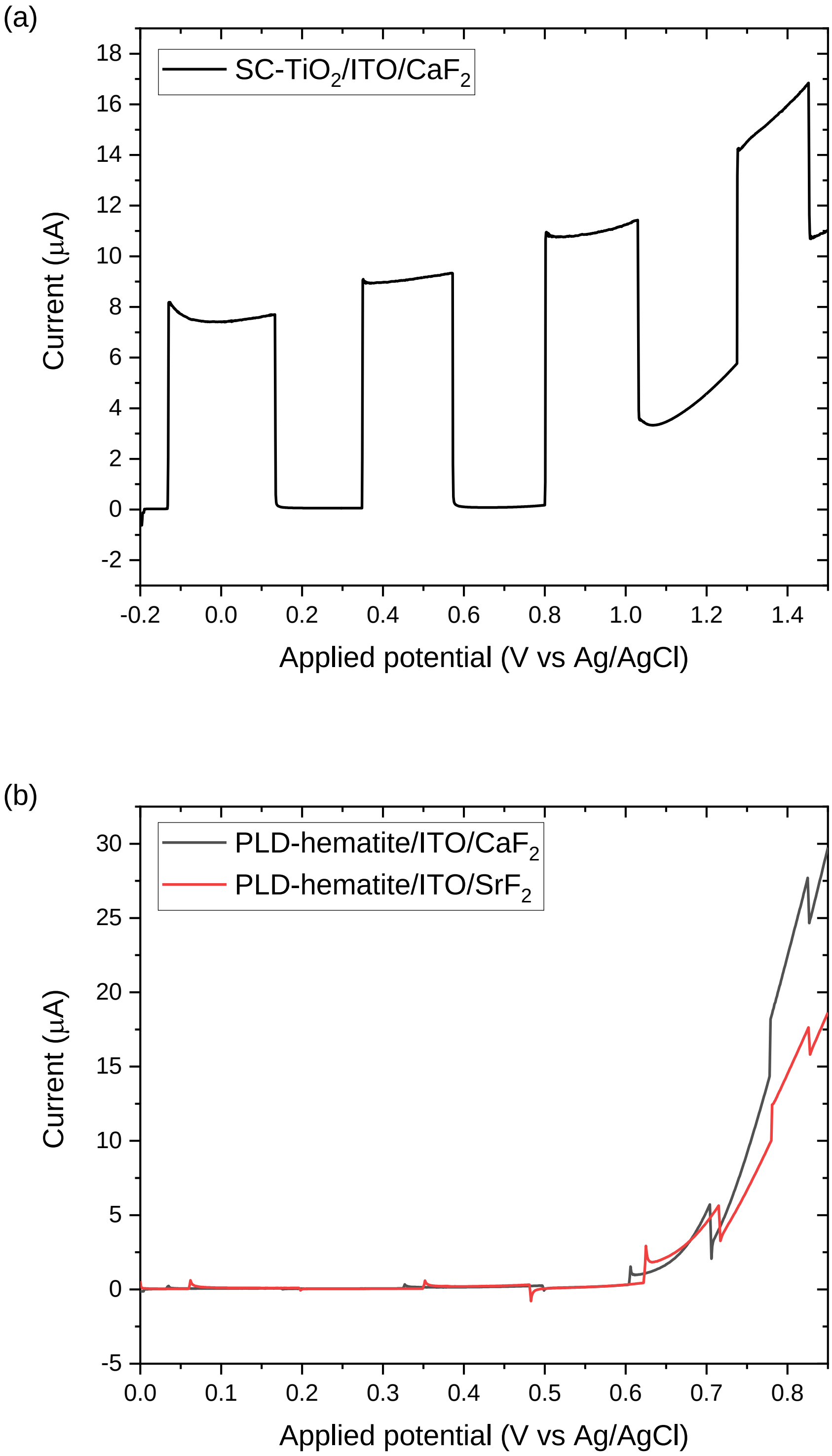

Figure 49: Chopped photoelectrochemical response of the TiO_2 (a) and hematite (b) electrodes used for later VSFG experiments. These experiments were carried out in a bulk electrochemical cell with a 1 M NaOH electrolyte and a conventional reference electrode (Ag/AgCl), while the later VSFG experiments were carried out with a more restricted electrolyte pathlength and a silver wire pseudo-reference electrode. LED illumination was provided by a 365 nm LED at ~ 15 mW cm^{-2} that was manually chopped by blocking the light source with an opaque card, giving a representation of the dark current and photocurrent.

3.2.2. VSFG of a buried catalytic interface:

Probing through the electrodes avoids IR absorbance in the water prior to the electrode/electrolyte interface but it also introduces further complications as there are now multiple interfaces between the back of the electrode and the electrode/electrolyte interface. The glass/TCO and TCO/metal oxide interfaces can both generate a sum-frequency signal. These interfaces are also within several hundred nanometres of each other, meaning the reflection of the SFG light at each interface will not be spatially separated enough to discriminate individual interfaces. To check the correct interface is being probed, the first set of experiments were carried out on the TiO_2 electrode under an atmosphere of methanol using an SFG spectrometer at the UK Central Laser Facility (CLF). Full experimental details can be found in Chapter 5.13., but briefly a 50 fs, 800 nm 10 kHz amplifier (Coherent) is used to pump a custom optical parametric amplifier (OPA) to provide tuneable broadband IR light (~500 cm^{-1} bandwidth, 200 µm spot diameter) which is spatially and temporally overlapped with an etalon-derived narrowband 800 nm beam (~300 µm spot diameter) and the reflected SFG signal is dispersed by a spectrograph (Holospec) and imaged on a CCD (Andor, iDus). Figure 50 shows a time delay scan of this TiO_2/CH_3OH system, where the time delay between the infrared and visible laser pulses is varied using a motorised delay stage for the visible to bring it in and out of temporal overlap with the infrared. Amongst a broad non-resonant background, two clear resonant features can be seen around 2846 and 2951 cm^{-1}, attributed to methanol adsorbed on the TiO_2 surface. The nonresonant background can be effectively suppressed at positive time delays, where the time-asymmetric visible pulse arrives after the IR pulse. The position of the 2846 cm^{-1} peak lies between the symmetric C-H stretches of a chemisorbed titanium-methoxy species (2828 cm^{-1}) and a physisorbed molecular methanol species (2855 cm^{-1}).[60] The same is true for the peak at 2951 cm^{-1} and the asymmetric C-H stretches of chemisorbed and physisorbed methanol at 2935 and 2968 cm^{-1}, respectively.[60] The resolution of the spectrometer (~12 cm^{-1}) may not be enough to resolve the methoxy and methanol species, but this initial study confirms that the correct interface is being probed.

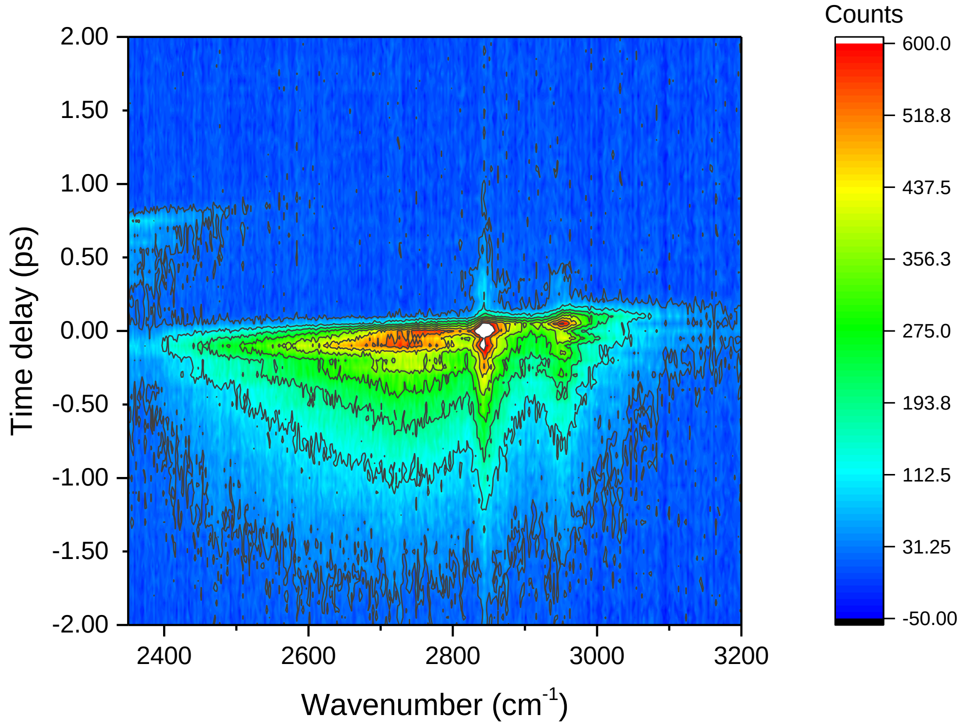

Figure 50: SFG time-delay scan of TiO_2/ITO/SrF_2 in the presence of MeOH vapour, 2 s averaging per spectrum. Features assigned to MeOH resonant modes are observed at ~2840 cm^{-1} and 2950 cm^{-1}, overlapped with a broad non-resonant background. Incident laser powers were 20 mW at 800 nm (s-pol) and 25 mW in the IR (p-pol). The VSFG polarisation was not controlled so the polarisation combination was xsp.

The stability of these surface modes of methanol was then investigated with various laser powers. The amplitudes of the both the symmetric and asymmetric stretches were monitored over time at two high incident 800 nm laser powers (40 and 70 mW). As can be seen in Figure 51, the amplitude of the asymmetric stretch (red axis) is relatively constant within each set of experiments at these high light intensities (note that most VSFG experiments were conducted at a much lower 800 nm laser power, typically around 20 mW). Conversely, the ratio between the symmetric and asymmetric stretch (black axis) does decrease significantly over the first two experiments, but appears to stabilise around unity by the last experiment. This could indicate some change in orientation of the surface methanol species due to laser-induced heating. Further experiments with different polarisation combinations could be used to investigate a possible change in orientation.

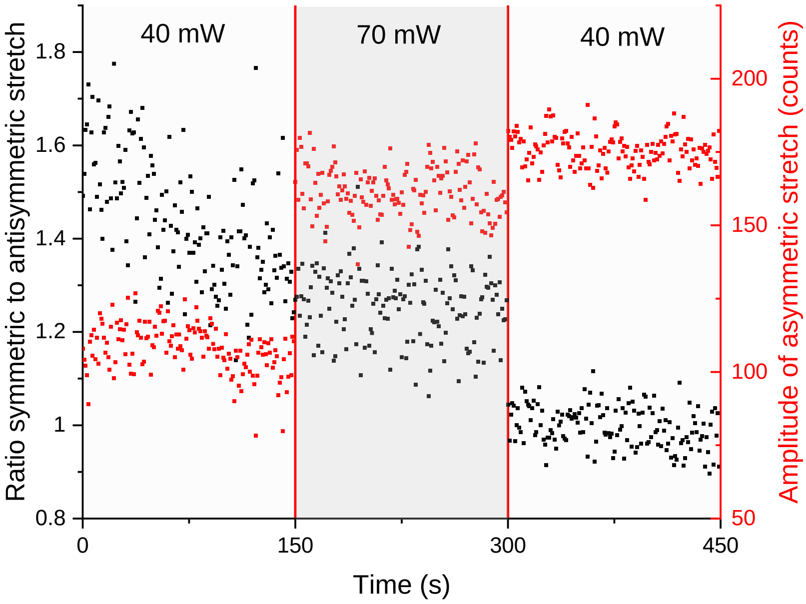

Figure 51: Change in ratio of symmetric (2846 cm^{-1}) to antisymmetric stretch (2951 cm^{-1}) of MeOH on TiO_2 surface over time. Red lines indicate a pause in the experiment to change the visible light intensity.

Now that we have confirmed we can study a buried interface by detecting the adsorbed methanol signatures through a multilayer device, the next step is to utilise the catalytic interface itself to see if we can perturb this signal. TiO_2 is a well-known photocatalytic material with many applications in self-cleaning devices.[61] Illuminating the surface with an appropriate wavelength of light (*i.e.* photon energies greater than the bandgap of TiO_2) has been shown previously to completely oxidise adsorbed alcohols into gaseous products.[62] Here we use a 355 nm LED that was focussed onto the front face of the electrode, while the IR & VIS are still incident through the back of the electrode. Despite attempts to filter and block the residual LED light there was still a substantial and randomly varying baseline from scattered LED light, so experiments could not be carried out while the LED was on. Instead, the sample was illuminated for 5 minutes, then the LED was turned off and a spectrum was recorded. This process was repeated 4 times and the change in peak area (from a Voigt fit) of the symmetric and asymmetric stretches is shown in Figure 52. These experiments were carried out in an atmosphere of methanol so readsorption of more methanol on the timescale of spectral acquisition (seconds) was likely, which could be suppressing further changes to the VSFG signal. Despite this, there is a clear decrease in intensity of both the symmetric and asymmetric stretches of adsorbed methanol, in contrast to the minimal changes in intensity observed under the high visible laser power alone (Figure 51).

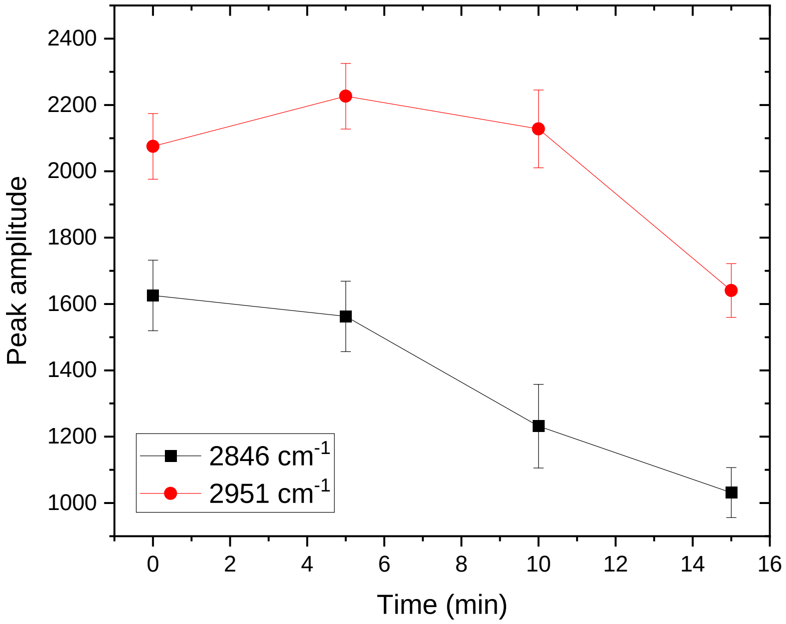

Figure 52: Change in peak amplitude (Voigt fits) for the symmetric (2846 cm^{-1}) and asymmetric (2951 cm^{-1}) C-H stretches of methanol adsorbed on a TiO_2 surface under ~10 mW cm^{-2} 355 nm CW LED illumination. Error bars represent the standard errors from the Voigt peak fits.

These initial tests not only confirm that we can probe a buried catalytic interface, but that the dynamic response of such an interface can also be monitored during photocatalysis. These experiments were purely a preliminary test of the experimental geometry, using methanol as a known probe molecule, before moving forwards with studying the interfacial water structure. However, there are many experimental improvements that could be made to address the mechanism of methanol oxidation at TiO_2 surfaces, which is of interest to the wider community.[63–68] These include carrying out experiments without an atmosphere of methanol to properly address the extent of reaction and using a pulsed laser to photoexcite the sample to both address issues with a large background signal from the pump source and to enable time resolved measurements to understand the complete mechanism. Such experiments highlight the utility of *in situ* VSFG experiments which can provide surface sensitive structural information that can then be complemented with insights into molecular orientation and dynamics when combined with polarisation studies and additional pump lasers.

3.2.3. *In situ* electrochemical VSFG spectroscopy:

The first *in situ* electrochemical VSFG experiments in this project were carried out on PLD-α-Fe_2O_3/ITO/CaF_2 and SC-TiO_2/ITO/SrF_2 electrodes at the CLF (see Chapter 5.13. for full details). The aim of these experiments was to test the through-electrode experimental geometry for studying interfacial water structure at semiconductor interfaces. Due to experimental limitations during the facility time, these experiments were limited to IR frequencies between 2000 and 3000 cm^{-1}. As a result, the initial experiments focused on the O-D stretch in D_2O based electrolyte, which should give comparable results to water-based systems, but at a lower vibrational frequency to remain within the available spectral window. The technique of nonresonant suppression discussed in Section 3.1.2 relies on introducing temporal delays between the IR and VIS pulses to selectively probe long-lived resonant vibrational mode, while ignoring the short-lived nonresonant polarisation. When studying the spectrally broad, but temporally short-lived O-H stretch vibrations this method is no longer suitable for nonresonant suppression as the lifetime O-H stretch vibration is comparable to the rise time of the etalon used to produce the time-asymmetric visible pulse. One consequence of studying the O-D stretching modes is that they have a longer vibrational lifetime, of around 2 ps, when compared to the 1 ps lifetime of O-H stretch mode.[69] Thus nonresonant suppression through time delays may be more suitable for the study of the O-D stretch vibration.

Figure 53 shows a time delay scan of the PLD hematite electrode immersed in 0.1 M NaOD in the spectroelectrochemical cell, but with no bias applied (OCP). A large broad signal is observed, matching the spectral profile of the IR beam. The point at which this signal is at a maximum defines the zero-delay time (t_0). Since the signal rapidly decays within a few hundred femtoseconds positive of t_0, it is assigned to a nonresonant SFG response of the surface. The resonant O-D stretching vibrations of water molecules at the surface are expected between 2200 and 2800 cm^{-1} and should persist for up to 2 picoseconds.[69] The non-observance of any obvious modes assignable to O-D stretches could be due to a lack of sufficient ordering at the interface, though some degree of ordering is expected even at OCP for this electrode as the electrolyte pH (13) is above the PZC of hematite (estimated to be between 6 and 9).[70,71] The negatively charged hematite surface at this pH would be expected to interact with the polar water molecules, leading to a net orientation where the hydrogen atoms point towards the surface.

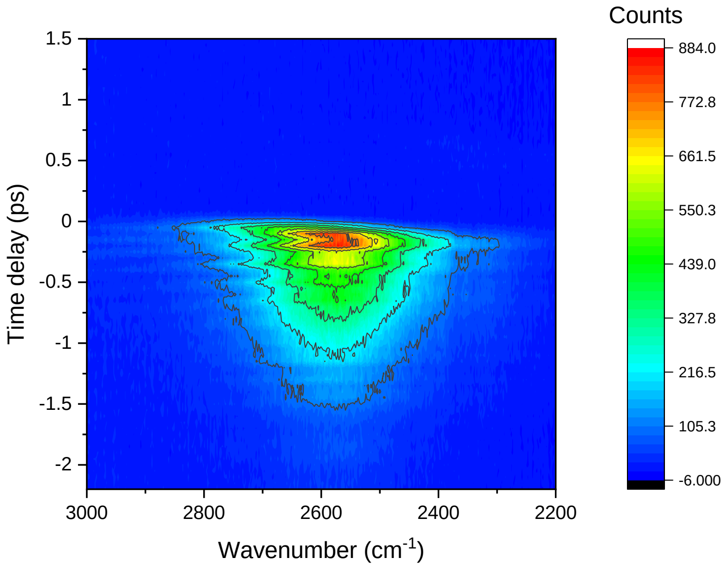

Figure 53: SFG time-delay scan of PLD-Fe_2O_3/ITO/CaF_2 in 0.1 M NaOD, 2 s averaging per spectrum. Incident laser powers were 20 mW at 800 nm (s-pol) and 30 mW in the IR (p-pol). The VSFG polarisation was not controlled so the polarisation combination was xsp.

The delay scans were then repeated with the hematite electrode held at positive applied potentials to see if this would change the ordering of interfacial water enough to produce an observable resonant signal for the O-D stretch vibrations. Since the signal appears to be dominated by a large nonresonant background, the data are plotted as time slices at 3 different vibrational frequencies in Figure 54 to look more closely for resonant modes, which would appear as non-zero values at positive time delays. The 3 different potentials are represented by the line style (solid, dashed or dotted) and the frequencies are represented by colour (black, red or blue). These 3 frequencies were chosen to match the nonresonant maximum (~2600 cm^{-1}) and the positions of expected O-D stretch modes at 2400 cm^{-1} (H-bonded O-D stretch) and 2700 cm^{-1} (free, non-H-bonded O-D stretch). Even with the applied bias there still do not appear to be any longer-lived features that could be assigned to resonant vibrational modes as all of the curves decay to zero within 300 fs. The three temporal profiles at 2400 cm^{-1} all peak slightly earlier than t_0 and subsequently decay earlier than the other frequencies. This is due to a slight temporal chirp of the IR pulse, which can be seen as a slight diagonal tilt in the contour plot above. A similar chirp was also observed in the TiO_2 data presented above in Figure 50, suggesting it is not a unique property of this system and does not hinder the ability to observe resonant modes using this nonresonant suppression technique.

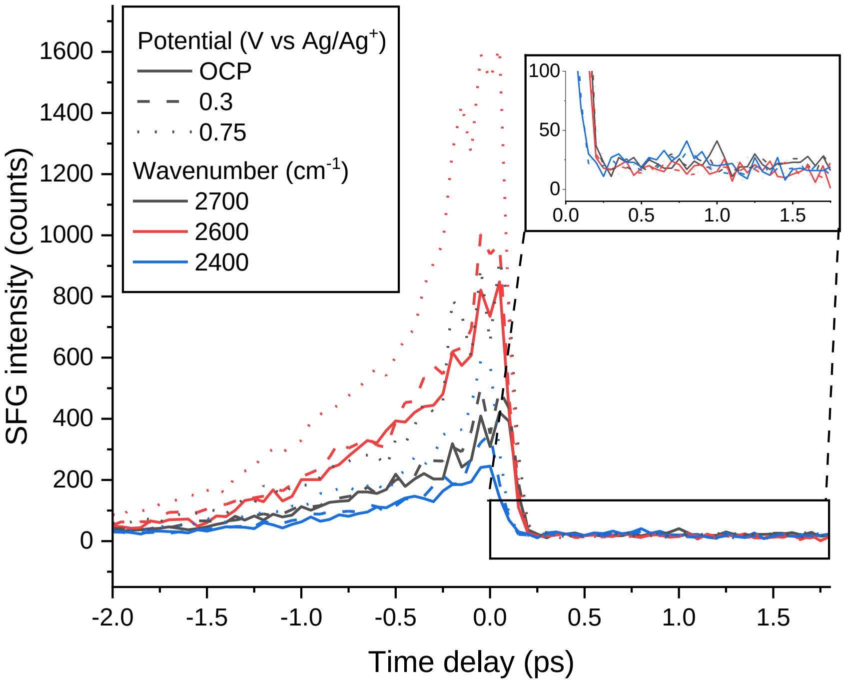

Figure 54: Temporal profiles of the SFG response of PLD-Fe_2O_3/ITO/CaF_2 in 0.1 M NaOD, either at OCP (solid lines) or held at 0.3 V (dashed lines) or 0.75 V vs Ag/AgCl (dotted lines), with an inset showing the decay close to t_0 on a different scale. The different colours represent three representative frequencies including 2700 cm^{-1} (black), 2600 cm^{-1} (red) and 2400 cm^{-1}.

Incident laser powers were 20 mW at 800 nm (s-pol) and 30 mW in the IR (p-pol), with 2 s averaging per spectrum. The VSFG polarisation was not controlled so the polarisation combination was xsp.

Another possibility is that the resonant signal could be much weaker than the nonresonant response, making it hard to detect the O-D stretch vibrations without saturating the detector from the comparatively much larger nonresonant. The spectra above were recorded with very short exposure times (2 seconds) and it is possible that longer acquisitions could enable detection of the modes of interest, though this can only be increased so much before the nonresonant background saturates the detector. Alternatively, much longer exposure times could be used at more positive time delays, where the nonresonant has decayed to zero but the O-D stretch vibrations are still expected. In the spectra above the nonresonant decays to zero within 300 fs, but the lifetime of the O-D stretch vibration could be up to 2 ps,[69] so making use of a positive time delay could enable detection of a weak resonant O-D mode. However, the weak resonant signal will also be strongest at t_0 and will decay with time. At moderate positive time delays and much longer exposure times it will still be difficult to distinguish any weak residual nonresonant from a similarly weak and broad resonant O-D stretching mode. Instead, since the nonresonant appears to be dominating the signal, its potential dependence was further investigated using cyclic voltammetry (CV). Further attempts at detecting resonant modes will be addressed later in this Chapter.

Initial CVs were carried out without any nonresonant suppression (*i.e.* at t_0), here just focusing on the potential dependence of the nonresonant signal alone. Four CV cycles were carried out on both TiO_2 and hematite electrodes scanning positive of the open circuit potential (OCP) until a significant OER current was being drawn (0.9 V). The α-Fe_2O_3 and TiO_2 electrodes show stark differences in their nonresonant potential dependence in Figure 55. The 4 CV cycle segments of both datasets were split into a total of 8 linear sweep segments and individual linear or 2nd order polynomial (quadratic) fits were carried out on the nonresonant VSFG responses. The TiO_2 electrodes show a quadratic change in VSFG intensity with applied potential with a decrease in intensity at potential positive of open circuit. In contrast the hematite electrodes show a linear change in VSFG intensity with potential with the signal increasing with applied potential. The shape of these responses can be understood based on the analysis of Rey & Dlott discussed above,[15] where the linear hematite response is indicative of an interfacial χ^2 term dominance, while the parabolic TiO_2 behaviour indicates the dominance of the χ^3 term which can act over a much larger distance. Neither of the fits are perfect, suggesting that either contributions from both χ^2 & χ^3 are present in the system or the interface is not experiencing a linear change in E_{DC}. Without further experiments on the TiO_2 system it is unclear whether this χ^3 related behaviour is due to the fields extending into the semiconductor over the space charge layer, or the fields extending into the electrolyte over the EDL.

The opposite sign of the potential dependence is also intriguing. In both cases the potential is scanned anodically until an OER current is drawn, so both electrodes are scanned past their flat band potentials within the CV window, however the hematite electrode shows a consistent increase in nonlinear signal, while the TiO_2 shows a decrease towards positive potentials. Since the TiO_2 signal appears to be dominated by the χ^3 term, the opposite signs of the interfacial fields at the semiconductor surface could be the cause of this anomalous behaviour, since the fields across the SCL and EDL propagate in opposite directions relative to the interface. Further experiments could involve changing the salt concentration to change λ_D or doping the TiO_2 layer to change the length of the SCL. While these parameters were not studied in detail using SFG in this chapter, such parameters were further investigated for electrodeposited hematite electrodes in Chapter 4 using *in situ* electrochemical second harmonic generation spectroscopy (SHG) spectroscopy. SHG is the degenerate case of SFG, where both incident frequencies are the same and the output frequency is double the input frequency, thus providing analogous data to nonresonant VSFG spectra, without complications of overlaid vibrational resonances.

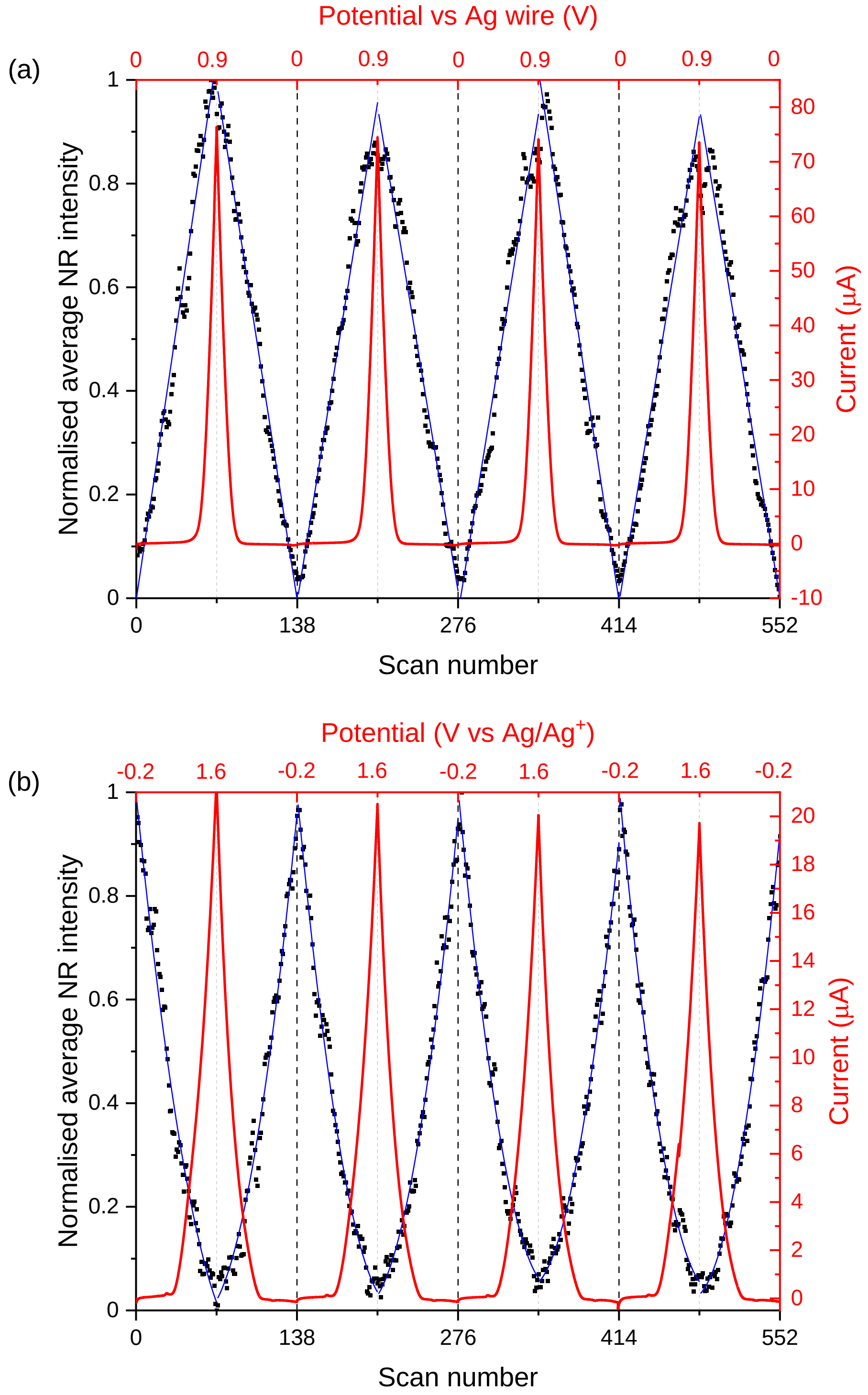

Figure 55: Normalised in situ SFG intensity at maximum of NR response over 4 CV cycles in 0.1 M NaOD for α-Fe$_2$O$_3$ (a) between 0 and 0.9 V vs Ag/Ag$^+$ at 10 mV s^{-1} and TiO$_2$ (b) between -0.2 and 1.6 V vs Ag/Ag$^+$ at 20 mV s^{-1}. Overlaid linear or parabolic fits are shown in blue and simultaneous current-voltage response is shown in the red axes. Both sets of SFG data were recorded with 1 s exposure time per spectrum and 20 mW incident visible power (s-pol) and 30 mW incident IR power (p-pol) centred at 2800 cm^{-1}, the reflected SFG signal polarisation was not controlled, giving the xsp polarisation combination.

The rest of this chapter will focus on detecting resonant vibrational modes in an attempt to address the identity and dynamics of interfacial molecular species. Our focus will be on detecting the O-D stretch vibrations of either interfacial water molecules or of surface hydroxyls. Ideally these experiments could also be coupled to a pump light source, but as discussed in the TiO_2/MeOH experiments, the use of a pump LED resulted in too much scattered light that could not be completely filtered or accurately subtracted from the VSFG signal. Furthermore, it is shown in the following chapter (Section 4.2.1) that the application of a voltage to initiate electrochemical water splitting appears to generate similar species to those in light-driven water splitting on hematite.

The following analysis method is explored using the delay scan data from Figure 54, under the assumption that the resonant modes of interest are very weak and the frequency-independent nonresonant response is dominating the signal. For each of the three different potentials (OCP, 0.3 V and 0.75 V vs Ag/Ag^+) the spectra at t_0 are selected, since this is where both the nonresonant and crucially the resonant signals should be largest. Examining a difference spectrum compared to OCP would be a useful tool in understanding any small potential-dependent changes in the resonant O-D modes. The data are first normalised from 0 to 1 to account for the large potential-dependent change in nonresonant signal discussed above, before subtracting the normalised OCP spectrum. While the nonresonant clearly changes with potential, it should be a frequency-independent change. Conversely, changes in resonant modes are by definition frequency-dependent and would appear as features in this difference spectrum. Though it is difficult to draw definitive conclusions about the line-shapes and peak positions without knowing the phase relationship between the resonant and nonresonant response, there are clear potential-dependent features in the difference spectra shown in Figure 56. It is not possible to access this phase information in the homodyne experiments presented here, but a heterodyne experiment can provide this information and is explored in Appendix B.

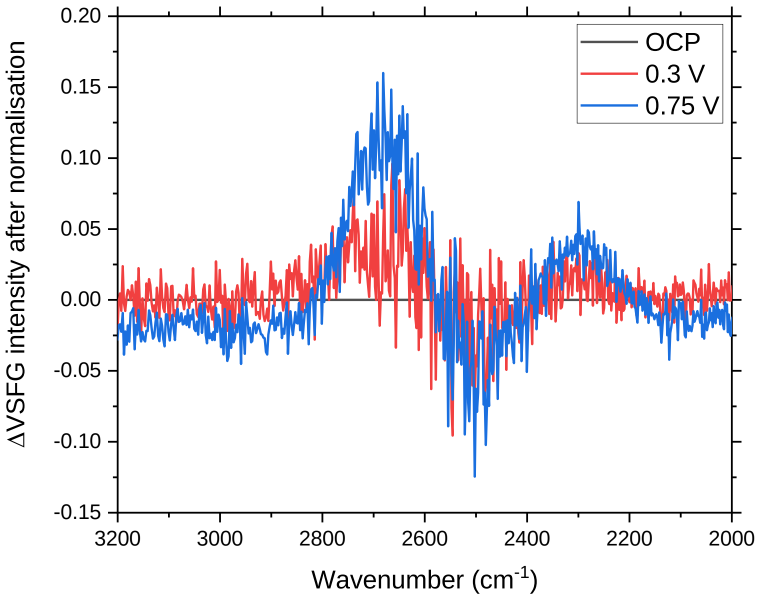

Figure 56: SFG difference spectra (compared to OCP) at t_0 of PLD-Fe_2O_3/ITO/CaF_2 in 0.1 M NaOD, at various potentials vs Ag/Ag^+. Each spectrum was normalised 0 to 1, then subtracted from the spectrum at OCP. Incident laser powers were 20 mW at 800 nm (s-pol) and 30 mW in the IR (p-pol), with 2 s averaging per spectrum. The VSFG polarisation was not controlled so the polarisation combination was xsp.

Qualitatively, the positive feature at around 2700 cm^{-1} is consistent with a free non-hydrogen bonded O-D stretch vibration. It is unclear whether the other features are a positive and negative band arising due to plotting a difference spectrum, or if it is a single feature with a distorted, derivative-like peak shape due to interference between the resonant and nonresonant response. Whether it is a single feature or two, in both cases the frequencies are compatible with hydrogen bonded O-D stretching vibrations. To further explore this potential dependence, CV experiments were carried out over a larger potential window. The *in situ* electrochemical response of a PLD-hematite electrode during such an experiment is shown in Figure 57, displaying the onset of an OER current around 0.7 V vs Ag/Ag^+.

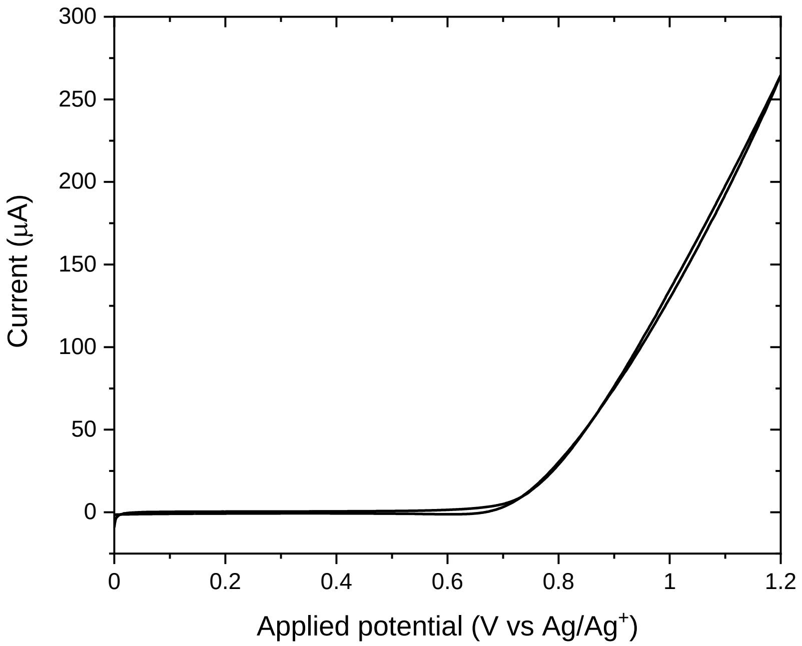

Figure 57: Electrochemical response of a PLD-hematite/ITO/CaF$_2$ during a 50 mV s^{-1} CV in 0.1 M NaOD. The voltammogram is recorded in situ while simultaneous VSFG spectra are recorded, displayed in Figure 58

The simultaneous VSFG difference spectra recorded during this CV cycle are shown in Figure 58, plotting each potential as a difference to the first spectrum (at 0 V vs Ag/Ag$^+$), where no current is being drawn. Similar features to those observed in Figure 56 (positive at 2700 cm^{-1} and negative at 2400 cm^{-1}) appear as the potential is scanned positive. The signal intensities increase with potential, though notably, all the features are present by the spectrum at 0.6 V, prior to the onset of an OER current. This suggests the proposed vibrational modes are not necessarily directly related to the OER reaction, but changes occurring at the surface before electrocatalysis. On the reverse sweep (Figure 58b) both the positive and negative features decrease in intensity as the potential is scanned cathodically. However, the final spectrum on the reverse sweep (at 0 V vs Ag/Ag$^+$) no longer resembles the flat line in the initial spectrum from the forward sweep, instead showing a negative feature at 2700 cm^{-1} and a positive one around 2500 cm^{-1}. This is likely a consequence of the vertex potential of the CV (0 V vs Ag/Ag$^+$) being slightly different to the OCP, so the initial 0 V bias involved a step change from OCP, while the reverse sweep approaches 0 V smoothly at 50 mV s^{-1}.

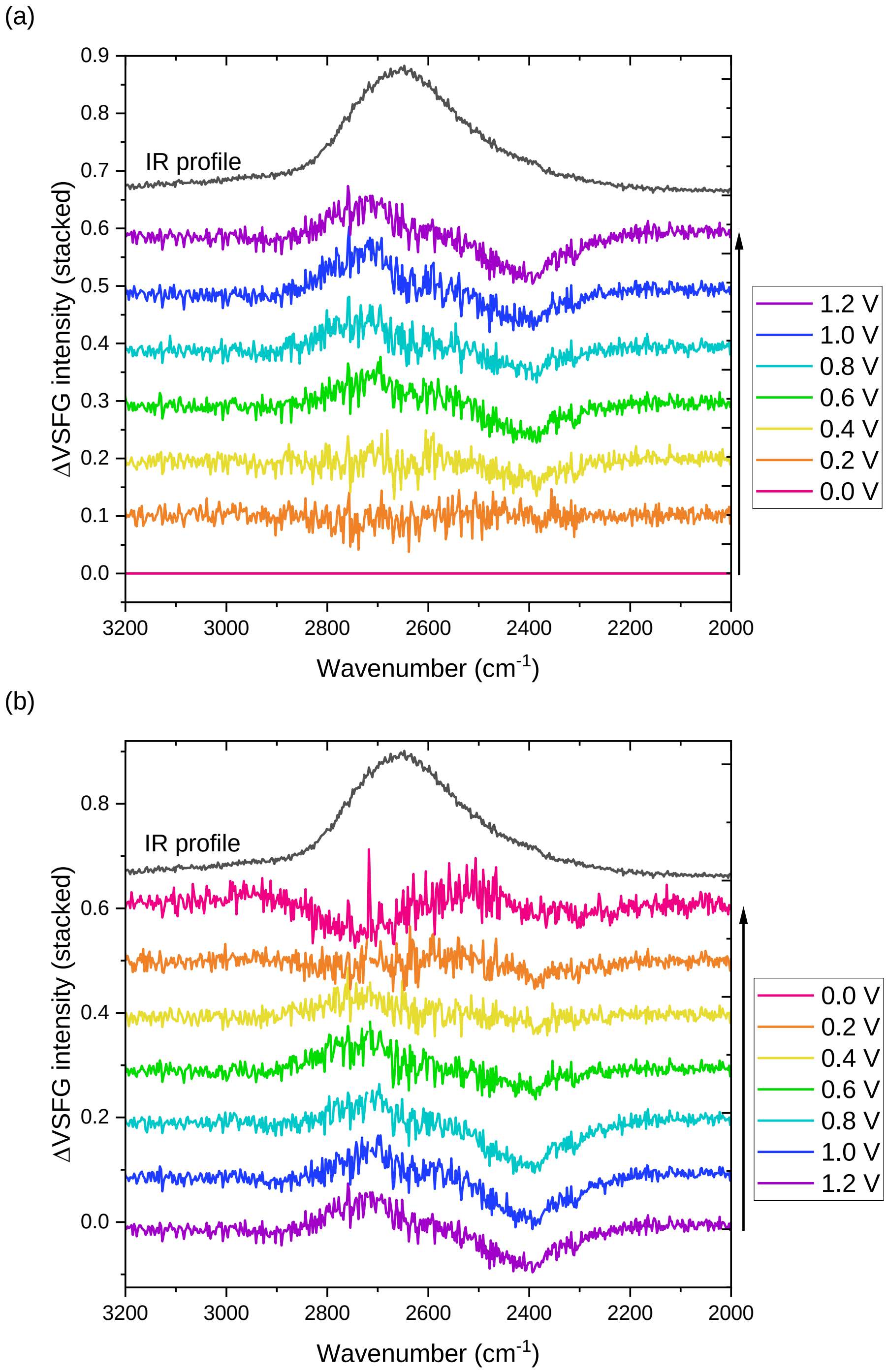

Figure 58: Stacked VSFG difference spectra (relative to the spectrum at 0 V vs Ag/Ag$^+$, after normalisation 0 to 1) for PLD-hematite/ITO/CaF$_2$ during a 50 mV s^{-1} CV in 0.1 M NaOD showing the forwards sweep in (a) and the reverse sweep in (b), with arrows indicating the scan direction. All spectra were recorded at t_0 with 1 s exposure time per spectrum and 20 mW incident visible power (s-pol) and 30 mW incident IR power (p-pol) centred at 2680 cm^{-1}, the reflected SFG signal polarisation was not controlled, giving the xsp polarisation combination. A raw spectrum (prior to subtracting the reference spectrum) is overlaid in black in both (a) and (b) to give an approximation of the IR profile.

The VSFG spectra recorded during voltammetry experiments were repeated over multiple CV cycles to account for such issues with a non-equilibrium state in the initial CV cycle. The potential dependence of the features at 2700 cm^{-1} and 2400 cm^{-1} are shown in Figure 59. The mode at 2700 cm^{-1}, assigned to free non-hydrogen bonded D_2O, shows the clearest and most reversible potential dependence across all 4 cycles. The intensity initially increases approximately linearly, but when the OER onsets and a catalytic current flows, the feature appears to reach a plateau. On the reverse sweeps, the plateau remains until the OER current stops flowing, after which the signal intensity linearly decreases again. An increase in the intensity of this non-hydrogen bonded O-D mode could be interpreted in multiple ways, including an increase in concentration of molecules vibrating at that frequency, or an increase in the ordering of the same number of molecules vibrating at that frequency.

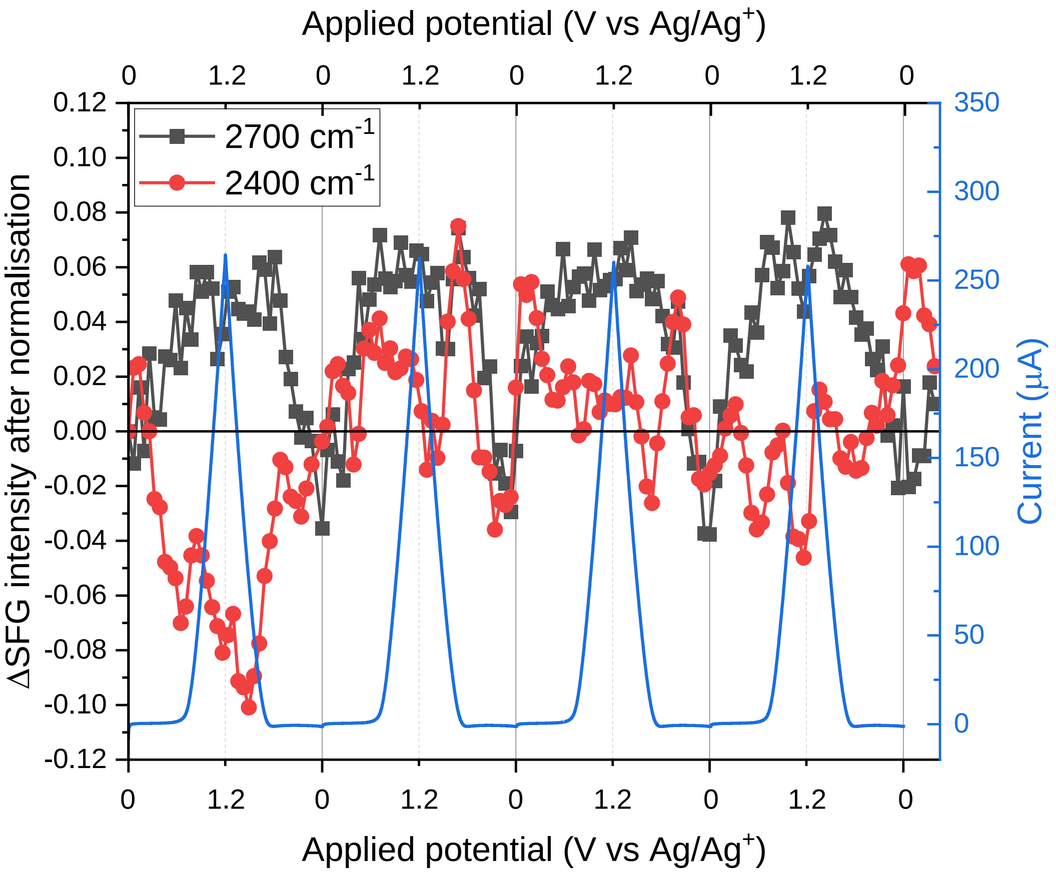

Figure 59: Intensity at 2700 cm^{-1} (black) and 2400 cm^{-1} (red) in VSFG difference spectra (relative to spectrum at 0 V vs Ag/Ag$^+$, after normalisation 0 to 1) as a function of applied potential for PLD-hematite/ITO/CaF_2 during 4 CV cycles at 50 mV s^{-1} in

0.1 M NaOD. All spectra were recorded at t_0 with 1 s exposure time per spectrum and 20 mW incident visible power (s-pol) and 30 mW incident IR power (p-pol) centred at 2680 cm^{-1}, the reflected SFG signal polarisation was not controlled, giving the xsp polarisation combination. Simultaneous CV data is overlaid in blue, with current plotted on the right axis.

Conversely, the 2400 cm^{-1} mode shows a clear linear decrease during the forward sweep and linear increase on the reverse sweep during the first CV, but no significant and reproducible changes in the subsequent CVs. The non-reversibility of this mode could be complicated by the existence of an additional mode below 2600 cm^{-1} that also has overlaid changes, especially since D_2O typically shows a doublet peak for the hydrogen-bonded O-D stretches around these frequencies.[29] This is likely further complicated by taking the first spectrum as the reference for all the difference spectra, as this spectrum captures the initial step change in voltage from OCP to 0 V vs Ag/Ag^+.

This is made clearer when viewing all of the difference spectra at 0 V for the subsequent CV cycles (Figure 60a), which all show a non-zero profile, indicating a different environment to the 0 V spectrum at the beginning of the first CV. However, each have a similar negative feature at 2700 cm^{-1} and a positive feature at around 2500 cm^{-1}, suggesting that the changes are reversible after the first cycle. Conversely, while the difference spectra at the most positive potential (1.6 V vs Ag/Ag^+) in the 4 CV cycles all show a similar intensity for the band at 2700 cm^{-1}, the features below 2600 cm^{-1} are different over the 4 CVs. The first cycle shows a negative band at 2400 cm^{-1}, while there is a positive band around 2300 cm^{-1} which grows in intensity in the subsequent cycles. These discrepancies below 2600 cm^{-1} suggest the changes at these frequencies, surface changes may not be fully reversible and are evolving over multiple experiments. For this reason, further analysis (discussed below) will focus on the 2700 cm^{-1} mode that shows clear reversible behaviour, as further experiments are likely required to fully understand these non-reversible changes.

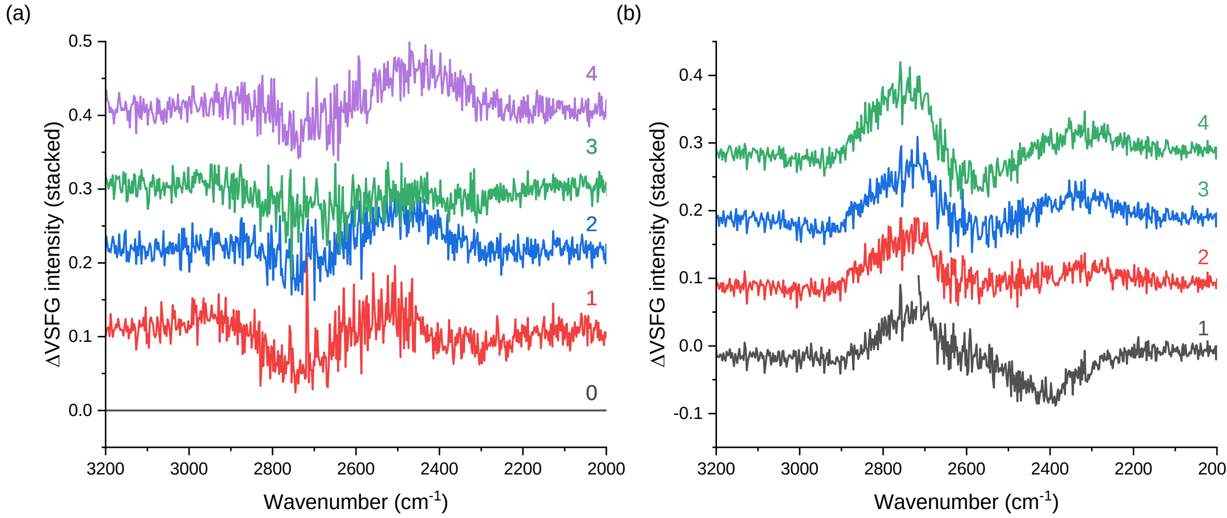

Figure 60: Stacked VSFG difference spectra at the vertex potentials in 4 CV cycles (relative to the initial spectrum at 0 V vs Ag/Ag$^+$, after normalisation 0 to 1) for PLD-hematite/ITO/CaF$_2$ at 0 V (a) and at 1.2 V vs Ag/Ag$^+$ (b), where the numbers (1 to 4) indicated the CV cycle order. All spectra were recorded at t_0 with 1 s exposure time per spectrum and 20 mW incident visible power (s-pol) and 30 mW incident IR power (p-pol) centred at 2680 cm^{-1}, the reflected SFG signal polarisation was not controlled, giving the xsp polarisation combination.

Similar experiments were also attempted on TiO$_2$ electrodes, but the observed VSFG signal was an order of magnitude lower under the same experimental conditions (only 200 counts per second *c.f.* 2000 counts per second for hematite). This disparity in signal size could be due to an inherent difference in the values of χ^2 for the two materials, or optical losses such as scattering. Hence, the first type of experiment on the TiO$_2$ electrodes involved recording spectra over much longer exposure times while holding an applied potential. Here the applied potential is held well before the OER onset for 60 seconds and then stepped to a potential above the OER onset for a further 60 seconds. This potential step was then repeated 15 times and the current response is shown in Figure 61.

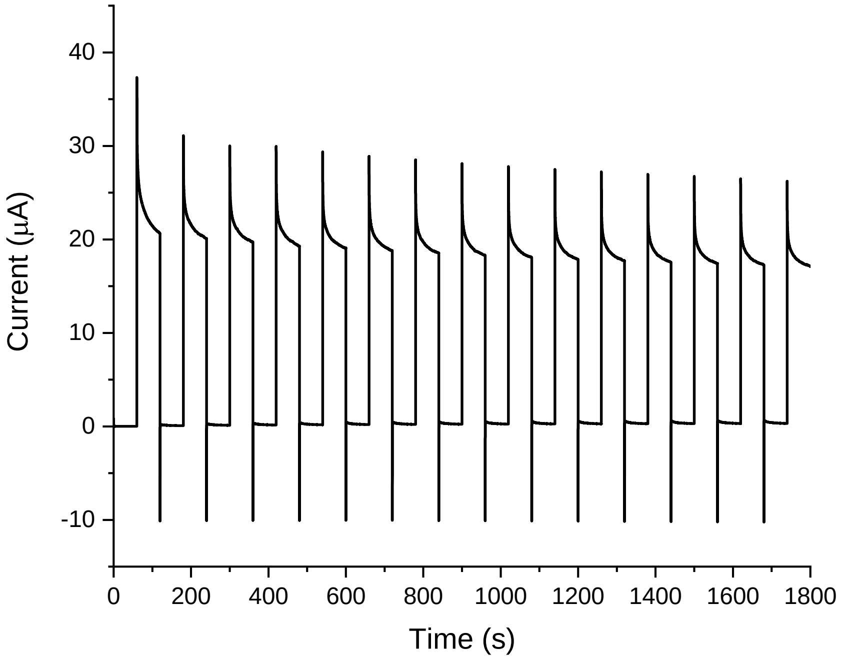

Figure 61: Example of a current vs time plot for potential step experiments on SC-TiO_2/ITO/SrF_2 in 0.1 M NaOD between 0 and 1.6 V vs Ag/Ag^+, where the potential was held for 60 s at each step.

Simultaneously, long exposure time VSFG spectra were recorded of the TiO_2 interface and analysed using the same normalisation and difference approach discussed above for hematite. These experiments were repeated at different centre wavelengths for the broadband IR pulse. This was to ensure any resonant changes are real modes and not artefacts of the analysis procedure, since the frequency of a resonant mode will not shift as the IR centre wavelength is varied. The resulting spectra in Figure 62 show a similar feature at 2700 cm^{-1} to the hematite spectra. The raw spectra prior to subtracting a reference spectrum are plotted below to provide an indication of the IR profile, which determines the spectral window that is probed.

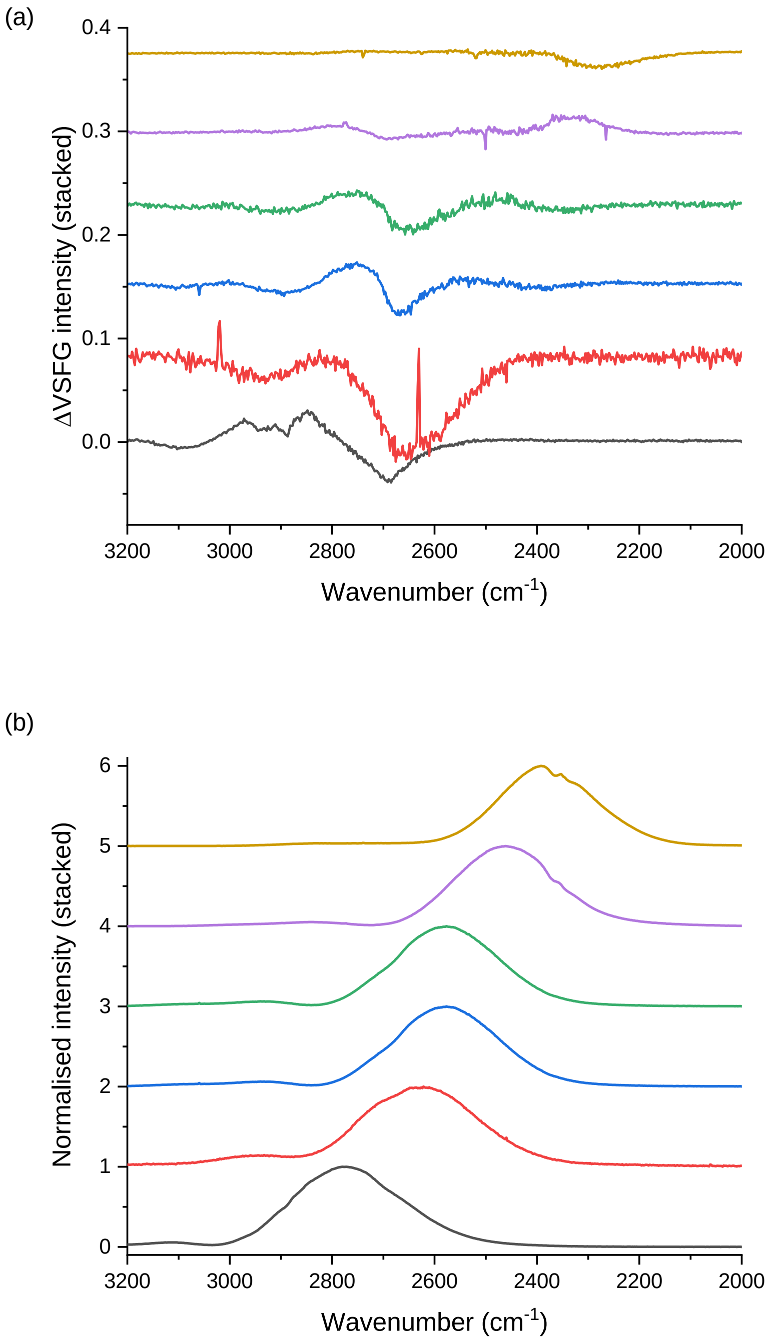

Figure 62: (a) Difference in VSFG intensity (after normalisation 0 to1) between spectra at 1.6 and 0 V vs Ag/Ag$_+$ for SC-TiO$_2$ electrodes in 0.1 M NaOD/D$_2$O electrolyte at t$_0$, with different infrared pulse centres. (b) Raw spectra (prior to subtracting a reference spectrum) to give an approximation of the IR profile for the difference spectrum of the same colour. Note the blue and green spectra are repeat experiments in the same spectral window. All the data shown here is for the average of 15 potential steps between 0 and 1.6 V, holding for 60 s at each potential. 20 mW incident visible power (s-pol) and 30 mW incident IR power (p-pol), the reflected SFG signal polarisation was not controlled, giving the xsp polarisation combination.

An issue with this method of analysis is that the Gaussian profile of the IR pulse has higher intensity in the centre and decreasing intensity towards the edges, making it difficult to compare spectral intensities of modes across spectra taken at different IR frequencies. This can be seen by the differences in amplitude and apparent frequency of the mode around 2700 cm^{-1} across the different IR centres in Figure 62. For this reason, VSFG spectra are typically normalised to a purely nonresonant signal, such as a bare gold surface, to account for the IR profile. It is important that the IR profile of the gold nonresonant sample accurately matches that of the sample to avoid artefacts in analysis. However, in this experimental setup it was not easy to swap between the spectroelectrochemical cell and gold nonresonant reference sample. It is worth noting that an isolated gold spot was added to future electrode designs to enable quick collection of reference spectra by simply translating the sample. However, for these first experiments such reference spectra were typically only recorded once or twice a day, while the IR profile could show significant variations throughout the day, especially when changing the IR centre frequency. This was less of a problem for comparing the hematite data above as they were all collected at the same IR centre frequency and over a very short time (1 to 2 s per spectrum) so the difference spectra were directly comparable. But the IR profile does need to be accounted for in these longer TiO_2 experiments as they are carried out at many different centre frequencies, during which the IR spectral profile could change significantly so the difference spectra are not suitable for comparison.

Thus, instead of a difference spectrum, VSFG spectra for the high potential (where an OER current is being drawn) are divided by the spectra at 0 V (where there is no current), giving a ratio in spectral intensities. This ratio both accounts for the shape of the IR profile at the time of the experiment and would still present any resonant vibrational changes as a change in shape of the ratio of the VSFG response. The averaged response plotted as a spectral ratio is shown in Figure 63a, which shows a significant negative peak around 2680 cm^{-1}. The peak maintains the same frequency when the IR centre wavelength is changed, suggesting it is not an artefact of the IR profile. A resonant band at this frequency would be consistent with either the free (non-hydrogen bonded) O-D stretch vibration of interfacial water or a surface TiO-D stretching vibration.[44,72] Such an assignment is strengthened by the fact that when exchanging the NaOD electrolyte with NaOH (Figure 63b), the resonant mode is not observed at any IR centre, indicating the feature is related to an O-D stretch.

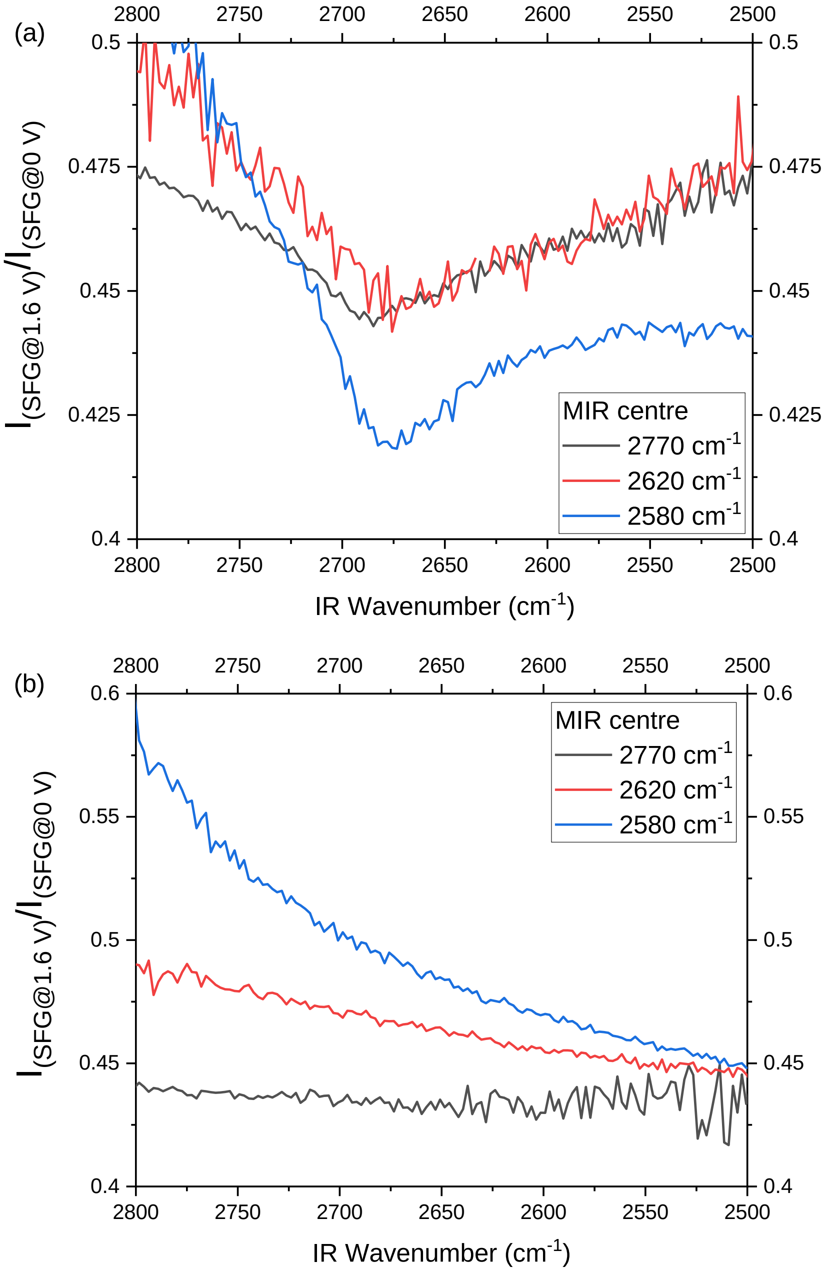

Figure 63: Ratio of SFG intensity at 1.6 and 0 V vs Ag wire for TiO_2 electrodes in 0.1 M NaOD/D_2O electrolyte (b) and in 0.1 M NaOH/H_2O (c) at different infrared pulse centres with 0 ps visible delay. The data shown here is for the average of 15 potential steps between 0 and 1.6 V, holding for 60 s at each potential. 20 mW incident visible power (s-pol) and 30 mW incident IR power (p-pol), the reflected SFG signal polarisation was not controlled, giving the xsp polarisation combination.

Without information of the relative phases of the resonant modes and nonresonant background it is hard to understand if this negative feature represents loss of species vibrating at this frequency, or growth of a species that is completely out-of-phase with the nonresonant. A similar vibrational mode has previously been observed by Ranasinghe *et al.* with transient IR absorption spectroscopy on similarly prepared TiO_2 photoelectrodes.[73] They observed a sharp vibrational mode at 2710 cm^{-1} upon photoexcitation of their TiO_2 electrode in a D_2O based electrolyte (0.1 M Na_2SO_4), which they assigned to a non-hydrogen bonded O-D stretch of D_2O. The intensity of this band decreased when their experiment was repeated at more positive applied biases, suggesting the vibration was from a molecule that is either consumed or changes hydrogen bonding environment under a higher rate of OER. In our experiments we only compare two potentials, close to OCP and under an OER current, so the influence of rate of consumption of intermediates cannot be addressed with this data, though further studies at additional potentials could address this.

Before further discussion of these results, it is first important to acknowledge issues with this ratio method of plotting spectra. The shape of the IR profile, especially at the edges, can lead to apparent peaks when taking ratios of the spectra at different voltages. As seen in Figure 64 from a second hematite electrode sample, which plots several spectral ratios at three different IR centres over the D_2O stretch region, but using a H_2O-based electrolyte so no resonant vibrational modes are expected above 2500 cm^{-1} (though the bend + libration combination centred at 2130 cm^{-1} may contribute below 2500 cm^{-1}).[74] The observed peaks appear to be artefacts of this method of analysis and shift when the IR centre is shifted. These artefacts arise when taking the ratio of the SFG signal at two different potentials, indicating they are somehow related to the electrochemical response of the system. The shape of the artefacts is very similar across the three spectra at different IR centres, showing a positive peak at higher frequencies, a diagonal portion in the middle and a negative peak at the lower frequencies.

The underlying ITO conductive layer in the electrode could provide an explanation for these artefacts. The optical properties ITO in the infrared are complex and depend greatly on free-carrier concentration.[75,76] In these electrochemical experiments, changes in the free-carrier concentration in the ITO layer due to current flow through the electrode could be inducing changes in its refractive index. This potential-dependent change in the refractive index could manifest as the observed artefacts, akin to a spectral chirp. Infrared reflectivity measurements could be carried out to assess whether such changes could be large enough to contribute to the observed SFG response, though preliminary experiments found it difficult to disentangle refractive index changes of the ITO from potential-dependent changes in the electrolyte itself.

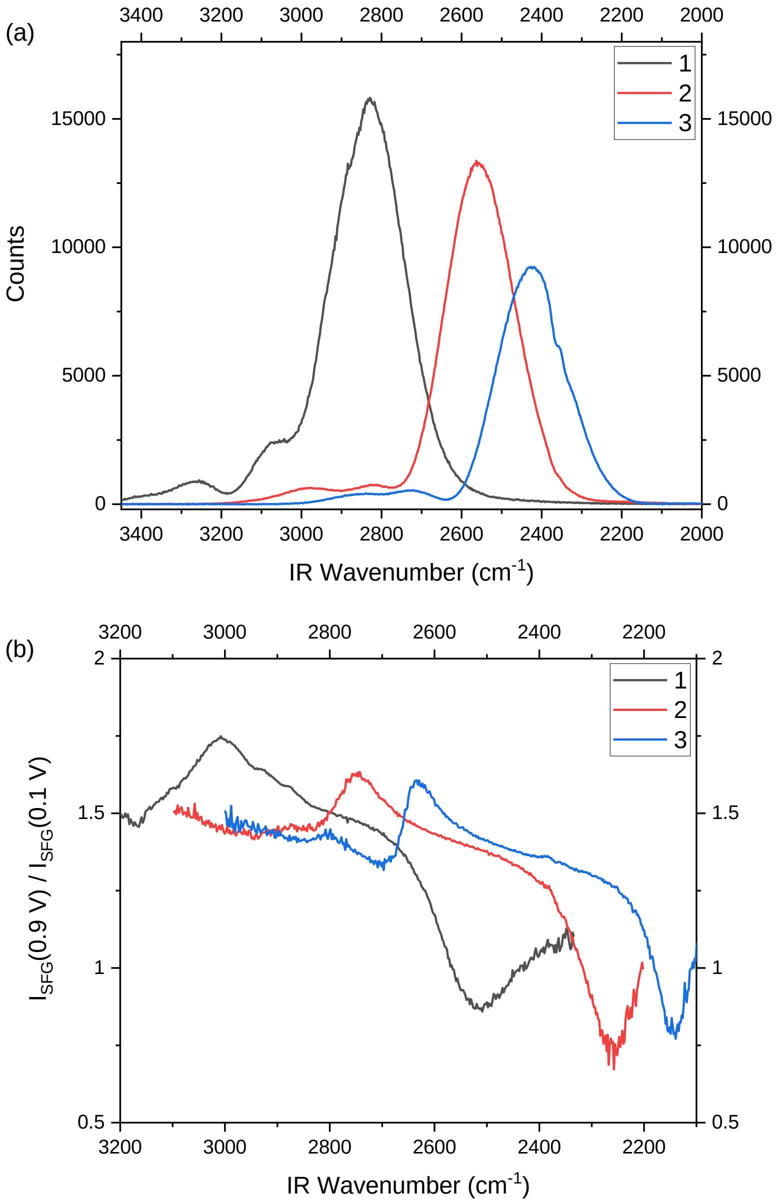

Figure 64: Shape of nonresonant response (as an indicator of the IR profile) for three different IR centre wavelengths (a) and ratio of SFG intensity between 0.9 and 0.1 V vs Ag wire for PLD-Fe_2O_3/ITO/SrF_2 in 0.1 M NaOH/H_2O electrolyte at different infrared pulse centres without any time delay for nonresonant suppression. Note this hematite sample is also a different sample to that used for the other data presented in this chapter. The data shown here is for the average of 15 potential steps between 0.1 and 0.9 V, holding for 60 s at each potential.

From above, it is clear that carrying out experiments at multiple IR centres is important to address these artefacts. This was carried out for the TiO_2 data in Figure 63, strengthening the assignment to a real vibrational change. However, the original hematite data under the same conditions was only carried out at a single IR centre during the facility time. Furthermore, unlike the TiO_2 data, the hematite experiments were not repeated in a H_2O-based electrolyte under the same conditions to check for the disappearance of apparent changes in the O-D stretch. The feature around 2700 cm^{-1} in the D_2O experiments is at least consistent over 4 different CV cycles, as shown above in Figure 59. Additionally, these experiments were carried out using a broad IR profile with the pulse centred around 2650 cm^{-1}, so the feature at 2700 cm^{-1} is unlikely to be a similar artefact to those observed in Figure 64 as it is not close to the edge of the IR profile.

Based on above we now have some confidence that a similar band around 2700 cm^{-1} appears during OER on two different electrode systems. The O-D stretching modes of non-hydrogen bonded water molecules are expected at around this frequency. Thus, the feature is tentatively assigned to the O-D stretch of non-hydrogen bonded water arising due to a disruption in the interfacial water structure under these conditions. From data recorded during a CV on hematite, the features start to appear prior to the OER onset, so any intermediates causing this disruption would have to precede the rate determining step. This suggests they are reporting on pre-catalytic changes at the electrode/electrolyte interface.

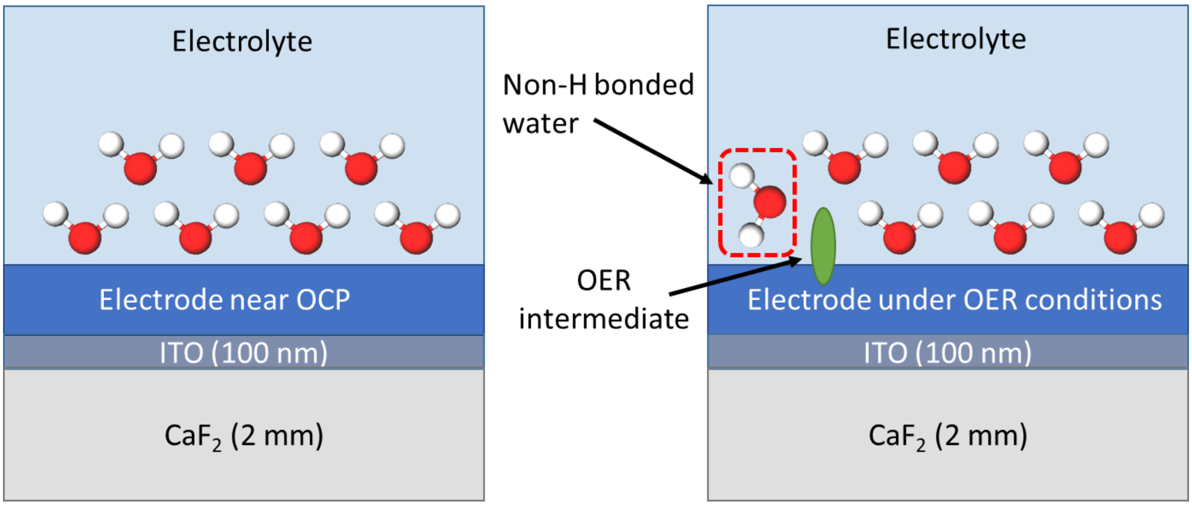

Figure 65: Diagram showing the ordered hydrogen bonded water structure at 0 V (left) and the disruption of this hydrogen bonded water structure under OER conditions at 1.2 V (right) at an electrode (either hematite or TiO_2) surface.

At this stage it is hard to rule out if the feature is due to the stretching modes of surface hydroxyls (TiO-D or FeO-D), which are expected at a similar spectral frequency. These species would not be stable under the experimental conditions as the solution pH>PZC for both TiO_2 and hematite, but it is not impossible that they appear transiently at high enough concentrations to be observed here. The fact that there is a difference in the apparent frequency of the band between hematite (2700 cm^{-1}) and TiO_2 (2680 cm^{-1}) provides some evidence that this could be true, as the surface hydroxyls are likely to have a different stretching frequency. Conversely, the frequency of a non-H bonded water molecule should be the same at both electrodes. However, if this non-H bonded water significantly interacts with the electrode surface the frequencies could be different across the two materials, and they would also display a Stark shift with potential. It was not possible to check for a Stark shift in the TiO_2 data as the 2680 cm^{-1} mode was only measured at a single potential. Furthermore, no significant Stark shift was observed for the 2700 cm^{-1} in hematite, suggesting this mode is not strongly interacting with the surface.

This difference in peak position could also arise due to the frequency dependent Fresnel factors,[40] which have not been accounted for here. Calculating these Fresnel factors is more difficult for multilayer structures as there are multiple refractive indices to account for. There are also further complications when working with transparent electrodes as the IR reflectivity of the ITO layer may change with potential due to changes in carrier concentrations within the conductive layer. To account for this the IR reflectivity with potential of an ITO/CaF_2 electrode would need to be measured in an appropriate electrolyte. On top of this, there is the issue that the linear optical response in the visible region may change with potential. As this is a multilayer system, this will affect the amount of light reaching the interface of interest. For both hematite and TiO_2 such spectroelectrochemical changes are generally observed far from the 800 nm “visible” light used here, but there are broad changes around 600 nm in hematite electrodes (Figure 66)[77] close to the SFG wavelength which would be around 660 nm when probing O-D stretching modes around 2700 cm^{-1}.

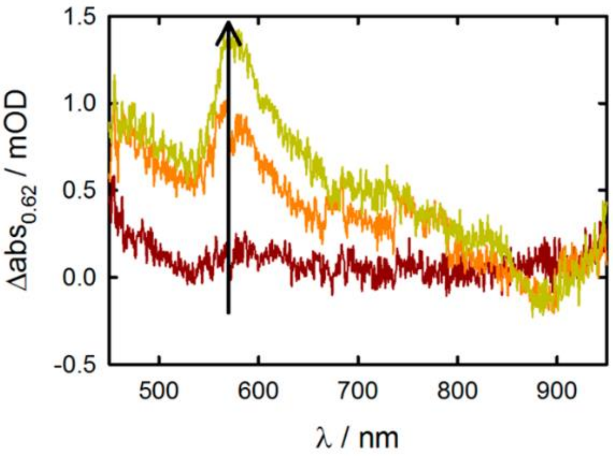

Figure 66: Spectroelectrochemical measurements at 0.82 V (red), 1.22 V (orange), and 1.62 V versus RHE (yellow) relative to the spectrum at 0.62 V vs RHE of a hematite electrode in 1 M NaOH under 0.1 mW cm^{-2} at 405 nm, reproduced with permission from Klahr et al.[77]

A counter-propagating geometry, depicted in Figure 67, can be used to address many of the issues with multilayer electrodes as it allows a single interface to be selectively addressed. This geometry was briefly investigated in this project during a second visit to the CLF, but finding a signal was substantially more difficult experimentally and electrochemical experiments were not attempted.

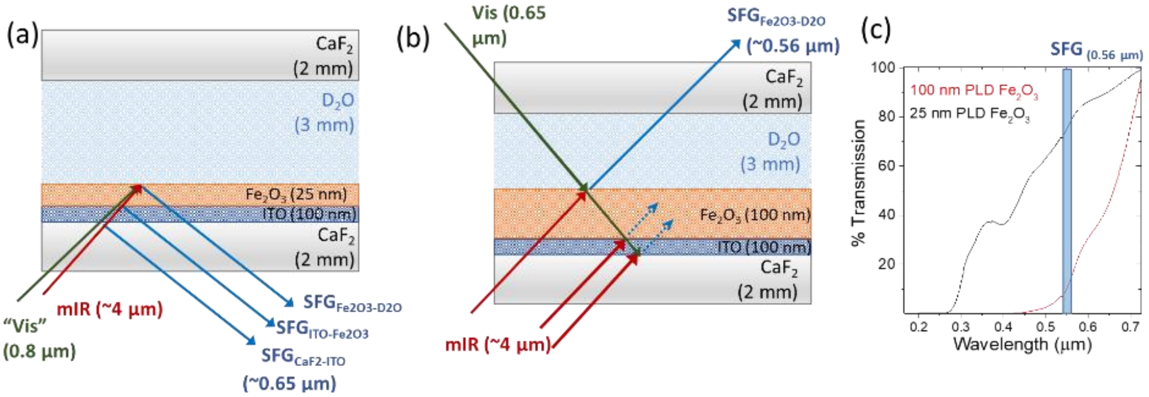

Figure 67: Conventional co-propagating geometry (a) and suggested experimental geometry for counter-propagating (b) VSFG experiments. The incident visible wavelength is changed to 650 nm and enters from the opposite side to the mid IR beam. The new SFG wavelength is 560 nm, which is partially absorbed by the hematite layer. By increasing the thickness of the hematite layer the transmission (c) of any SFG signal from the underlying layers is significantly reduced, while the interface of interest (Fe_2O_3/electrolyte) is unchanged.

Over the course of this PhD a new VSFG spectrometer has been developed in the University of Liverpool (more details on the development of this spectrometer can be found in Appendix B), which was used to test further hematite samples in an attempt to replicate some of the above results. The original hematite electrode used for these experiments was broken during the first facility time. Since then, multiple new samples have been synthesised following the same procedures, but their potential dependent response is always proportionally smaller than the first sample. Figure 68a shows the spectral ratio in O-D stretch region of a newer PLD hematite electrode recorded with the University of Liverpool spectrometer, there are no obvious changes in the spectrum that are consistent across all of the IR centres studied. The first hematite sample studied at the CLF showed much larger changes with potential (intensity changes by a factor of ~3 between the lowest and highest potentials studied) compared to the samples shown here (factor of ~ 1.1), suggesting that spectra are not reporting on the same processes. A key discrepancy with the new samples is that their transmission in the IR is also significantly lower, as seen in Figure 68b. This is indicative of a thicker than expected ITO layer as the overlaid hematite is not likely to absorb in this spectral region. Thus, the signals observed in the more recent experiments are likely dominated by this thicker ITO layer, which could explain the much smaller potential dependence.

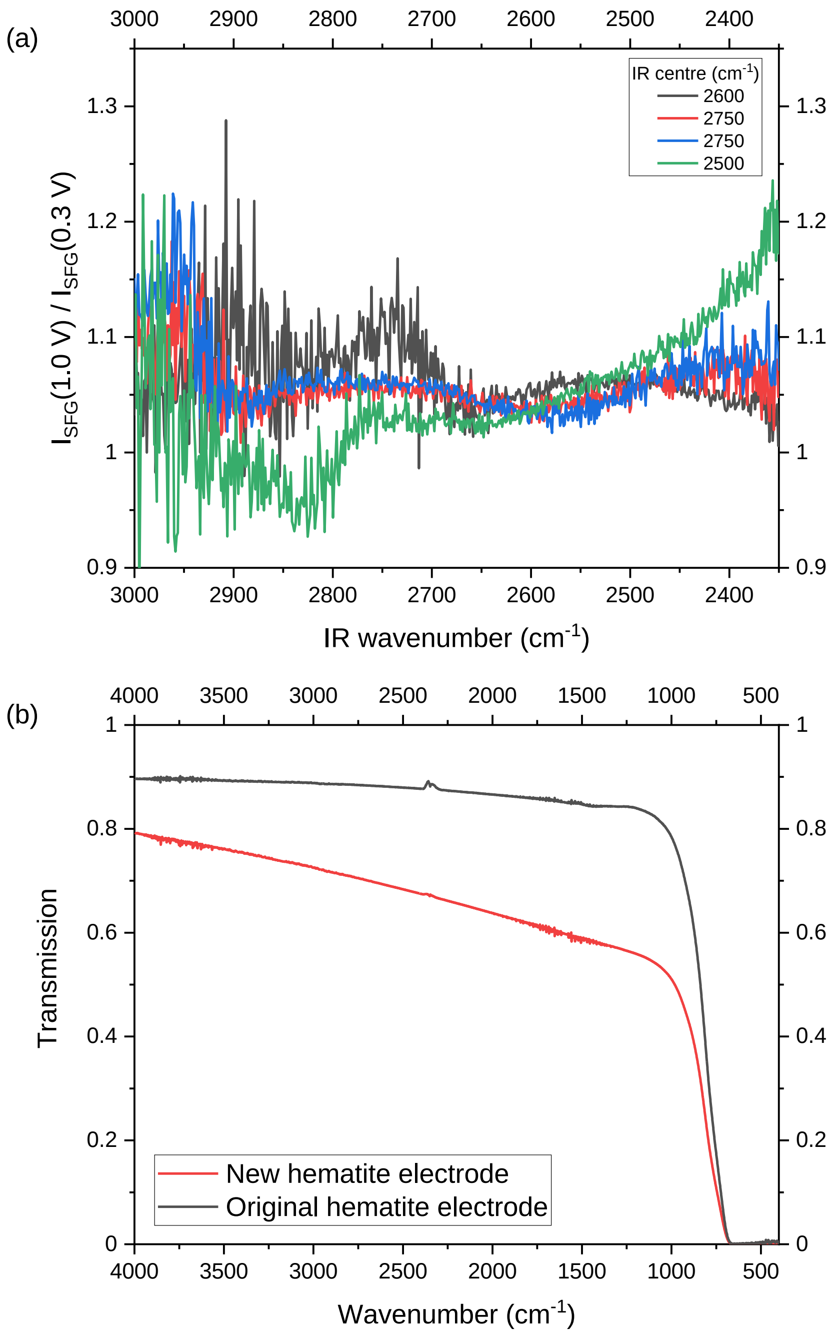

Figure 68: PLD-Fe_2O_3/ITO/CaF_2 0.1 M NaOD, 1028 nm@64 mW, stated IR wavelength@28 mW, xsp polarisation, 5 s per spectrum, 0 ps delay, 4 CV cycles 0.3 to 1.0 V, 2 mV s^{-1}.

Heterodyne detected (HD) VSFG spectroscopy can also address many of the problems with studying these electrode systems for water splitting. In HD-VSFG the phase of the nonresonant response can be determined, allowing access to the true line-shapes of the vibrational modes without the need for introducing time delays.[14] This would address a lot of the uncertainty in assignments of broad O-H/O-

D stretch vibrations by deconvoluting the spectra from the underlying nonresonant response. Furthermore, HD-VSFG increases the lower detection limit as the signal size is approximately linearly proportional to concentration compared to the quadratic concentration dependence observed in conventional homodyne VSFG.[14] This could be very useful for detecting small concentrations of intermediates or disrupted water molecules during an electrochemical experiment. Finally, the additional phase information allows accessing the orientation of interfacial water molecules, which can further aid assignments. During this project an *in situ* electrochemical HD-VSFG experiment was developed at the CLF based on the design of Vanselous and Petersen.[78] At the time of the experiments this had not been reported for any electrochemical system, though the first *in situ* electrochemical VSFG spectra have since been published by Sayama *et al*.[79] Details of the development of this HD-VSFG spectrometer and initial *in situ* experiments studying a [Mo(bpy)(CO)$_4$] CO$_2$ reduction catalyst on a gold electrode can be found in Appendix B.

3.3. Conclusions and future work:

This Chapter has detailed the development of a new "through-electrode" experimental geometry for VSFG spectroscopy and demonstrated its application to the study of buried catalytic interfaces. The technique works especially well with sharp, long-lived, resonant modes, where a time delay can be used to suppress the nonresonant response. This is highlighted by the results on the TiO$_2$/MeOH test system where the C-H stretch modes of adsorbed methanol species are used to monitor a photocatalytic reaction. This type of NR-suppressed experiment would translate well to studying the proposed OER intermediates (oxo, peroxo, superoxo *etc.*) discussed in Chapter 2 and the newly built VSFG spectrometer at the University of Liverpool is designed to produce sufficient IR light within this spectral region.

Next the technique was extended to electrochemical systems, where the O-D stretch vibrations of interfacial water molecules are probed at hematite and TiO$_2$ electrodes. Evidence for the generation of a non-hydrogen bonded water species is observed in both electrode systems under catalytic OER conditions. This tentative assignment is suggested to occur as a result of OER intermediates disrupting the H-bonding network of interfacial water molecules. The uncertainty in these assignments due to the complexity of the multi-layer electrodes is discussed, but further experiments were limited due to inconsistencies in sample response.

Initial work has also been carried out on alternative experimental designs to address some of these problems, including the suggested counter-propagating geometry and HD-VSFG spectroscopy (Appendix B). Both of these modifications have shown some promise, but further work is required to translate the techniques to the study of interfacial water at semiconductor photoelectrodes. Some of these issues will be explored in the next Chapter where the potential dependent SHG response of a slightly different kind of hematite electrode will be studied. Finally, pump light sources can be a useful tool for studying semiconductor photoelectrodes. Scattered light from the pump LED used in this chapter interfered with detection of the comparatively weak VSFG signal, limiting most experiments to pure electrochemical perturbations. Pump laser sources on the other hand are much more collimated, which could be more readily filtered, enabling the study of photoexcited samples using VSFG as a probe of the interfacial structure.

3.4. References:

1 C. Roy, B. Sebok, S. B. Scott, E. M. Fiordaliso, J. E. Sørensen, A. Bodin, D. B. Trimarco, C. D. Damsgaard, P. C. K. Vesborg, O. Hansen, I. E. L. Stephens, J. Kibsgaard and I. Chorkendorff, *Nat. Catal.*, 2018, **1**, 820–829.

2 O. Diaz-Morales, D. Ferrus-Suspedra and M. T. M. M. Koper, *Chem. Sci.*, 2016, **7**, 2639–2645.

3 J. B. Gerken, J. G. McAlpin, J. Y. C. Chen, M. L. Rigsby, W. H. Casey, R. D. Britt and S. S. Stahl, *J. Am. Chem. Soc.*, 2011, **133**, 14431–14442.

4 P. B. Petersen and R. J. Saykally, *Chem. Phys. Lett.*, 2008, **458**, 255–261.

5 E. Codorniu-Hernández and P. G. Kusalik, *Proc. Natl. Acad. Sci. U. S. A.*, 2013, **110**, 13697–13698.

6 Y. Shao, H. J. M. De Groot and F. Buda, *J. Phys. Chem. Lett.*, 2019, **10**, 7690–7697.

7 R. Zhang, P. E. Pearce, Y. Duan, N. Dubouis, T. Marchandier and A. Grimaud, *Chem. Mater.*, 2019, **31**, 8248–8259.

8 A. G. Lambert, P. B. Davies and D. J. Neivandt, *Appl. Spectrosc. Rev.*, 2005, **40**, 103–145.

9 Y. R. Shen, *The principles of nonlinear optics.*, New York : Wiley, 1984., 1984.

10 Y. R. Shen, *Nature*, 1989, **337**, 519–525.

11 X. D. Zhu, H. Suhr and Y. R. Shen, *Phys. Rev. B*, 1987, **35**, 3047–3050.

12 P. Guyot-Sionnest and A. Tadjeddine, *Chem. Phys. Lett.*, 1990, **172**, 341–345.

13 A. Lagutchev, S. A. Hambir and D. D. Dlott, *J. Phys. Chem. C*, 2007, **111**, 13645–13647.

14 I. V. Stiopkin, H. D. Jayathilake, A. N. Bordenyuk and A. V. Benderskii, *J. Am. Chem. Soc.*, 2008, **130**, 2271–2275.

15 N. G. Rey and D. D. Dlott, *J. Electroanal. Chem.*, 2017, **800**, 114–125.

16 M. A. Brown, A. Goel and Z. Abbas, *Angew. Chemie - Int. Ed.*, 2016, **55**, 3790–3794.

17 S. Ong, X. Zhao and K. B. Eisenthal, *Chem. Phys. Lett.*, 1992, **191**, 327–335.

18 E. H. G. Backus, J. Schaefer and M. Bonn, *Angew. Chemie - Int. Ed.*, 2021, **60**, 10482–10501.

19 Y. R. Shen and V. Ostroverkhov, *Chem. Rev.*, 2006, **106**, 1140–1154.

20 L. Zhang, C. Tian, G. A. Waychunas and Y. R. Shen, *J. Am. Chem. Soc.*, 2008, **130**, 7686–7694.

21 M.-P. Gaigeot, M. Sprik and M. Sulpizi, *J. Phys. Condens. Matter*, 2012, **24**, 124106.

22 K. A. Becraft and G. L. Richmond, *Langmuir*, 2001, **17**, 7721–7724.

23 S. Schrödle, F. G. Moore and G. L. Richmond, *J. Phys. Chem. C*, 2007, **111**, 10088–10094.

24 V. Ostroverkhov, G. A. Waychunas and Y. R. Shen, *Chem. Phys. Lett.*, 2004, **386**, 144–148.

25 Q. Du, E. Freysz and Y. R. Shen, *Phys. Rev. Lett.*, 1994, **72**, 238–241.

26 M. Kosmulski, *Adv. Colloid Interface Sci.*, 2020, **275**, 102064.

27 M. Sovago, R. K. Campen, G. W. H. Wurpel, M. Müller, H. J. Bakker and M. Bonn, *Phys. Rev. Lett.*, 2008, **100**, 173901.

28 A. A. Kananenka and J. L. Skinner, *J. Chem. Phys.*, 2018, **148,** 244107.

29 M. Sovago, R. Kramer Campen, H. J. Bakker and M. Bonn, *Chem. Phys. Lett.*, 2009, **470**, 7–12.

30 S. H. Urashima, A. Myalitsin, S. Nihonyanagi and T. Tahara, *J. Phys. Chem. Lett.*, 2018, **9**, 4109–4114.

31 A. Myalitsin, S. H. Urashima, S. Nihonyanagi, S. Yamaguchi and T. Tahara, *J. Phys. Chem. C*, 2016, **120**, 9357–9363.

32 S. Nihonyanagi, S. Yamaguchi and T. Tahara, *Chem. Rev.*, 2017, **117**, 10665–10693.

33 K. C. Jena, P. A. Covert and D. K. Hore, *J. Phys. Chem. Lett.*, 2011, **2**, 1056–1061.

34 A. M. Darlington, T. A. Jarisz, E. L. Dewalt-Kerian, S. Roy, S. Kim, M. S. Azam, D. K. Hore and J. M. Gibbs, *J. Phys. Chem. C*, 2017, **121**, 20229–20241.

35 T. Joutsuka and A. Morita, *J. Phys. Chem. C*, 2018, **122**, 11407–11413.

36 C. Schnitzer, S. Baldelli and M. J. Shultz, *J. Phys. Chem. B*, 2000, **104**, 585–590.

37 K. C. Jena and D. K. Hore, *J. Phys. Chem. C*, 2009, **113**, 15364–15372.

38 P. E. Ohno, H. F. Wang and F. M. Geiger, *Nat. Commun.*, 2017, **8**, 1–9.

39 S. Kataoka, M. C. Gurau, F. Albertorio, M. A. Holden, S. M. Lim, R. D. Yang and P. S. Cremer, *Langmuir*, 2004, **20**, 1662–1666.

40 E. H. G. Backus, N. Garcia-Araez, M. Bonn and H. J. Bakker, *J. Phys. Chem. C*, 2012, **116**, 23351–

23361.

41 C. S. Tian and Y. R. Shen, *J. Am. Chem. Soc.*, 2009, **131**, 2790–2791.

42 C. Tian, N. Ji, G. A. Waychunas and Y. R. Shen, *J. Am. Chem. Soc.*, 2008, **130**, 13033–13039.

43 O. Isaienko and E. Borguet, *Langmuir*, 2013, **29**, 7885–7895.

44 C. Y. Wang, H. Groenzin and M. J. Shultz, *Langmuir*, 2003, **19**, 7330–7334.

45 T. Seki, C. C. Yu, X. Yu, T. Ohto, S. Sun, K. Meister, E. H. G. Backus, M. Bonn and Y. Nagata, *Phys. Chem. Chem. Phys.*, 2020, **22**, 10934–10940.

46 T. Seki, K. Y. Chiang, C. C. Yu, X. Yu, M. Okuno, J. Hunger, Y. Nagata and M. Bonn, *J. Phys. Chem. Lett.*, 2020, **11**, 8459–8469.

47 C. J. Moll, J. Versluis and H. J. Bakker, *Phys. Rev. Lett.*, 2021, **127**, 116001.

48 A. Kundu, S. Tanaka, T. Ishiyama, M. Ahmed, K. I. Inoue, S. Nihonyanagi, H. Sawai, S. Yamaguchi, A. Morita and T. Tahara, *J. Phys. Chem. Lett.*, 2016, **7**, 2597–2601.

49 J. Petersen, K. B. Møller, R. Rey and J. T. Hynes, *J. Phys. Chem. B*, 2013, **117**, 4541–4552.

50 H. Noguchi, T. Okada and K. Uosaki, *Electrochim. Acta*, 2008, **53**, 6841–6844.

51 S. Nihonyanagi, S. Ye, K. Uosaki, L. Dreesen, C. Humbert, P. Thiry and A. Peremans, *Surf. Sci.*, 2004, **573**, 11–16.

52 Z. D. Schultz, S. K. Shaw and A. A. Gewirth, *J. Am. Chem. Soc.*, 2005, **127**, 15916–15922.

53 L. B. Dreier, Z. Liu, A. Narita, M. J. Van Zadel, K. Müllen, K. J. Tielrooij, E. H. G. Backus and M. Bonn, *J. Phys. Chem. C*, 2019, **123**, 24031–24038.

54 J. E. Bertie and Z. Lan, *Appl. Spectrosc.*, 1996, **50**, 1047–1057.

55 M. Grundmann, in *The Physics of Semiconductors, Graduate Texts in Physics*, 2016, pp. 575–579.

56 H. Zheng, R. J. Zhang, D. H. Li, X. Chen, S. Y. Wang, Y. X. Zheng, M. J. Li, Z. G. Hu, N. Dai and L. Y. Chen, *Nanoscale Res. Lett.*, , DOI:10.1186/s11671-018-2563-9.

57 A. Conde-Gallardo, M. Guerrero, N. Castillo, A. B. Soto, R. Fragoso and J. G. Cabañas-Moreno, *Thin Solid Films*, 2005, **473**, 68–73.

58 M. Todeschini, A. Bastos Da Silva Fanta, F. Jensen, J. B. Wagner and A. Han, *ACS Appl. Mater. Interfaces*, 2017, **9**, 37374–37385.

59 K. D. Malviya, H. Dotan, D. Shlenkevich, A. Tsyganok, H. Mor and A. Rothschild, *J. Mater. Chem. A*, 2016, **4**, 3091–3099.

60 C. Wang, H. Groenzin and M. J. Shultz, *J. Phys. Chem. B*, 2004, **108**, 265–272.

61 A. Fujishima, X. Zhang and D. A. Tryk, *Surf. Sci. Rep.*, 2008, **63**, 515–582.

62 W. Y. Teoh, F. Denny, R. Amal, D. Friedmann, L. Mädler and S. E. Pratsinis, *Top. Catal.*, 2007, **44**, 489–497.

63 Q. Guo, C. Xu, Z. Ren, W. Yang, Z. Ma, D. Dai, H. Fan, T. K. Minton and X. Yang, *J. Am. Chem. Soc.*, 2012, **134**, 13366–13373.

64 H. Feng, S. Tan, H. Tang, Q. Zheng, Y. Shi, X. Cui, X. Shao, A. Zhao, J. Zhao and B. Wang, *J. Phys. Chem. C*, 2016, **120**, 5503–5514.

65 C. Fu, F. Li, J. Zhang, D. Li, K. Qian, Y. Liu, J. Tang, F. Fan, Q. Zhang, X. Gong and W. Huang, *Angew. Chemie*, 2021, **133**, 6225–6234.

66 M. Setvin, X. Shi, J. Hulva, T. Simschitz, G. S. Parkinson, M. Schmid, C. Di Valentin, A. Selloni and U. Diebold, *ACS Catal.*, 2017, **7**, acscatal.7b02003.

67 A. A. Liu, S. Liu, R. Zhang and Z. Ren, *J. Phys. Chem. C*, 2015, **119**, 23486–23494.

68 R. Zhang, H. Wang, X. Peng, R. Feng, A. Liu, Q. Guo, C. Zhou, Z. Ma, X. Yang, Y. Jiang and Z. Ren, *J. Phys. Chem. C*, 2019, **123**, 9993–9999.

69 J. C. Deàk, S. T. Rhea, L. K. Iwaki and D. D. Dlott, *J. Phys. Chem. A*, 2000, **104**, 4866–4875.

70 S. Chatman, P. Zarzycki and K. M. Rosso, *Phys. Chem. Chem. Phys.*, 2013, **15**, 13911–13921.

71 L. Čerović, G. Lefèvre, A. Jaubertie, M. Fédoroff and S. Milonjić, *J. Colloid Interface Sci.*, 2009, **330**, 284–291.

72 X. Xu, Y. R. Shen and C. Tian, *J. Chem. Phys.*, 2019, **150**, 144701.

73 C. S. K. Ranasinghe and A. Yamakata, *Phys. Chem. Chem. Phys.*, 2018, **20**, 3388–3394.

74 P. K. Verma, A. Kundu, M. S. Puretz, C. Dhoonmoon, O. S. Chegwidden, C. H. Londergan and M. Cho, *J. Phys. Chem. B*, 2018, **122**, 2587–2599.

75 A. Tamanai, T. D. Dao, M. Sendner, T. Nagao and A. Pucci, *Phys. Status Solidi Appl. Mater. Sci.*, 2017, **214**, 1–8.

76 J. W. Cleary, E. M. Smith, K. D. Leedy, G. Grzybowski and J. Guo, *Opt. Mater. Express*, 2018, **8**, 1231.

77 B. Klahr and T. Hamann, *J. Phys. Chem. C*, 2014, **118**, 10393–10399.

78 H. Vanselous and P. B. Petersen, *J. Phys. Chem. C*, 2016, **120**, 8175–8184.

79 A. Sayama, S. Nihonyanagi, Y. Ohshima and T. Tahara, *Phys. Chem. Chem. Phys.*, 2020, **22**, 2580–2589.

Chapter 4

Probing interfacial electric fields at hematite photoelectrodes during water splitting

This chapter describes investigations on hematite photoelectrodes using PIA and SHG spectroscopy. The custom PIA spectrometer was originally built by myself during an undergraduate project with the Cowan group, based loosely on the existing nanosecond transient absorption spectrometer and its LabView software. Before starting the PhD project, the PIA spectrometer had been disassembled, so a new and improved version was rebuilt during the PhD project and used for all experiments shown here. The SHG spectrometer is simply a slight modification of the SFG spectrometer described in Chapter 3.

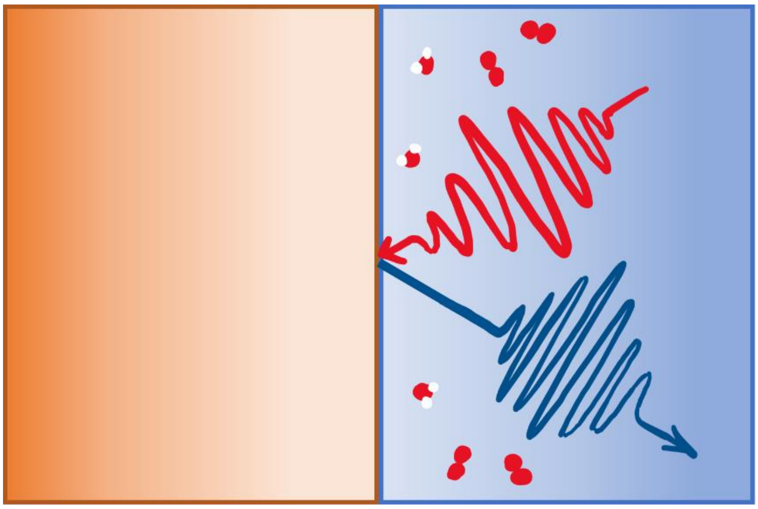

4.1. Introduction:

One of the main motivations for the mechanistic studies carried out in this project has been to gain an understanding of the underlying physico-chemical phenomena and use this to rationalise the efficiency of current water splitting materials. This understanding can then be exploited to inform the design of improved materials in the future. Many of these physical processes can affect the interfacial electric field, for example, the formation and dynamics of the electrochemical double layer induces an electric field gradient extending into the electrolyte. Similarly, depletion of charge carriers within the semiconductor lead to the formation of a space charge layer within the semiconductor, resulting in another electric field gradient away from electrode/electrolyte interface. Having a direct probe of these electric fields would be an incredibly powerful tool to add to the arsenal for mechanistic studies of such electrodes. This chapter will explore the feasibility of using electric field-induced second harmonic generation spectroscopy (EFISHG) to monitor interfacial electric fields at hematite photoelectrodes, attempting to address the much-debated role of surface trap states on these fields and their implications on device efficiency.

Hole trapping at the surface of semiconductor photoanodes is an incredibly important process in determining the efficiency of the material as a catalyst for water oxidation and the nature of such surface states has been debated in recent years.[1] Energetically, these trap states are located between valence and conduction band edges, so the process of charge carrier trapping involves some loss of potential energy, reducing their reactivity. Conversely, surface traps necessarily increase the charge carrier lifetime, which can have a net positive effect on the efficiency of the photoelectrode. The exact nature of the trapped holes on a hematite surface is also debated, some reports claim the trapped holes are themselves the water oxidation intermediates and the sluggish kinetics of the water oxidation reaction lead to their long lifetime on the surface.[2] Others refer to them exclusively as electronic states that are not chemically involved with the water oxidation process.[3] Further investigation of the charge carrier kinetics in such materials is likely key to understanding their activity and identifying methods of improving it.

The photoexcited state of hematite has several key visible light absorptions that can be assigned to generation of trapped electrons within the SCL (leading to a narrow transient UV/Vis band at 575 nm on an ultrafast timescale)[4] and surface holes (broad band above 600 nm on ms-s time scale).[5] The rate-limiting step in the water oxidation reaction on hematite electrodes is often attributed to inefficient transfer of surface holes to water species in the electrolyte, leading to the observed sluggish kinetics. The nature and long lifetime of these trapped surface holes will likely have a significant impact on the energetics and kinetics of this rate-limiting process.

Photoinduced absorption spectroscopy (PIA) is a promising technique to investigate the slow hole dynamics in hematite electrodes and has recently been used to identify a possible change in mechanism at higher light intensities.[6] PIA is a pump-probe technique analogous to TAS, but using continuous wave (CW) illumination for both the pump and the probe (instead of laser pulses), sacrificing time resolution but enabling more detailed study of slow charge carrier kinetics over much longer time scales. By eliminating the need for lasers, the technique is much simpler, cheaper and safer than conventional TAS experiments, making it a more accessible approach to investigating kinetics. Furthermore, the conditions employed during a PIA experiment are closer to the normal operating conditions for a photoelectrode, in that a CW light source more closely resembles solar radiation than a pulsed laser. The main implication of this relates to charge carrier concentrations under operating conditions, which are dependent upon light intensity. Under high CW light intensities (*i.e.* resembling solar radiation), significant charge accumulation occurs within the photoelectrochemical system, which can have dramatic effects on the mechanism of action as shown by Le Formal *et al*.[6]

More recent TAS studies have also highlighted the importance of using CW illumination alongside the pulsed lasers for TAS.[7] A distinction is made between the two sets of conditions, where conventional TAS experiments with pulsed lasers are referred to as *in situ* experiments and TAS experiments with an additional CW light source are referred to as *operando* conditions, as they more closely resemble the real working conditions of the photoelectrochemical device, with comparability to real working conditions also confirmed by on-line product detection.[8] A summary of these recommendations for operando measurements is presented in from Forster *et al.*[7] The study also demonstrated the impact of temperature-dependent optical changes within the sample, which can be hard to distinguish from signals from the photoexcited sample.[7] It was noted that the high peak powers from the pulsed laser that are often used in TAS studies can also induce localised temperature changes within the material, which can then manifest as further optical changes within the sample. Using CW light sources mostly avoids this problem and any slight thermal contributions in such studies would be comparable to that observed under solar radiation.

Table 2: Guidelines for operando transient absorption studies of photoelectrodes, reproduced with permission from a Perspective article by Forster et al.[7]

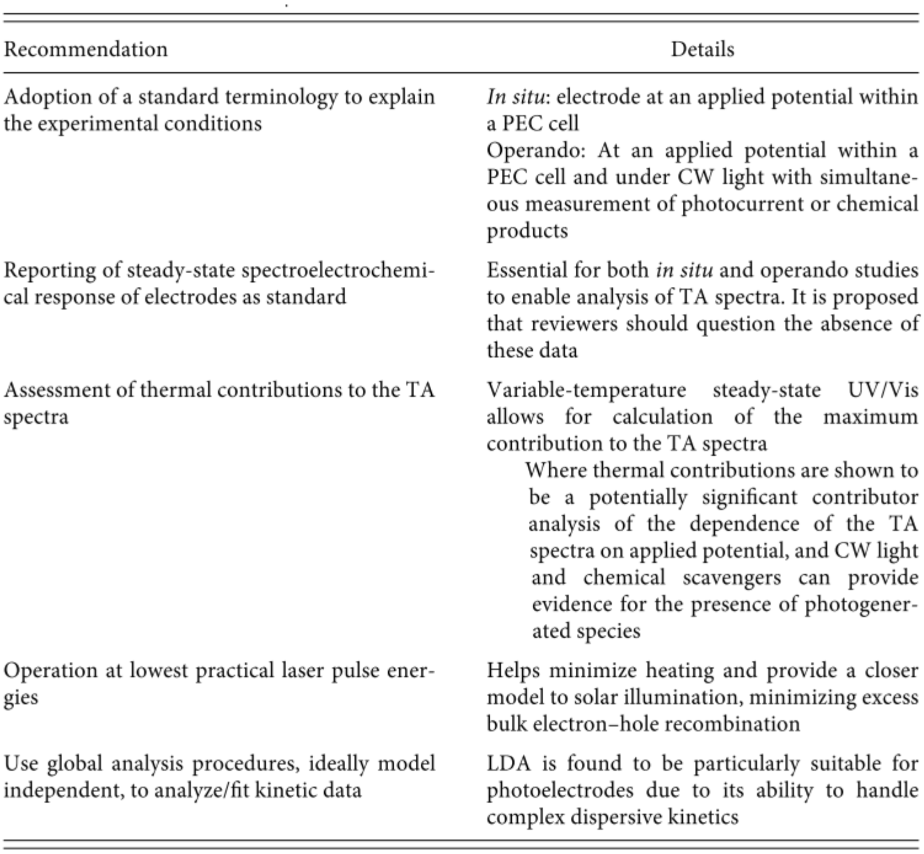

Recommendation	Details
Adoption of a standard terminology to explain the experimental conditions	*In situ*: electrode at an applied potential within a PEC cell Operando: At an applied potential within a PEC cell and under CW light with simultaneous measurement of photocurrent or chemical products
Reporting of steady-state spectroelectrochemical response of electrodes as standard	Essential for both *in situ* and operando studies to enable analysis of TA spectra. It is proposed that reviewers should question the absence of these data
Assessment of thermal contributions to the TA spectra	Variable-temperature steady-state UV/Vis allows for calculation of the maximum contribution to the TA spectra Where thermal contributions are shown to be a potentially significant contributor analysis of the dependence of the TA spectra on applied potential, and CW light and chemical scavengers can provide evidence for the presence of photogenerated species
Operation at lowest practical laser pulse energies	Helps minimize heating and provide a closer model to solar illumination, minimizing excess bulk electron–hole recombination
Use global analysis procedures, ideally model independent, to analyze/fit kinetic data	LDA is found to be particularly suitable for photoelectrodes due to its ability to handle complex dispersive kinetics

Another important consequence of such surface trap states is their effect on the interfacial potential. The accumulation of holes at the surface due to sluggish water oxidation kinetics can result in a build-up of positive charge at the interface that counteracts the internal space charge field (which is responsible for separating the photogenerated charges in the first place), inhibiting further separation of charges. The presence of electronic trap states can have a further effect on this space charge field through fermi-level pinning, where increasingly anodic potentials do not induce band-bending in the semiconductor until these surface electronic states are completely emptied. The question of whether either of these two mechanisms can be used to address the apparent change in mechanism mentioned above has recently been highlighted.[9]

4.2. Results and discussion:

4.2.1. PIA on hematite:

This next section describes the application of the same rate law analysis procedure used by Le Formal *et al*. in their study of hole kinetics in hematite photoelectrodes.[6] The aim of this section is to confirm that the electrodeposited hematite samples used in this project exhibit the same switch in mechanism at high light intensity as observed in the literature, enabling further analysis using EFISHG spectroscopy to better understand the potential role of interfacial electric fields on this change in mechanism. The PIA spectrometer shown in Figure 69 was developed during this project (more details can be found in Chapter 5.14.) and used to confirm this change in mechanism on electrodeposited hematite photoelectrodes at high light intensities.

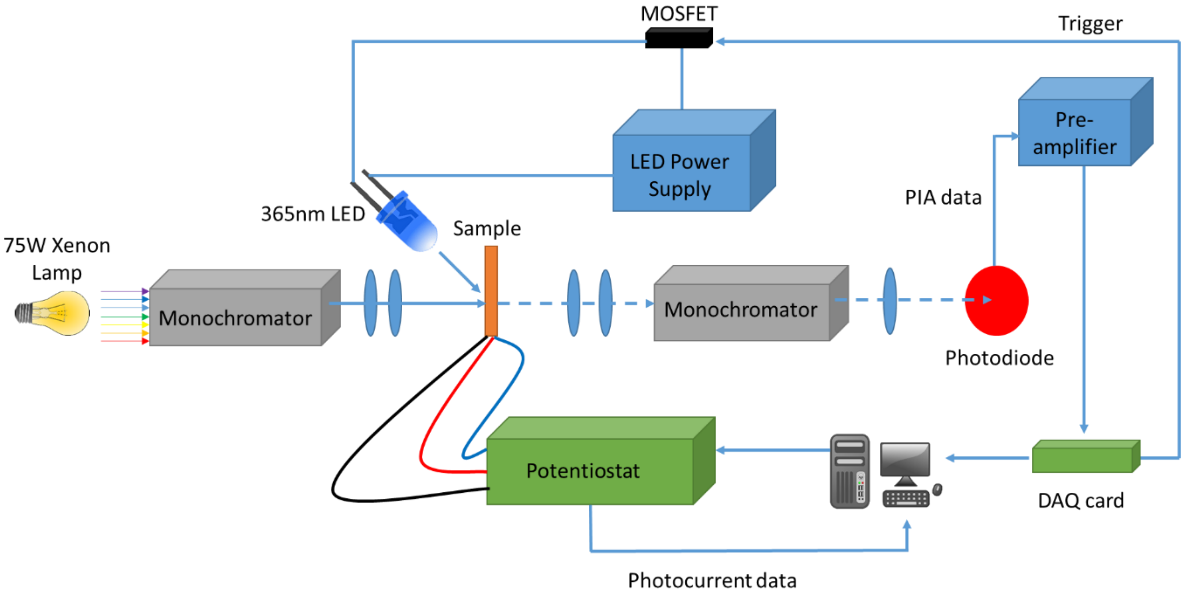

Figure 69: Diagram of PIA setup used in this chapter. The output of a 75 W Xenon lamp is passed through a first monochromator and a series of collimating and focussing lenses onto the sample before being re-collimated and focussed after the sample and passed through a second monochromator, which also contains 400 nm LP filters to remove residual pump light. The transmitted light is detected using a biased avalanche photodiode and the raw voltage output is passed through a low-noise pre-amplifier before being detected using a NI-DAQ card. Simultaneously a potentiostat (PalmSens EmStat) is used to apply a bias voltage to the electrochemical cell. A homemade LabView programme is used to trigger the MOSFET to turn the LED on/off as well as to simultaneously record the DAQ input and display the PIA data.

These experiments monitor changes in intensity of transmitted probe light through the sample before and after perturbation by the pump LED. The signal intensity is represented as an optical density (OD):

$$OD = \log\left(\frac{I_0}{I_t}\right) \qquad \textit{Eq. 4.1.}$$

Where I_0 is the incident light intensity and I_t is the intensity of light transmitted through the electrode. In a PIA experiment we compare the signal in the dark before illumination with the signal under illumination:

$$\Delta OD = \log\left(\frac{I_0}{I_{t,illuminated}}\right) - \log\left(\frac{I_0}{I_{t,dark}}\right) \qquad \textit{Eq. 4.2.}$$

Which, with a stable probe light source (I_0), simplifies to:

$$\Delta OD = \log\left(\frac{I_{t,dark}}{I_{t,illuminated}}\right) \qquad \text{Eq. 4.3.}$$

A series of PIA experiments were carried out various probe wavelengths by selecting the appropriate wavelengths from the xenon lamp on both monochromators. The amplitude of the PIA signal while the LED is on is plotted as a function of probe wavelength in Figure 70. The signal shows a positive change in optical density across the whole spectrum, representing an increase in absorption due to an increase in concentration of excited states by the pump LED. This broad change above 600 nm has previously been assigned to absorption from surface hole species.[5] The kinetics of these surface holes can thus be investigated by selecting a probe wavelength within this broad region above 600 nm and monitoring the PIA amplitude with time. The signal also appears to show a small decrease in signal below 600 nm, which is indicative of a known narrow transient negative absorption from electrons at 575 nm.[4] While the hole signal is highest at 600 nm, a slightly longer probe wavelength is chosen for further experiments to avoid interference from this narrow negative electron signal.

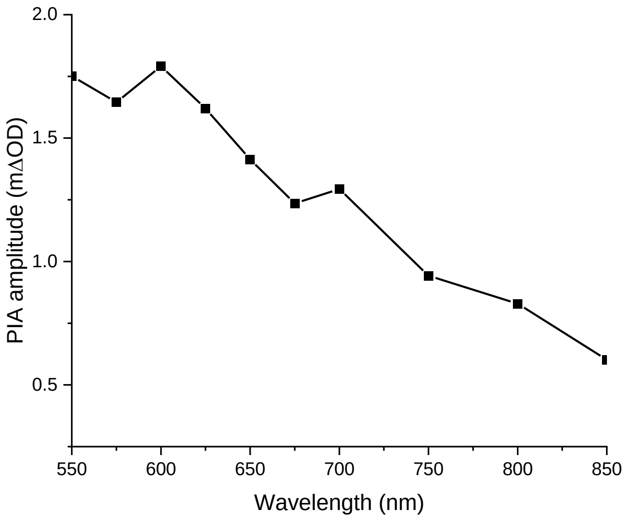

Figure 70: PIA spectrum of an ED-Fe_2O_3/FTO electrode under 365 nm LED front illumination (~ 27 mW cm^{-2}). The electrode was held at 0.2 V vs Ag/Ag$^+$ in 0.1 M NaOD for all experiments. Each point represents the signal amplitude once the system is illuminated and allowed to reach equilibrium.

In these first set of kinetics experiments, the absorption at 625 nm in photoexcited hematite electrodes (attributed to surface holes) is monitored before, during and after 5 seconds of CW illumination by a 365 nm LED. These measurements are repeated over several different LED light intensities, which can be easily modulated by changing the voltage on the LED power supply. The concentration of surface holes is essentially controlled by changing the incident light intensity under the assumption that more incident photons would increase the flux of holes to the surface. This is reflected in the data shown in Figure 71, showing a clear increase in PIA amplitude as the incident light intensity is increased, indicating a greater concentration of surface holes.

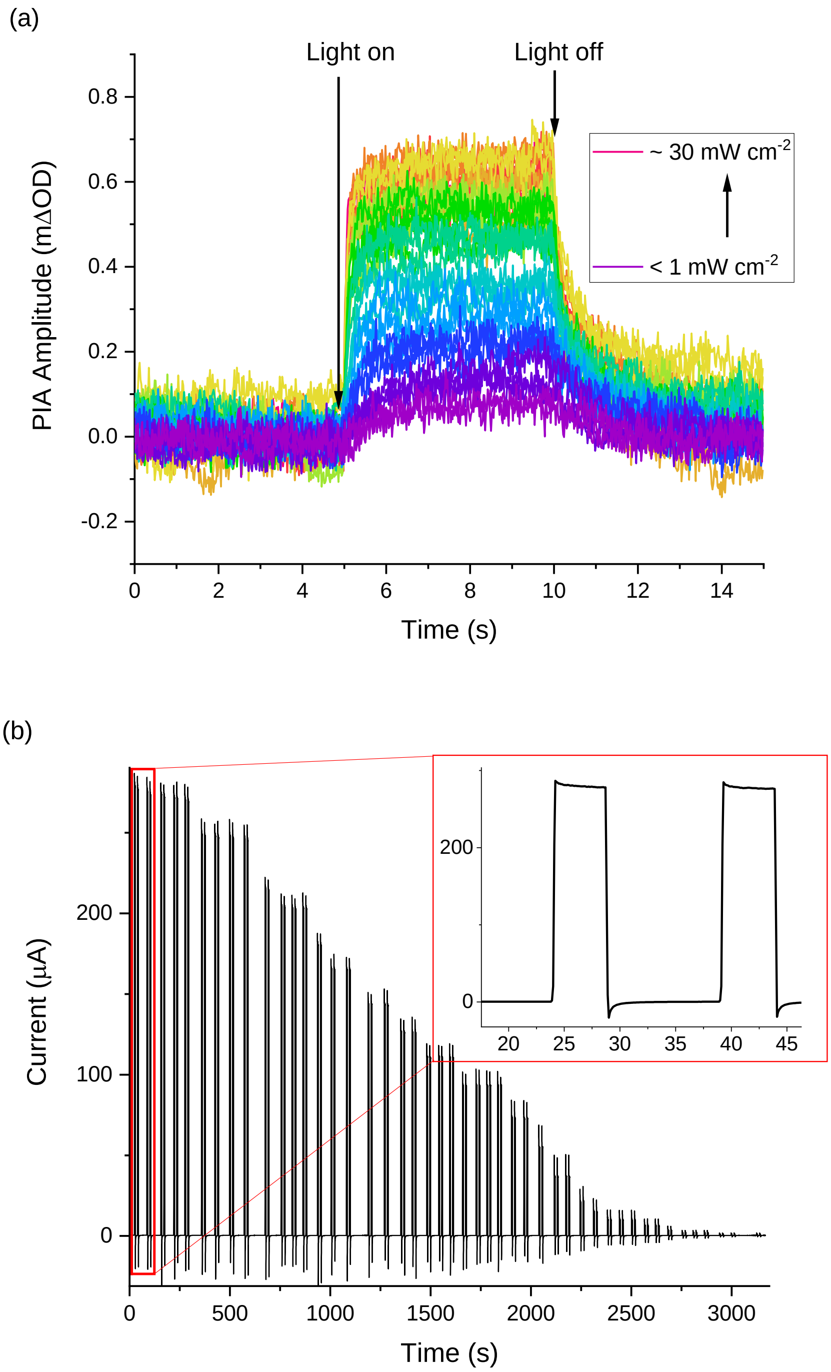

Figure 71: PIA amplitude probed at 625 nm (a) and simultaneous photocurrent measurements (b) for an ED-Fe_2O_3 film in 1 M NaOH held at 0.2 V vs Ag/Ag^+. The 365 nm LED pump intensity was varied between ~0.1 & 30 mW cm^{-2}.

Under these CW illumination conditions a plateau in the PIA amplitude over time is quickly reached. This plateau region indicates that the flux of holes and electrons has reached a steady state and that the concentration of holes at the surface ($[h^+]_s$) is not experiencing any net change.

$$\frac{d[h^+]_s}{dt} = 0 \qquad \text{Eq. 4.4.}$$

Since the photocurrent also reaches a plateau in this region, it can be stated that the flux of holes to the surface (J_{h+}) is equal to rate of water oxidation by surface holes (Figure 72), where k_{wo} is the rate constant for water oxidation and α is the reaction order with respect to surface holes:

$$\frac{d[h^+]_s}{dt} = J_{h^+} - k_{wo} \times [h^+]_s^{\alpha} \qquad \text{Eq. 4.5.}$$

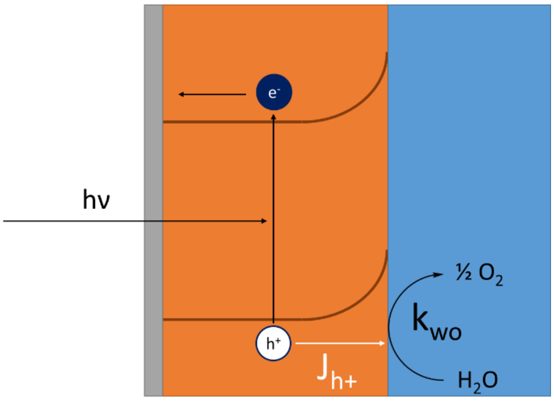

Figure 72: Schematic of the SCLJ showing the relevant kinetic terms, where the grey layer is the back FTO contact, the orange layer is the hematite electrode and the blue layer is the electrolyte. J_{h+} represents flux of holes to the surface and k_{wo} represents the rate constant for the water oxidation reaction.

The relationship between average PIA amplitude and photocurrent during this plateau region over the different light intensities studied is displayed below in Figure 73. The photocurrent shows the expected linear light intensity dependence, but the PIA amplitude has a clear non-linear dependence on light intensity, reaching a plateau at the highest light intensities studied. It appears that within this high light intensity region the surface is becoming saturated with holes and the increase in the photocurrent in this region and beyond is no longer limited by surface hole concentration.

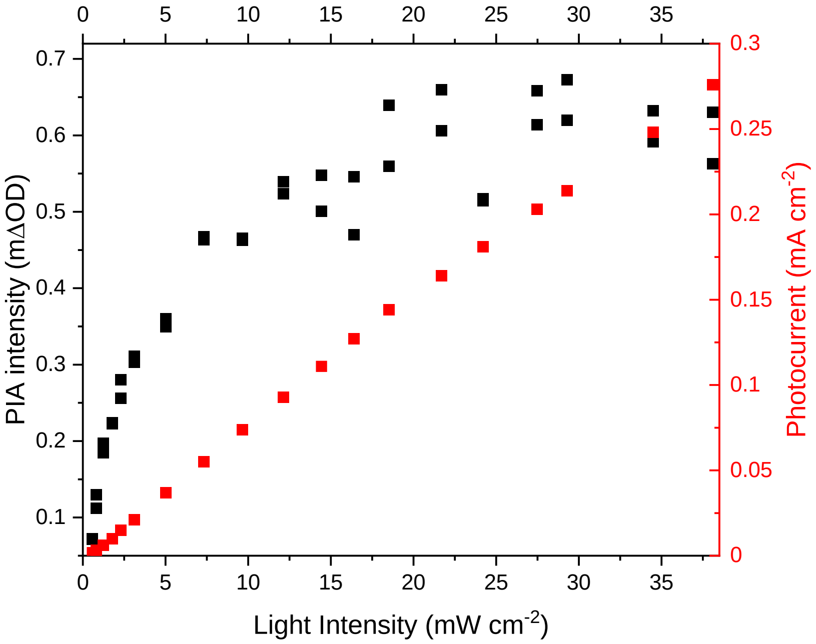

Figure 73: Averaged steady state PIA amplitude probed at 625 nm (black) and simultaneous photocurrent (red) during 365 nm LED illumination at the stated light intensities. ED-Fe_2O_3 electrode in 1 M NaOH held at 0.2 V vs Ag/Ag^+ (prior to the dark OER onset).

Building on the previous kinetic model,[6] the reaction order with respect to surface hole concentration can be calculated by combining and linearising Eq. 4.4. & 4.5.

$$J_{holes} - k_{wo} \times [h^+]_s{}^{\alpha} = 0 \qquad \text{Eq. 4.6.}$$

$$J_{holes} = k_{wo} \times [h^+]_s{}^{\alpha} \qquad \text{Eq. 4.7.}$$

$$log_{10}(J_{holes}) = log_{10}(k_{wo}) + \alpha \times log_{10}[h^+]_s \qquad \text{Eq. 4.8.}$$

According to Eq. 4.8., a log-log plot of flux of holes to the surface (equivalent to the steady-state photocurrent density) against surface hole concentration (proportional to the PIA amplitude) would give the reaction order with respect to surface holes as the gradient. The exact value of the reaction order from this kind of analysis relies on converting the PIA amplitude value into a concentration of surface holes (per unit area), necessitating accurate determination of both the extinction coefficient for the surface hole species at 625 nm and the surface roughness of the electrode. Le Formal *et al.*

identified methods for estimating both of these values,[6] firstly, by using transient photocurrent spikes to estimate the extinction coefficient for the holes and secondly using dye-adsorption experiments to measure the surface roughness. I have previously examined both of these methods for hematite electrodes during an undergraduate research project but obtained implausibly high values for surface hole densities (more details can be found in Appendix C). Based on the inaccuracy of these methods in previous experiences they were not used for the electrodes used in this Chapter.

The main aim of these initial experiments is to identify if there is a transition in reaction order at the different light intensities studied. Analysing the relationship between the observed gradients of the log-log plots of PIA amplitude vs. photocurrent at low and high light intensities is a simpler way of addressing this change in mechanism, without requiring the more complex (and often inaccurate) experiments for measuring the extinction coefficient and accurate surface area. It is clear from Figure 74 that there is an increase in gradient at high light intensities, indicating a change in α and supporting the hypothesised transition in mechanism at the higher light intensities. The ratio between the gradients of the red and blue regions indicates an approximately 2.4 times relative change in α at higher light intensities. Without an absolute value for α it is difficult to directly compare to previous literature, but this relative change is close to the reported values, especially when taking into account that there will likely be a small transition region in the plot at moderate light intensities. Regardless, this at least confirms that these electrodeposited hematite films show a similar light intensity-dependence observed on other hematite films in the literature.[6] This allows further analysis to be carried out on the origin of this proposed transition in reaction mechanism between these two regions using EFISHG.

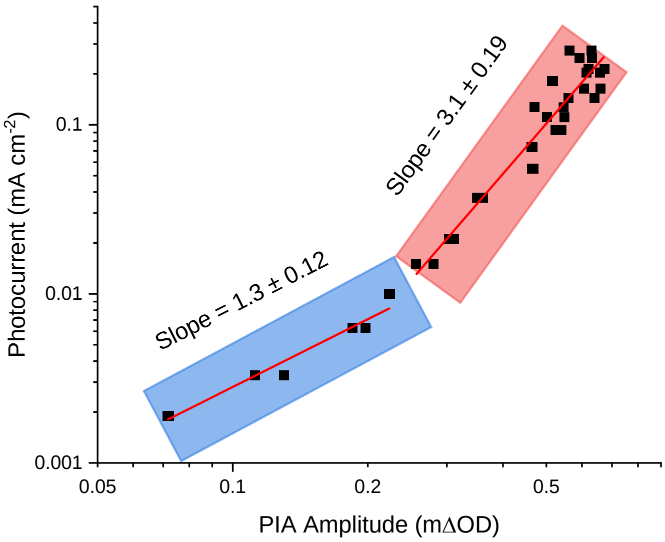

Figure 74: Log-log plot of photocurrent vs PIA amplitude probed at 625 nm for an ED-Fe_2O_3 sample in 1 M NaOH under illumination from a 365 nm LED, held at 0.2 V vs Ag/Ag^+. The two shaded areas represent a transition in reaction order from low light intensities (blue) to high light intensities (red).

Before the EFISHG experiments, these PIA experiments were then repeated on the same type of electrodeposited hematite electrodes but at the conditions that will be used in the forthcoming EFISHG experiments. One key parameter that can be used to address the nature of interfacial electric fields, especially the potential drop across electrolyte, is the ionic strength of the solution. At higher electrolyte concentrations, the charge from the electrode surface is screened by oppositely charged counter ions in solution, effectively shrinking the Debye length, which in turn would be expected to alter the χ^3 term's contribution to the observed signal. The first alteration in experimental conditions was to change electrolyte from 1 M NaOH to 0.1 M NaOH, which will allow a wider range of ionic strengths to be studied. Furthermore, the CW illumination has so far been provided by a 365 nm LED with a spectrally broad profile with a tail to longer wavelengths (Figure 75), which may lead to residual pump light reaching the detector in the SHG experiment. The detector in this system is incredibly sensitive in order to be able to detect the weak SFG/SHG signals, so even a small number of stray photons from the pump LED could overwhelm the partially overlapping SHG signal. It is therefore pertinent to understand if the same processes can occur using dark electrochemical methods, in case the presence of a pump LED would limit the detection of an SHG signal.

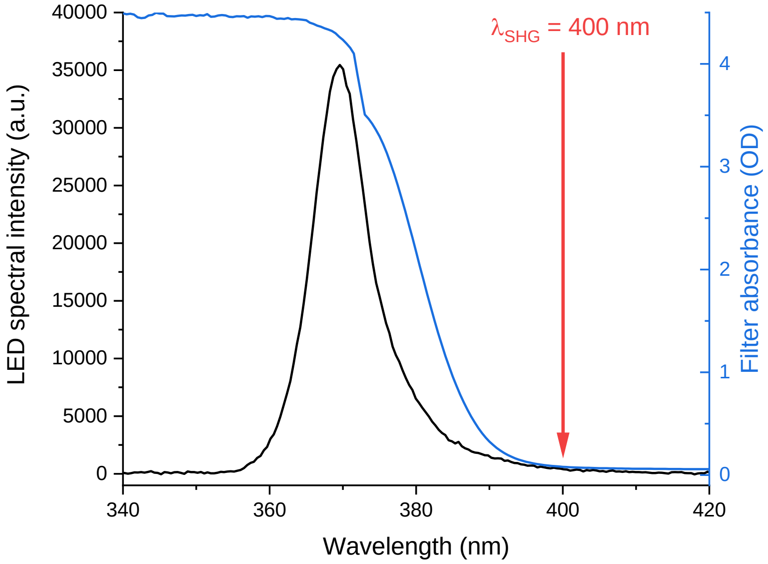

Figure 75: Comparison of spectral intensity profile of the 365 nm LED used to pump the PIA experiments against the absorbance of the chosen long pass filter. The profile of the LED has a non-zero value at 400 nm, which could complicate analysis of SHG photoelectrochemical SHG experiments, especially as the chosen LP filter must be mostly transmissive at 400 nm to allow the SHG light through.

The kinetics of the surface hole signal at 625 nm was investigated using a change in applied voltage to see if the same apparent change in mechanism can be observed based solely on a dark current. The experiment is analogous to the PIA experiment, but instead of toggling a CW light source on and off, the applied bias is stepped between two potentials, always starting from the same bias voltage as the PIA experiments and stepping to more positive potentials. To distinguish the two versions of the technique, the dark electrochemical version will be referred to as voltage-induced absorption (VIA) spectroscopy. The range of potential steps were chosen to cover the same range of currents obtained from the previous PIA experiments.

The results of PIA & VIA analysis for the same film (that was later used for the EFISHG analysis) are shown in Figure 76. These experiments were carried out at a lower electrolyte concentration (0.1 M

NaOH) to enable comparison to the wider range of ionic strengths that will be studied by EFISHG. Both the conventional front-illumination PIA response and the VIA response show a change in gradient (proportional to reaction order) at higher current densities, but the all the values are shifted to higher PIA amplitudes. This is likely due to recombination losses in back illumination PIA and VIA as the holes generated near the back contact of the electrode need to be transported through the bulk to the surface. Thus, a higher hole concentration (represented by a larger PIA amplitude) is required to achieve the same photocurrent density to account for recombination between the back and front of the electrode. The major observation from these results, however, is that a change in gradient at the higher current densities is still observed in all cases, making this type of electrode suitable for further study using EFISHG. It is difficult to precisely define when this transition in reaction order occurs as there is not a sudden step-change in gradient. Though in both back illumination PIA and VIA, the switch in reaction order occurs at current densities between 0.001 and 0.01 mA cm^{-2}.

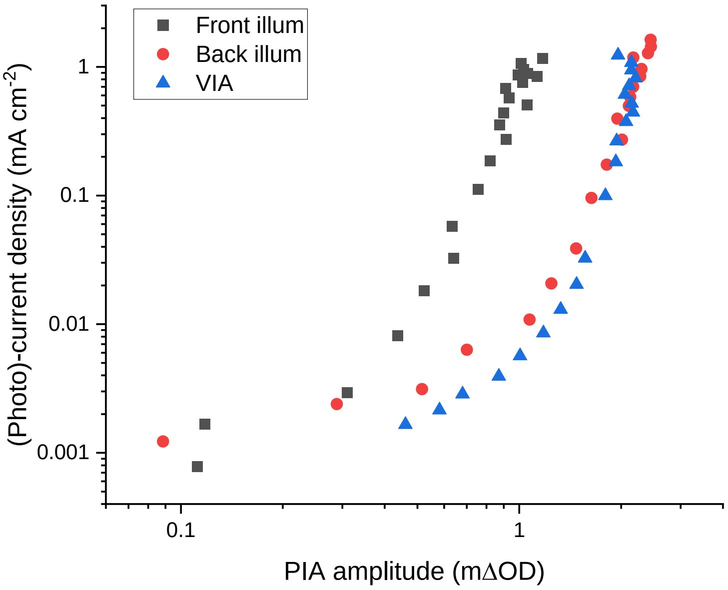

Figure 76: Log-log plot of (photo)-current vs PIA amplitude probed at 625 nm for an ED-Fe$_2$O$_3$ sample in 0.1 M NaOH under illumination from a 365 nm LED, held at 0.2 V vs Ag/Ag$^+$(black and red) and the analogous VIA response (blue) where the applied potential was stepped from 0.2 V vs Ag/Ag$^+$.

4.2.2. Electric Field Induced Second Harmonic Generation:

Second harmonic generation spectroscopy (SHG) is the degenerate case of SFG spectroscopy, where the frequency of both incoming photons is the same (*i.e.* $\omega_1 = \omega_2$) and the SHG photon is at double this frequency ($\omega_{SHG} = 2\omega_1$). Since SHG is still a second order nonlinear optical process, the same arguments for surface specificity from SFG spectroscopy still remain. The major difference is that the (usually) visible laser wavelengths are no longer resonant with molecular vibrations, so the resulting SHG spectra can be thought of as analogous to the nonresonant component of the SFG spectra, without complicated interference from the resonant vibrational modes. The interaction of the additional E_{DC} field (from the charged electrode interface) with the third order nonlinear susceptibility is also still present, so the SHG signal is also sensitive to the electric field at the interface being probed. This results in electric field-induced second harmonic generation (EFISHG), which, under the right conditions, can be used to quantify electric fields at charged interfaces.[10] On a simpler level, the information gained from EFISHG spectra collected during our electrochemical measurements could qualitatively report on changes in the interfacial electric fields in our photoelectrochemical systems.

Unlike in metal electrodes, the semiconductor-electrolyte interface has fields emanating in both directions normal to the interface. This is a consequence of the semiconductor liquid junction discussed in briefly in Chapter 1, where it was shown that in the case of an n-type semiconductor a uniform positive space charge layer is formed in the semiconductor, known as a depletion layer. This positive charge is balanced by a layer of negatively charged ions in the electrolyte, the resulting potential distribution is shown in Figure 77. Thus, for these electrodes there are three electric fields emanating from the interface of interest, the internal space charge field (E_{SC}) within the bulk electrode material across the depletion layer, the Helmholtz potential (E_H) extending into the electrolyte over the Stern layer and the Gouy Chapman potential (E_{GC}) over the diffuse layer further from the electrode.

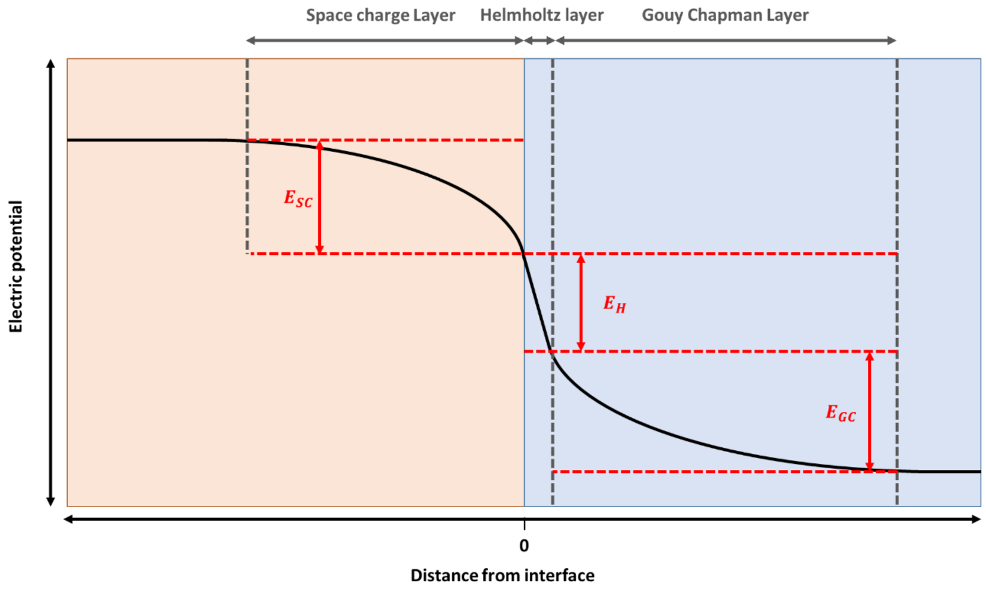

Figure 77: Potential distribution in a typical semiconductor electrolyte junction. Note the distances and relative sizes of potential drop are not to scale as they can vary significantly between different materials and electrolyte compositions.

One of the key characteristics of the interfacial electric field is the width of the space charge layer (W_{sc}), which heavily depends on the dopant concentration within the semiconductor, with typical values being on the order of tens of nanometres. Conversely, the charge in the electrolyte is localised over a much smaller width, ranging from 0.1 to 1 nm, depending on the adsorption, hydration and size of the ions in solution. In a typical semiconductor, with a large W_{SC} and a high electrolyte concentration (> 0.1 M) most of the potential drop takes place over the space charge layer. However, high dopant concentrations can significantly decrease W_{SC}, with extreme cases for hematite going as low as W_{SC} = 1 nm when the dopant density reaches around 1 x 10^{21} cm^{-3}.[11] While the dopant density was not explicitly calculated for the films studied in this project, they were synthesised following a procedure established in literature which produced films with a relatively high dopant density of 7.35 x 10^{20},[12] giving W_{SC} = 1 to 2 nm according to Figure 78. Under such conditions, a significant proportion of the potential drop can occur over the Helmholtz layer within the electrolyte as W_{SC} becomes comparable to width of the Stern layer.[11] Both field directions will likely contribute to the EFISHG signal, though much of the literature on EFISHG thus far has been carried out on metal electrodes, where there would not be any contribution from E_{SC}. It is unclear which of these fields will dominate in the EFISHG spectrum in our system. Since the dopant density for a specific semiconductor sample is constant, E_{SC} would be constant at a fixed potential. By changing the salt concentration and hence E_{GC} these different contributions can be differentiated at fixed potentials. Thus, carrying out the same experiments at different salt concentrations can be used to investigate whether the EFISHG signal in our experiments contains any significant contributions from E_{GC}.

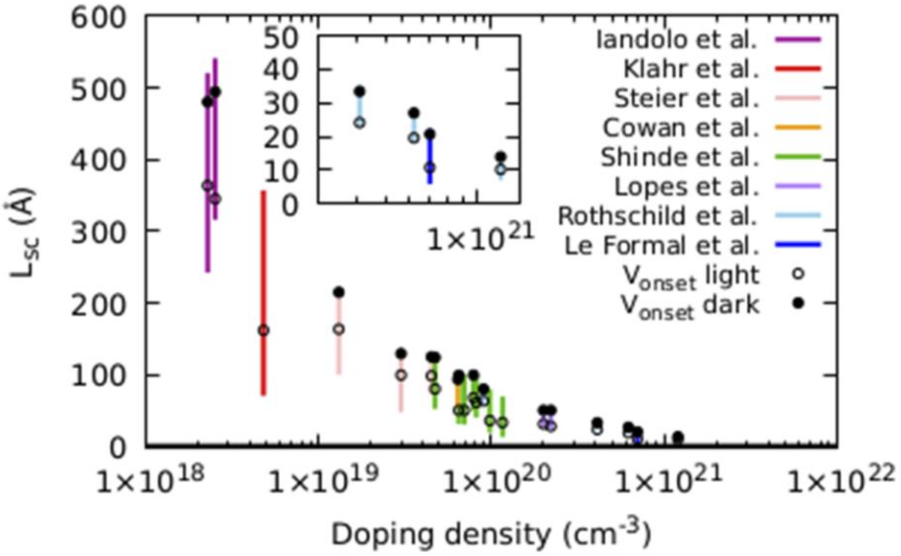

Figure 78: Calculated space charge layer thickness (LSC) as a function of doping density for various hematite electrode reported in the literature, reproduced with permission from Delcompare-Rodriguez et al.[11] White and dark spots represent 1 sun illumination and dark conditions, respectively.

One major advantage of using SHG to probe this electric field at the electrode/electrolyte interface is that only a single, visible, wavelength needs to be used. By removing the infrared wavelength, the input radiation is no longer attenuated by the water in the electrolyte allowing a more conventional, through-electrolyte, geometry to be used. Furthermore, careful selection of the wavelength of the input radiation can allow only the interface of interest to be probed. With a sufficiently thick layer of hematite as the active electrode material, the electrode itself can act as an optical filter for the (unwanted) underlying interfaces (hematite/FTO and FTO/glass), as seen in Figure 79. An incident wavelength of 800 nm was selected for these experiments as it would produce SHG light at 400 nm, which is almost completely absorbed by the hematite layer in these electrodes. A combination of less 800 nm light reaching the back interfaces, and then subsequent absorption of the resulting small amount of reflected SHG light would mean that any SHG signal observed would come selectively from the interface of interest (hematite/electrolyte).

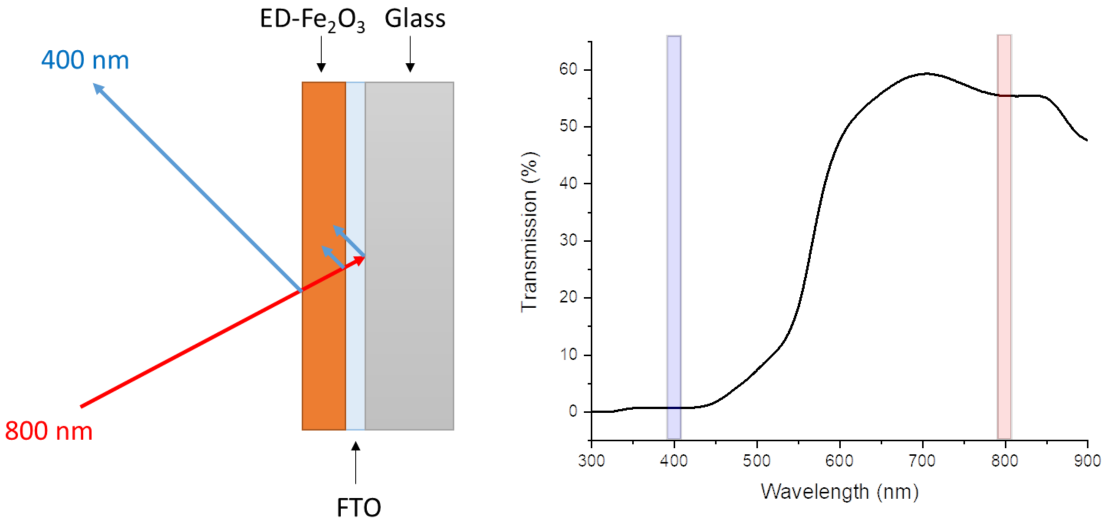

Figure 79: Experimental geometry for reflection SHG experiments (left), highlighting the absorption of SHG photons from the buried interfaces by the layer of hematite on commercial FTO coated glass. UV-Vis in transmission of the ED-Fe_2O_3 electrode used for SHG experiments (right), with highlights for the input radiation (800 nm, red rectangle) and the SHG (400 nm, blue rectangle) wavelengths. Note that the high annealing temperature had caused the underlying glass structure of the electrode to lose some transparency across the spectrum due to scattering. The data here is shown as a % transmission relative to air as no suitable background sample (e.g. bare FTO or annealed bare FTO) could be used due to this scattering.

The general experimental setup for the SHG experiments involved some minor alterations to the existing SFG setup, displayed in Figure 80. The 800 nm output from an Orpheus (Light Conversion) OPA in the neighbouring ultrafast transient absorption spectrometer was re-routed to the SFG/SHG sample area. One key point is that the half-waveplate (λ/2) used to control the polarisation of the 800 nm beam was made of crystalline quartz, which is does not contain a centre of symmetry within its crystal structure. This means it also produced a substantial background SHG signal at 400 nm from SHG the quartz. This was filtered out before the sample using a 450 nm long-pass filter (Thorlabs FEL450). Furthermore, the bare gold mirrors in the setup after the sample were replaced with UV-enhanced aluminium mirrors to improve transmission at shorter wavelengths for the SHG signal. A series of 550 nm short-pass filters (Thorlabs FESH550) were placed before the spectrograph to remove all residual 800 nm light, while allowing the SHG signal at 400 nm to pass through. The final change to the setup was replacing the spectrograph grating from one blazed at 800 nm to one blazed at 350 nm, improving the collection efficiency at the shorter SHG wavelength.

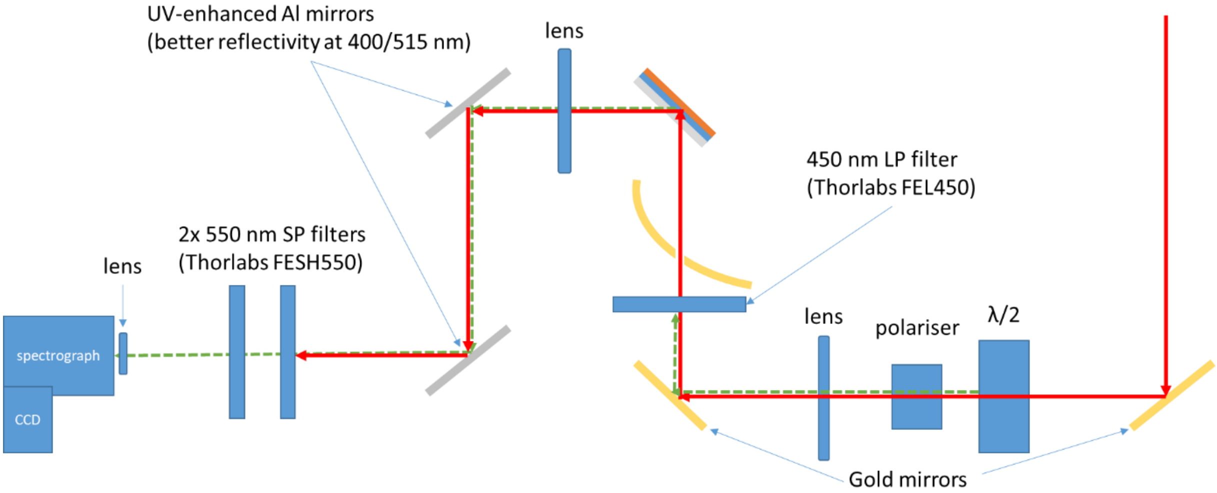

Figure 80: Diagram displaying the key modifications made to the SFG setup to allow SHG experiments to take place. Red lines indicate 800 nm beam path, while green lines show SHG light at 400 nm.

The same type of electrodeposited hematite electrodes used in the above PIA studies were then examined by *in situ* electrochemical SHG spectroscopy. Experiments were initially carried out in the dark during relatively slow CV cycles (2 mV s^{-1}) on both ED-Fe_2O_3 electrodes and bare FTO electrode, showing a clear difference in both signal size and shape of potential-dependent response in Figure 81. The ED-Fe_2O_3 surface shows a much larger SHG response as well as a larger current and does not respond linearly with applied potential. As discussed in Chapter 3, the shape of this response (linear or parabolic) on a conventional metal electrode depends on the relative contributions of the second and third order nonlinear susceptibilities.

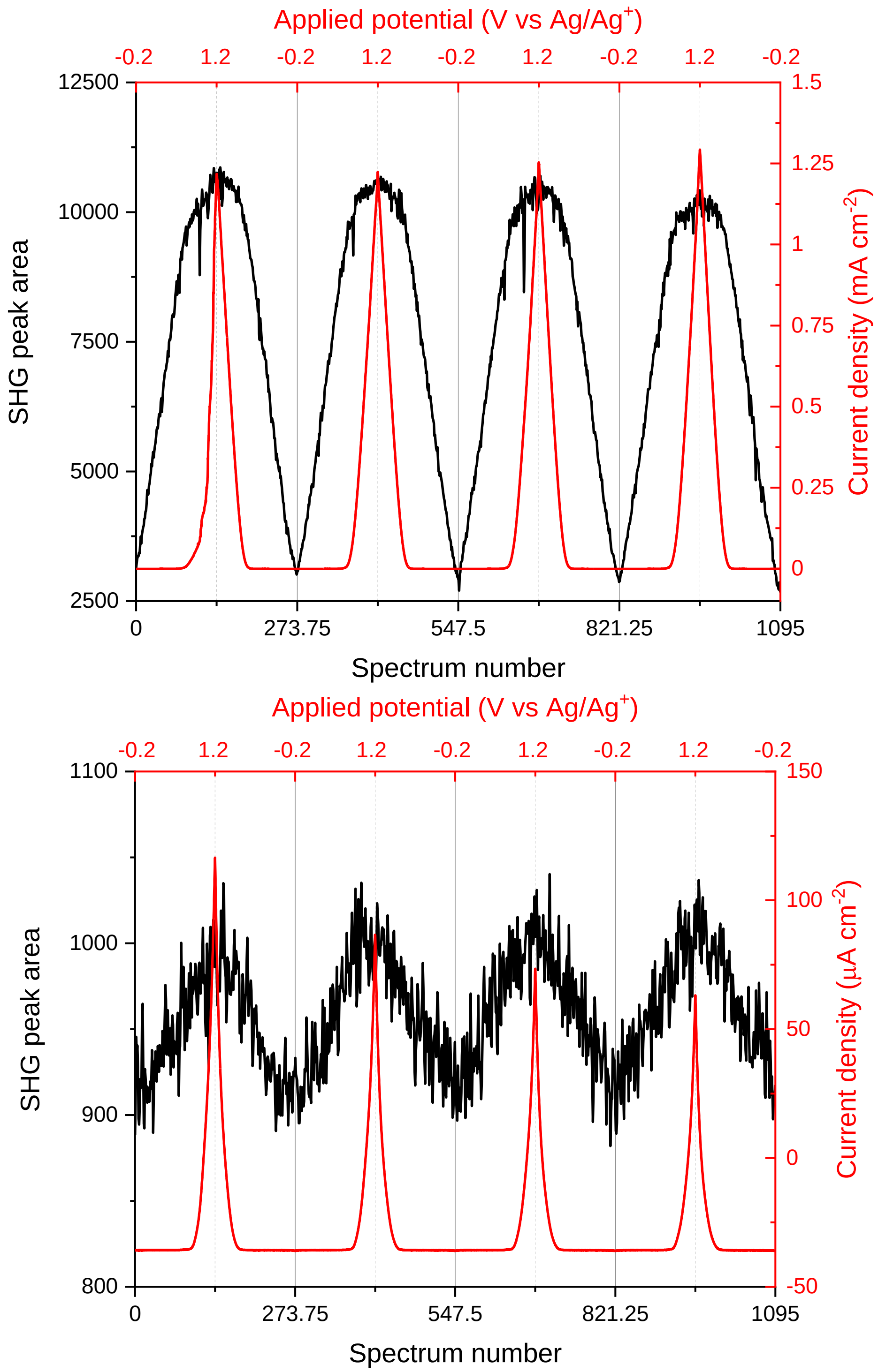

Figure 81: Integrated SHG peak area (λ_{SHG} = 400 nm, based on incident light at 800 nm at 25 mW) on ED-Fe2O3 (top) and FTO (bottom) electrodes over 4 CV cycles at 2 mV s^{-1} in 0.1 M NaOH. Simultaneous current response shown in red.

As in the case of the SFG response of an electrochemical interface at metal electrodes,[13] the SHG polarisation ($P_{2\omega}$) can be summarised as:

$$P_{2\omega} \propto \chi^{(2)}(E_\omega)(E_\omega) + \chi^{(3)}(E_\omega)(E_\omega)(E_{DC}) \qquad \text{Eq. 4.9.}$$

Building on Eq. 4.6., the intensity of the SHG signal is proportional to the square of the nonlinear susceptibilities:

$$I_{2\omega} \propto \left|\chi^{(2)}(E_\omega)(E_\omega) + \chi^{(3)}(E_\omega)(E_\omega)(E_{DC})\right|^2 \qquad \text{Eq. 4.10.}$$

Which can be expanded to give:

$$I_{2\omega} \propto \left|\chi^{(2)}(E_\omega)(E_\omega)\right|^2 + 2\left(\chi^{(3)}(E_\omega)(E_\omega)(E_{DC})\right)\left(\chi^{(2)}(E_\omega)(E_\omega)\right) + \left|\chi^{(3)}(E_\omega)(E_\omega)(E_{DC})\right|^2 \qquad \text{Eq. 4.11.}$$

In an electrochemical SHG experiment, only the E_{DC} term is varied, so only the last two terms in Eq. 4.11. will contribute to the changing signal. When a system is dominated by the interfacial $\chi^{(2)}$ term (orange in Eq. 4.11.) a linear dependence on E_{DC} would be expected (under the assumption that $\chi^{(2)}$ >> $\chi^{(3)}$ so the orange term is dominating the signal). Conversely, a system dominated by the $\chi^{(3)}$ (blue in Eq. 4.11.) term, would change proportional to ${E_{DC}}^2$, so would show a quadratic potential dependence. At a glance, the shape in of the hematite response appears quadratic, while the FTO electrode appears to show a linear response. However, when attempting to fit the hematite data to a quadratic response some clear deviations from a parabolic curve can be seen in Figure 82. The electrochemical response from the first CV cycle (Figure 82a) contains some additional features on the outwards sweep, which could be due to oxidation of surface contaminants. For this reason, the data is plotted separately to the average of the other three cycles, which are shown in Figure 82b. In both cases, the residuals from the quadratic fits indicate that deviations from the ideal quadratic potential-dependent behaviour occur close to the onset of OER. The PIA/VIA analysis above determined that an apparent change in mechanism occurs at current densities between 0.01 and 0.1 mA cm^{-2} in both light-induced and potential-induced measurements. In agreement with previous literature,[6] these two current regimes represent a change in reaction order with respect to surface holes going from first to third order (as shown in Figure 76). These two different regions are highlighted in Figure 82b, almost completely coinciding with a change in sign of the residuals of the quadratic fit. Analysis of these residuals highlights that the model based on Eq. 4.11. may not be sufficient to describe semiconductor electrodes. The remainder of this chapter will explore a more detailed method of analysis that incorporates the additional interfacial fields in semiconductor electrodes.

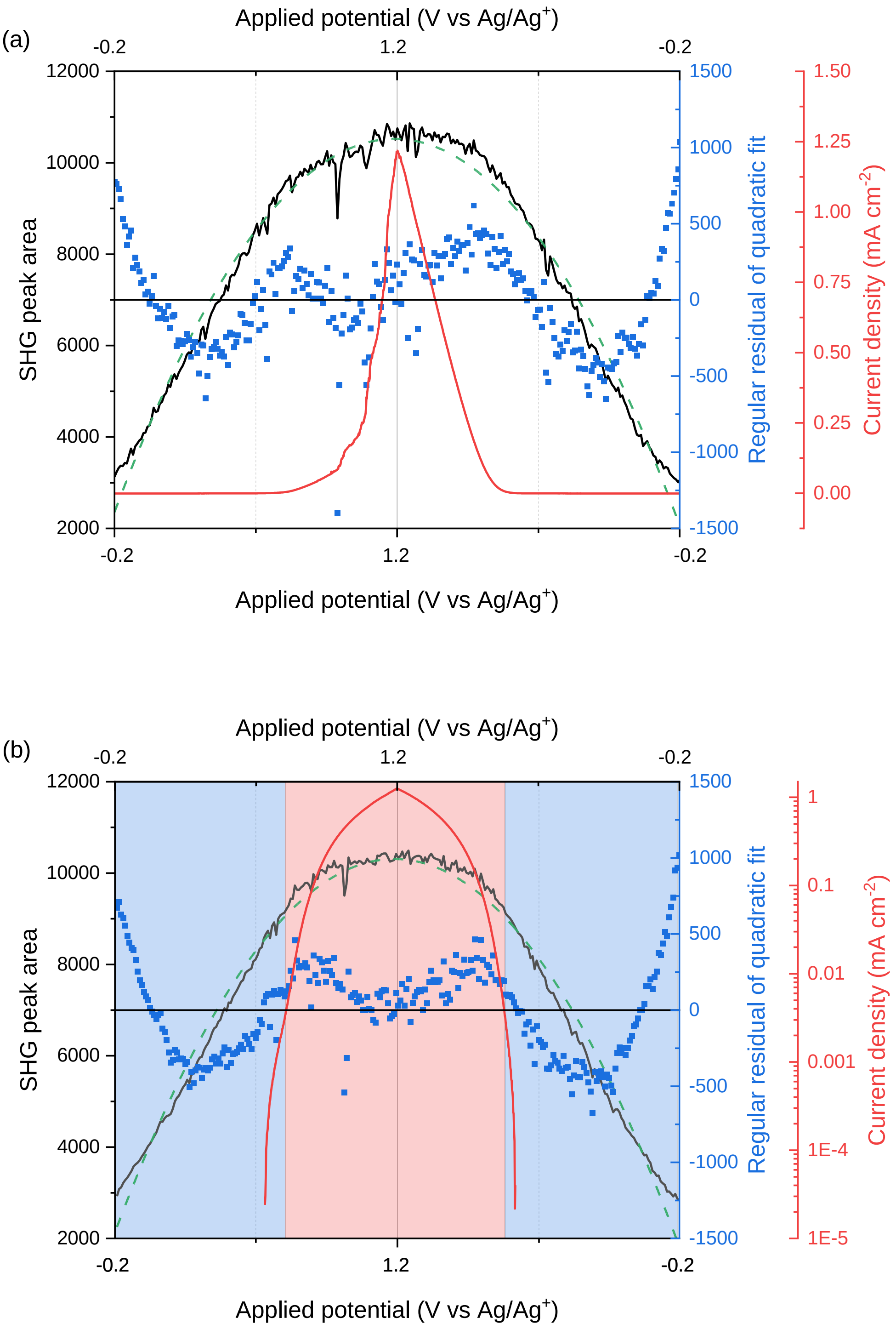

Figure 82: Potential-dependent SHG response from the (a) the first CV cycle and (b) the average of the remaining three CV cycles of an ED-Fe$_2$O$_3$/FTO electrode in 0.1 M NaOH from Figure 81. The black curves show potential-dependence of the SHG peak area, with the dotted green line representing a 2nd order polynomial fit. The blue line (and blue y-axis) shows the residuals of this fit and the simultaneous current is plotted in red (with the red y-axis). Note the current in (b) is shown on a logarithmic scale to enable comparison to the PIA results presented above. From this comparison, the blue shaded regions represent the first order regime and the red shaded regions represent the third order regime.

To build on the existing model for EFISHG, the disparate nature of surface fields in semiconductors compared to metals needs to be addressed. Firstly, the overall interfacial field (E_{DC}) can be considered the sum of the constituent interfacial fields:

$$E_{DC} = E_{SC} + E_H + E_{GC} \qquad \textit{Eq. 4.12.}$$

It is worth noting that these electric fields are vector quantities oriented in a surface normal direction. The direction relative to the position of the electrode/electrolyte interface (*i.e.* into the semiconductor *vs.* into the electrolyte) will need to be accounted for in their sign.

Neglecting the possible potential dependence of the nonlinear susceptibilities (χ^2 and χ^3) for now, the main contribution to the changing SHG signal during an electrochemical experiment will be E_{DC}, which is varied continuously during a CV experiment. However, all three of the fields contributing to E_{DC} are also sensitive to the operating conditions of the photoelectrochemical cell. For example, the E_{GC} term can be neglected at high electrolyte concentrations as the length of the diffuse layer becomes negligible due to screening of surface charges by ions in solution. Additionally, drastic changes in both E_{SC} & E_H can occur under Fermi-level-pinning conditions, where occupied surface states close to the band edge are emptied as the potential is scanned.[14] In this regime, there is no further potential drop across the space charge layer ($\Delta E_{SC} = 0$) while these states are being emptied and the overall potential drop occurs solely over the electrolyte.

Considering these last points, the presence of trapped charges at the semiconductor surface could have a significant impact on both E_{SC} & E_H, which can be addressed by these electrochemical EFISHG experiments. Hamann *et al.* have previously shown that the relative energy levels of surface trap states in hematite electrodes can be measured using dark electrochemical measurements.[2] Here, a substantial population of trapped holes is generated by holding the electrode at a positive potential under illumination for one minute. The potential is then rapidly scanned cathodically in the dark (at 200 mV s^{-1}), depopulating the trap states, which can be seen as negative peaks in Figure 83. The presence of the two different reduction peaks (labelled A & B) indicates the existence of two different types of surface trap populations. Energetically, population A is reduced close to the onset of the water oxidation current and a similar feature has previously been assigned to trapped surface holes by dark CV measurements,[2] electrochemical impedance spectroscopy[15] and operando x-ray absorption spectroscopy.[16] This trap state has been proposed to be an intermediate involved in the OER. Hamann *et al.* also observed an additional reduction at potentials cathodic of the onset of water oxidation, which they assigned to a deeper-lying trap state that is not involved in the water oxidation reaction. The further reduction, labelled B, matches this description and is thus assigned to a deep-lying trap state population that does not participate in the OER.

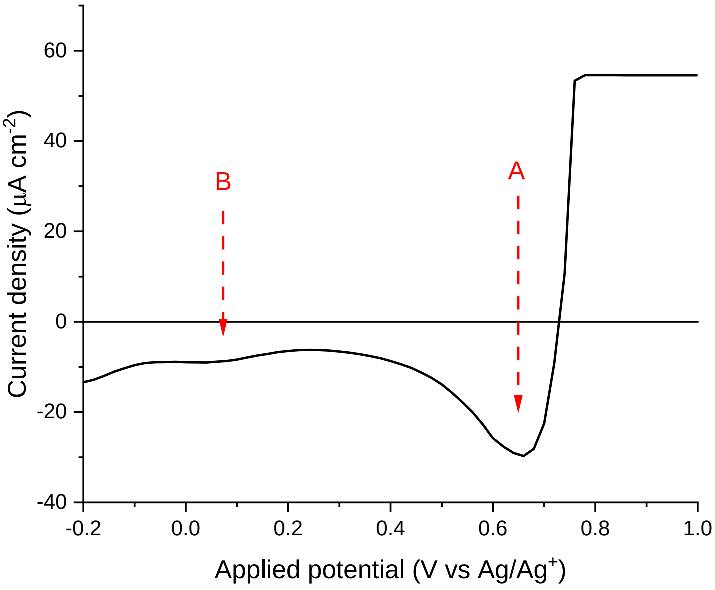

Figure 83: Fast (200 mV s^{-1}) reverse LSV of an ED-Fe_2O_3 electrode in 0.1 M NaOH from 1.2 V to -0.2 V vs Ag/Ag$^+$ after holding at 1.2 V for 1 minute under ~30 mW cm^{-2} 365 nm LED illumination to build up a large population of trapped holes. Note that the analogue potentiostat used for these measurements was manually set to a lower current range to distinguish the small reduction peaks. Current values above ~ 50 µA were too large for this range, hence the plateau in current at the most positive potentials.

Changes in any one of the fields contributing to E_{DC} could lead to deviations in the gradient of the potential dependent SHG response. The first derivative of the SHG peak area during an electrochemical experiment allows visualisation of any such changes in gradient. Taking the two extremes discussed previously from Eq. 4.11., a $\chi^{(2)}$ dominated response (which gave a linear potential-dependent SHG response) would show a flat line when plotting the gradient against potential, while a $\chi^{(3)}$ dominated response (quadratic potential dependent SHG signal) would give a line with a non-zero slope when plotting the gradient against the potential. This is perhaps best visualised using the basic linear and parabolic functions and their first derivatives in Figure 84. Deviations from these ideal responses could be indicators in local changes in field.

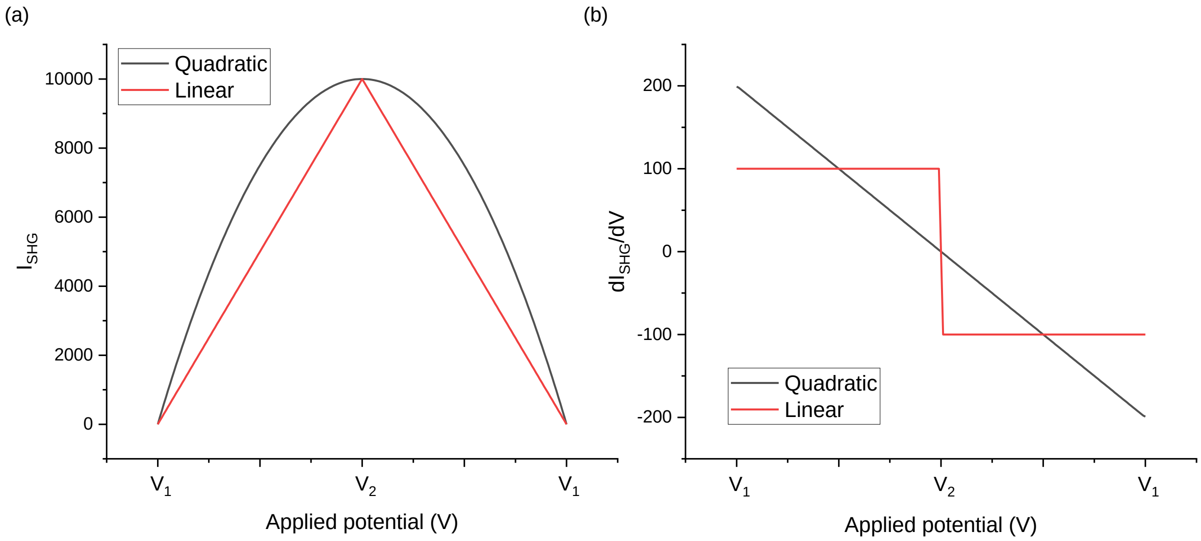

Figure 84: Basic linear and quadratic functions (a) and their first derivatives (b). To be used as a comparison for the potential-dependent SHG response on electrochemical systems, which ideally respond either linearly (dominated by $\chi^{(2)}$, red lines) or quadratically (dominated by $\chi^{(3)}$) with applied potential.

This type of gradient analysis was applied to the electrochemical SHG data from an ED-Fe_2O_3 electrode (data from Figure 81) and is plotted in Figure 85. The analysis procedure here involves taking the intensity of the SHG signal from the area of the peak at 400 nm and differentiating with respect to potential. There appears to be a remarkable correlation between the changes in SHG gradient and the reduction/oxidation of the trap states shown in Figure 83. Initially during the forwards sweep (Figure 85a) the gradient is increasing slightly between -0.2 and 0.6 V vs Ag/Ag$^+$, indicative of a quadratic dependence of the SHG intensity with E_{DC} during this region. Around 0.6 V vs Ag/Ag$^+$ there is a sudden decrease in the gradient, which coincides with onset of a dark OER current. It is around these potential (just before the OER onset) that the surface hole trap state labelled A will also start to become populated. Populating these hole states, which can also be thought of as emptying the electrons from a filled state at the surface, could explain the sudden decrease in gradient after 0.6 V vs Ag/Ag$^+$. Prior to this potential, most of the potential drop occurs over the space charge layer as the potential is swept anodically. However, as the potential is scanned over this surface state, the system can enter a Fermi level pinning regime (Figure 86), where no further drop in E_{SC} can occur until the surface state is empty of electrons (*i.e.* full of holes). Thus, instead of the EFISHG gradient continuing to increase, there is a sudden decrease as the potential drop in this regime is instead occurring over the Helmholtz layer, which has an electric field pointing in the opposite direction to the space charge field. The SHG gradient stops decreasing significantly above 0.9 V vs Ag/Ag$^+$, where these surface states are now fully empty of electrons and the potential drop continues to occur in the space charge layer. The reverse sweep data in Figure 85b shows a change in gradient that coincides with the reduction of trap state A, which can be thought of as the reverse of the process described above. State A has previously been suggested to be a surface hole trap state that is an intermediate in the OER, which would fit with the model outlined above as a substantial current is only drawn after the state A is populated, indicated by the end of the Fermi level pinning.

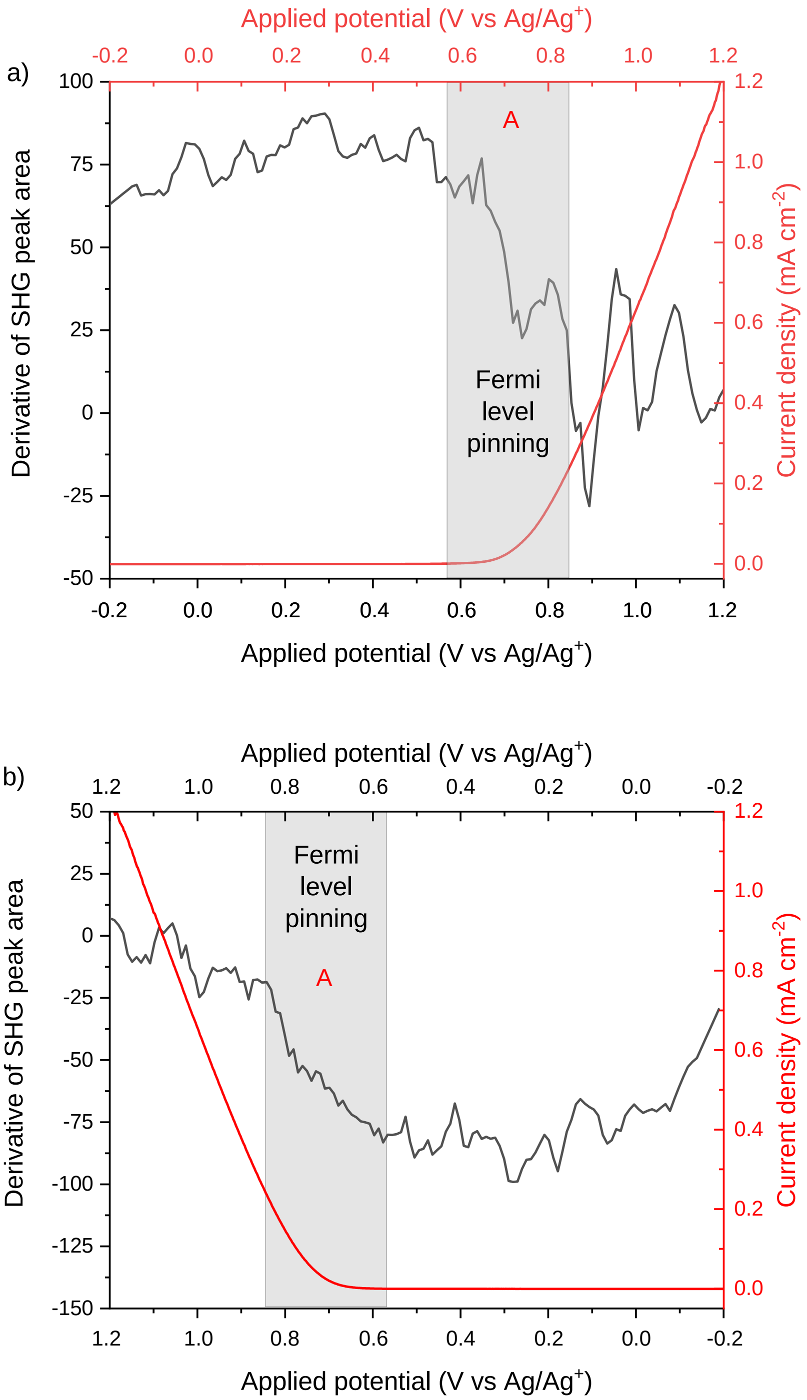

Figure 85: First derivative of the SHG peak area with respect to applied potential for the forward (a) and reverse (b) sweeps in the data from Figure 81. The simultaneous electrochemical response is shown in (a) to illustrate the onset of the dark water oxidation current. The positions of the reduction peaks assigned to different types of trapped holes are highlighted in (b).

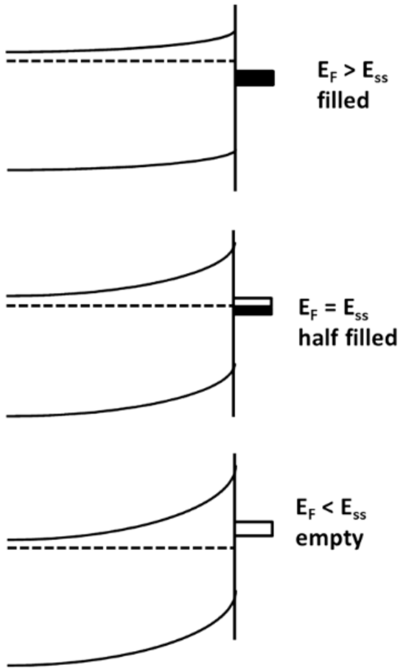

Figure 86: Diagram depicting Fermi-level pinning in an n-type semiconductor as an increasingly positive bias is applied from top to bottom, reproduced with permission from ref [17]*. A positive applied bias has the effect of lowering the Fermi level (E_F). Initially, E_F is above a surface state filled with electrons. As the positive bias is applied, the potential drop occurs over the space charge layer, leading to increased band bending. However, as E_F approaches the energy level of the surface states (E_{SS}), a more positive bias has the effect of emptying the surface states, so the potential drop no longer occurs over the space charge layer, so no band bending can occur until the surface state is empty. Once the surface state is empty a positive bias continues to induce further band bending.*

To further address the origin of these deviations from ideal potential dependence, experiments with a known hole scavenger, H_2O_2, were carried out. Here it is hypothesised that any trapped holes at the surface will readily oxidise H_2O_2, so the accumulation of holes at the surface will no longer occur. Figure 87 shows that in the presence of H_2O_2 there is a clear shift in the onset of a catalytic current to earlier potentials and that there is a non-zero current even at the earliest potentials explored here. The SHG gradient in the presence of H_2O_2 (blue in Figure 87a) starts decreasing earlier (at ~ 0.3 V vs Ag/Ag$^+$) than the control experiment (at ~ 0.6 V vs Ag/Ag$^+$), suggesting this change is sensitive to the earlier onset in oxidising current. What is especially interesting is the shape of the gradient response in H_2O_2, which is approximately linear between 0.4 and 1.2 V vs Ag/Ag$^+$ and also continues with this same linear trend on the reverse sweep from 1.2 to 0.3 V vs Ag/Ag$^+$. As shown previously in Figure 84, the gradient of a parabolic potential response would show such a straight line, representing an ideal system that is dominated by the $\chi^{(3)}$ term. For this system, the significant changes appear to be associated with trap state B. Between -0.2 and 0 V vs Ag/Ag+ on the forward sweep the gradient is increasing, however once reaching the potential at which state B is populated, this increase in gradient is halted. As above, this could signify Fermi level pinning as the B trap states are populated, causing an abrupt change in the gradient. After all the B states are populated, the H_2O_2 oxidation onset is reached and the gradient shows the ideal linear response of a system dominated by $\chi^{(3)}$ term. The absence of any change in gradient around the potentials where trap state A is populated indicate that it is not involved in the oxidation of H_2O_2. Instead, the changes in gradient now occur after populating state B, possibly suggesting it is the primary intermediate in H_2O_2 oxidation.

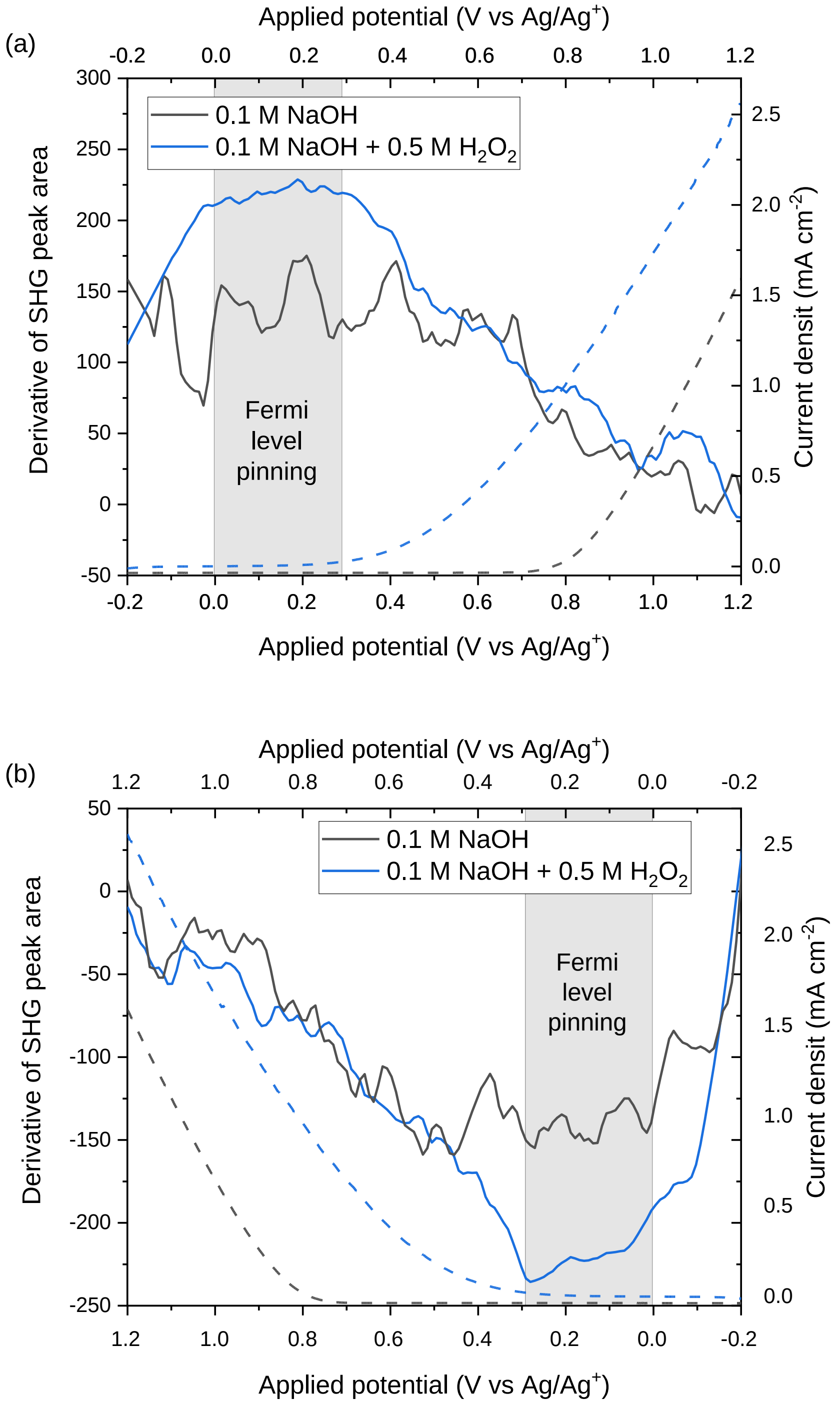

Figure 87: First derivative of the SHG peak area with respect to applied potential for an ED-Fe_2O_3 electrode in the stated electrolytes. Incident light was at 800 nm at a power of 25 mW, recording the SHG response at 400 nm and each spectral image involved 5 s exposure time on the CCD (multitrack mode over 15 vertical pixels). The data shown here are the averaged forward (a) and reverse (b) sweeps from 4 CV cycles at 2 mV s^{-1}. The current-voltage response is overlaid in dashed lines using the right axis.

These initial assignments are tentative and some assumptions made during these experiments need to be addressed. Firstly, of the few articles that explore the potential-dependent SHG response at semiconductor/electrolyte interfaces, all neglect the contribution of the fields extending into the electrochemical double layer (E_H & E_{GC}).[10,18–20] The stated reasoning behind this is that the relatively low conductivity of the semiconductor bulk compared to the electrolyte would mean that in most cases the majority of the potential drop occurs over the space charge layer (E_{SC} >> $E_H + E_{GC}$). As discussed above, the high dopant density of these films (7×10^{20} cm^{-3}) shrinks W_{SC} down to 1 to 2 nm, under which conditions a significant proportion of the potential drop can occur over the electrolyte.[11] Thus these previous assumptions that E_{SC} >> $E_H + E_{GC}$ may not apply to this system. To explore whether this assumption holds true for the hematite system studied here, a series of electrochemical SHG experiments were carried out with different ionic strength solutions. The same hydroxide concentration of 0.1 M NaOH was used throughout, while differing amounts of $NaClO_4$ were used to change the ionic strength, while maintaining the same pH. The data presented in Figure 88 had significant interference from bubbles during experiments, which appear as dropouts/spikes in the potential dependent plot. To compensate for this, only cycles without significant dropouts were averaged before carrying out the gradient analysis in Figure 88b. There is significant difference in absolute signal intensity (from the SHG peak area) for some of the ionic strengths studied, though it is difficult to say whether these are inherent differences due to changes in interfacial fields or due to the presence of small bubbles on the surface. As can be seen in the 1 M concentration data (blue curve in Figure 88a), the signal is completely lost in the first cycle due to bubbles. Once the bubbles move away from the surface, the signal can recover, such as at the beginning of the second cycle. However, the signal can also be partially lost, which can be observed as the sharp drop just before the maximum in the second cycle. The possibility of a partial loss of signal due to bubbles makes it difficult to compare signal intensities across different experiments. Regardless, there do not appear to be any significant differences in the SHG gradient plots across the different ionic strengths (Figure 88b), especially between the two extremes studied here (0.1 M and 2 M) where the largest difference would be expected. The gradient plot for 0.5 M (red curve) does have slightly smaller changes in both the forward and reverse sweep, but it also has the lowest initial intensity which could arise from partial loss of signal due to bubbles in the initial test CVs.

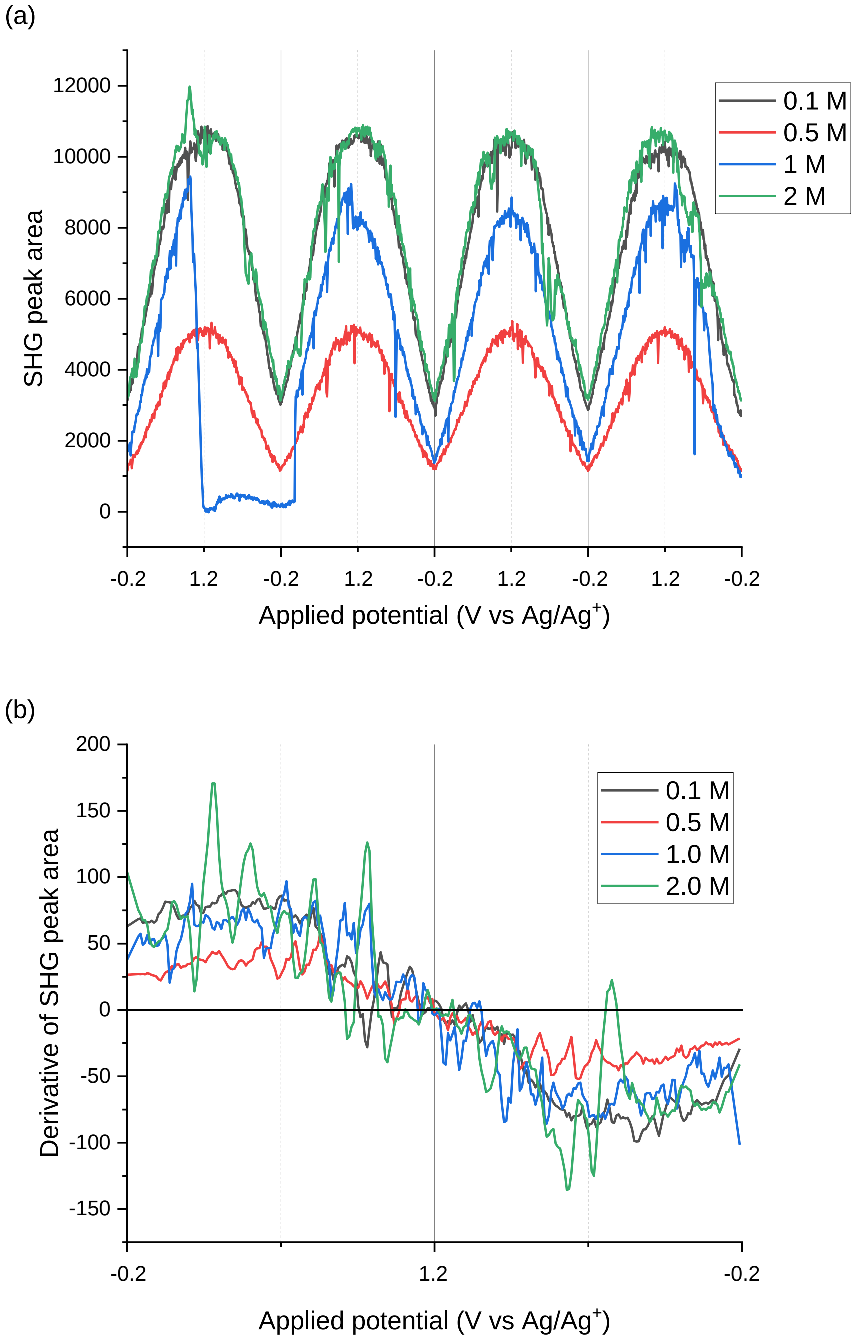

Figure 88: First derivative of the SHG peak area with respect to applied potential for an ED-Fe_2O_3 electrode in 0.1 M NaOH adjusted to the stated ionic strength with NaClO4. Incident light was at 800 nm at a power of 25 mW, recording the SHG response at 400 nm and each spectral image involved 5 s exposure time on the CCD (multitrack mode over 15 vertical pixels). The data shown here are the averaged reverse sweeps from 4 CV cycles at 2 mV s^{-1}.

Despite lowering the electrolyte concentration from 1 M in the initial PIA experiments to 0.1 M NaOH, the lowest ionic strength studied here is likely still too high for E_{GC} to play a major role in the EFISHG signal. Changing the salt concentration from 0.1 to 2 M only results in a small change of 0.7 nm in the Debye length from Figure 89 using Eq. 4.9. for monovalent cations:

$$\lambda_D = \sqrt{\frac{\varepsilon_0 \varepsilon_r k_b T}{2 N_A c e^2}} \qquad \text{Eq. 4.9.}$$

Where c is the ionic strength of the solution (in mol m^{-3}), T is set as 298 K, ε_r is the dielectric constant of the solvent (a value of 80 is used here for water) and the rest of the terms are standard constants.

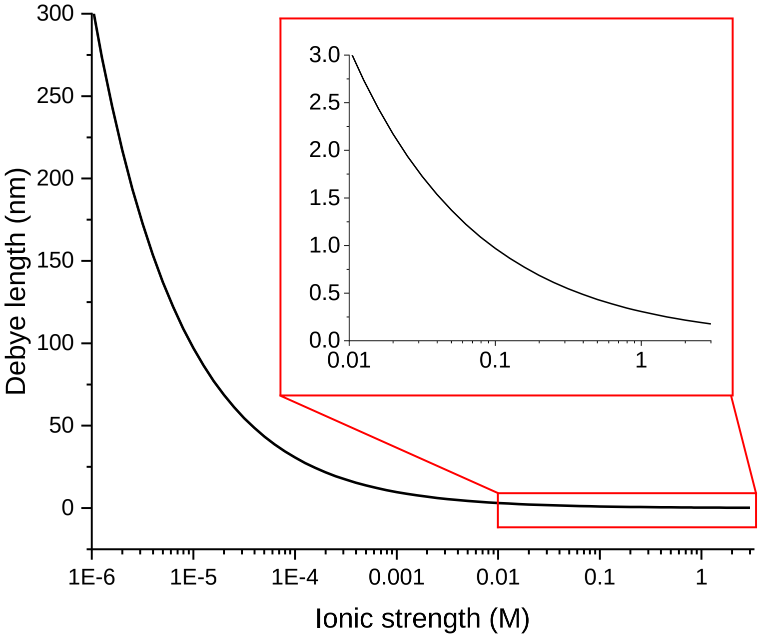

Figure 89: Debye length as a function of ionic strength of solution, assuming purely monovalent cations. Calculated using Eq. 4.9.

These calculations suggest that the ionic strengths studied above would likely not significantly influence the fields extending into the electrolyte. While the initial hydroxide concentration could theoretically be lowered further in an attempt to address larger changes in the electrolyte fields, it would be difficult to disentangle the effect of a simultaneous decrease in pH on the mechanism.

There are still several other possible explanations that need to be ruled out before assigning these deviations to trapping/detrapping. For example, current induced second harmonic generation (CISHG) has also been noted as a distinct phenomenon to EFISHG since it can be observed in transient currents that are generated without an electric field.[21,22] All of the electrochemical SHG data shown above could potentially be explained by a CISHG contribution to the response, since the major changes seem to coincide with the onset of an OER current, though this is unlikely to be the case as the experimental demonstrations of the CISHG phenomenon have thus far required very high current densities (10^5 A cm^{-2}) that are not accessed during these experiments.[22]

Another possible explanation for the results could be related to a potential-dependence of the nonlinear susceptibilities, χ^2 & χ^3. So far we have assumed that these values are independent of applied bias, but potential-dependent changes in the structure of the electrochemical interface and their impact on the values of χ^2 & χ^3 have previously been used to explain deviations from ideal responses in studying lithium ion batteries.[23] Such a drastic impact on the electrochemical response is not expected on the ED-Fe_2O_3 electrodes as, unlike in the lithium ion battery system, there is not a formation of a new solid-electrolyte interphase. Though changes in the water structure close to the hematite surface could potentially have a similar impact on the values χ^2 & χ^3, which do appear to be occurring according to the SFG results presented in Chapter 3. This demonstrates the importance of developing a technique like electrochemical SFG to probe interfacial water structure and future SFG experiments on these same type of electrodeposited hematite electrodes could be used to address these highlighted issues.

4.3. Conclusions and further work:

This chapter has explored the role of surface trap states on interfacial electric fields using two complimentary spectroscopic techniques. First a PIA spectrometer was (re-)built to track charge carrier trapping within hematite electrodes on relatively slow time-scales, but closer to *operando* conditions. Electrodeposited hematite electrodes were studied using PIA, confirming an apparent change in mechanism at high light intensities that has been reported in the literature.[6] This same kind of change was replicated using purely dark electrochemical measurements, which showed a very similar response to back-illuminated PIA experiments.

Then, initial experiments addressing changes in the interfacial electric fields using EFISHG spectroscopy were carried out. Careful choice of incident wavelength allowed the electroactive interface to be selectively probed. The results showed deviations from the ideal potential-dependent response, which was further analysed by examining the derivative of the SHG signal with respect to potential. Significant changes in this gradient were assigned to changes in surface trap state populations, manifesting as a switch in dominant field direction between E_{SC} and E_H.

PIA and EFISHG were shown to be potentially useful techniques in improving understanding of charge carrier kinetics and interfacial electric fields. The results in this chapter focused on a single type of electrodeposited hematite electrode, though the techniques could be readily applied to other types of hematite electrodes to help understand differences in synthetic methods on device performance, an issue which has recently been highlighted by Mesa *et al.*[24] Furthermore, previous results have demonstrated that surface trap states clearly play an important role in the activity of such electrodes and their deleterious effects can be diminished by passivating surface states with overlayers.[25,26] The techniques described here could be used to further investigate such surface modifications and their effects on trap states and interfacial fields. Crucial future experiments could involve precisely controlled synthesis of semiconductors at various dopant concentrations to systematically study the effect of W_{SC} on the observed signals. Similarly, a range of much lower ionic strengths (<0.1 M) could be used to properly address the effect of the Debye length.

4.4. References:

1 K. Sivula, *J. Phys. Chem. Lett.*, 2013, **4**, 1624–1633.

2 B. Klahr, S. Gimenez, F. Fabregat-Santiago, J. Bisquert and T. W. Hamann, *Energy Environ. Sci.*, 2012, **5**, 7626.

3 F. Le Formal, K. Sivula, M. Gra, F. Le Formal, K. Sivula and M. Grätzel, *J. Phys. Chem. C*, 2012, **116**, 26707–26720.

4 S. R. Pendlebury, X. Wang, F. Le Formal, M. Cornuz, A. Kafizas, S. D. Tilley, M. Grätzel and J. R. Durrant, *J. Am. Chem. Soc.*, 2014, **136**, 9854–9857.

5 M. Barroso, S. R. Pendlebury, A. J. Cowan and J. R. Durrant, *Chem. Sci.*, 2013, **4**, 2724.

6 F. Le Formal, E. Pastor, S. D. Tilley, C. A. Mesa, S. R. Pendlebury, M. Grätzel and J. R. Durrant, *J. Am. Chem. Soc.*, 2015, **137**, 6629–6637.

7 M. Forster, D. W. F. Cheung, A. M. Gardner and A. J. Cowan, *J. Chem. Phys.*, 2020, **153**, 150901.

8 M. A. Bañares, *Catal. Today*, 2005, **100**, 71–77.

9 S. Zhang and W. Leng, *Nat. Chem.*, 2020, **12**, 1097–1098.

10 J. M. Lantz, R. Baba and R. M. Corn, *J. Phys. Chem.*, 1993, **97**, 7392–7395.

11 P. A. Delcompare-Rodriguez and N. Seriani, *J. Chem. Phys.*, 2021, **155**, 114701.

12 O. Zandi, A. R. Schon, H. Hajibabaei and T. W. Hamann, *Chem. Mater.*, 2016, **28**, 765–771.

13 N. G. Rey and D. D. Dlott, *J. Electroanal. Chem.*, 2017, **800**, 114–125.

14 A. J. Bard, A. B. Bocarsly, F. R. F. Fan, E. G. Walton and M. S. Wrighton, *J. Am. Chem. Soc.*, 1980, **102**, 3671–3677.

15 B. Klahr, S. Gimenez, F. Fabregat-Santiago, J. Bisquert and T. W. Hamann, *J. Am. Chem. Soc.*, 2012, **134**, 16693–16700.

16 A. Braun, K. Sivula, D. K. Bora, J. Zhu, L. Zhang, M. Grätzel, J. Guo and E. C. Constable, *J. Phys. Chem. C*, 2012, **116**, 16870–16875.

17 L. M. Peter, in *Royal Society of Chemistry*, 2016, pp. 1–28.

18 J. M. Lantz and R. M. Corn, *J. Phys. Chem.*, 1994, **98**, 9387–9390.

19 H. Bian, Y. Guo and H. Wang, *Phys. Chem. Chem. Phys.*, 2018, **20**, 29539–29548.

20 J. L. Daschbach, P. R. Fischer, D. E. Gragson and G. L. Richmond, *J. Phys. Chem.*, 1995, **99**, 3240–3250.

21 J. B. Khurgin, *Appl. Phys. Lett.*, 1995, **67**, 1113.

22 B. A. Ruzicka, L. K. Werake, G. Xu, J. B. Khurgin, E. Y. Sherman, J. Z. Wu and H. Zhao, *Phys. Rev. Lett.*, 2012, **108**, 1–5.

23 B. G. Nicolau, N. García-Rey, B. Dryzhakov and D. D. Dlott, *J. Phys. Chem. C*, 2015, **119**, 10227–10233.

24 C. A. Mesa, L. Steier, B. Moss, L. Francàs, J. E. Thorne, M. Grätzel and J. R. Durrant, *J. Phys.*

Chem. Lett., 2020, **11**, 7285–7290.

25 F. Le Formal, N. Tétreault, M. Cornuz, T. Moehl, M. Grätzel and K. Sivula, *Chem. Sci.*, 2011, **2**, 737–743.

26 R. Liu, Z. Zheng, J. Spurgeon and X. Yang, *Energy Environ. Sci.*, 2014, **7**, 2504–2517.

Chapter 5

Experimental

5.1. UV-Vis spectroscopy:

All UV-Vis spectra in this thesis were taken on a Shimadzu UV-2600 spectrophotometer. Typically, this was used in transmission mode with the internal detector, using air as a background unless otherwise stated. An integrating sphere attachment (Shimadzu ISR-2600Plus) was also occasionally used for its external detector with an extended range.

Solution measurements were carried out in a 1 cm pathlength quartz cuvette.

Transmission spectra of films made use of a metal mask to restrict the probe beam to the area of interest on the film and the same mask was also used for the background in that measurement.

5.2. FTIR spectroscopy:

All FTIR spectra were recorded on a Bruker Tensor II FTIR spectrometer in transmission using air as a background unless otherwise stated.

Transmission spectra of both films and liquids were carried out using either a Harrick Demountable Liquid Cell, or a custom-machined PEEK cell with CaF_2 or SrF_2 windows (25 mm x 2 mm, Crystran).

5.3. Electrochemistry:

Potentiostats used over the course of this project include a PalmSens EmStat, a PalmSens1 (double-ranged), a PalmSens3, a Biologic SP-200 and a custom analogue potentiostat from Whistonbrook Technologies Ltd. that was controlled by a home-made LabView (National Instruments) programme.

Most electrolytes were aqueous dilutions (with Milli-Q water) of the following salts NaOH (Sigma, $\geq$ 98%), $NaClO_4$ (Sigma, $\geq$ 98% monohydrate), HCl (Sigma, 37%), NaCl ($\geq$ 99%), NaOD (Sigma, 40 wt.%, 99.5 atom % D). D_2O-based electrolytes used deuterium oxide (Sigma, 99.9 Atom % D) instead of Milli-Q water.

General electrochemical experiments, electrode testing and electrodepositions were carried out in a glass three-necked pear-shaped flask, typically using a Pt Flag counter electrode and either a homemade Ag/AgCl reference electrode or a silver wire pseudo-reference electrode.

Photoelectrochemical measurements and transmission PIA experiments used a glass 3-neck cell with flat sides to allow even illumination.

The various different kinds of spectroelectrochemical measurements used were either commercially available (Harrick) or custom-made cells designed over the course of this project, some of which are shown below:

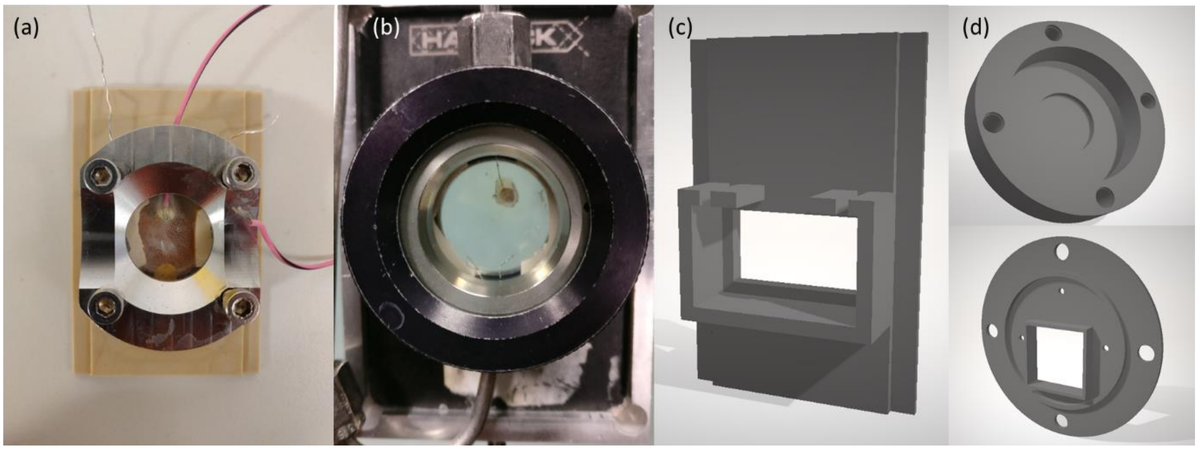

Figure 90: Custom designed and machined PEEK cell for SFG experiments (a), Harrick Demountable liquid cell (b), final design for SHG cell (c) and final design for SHINERS cell (d). The backplate dimensions are the same (50 x 75 mm) for a, b & c and the cell in d has an outer diameter of 50 mm.

Both the Harrick cell and the PEEK cell in Figure 90a & b were used for SFG experiments, designed to fit electrodes that are deposited onto standard size IR windows (25 mm x 2 mm). In both cases, electrolyte is sandwiched between the working electrode and another IR window, where spacers between the windows control the electrolyte path-length. A liquid-tight seal is created using Viton O-rings and compression provided by the stainless steel front-plate. Holes are included at the top of the PEEK cell to allow connectors for working, reference and counter electrodes, while PTFE-coated wires for electrode connections have to be threaded through the thin flow inlet/outlet tubes in the Harrick cell. The SHG cell in Figure 90c has the same back-plate dimensions as a and b (50 x 75 mm, designed to slide into standard FTIR transmission mounts) but features a much larger window aperture to enable easier alignment and a much larger volume for electrolyte. Not shown here is the complimentary “lid” component of the SHG cell, which mounts the electrode and is glued onto the rectangular aperture in the cell to form a leak-free seal. The epoxy is strong enough to hold the components together, but can be can also pried open and peeled off to allow the cell components to be reused in mounting further samples. Figure 90d shows the final cell design for the SHINERS cell including the electrolyte and working electrode mounting chamber (top) and the lid with a raised front window (bottom) that allows study of FTO-based electrodes without problems with the raised epoxy contact, as discussed in Chapter 2.2.4 .

5.4. Acid washing of glassware:

Due to susceptibility of SHINs to contaminants any new glassware used in their synthesis is initially washed with Piranha solution made with 5 parts sulphuric acid (H_2SO_4, Sigma, 98%) to 1 part hydrogen peroxide (H_2O_2, Sigma, 40 wt. % in water) to remove traces of organic compounds. After rinsing thoroughly with Milli-Q water, the glassware is boiled in Milli-Q water 3 times prior to use. After use glassware is washed with Aqua Regia made with 1 part nitric acid (HNO_3, Sigma, 70%) to 3 parts Hydrochloric acid (HCl, Sigma, 37%) followed by subsequent washes in boiling water as before. All glassware is then stored in Milli-Q water and reserved only for SHINs synthesis.

5.5. SHINs synthesis:

55 nm Au nanoparticles are prepared by a method previously reported (reaction shown below in Scheme 5.1.).[1] A stock solution of chloroauric acid ($HAuCl_4$, Sigma, 99.995% trace metals basis) in Milli-Q water (7 ml, 9.8 mM) is added to a further 200 ml Milli-Q water in a round bottom flask and refluxed at 200 °C with stirring. A fresh 1 wt. % stock solution of trisodium citrate (Sigma, ≥ 99%) solution in water is made and 1.4 ml of this stock solution is added and refluxed for 40 minutes. The initial yellow

solution turns red/purple by the end of the reflux. This solution is returned to room temperature and stored in the dark.

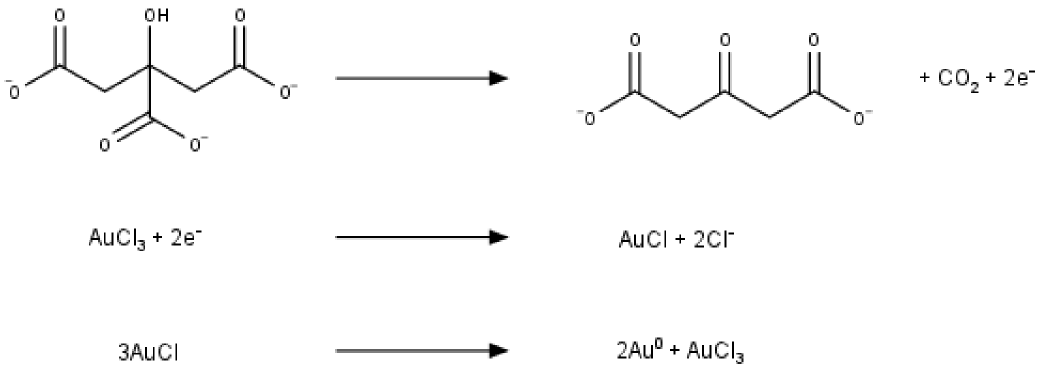

Scheme 5: Reaction steps involved in the reduction of the auric salt ($AuCl_3$) from chloroauric acid ($HAuCl_4$) to form gold (Au^0) nanoparticles. Trisodium citrate acts as the reducing agent, releasing carbon dioxide to form dicarboxy acetone. This enables the reduction of the auric salt to AuCl, which undergoes disproportionation to form gold nanoparticles.

A stock solution of (3-Aminopropyl)trimethoxysilane (APTMS, Sigma, 97%) is freshly prepared (22 µL in 100 ml Milli-Q water) and 0.4 ml of this stock solution is added to a sample of the gold nanoparticle suspension (30 ml) with vigorous stirring at room temperature for 20 minutes to allow the APTMS to exchange with citrate ligands. Meanwhile a solution of sodium silicate at pH 10.3 is prepared by making up 3.8 ml HCl (1 M) and 2 ml sodium silicate solution to 100 ml with Milli-Q water and shaking vigorously. 3.2 ml of this solution is added to the gold nanoparticle/APTMS suspension after 20 minutes have elapsed and left to stir at room temperature for 5 minutes. It is then transferred to a preheated water bath at 93 °C and left stirring. The time left stirring at this stage controls the thickness of the SiO_2 shell. Every 10 minutes 2 samples (1 ml each) are taken and cooled in ice to halt shell growth. Once cool, the samples are centrifuged at 5500 RPM for 15 minutes and the supernatant is removed. The particles are then resuspended in 1 ml water and centrifuged again at 5500 RPM for 15 minutes. The supernatant is removed again and resuspended in water. Half the samples (1 from each time step) are stored, while the other half are centrifuged again for another washing step. The first set of SHINs (that were only washed once) are kept in case the nanoparticles in the second set aggregate, which can often occur on the second washing step. The SHINs are kept at room temperature in the dark and used within a few weeks.

5.6. IrO_x electrodeposition:

Anodically deposited IrO_x films were prepared on glassy carbon electrodes based on the procedure reported by Mallouk *et al.*[2] An aqueous solution of $[Ir(OH)_6]^{2-}$ is prepared by dissolving 0.2 mmol potassium hexachloroiridate (K_2IrCl_6, Sigma, 99.99% trace metals basis) in 100 ml NaOH (0.1 M) and heating to 70 °C, where an immediate colour change from yellow to colourless is observed. The solution is then rapidly cooled in ice and can be stored in the refrigerator (2 °C) for several weeks.

Electrodeposition is carried out with a diluted $[Ir(OH)_6]^{2-}$ solution (15ml, 0.8 mM) in a 3-neck pear-shaped electrochemical cell. The glassy carbon electrode is selected as the working electrode, a platinum flag is used as the counter electrode and a homemade Ag/AgCl electrode is used as the reference. To aid deposition the solution is adjusted to pH 8 by addition of HCl. The electrode is held at 1.4 V for 2 hours with (low) 200 RPM stirring with a small magnetic stirrer bar.

5.7. Hematite electrodeposition:

The electrodeposition procedure is adapted from Zandi *et al.*[3] FTO electrode substrates (NSG-Pilkington, TEC-15) are cleaned by successive sonication in acetone, then ethanol, then water (10 mins each). $FeCl_2$ (0.1 M, 20 ml) is adjusted to pH ~4 with HCl and held at 60 °C with gentle stirring. Cleaned FTO substrate (~1x1 cm submerged in electrolyte) is held at 1.2 V vs Ag wire (with a Pt wire counter electrode) until 0.5 C charge passed. The resulting films are gently rinsed with water, then annealed at 700 °C (ramp rate not controlled) in air for 1 hour and allowed to cool to room temperature in the furnace.

5.8. *In situ* electrochemical SHINERS experiments:

All Raman spectra shown in this thesis were recorded on a Renishaw InVia Confocal Raman Microscope.

In situ Raman experiments on IrO_x electrodes were carried out in a custom-made spectroelectrochemical cell (developed by researchers in Xiamen University) with a Pt wire counter electrode and a silver wire pseudo-reference electrode. 2 µl of the SHINs suspension is dropped onto the electrodeposited IrO_x/GCE working electrode and allowed to dry in air and then the electrode is mounted and screwed in to position approximately 50 µm away from the front window. The exact distance between the front window and electrode surface could be measured using the computer-controlled micrometre stage within the Raman microscope. The z- coordinate axis of the stage can be calibrated to µm by focussing on either face of the front window (of known thickness) of the Raman cell. The difference in the z-axis coordinates when the inner face of the front window and when the electrode surface are in focus can then be converted to a distance in micrometres. Due to the non-uniform distribution of SHINs from the drop-casting, a quick Raman peak-intensity-map of the electrode surface was carried out prior to experiments to identify spots that gave a more enhanced signal. It should be noted that a significant “coffee-ring” effect was observed in this drop casting, where the edges of the drop had thick layers of SHINs that block the Raman signal of the underlying IrO_x surface; all SHINER spectra were taken from spots away from this ring, towards the centre of the drop. Typical experiments involved 20 s exposure time to a 633 nm laser.

5.9. 3D printing:

Custom cells were printed on a BCN3D Sigma 3D printer using either polylactic acid (PLA, RS components), acrylonitrile butadiene styrene (ABS, RS components) or Nylon (Taulman 645) filaments. Generally, PLA was used for any components not touching chemicals (*e.g.* cell mounts), ABS was used for components in contact with aqueous electrolytes and nylon used for components in contact with organic electrolytes.

5.10. Sputtering:

TCO-coated infrared windows were prepared by Prof. Tim Veal's group (University of Liverpool) by magnetron sputtering of standard ITO (90:10 wt.) or AZO (98:2 wt.) targets onto CaF_2 or SrF_2 (⌀-25 mm, 2 mm thick) windows. Sputtering was carried out using an ATC Orion Series Sputtering System (AJA International) at 100 W power under 2 mTorr pressure with a substrate temperature of 200 °C for 1 hour (AZO) and at 400 °C for 4 minutes (ITO). These parameters give <100 nm thick films of the TCO materials (measured by profilometry) with a sheet resistance <1 kΩ/sq.

5.11. Pulsed laser deposition:

Pulsed laser deposition of hematite was carried out by the Rosseinsky group (University of Liverpool) using a procedure reported previously in the literature.[4] Sn-doped hematite films with a 1% Sn cation concentration were prepared by mixing the appropriate amounts of high purity Fe_2O_3 and SnO_2 powders. The mixture was ball-milled and then pressed in a stainless-steel mould for sintering in air at 1200 °C for 12 hours to create the PLD target. A 25 nm thick layer of Sn-doped hematite was deposited with a Neocera PLD instrument using a substrate temperature of 450 °C. Film growth was monitored with a STAIB instruments double-differentially pumped high pressure reflection high energy electron diffraction.

5.12. Spray pyrolysis:

Spray pyrolysis to form TiO_2 on TCO coated glass and IR windows was carried out following the procedure laid out by Conde-Gallardo et al.[5] Cleaned substrates are placed on a hot plate and heated to 400 °C. A solution of titanium (triethanolaminato)isopropoxide (TYZOR, 80 wt.% in isopropanol) was prepared in ethanol (0.2 M) and sprayed over substrates from ~ 5 cm away for 100 coats using a glass spray nozzle in a conical flask and an aspirator. The films are left to dry for an hour on the hot plate and then placed in a furnace ramping up to 450 °C over 1 hour and then holding at 450 °C for 1 hour to obtain the anatase phase of TiO_2.

5.13. SFG spectrometer at CLF:

5 W of the output of a 20 W, 10 kHz, 50 fs, 800 nm Ti:Sapphire amplifier system (Coherent) is used to pump an OPA with two BBO and a $AgGaS_2$ DFG stage. The output of the OPA, a tuneable IR source of ca. 500 cm^{-1} usable bandwidth was focused onto the electrode surface (ca. 200 µm spot diameter, 1-4 µJ pulse) and overlapped spatially with a femtosecond derived picosecond 800 nm beam (ca. 300 µm spot diameter, 0.3-1.2 µJ pulse). The narrow-band femtosecond derived 800 nm beam is generated by passing 5 W of the amplified 800 nm through two air-spaced etalons (SLS optics, 21 and 9.5 cm^{-1} transmission) which is passed through a band-pass filter. To suppress the non-resonant signal a short time delay can be introduced between the IR and visible pulses by translation of the visible delay line. Generated VSFG signals were imaged with a 3 cm PCX lens, passed through a short pass filter (<750 nm, Semrock) and focused into a spectrograph (Holospec) and detected using a CCD array (Andor, Idus).

5.14. PIA spectrometer

PIA experiments were carried out on a home-built spectrometer based on an existing nanosecond transient absorption spectrometer. The output of a 75 W xenon lamp (PTI-A1010B) is passed through monochromator (PTI) to generate the probe beam, which is sent through a collimating lens and focussing lens onto the sample area. Transmitted light through the sample is then re-collimated and focussed through a second monochromator, which includes additional 400 nm longpass filters (2x FEL400, Thorlabs) before hitting a reverse biased avalanche photodiode. The raw voltage output of this photodiode is passed through a low-noise pre-amplifier (Stanford Research Systems SR560) and received by the LabView software through a DAQ card (National Instruments, NI-USB-6211) interface. A MOSFET circuit between the LED and its power supply is connected to an output of the DAQ card, allowing computer controlled switching on/off of the LED. In these experiments, a potentiostat (PalmSens, PalmSens3) is used to hold a constant applied bias for the duration of the experiment and records the simultaneous photocurrents.

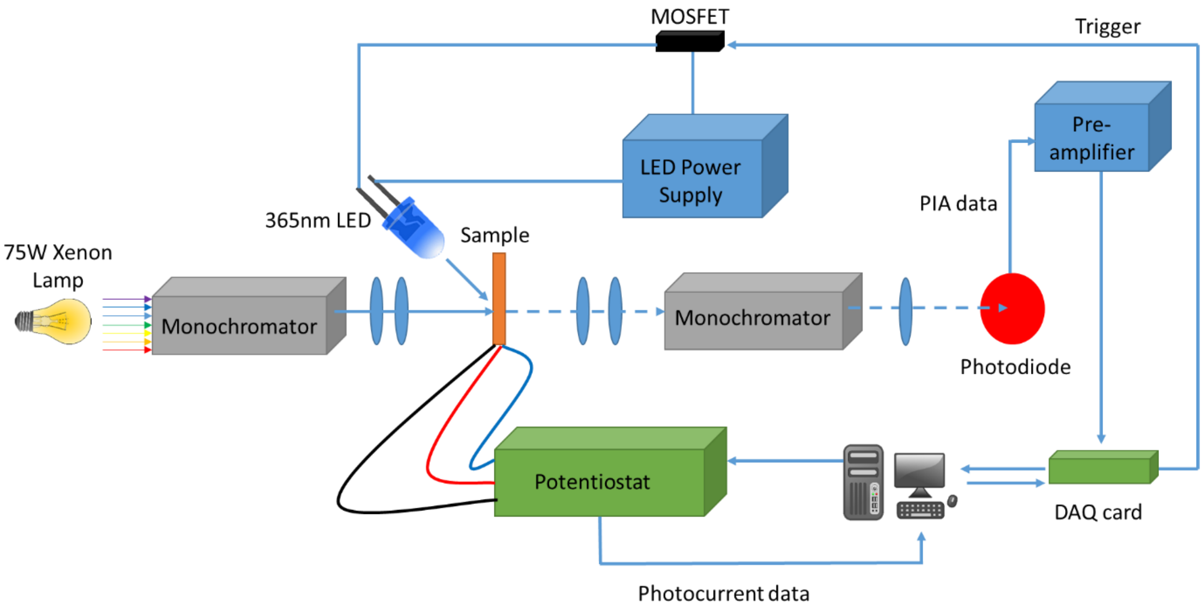

Figure 91: Schematic diagram of the PIA spectrometer built during this project, where a 75 W Xenon lamp provides the probe beam and variable power supply and 365 nm LED allow for variable pump powers. Blue ovals here represent lenses within the setup.

5.15. SHG spectrometer

The SHG spectra recorded in this project made use of the existing SFG setup (see Appendix B) with a few adjustments. The main adjustment was the addition of another beamline at 800 nm using the visible OPA from the neighbouring transient absorption spectrometer (pumped by the same PHAROS laser as the VSFG experiment). This enabled the hematite internal filter experiments as discussed in Chapter 4.3. Further adjustments included changing the half-wave plate to one suitable for 800 nm and adding a 450 nm long pass filter (Thorlabs FEL0450) before the sample to remove the residual SHG response from the quartz in the waveplate (quartz has no centre of symmetry in its crystal structure so is bulk active for 2nd order nonlinear processes like SHG). The gold mirrors after the sample are replaced with UV-enhanced aluminium mirrors (Thorlabs) to enable better reflectivity at the now shorter SHG wavelength of 400 nm. Finally, a series of 550 nm short pass filters (Thorlabs FESH0550) are included to filter out residual 800 nm light.

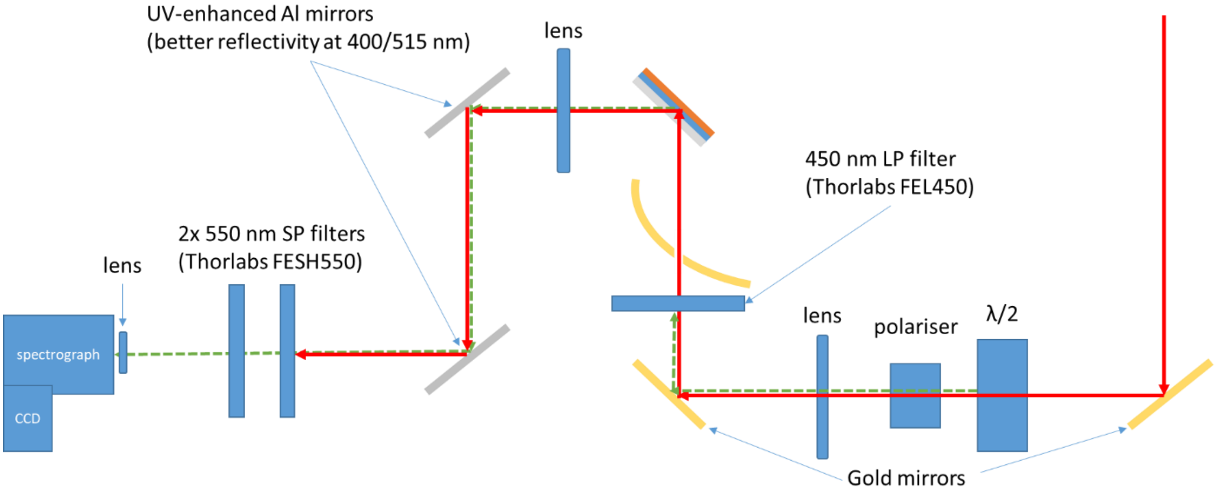

Figure 92: Schematic diagram of the modifications to the SFG spectrometer to enable SHG experiments. Here the red lines represent the incident 800 nm light and the dotted green lines represent the generated SHG response.

5.16. References:

1 J. F. Li, X. D. Tian, S. B. Li, J. R. Anema, Z. L. Yang, Y. Ding, Y. F. Wu, Y. M. Zeng, Q. Z. Chen, B. Ren, Z. L. Wang and Z. Q. Tian, *Nat. Protoc.*, 2013, **8**, 52–65.

2 Y. Zhao, N. M. Vargas-barbosa, E. A. Hernandez-Pagan, T. E. Mallouk, E. A. Hernandez- and T. E. Mallouk, *Small*, 2011, **7**, 2087–2093.

3 O. Zandi, A. R. Schon, H. Hajibabaei and T. W. Hamann, *Chem. Mater.*, 2016, **28**, 765–771.

4 K. D. Malviya, H. Dotan, D. Shlenkevich, A. Tsyganok, H. Mor and A. Rothschild, *J. Mater. Chem. A*, 2016, **4**, 3091–3099.

5 A. Conde-Gallardo, M. Guerrero, N. Castillo, A. B. Soto, R. Fragoso and J. G. Cabañas-Moreno, *Thin Solid Films*, 2005, **473**, 68–73.

Appendix A

SHINERS supplementary information

i. Improving the SHINs drop-casting procedure:

This section describes attempts at an improved drop-casting procedure for applying the SHINs used in Chapter 2 to surfaces. An approach to overcome the problem of SHINs distribution was investigated, addressing the cause of the coffee-stain effect. This phenomenon arises in cases where the contact line of the drop is pinned to its starting position, as is the case for water drops on most surfaces. Evaporating water molecules from the edges of the drop are replenished by water from within the drop, creating a flow of suspended particles towards the edges of the drop. Under normal drying conditions this leads to a large excess of suspended particles at the edges, which manifests as a thick ring upon drying. Drop-casting under an atmosphere of a low surface tension solvent, such as ethanol, induces Marangoni flow in in the droplet, leading to constant movement of the suspended particles and a reduced coffee-stain effect.[1] Marangoni flow arises here due to the ethanol vapour mixing with the water at the edges of the drop creating a surface tension gradient across the drop, providing a mechanism for circulation of the suspended particles and resulting in a more uniform deposition during the drying process.

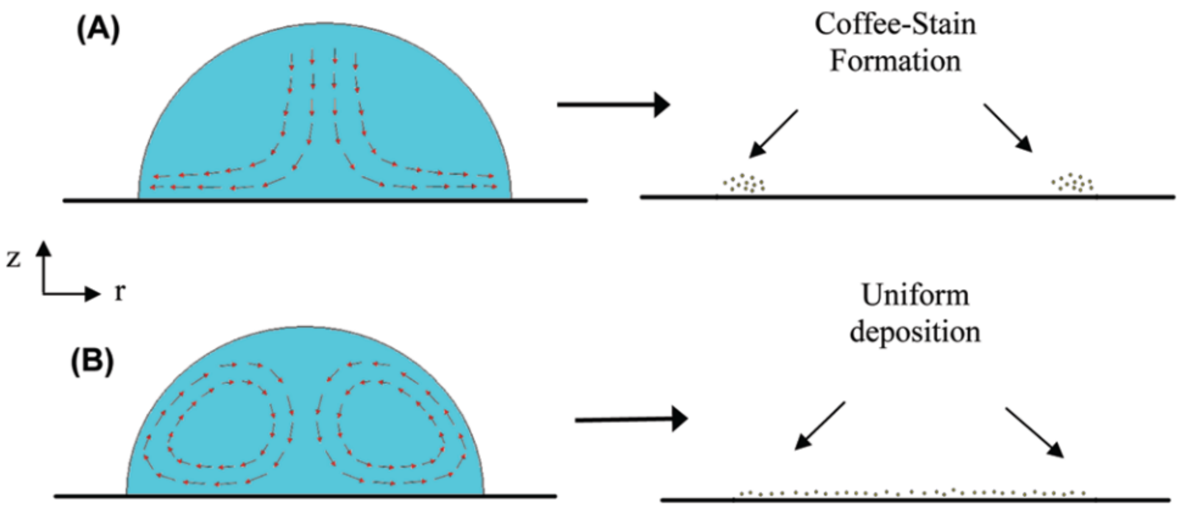

Figure 93: Motion of particles in a droplet under standard air-drying (b) during drop-casting and under the influence of Marangoni flow (b) reproduced with permission from Majumder et al.[1]

This effect was explored by drop-casting an aqueous suspension of SHINs onto a gold wafer and allowing it to dry under an ethanol vapour saturated atmosphere. It is clear from Figure 94 that the coffee-stain effect is significantly reduced when dried under an ethanol atmosphere. This highlights that there is scope for the improvement of the distribution of SHINs on electrode surfaces and simple techniques could be employed to great effect.

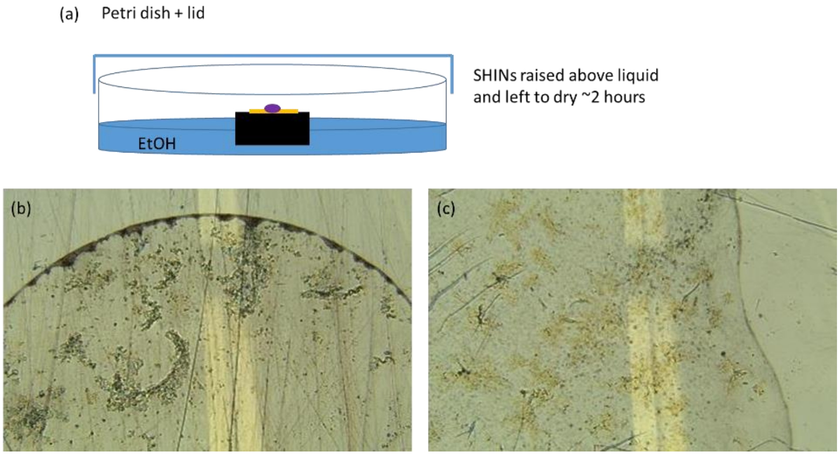

Figure 94: (a) Setup for drying SHINs under ethanol atmosphere. Microscope images for SHINs on gold wafer dried under air (b) and dried under ethanol atmosphere (c)

The effect of this method of drop-casting on the enhancement of Raman signals of interest was investigated on an IrO_x film on a glassy carbon electrode. A clear enhancement of the Raman signal from the IrO_x is observed in the SHINs dried under ethanol. However additional peaks around 2900 cm^{-1} are also present, assigned to C-H stretch vibrations either from adsorbed ethanol or other volatile organic contaminants from the ethanol vapour drying process. The peaks arising from these contaminants persist after several CV cycles (while drawing significant water oxidation currents) without any changes in their intensity. It would be expected that such an electrochemical treatment would be sufficient to also oxidise any alcohols adsorbed to the surface. The presence of such contaminants would be detrimental to studying the water oxidation reaction on the surface, so this method of drop-casting was not used for further experiments. Instead, most *in situ* Raman experiments in this project made use of a quick Raman intensity map prior to extended data acquisition to identify sites with good enhancement to address the spatial variation in signal due to drop-casting.

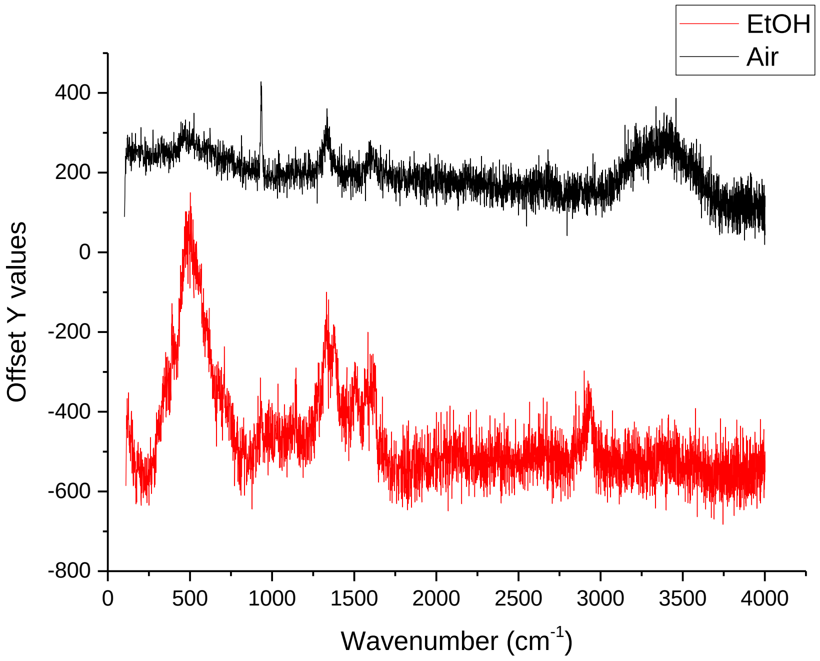

Figure 95: SHINERS spectra of IrO$_x$/glassy carbon surface when the SHINs were dried under air or under an ethanol atmosphere. Both sets of spectra were taken in 1 M NaClO$_4$ electrolyte and around 50 µm distance between the front window and the electrode surface.

ii. Peak fitting parameters for main IrO$_x$ SHINERS dataset:

This section described the fitting procedure for the SHINERS experiments on iridium oxide in Chapter 2, focusing on the proposed water oxidation intermediate, η. Fitting of the main feature between 400 and 850 cm^{-1} involves deconvolution of at least 5 features at each potential. To avoid unnecessary uncertainty, the fitting is restricted to between 700 and 1000 cm^{-1} and fit the broad response up to 750 cm^{-1} is fit to a single Lorentzian to focus on monitoring the potential dependent behaviour of the η peak at 815 cm^{-1}, assigned to an iridium oxo stretching mode, which is only present during catalytic oxygen evolution between 1.5 and 1.9 V vs Ag/Ag$^+$. Below 1.4 V, a new feature, centred at 803 cm^{-1} (assigned to ζ in the main text), better fits the spectrum instead of η. This feature is redshifted at lower potentials (see spectrum at 0.9 V) to around 743 cm^{-1} (in the spectrum at 0.5 V), where it corresponds to the peak labelled ε in the main text. The purpose of this fitting is solely to monitor changes in the η peak; while the fitting of ε and ζ may not be accurate, they are shown here to indicate that a peak around 815 cm^{-1} (η) no longer fits the spectrum.

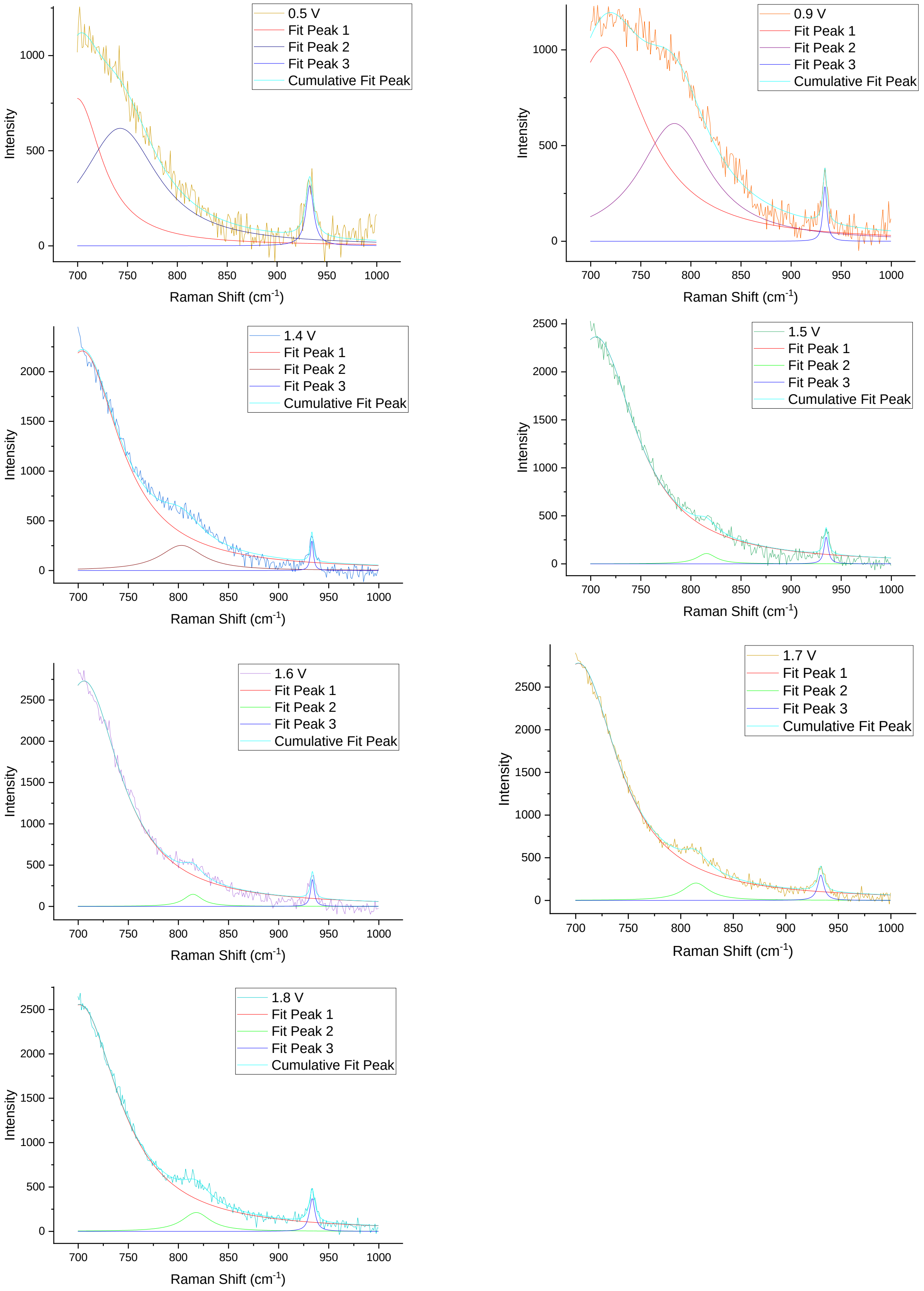

Figure 96: Lorentzian peak fitting between 700 and 1000 cm^{-1} of main IrOx SHINERS dataset from Chapter 3 focussing on η peak (green) around 815 cm^{-1}. The blue band at 933 cm^{-1} is the ClO_4^- band from the electrolyte and the red and purple fits are included to account for the other changing Ir-O-Ir vibrations.

iii. References:

1 M. Majumder, C. S. Rendall, J. A. Eukel, J. Y. L. Wang, N. Behabtu, C. L. Pint, T. Y. Liu, A. W. Orbaek, F. Mirri, J. Nam, A. R. Barron, R. H. Hauge, H. K. Schmidt and M. Pasquali, *J. Phys. Chem. B*, 2012, **116**, 6536–6542.

Appendix B

SFG supplementary information

i. Developing an SFG spectrometer at The University of Liverpool:

The experiments described in Chapter 3 were all carried out during several visits to the Central Laser Facility (CLF) utilising the homodyne SFG spectrometer setup on the ULTRA-B experiment. Over the course of this PhD a new VSFG spectrometer has been developed at the University of Liverpool by Dr Adrian Gardner, with the help of myself. An overview of the setup can be seen in Figure 97. At the heart of the system is a near-IR (NIR) ytterbium femtosecond laser (PHAROS-PH1-SP, Light Conversion, 1030 nm, 10 kHz, 10 W, 167 fs pulse duration). Around 75% of the output of the PHAROS is used to pump a mid-IR OPA (ORPHEUS-ONE-HE + DFG), which provides tuneable output between 1.35 to 16 µm (7400 to 625 cm^{-1}) with a bandwidth of ~100 cm^{-1} or 140 cm^{-1} depending on configuration. The DFG output of the OPA is polarised vertically (perpendicular to the plane of incidence to the sample, *i.e.* s-pol), while the idler output of the OPA is polarised horizontally (*i.e.* p-pol for the sample). The periscope arrangement before the sample is to rotate the DFG output polarisation to horizontal (*i.e.* p-pol for the sample). If the idler output is required, this periscope can either be removed, or suitable IR wave plate can be used after the periscope to revert the polarisation back to p-pol.

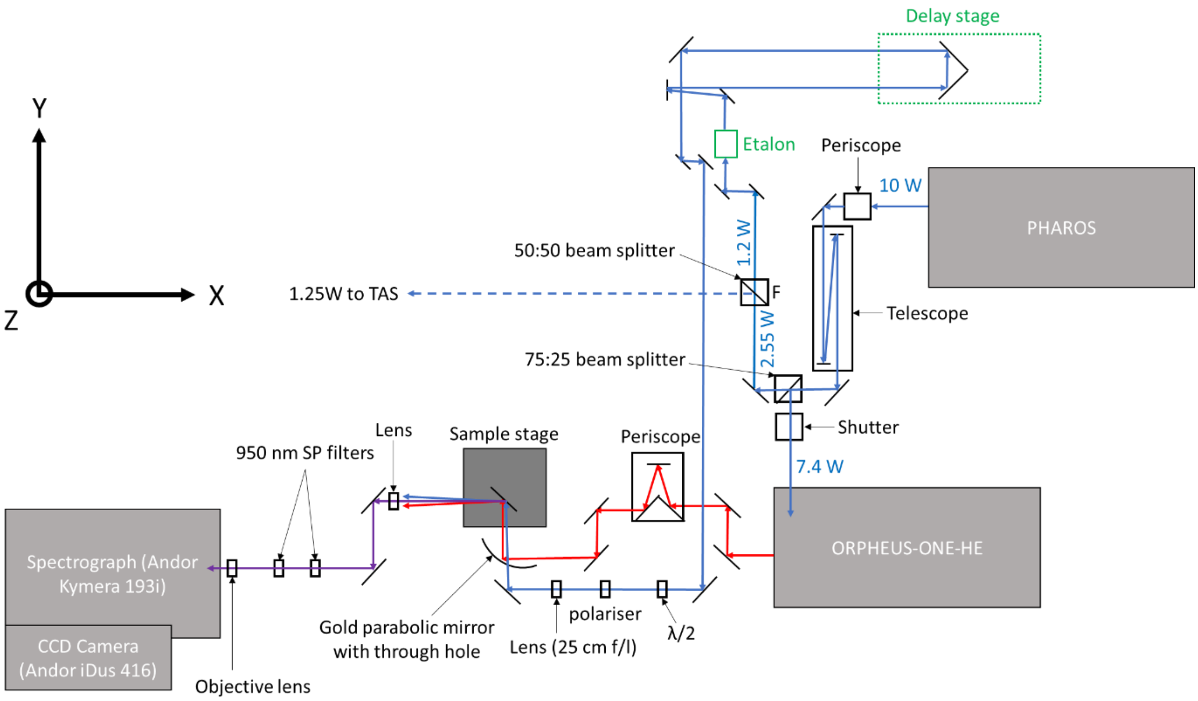

Figure 97: Schematic diagram of VSFG spectrometer at The University of Liverpool. Blue lines represent the 1030 nm "visible" beam-path, red lines show the mid-IR beam-path and purple represents the sample VSFG signal. All mirrors shown here were gold mirrors.

The remaining 25% of the output is further split in half to drive an adjacent transient absorption spectrometer and provide the “visible” (NIR) component of the VSFG spectrometer. The remaining PHAROS output used for the VSFG spectrometer undergoes pulse shaping through an air-spaced etalon to produce a time asymmetric pulse with a pulse width of ~2 ps and a linewidth of ~10cm^{-1}. This bandwidth of this pulse ultimately limits the resolution of the VSFG spectra, and the time asymmetric shape enables the nonresonant suppression technique by time delays as detailed by Lagutchev *et al.*[1] This output is passed through a variable delay line before being directed to the sample stage, allowing variable time delay scans to find temporal overlap of the mid-IR and NIR, as well as enabling the aforementioned nonresonant suppression. The sample stage is composed of three high precision linear stages allowing precise control of sample position in three dimensions. NIR power and polarisation are controlled with a combination of a half-wave plate (λ/2) and linear polariser. A plano-convex lens (25 cm focal length) focusses the NIR to ~300 µm beam diameter and a gold parabolic mirror focusses the IR to a slightly smaller diameter. This parabolic mirror contains a through-hole in the centre to allow the NIR to pass close to collinear with the mid-IR.

The VSFG signal from the sample is collected using another focussing lens and directed towards the spectrograph by a series of mirrors, through two 950 nm short-pass filters (Thorlabs, FESH0950) and a final objective lens to focus the light onto the slits of the spectrograph. Spectra are recorded using the Andor Solis programme, using multi-track image acquisition setting to restrict the readout to a small range of the vertical pixels to reduce dark noise. Typically, the VSFG signal is recorded over 10-20 rows of pixels out of a total of 256 rows.

In order to record a VSFG signal, the IR and NIR beams need to be both spatially and temporally overlapped. Firstly, the length of the delay line is chosen to approximately compensate the additional beam path within the OPA, this brings the IR and NIR close to temporal overlap, which can be fine-tuned later with the motorised delay stage. Similarly, the IR and NIR beams are roughly overlapped by eye using a heat sensitive IR-viewing card, with the angle of the NIR beam at 45° to the sample surface.

Key to acquiring strong SFG signals is placing the sample as close as possible to the focus of the IR beam. This focal position can be found by placing a 200 µm pinhole (mounted on the same face of a lens mount as the other optics used) on the sample stage and passing the IR beam through it. The pinhole is translated in and out of the focus of the IR beam (along the Y-axis in Figure 97) with a power meter behind the pinhole. Since the pinhole is slightly smaller than the IR beam diameter, the focal point can be found when the power passing through the pinhole is at a maximum. Once this focal point is found, the position along the Y-axis is fixed and the pinhole is translated in the X- and Z-axes so that the NIR beam is passing through and then the pointing of the IR beam is adjusted slightly to also pass through this pinhole position.

Now that the beams are spatially overlapped in the focus of the IR beam, the pinhole is removed and replaced with a ZnS crystal (Cleartran) mounted in a lens mount. The zincblende crystal structure of ZnS does not contain a centre of symmetry, so it gives a strong bulk SFG signal. This property is exploited to help find the temporal overlap of the IR and NIR beams. When using an 800 nm laser at the CLF, the SFG from ZnS could be readily observed by eye as a pink glow. Unfortunately, we are using a 1030 nm NIR laser as the "visible" beam, which means that the wavelength of the SFG is also not visible by eye. For this reason, the ZnS SFG is detected using the spectrograph and camera instead. Since the reflected SFG closely follows the reflected NIR beam from the ZnS, this NIR beam is directed towards the slits of the spectrograph (with the CCD shuttered) using a viewing card and then the pulse picking option on the Pharos is used to turn the 10 kHz repetition rate of the laser down to 10 Hz to avoid saturating the camera. With all the appropriate short-pass filters back in place, the camera is set to record short exposure images as the motorised delay line is scanned. Initially large, course, steps are used to find the approximate temporal overlap and then smaller steps are used for fine adjustments. Note, the pointing of either the IR or the NIR beams is not optimised on the ZnS sample as this could move the overlap point to further inside the crystal rather than the front interface, which is the desired position for all other samples. The signal is so large from the ZnS crystal that it reaches the detector even before optimising the steering of the SFG into the spectrometer. This step is then repeated on a bare Au mirror to find the optimal overlap for a surface-only signal, since the optimal temporal overlap for a bulk-active material will be slightly different to surface sum-frequency signal.

The spectrograph is calibrated by shining a standard Ne pen lamp onto the slits (which are set to their smallest slit width) and using the emission lines to accurately calibrate the horizontal pixels to wavelength values. The frequency of the tuneable IR beam can be determined from measuring a nonresonant spectrum from a bare gold mirror and observing the positions of dips due to absorption of the IR either by CO_2 vapour from air or a standard polypropylene film and comparing the dips to its FTIR spectrum. As can be seen from their respective FTIR spectra in Figure 98, these two IR references provide suitable coverage from 3200 cm^{-1} to well below 1500 cm^{-1}, which includes the spectral regions for C-H, O-D and C=O stretching vibrations.

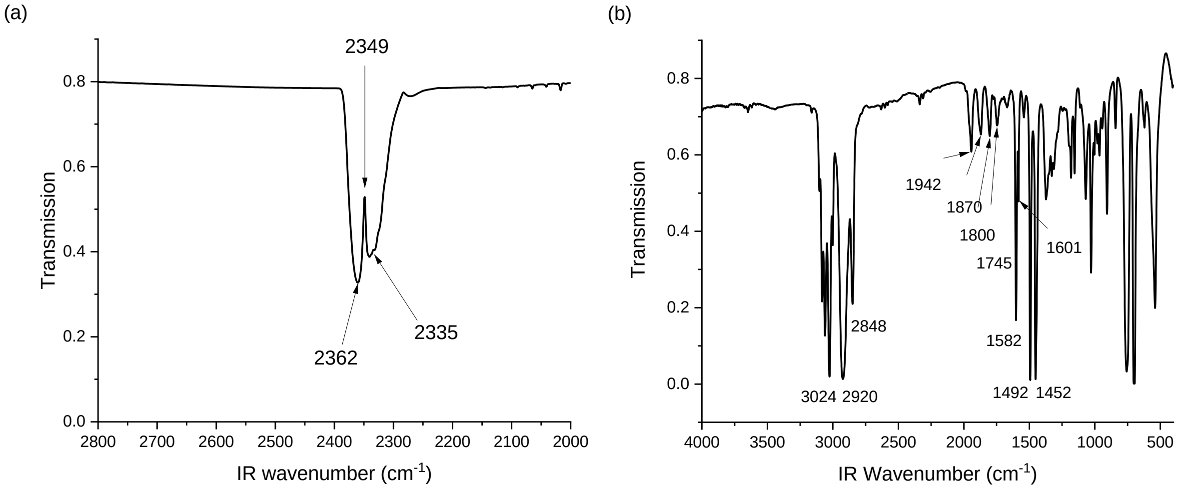

Figure 98: FTIR spectra of (a) CO_2 in air and (b) a polypropylene film, both of which were used to monitor the IR frequency used in the SFG experiments.

While the propensity of gases in air, such as CO_2 and water vapour, to absorb IR radiation is useful for checking the IR wavelength, this phenomenon is extremely detrimental to recording sample spectra close to these frequencies. Most obviously they reduce the intensity of IR light reaching the sample at those frequencies, causing significant distortion of the intensity profile of any resonant modes close to these frequencies. A further implication of “punching out” part of the Gaussian IR profile prior to the sample arises due to Fourier relationship between the frequency spectrum and the time profile of the short IR pulse. Removing certain frequencies from the IR pulse causes it to extend in the time domain. This effect can be seen when comparing the purged and unpurged time delay scans in Figure 99, which monitors the SFG signal from a bare gold mirror over various time delays. This type of scan is recorded by automatically stepping the motorised delay stage (in 0.015 mm steps, corresponding to time steps of 100 fs) and simultaneously recording SFG spectra. In the negative delays for the unpurged spectra there is a clear loss in intensity around 2350 cm^{-1} due to the asymmetric stretching mode of CO_2. The gold is not expected to contain any resonant features, so the completely nonresonant signal should almost completely decay within around 300 fs. This is the case across most of the spectrum, but there is still residual intensity around the 2350 cm^{-1} region for up to a picosecond. This is presumed to be a result of the aforementioned extension of the temporal profile of the IR pulse. When the IR beam-path is flushed with a CO_2-free purge gas the dip in the profile is reduced, as are the features at positive time delays. It should be noted that the purge setup at the time of recording these spectra was not ideal and could not completely remove the CO_2 dip from the IR profile. This has since been improved by encasing all of the IR optics in tubing to reduce the total volume required to be purged.

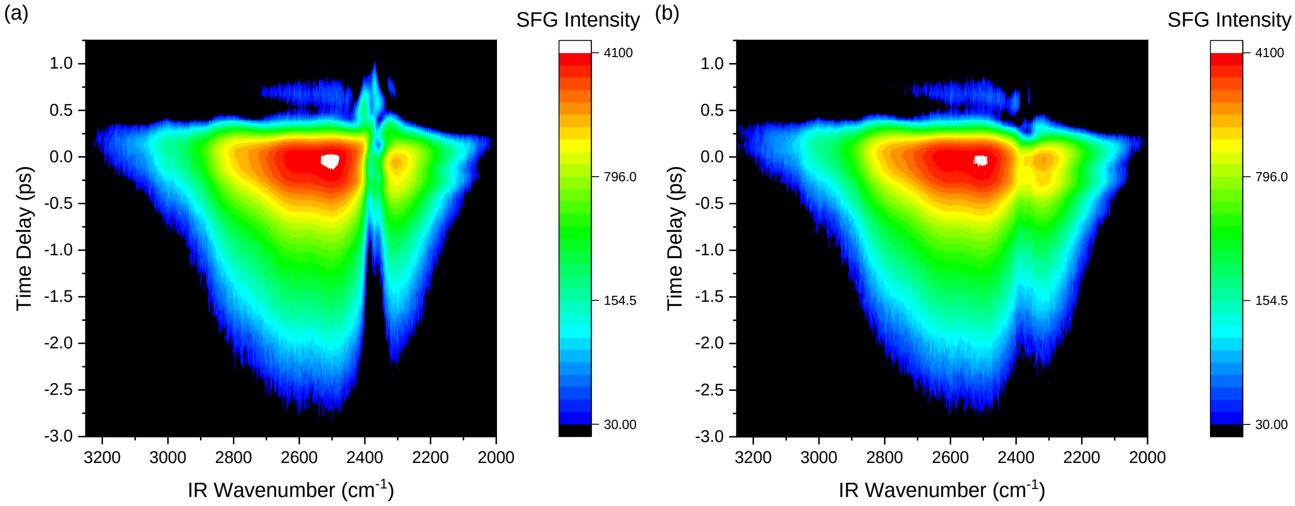

Figure 99: Nonresonant VSFG spectra of a bare gold mirror with the IR beam either (a) unpurged or (b) purged using an IR purge gas generator. Spectra are plotted as a function of time delay between the IR and NIR beams, where a positive delay

indicates that the IR pulse arrives first and the NIR pulse is delayed. Note the small, broad feature between 2400 and 2700 cm^{-1} at positive time delays is likely due to an additional pulse from the etalon.

Control of the time delay allows suppression of the nonresonant by delaying the NIR pulse after the IR to only probe the longer lived resonant vibrational modes at the surface.[1] However, the features observed here due to CO_2 absorption could easily be confused for resonant vibrational modes from the surface of interest as they persist for longer time delays than the rest of the nonresonant and appear as positive peaks rather than dips. This highlights the importance of sufficient purging of the IR beam-path to avoid spectral artefacts, but also indicates that similar artefacts can occur due to other IR absorptions in the beam-path. A similar effect can occur in electrochemical experiments using a liquid electrolyte that contains any molecules with IR-active vibrations. Thus, the IR spectra of the electrolyte and any window materials should be carefully considered for electrochemical experiments.

The time delay scans on a bare gold mirror from Figure 99 can be used to assess the temporal profile of the etalon-derived NIR pulse. A time slice through the centre of the gold nonresonant at 2500 cm^{-1} is shown in Figure 100, where the decay of the signal towards positive time delays gives the rise time of the etalon, which in this case is 400 fs. This means that most of the nonresonant decays within this 400 fs window, so time-delays greater than 400 fs are suitable for recording nonresonant-suppressed VSFG spectra.

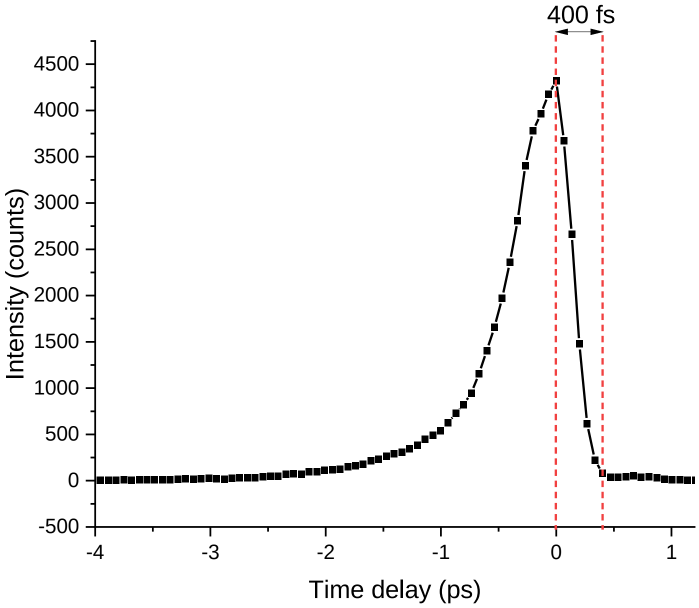

Figure 100: Time profile at 2500 cm^{-1} of the nonresonant SFG signal of bare gold mirror from Figure 99b. The rise-time of the etalon is displayed as 400 fs.

One of the first systems used to test this VSFG spectrometer was a thin crystal of D-fructose grown on a CaF_2 substrate. The natural chirality of sugars automatically fulfils the criteria of a non-centrosymmetric crystal structure, so sugar crystals can generate strong bulk SFG signals and are also cheap, safe to handle and easy to grow. Furthermore, fructose contains many different C-H bonds, leading to a congested spectrum in C-H stretch region. This congested spectral region can be used to test resolution of our VSFG spectrometer. For these experiments a saturated solution of D-fructose in methanol is dropped onto a clean 25 mm diameter CaF_2 window and allowed to dry, resulting in a large crystal of D-fructose on the CaF_2 surface. The VSFG of spectra of this D-fructose crystal as a function of time delay are shown in Figure 101, immediately demonstrating the very large signal size of a bulk-active SFG signal. Despite only being recorded at 1 s exposure times, the signal size is close to saturating the detector at complete temporal overlap, necessitating the logarithmic colour scale to be able to see all features. Unlike with the gold time delay scans above, the signal for D-fructose is dominated by the resonant C-H stretching vibrational modes, which persist for more than six picoseconds after the nonresonant signal has decayed. The intensities of these resonant modes oscillate in time due to a phenomenon known as quantum beating,[2] which is a result of interference between the freely decaying polarisations of different nearby resonant vibrational frequencies.

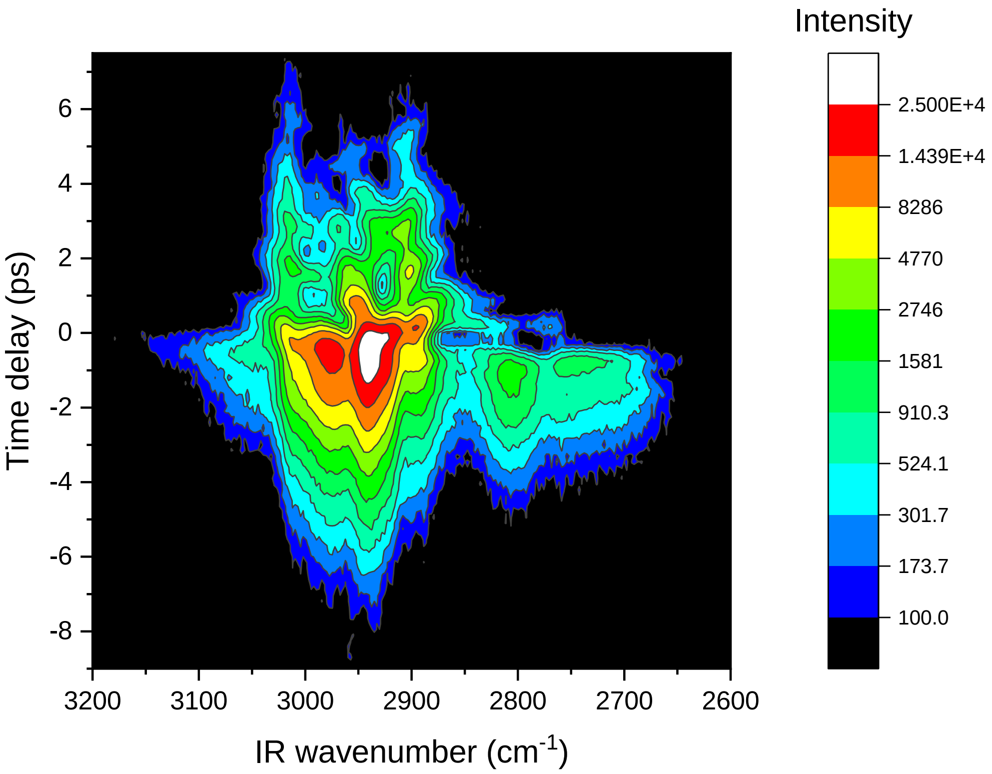

Figure 101: VSFG spectra in the C-H stretch region as a function of time delay between the IR (16 mW, p-pol) and NIR (6 mW, s-pol) of a D-fructose crystal deposited on a CaF_2 window, with 1 s exposure per spectrum. Note that the colour map for the intensity is on a logarithmic scale to discern all features in one plot. A time delay of zero represents complete temporal overlap and a positive time delay indicates that the IR pulse arrives first, with the NIR pulse being delayed. The polarisation of the SFG was not controlled, giving the xsp polarisation combination.

Due to this oscillatory behaviour of the peak intensities, it is difficult judge the resolution of the spectrometer using a spectrum at a single time delay. Several nonresonant-suppressed VSFG spectra of the D-fructose crystal are overlaid with the Raman spectrum in Figure 102. All the peaks in the Raman spectrum can be resolved in the SFG spectrum in at least one of the time delays, indicating peaks separated by as little as 20 cm^{-1} can be resolved. The limit for the resolution of the VSFG spectrometer is determined by the bandwidth of the etalon-derived NIR pulse (around 10 cm^{-1}), which would require a different system with an even more congested spectrum to fully test. Furthermore, tuning the tilt angle of an etalon results in a small shift in its transmission wavelength. Comparisons between the peak positions of the C-H stretches in D-fructose in the Raman and VSFG spectra were used to calculate a corrected value for the NIR wavelength after passing through the etalon. Since the SFG wavelength is known accurately due to the calibration of the spectrometer using the Ne lamp and the IR frequencies are known by matching the peaks in between the SFG and Raman spectra, the wavelength of the NIR after passing through the etalon can be calculated by subtracting the IR frequency from the SFG frequency. Using an average of the six C-H peaks of D-fructose form Figure 102 a value of 1028.8 nm is determined for the NIR wavelength.

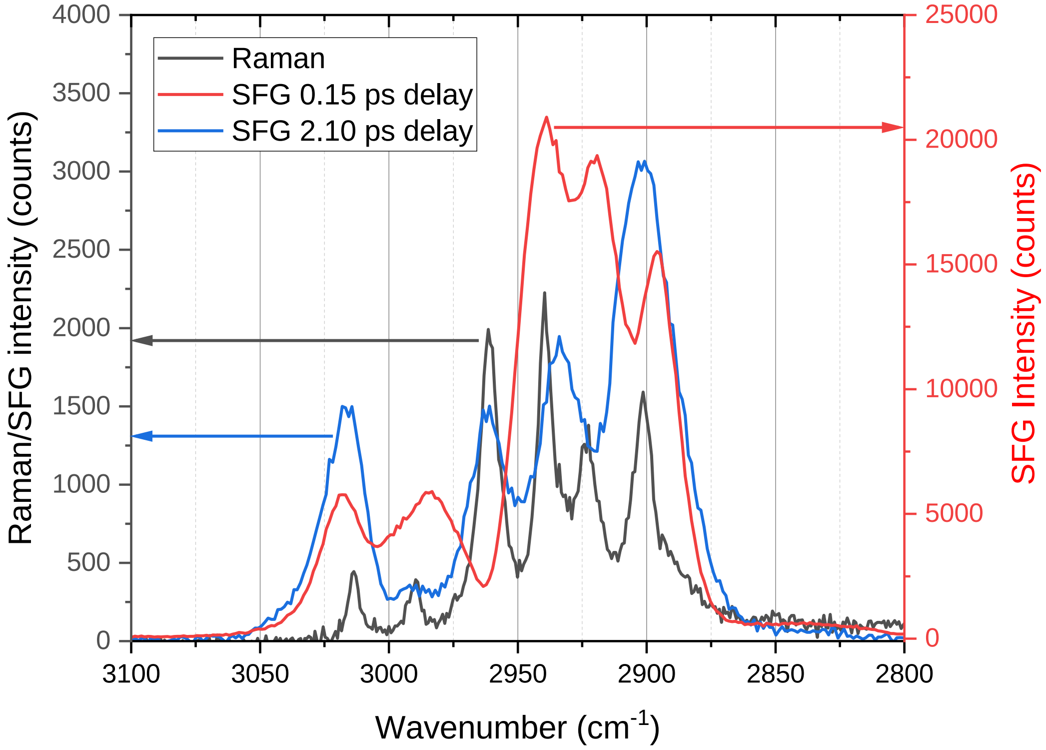

Figure 102: Raman and VSFG spectra of a D-fructose crystal deposited on a CaF_2 window. The Raman spectrum was recorded on a Renishaw InVia microscope with a 633 nm laser at 10% power with a 60 s exposure time. The VSFG spectra were recorded with a 1 s exposure time, with the NIR beam (6 mW, s-pol) either heavily (2.1 ps) or lightly (0.15 ps) delayed compared to the IR beam (16 mW, p-pol). The polarisation of the SFG was not controlled, giving the xsp polarisation combination.

This section has described the development of the VSFG experiment at The University of Liverpool, which has since been used for a variety of *in situ* electrochemical VSFG experiments on a variety of different systems, including molecular CO_2 reduction catalysts at metal electrodes and water oxidation at transparent semiconductor photoelectrodes. These *in situ* electrochemical experiments made use of a variety of spectroelectrochemical cells including, the Harrick Demountable Liquid Cell and the custom PEEK cell for photoelectrodes, as discussed in Chapter 5.3. An analogue potentiostat (Whistonbrook Technologies Ltd.) is used to synchronise SFG data acquisition and electrochemical measurements, using a TTL trigger pulse and a custom LabView programme.

ii. Heterodyne VSFG experiments at CLF:

The conventional (homodyne) VSFG spectrometer at the Central Laser Facility (CLF) is used in Chapter 3 to successfully study dynamic catalytic processes at buried semiconductor interfaces. However, homodyne spectrometers typically suffer from three major drawbacks: weak resonant surface signals, large (and hard to deconvolute) nonresonant backgrounds and no information on the phase of the resonant signals. To build on this work, a further application for facility time was aimed at developing a heterodyne detected (HD) SFG experiment at the CLF, which would address all three of these limitations of homodyne experiments. Firstly, the signal intensity in HD-VSFG spectroscopy decreases approximately linearly with surface coverage, while homodyne-VSFG intensity decreases quadratically, as shown in Figure 103 from Stiopkin *et al.*[4] For example, a 10% surface coverage can lead to a factor of 100 decrease in homodyne signal when compared to a complete monolayer, while in HD-VSFG this would only be a factor of 10 decrease in signal. This improves the signal at very low surface coverages, such as those expected for transient surface intermediates at the semiconductor photoelectrodes under OER conditions. Secondly, HD-VSFG allows direct measurement of the imaginary component of the second order nonlinear susceptibility ($\mathrm{Im}[\chi^2]$), which reports on the molecular vibrations and is comparable to linear IR absorption spectra.[5] This is especially appealing for studying the O-H stretch vibrations which have a very short vibrational lifetime, making it unsuitable to remove nonresonant background using time delays as discussed above.[1] Finally, the phase of the resonant VSFG signal can be directly accessed using HD-VSFG, allowing orientational information of the vibrating molecules to also be obtained.

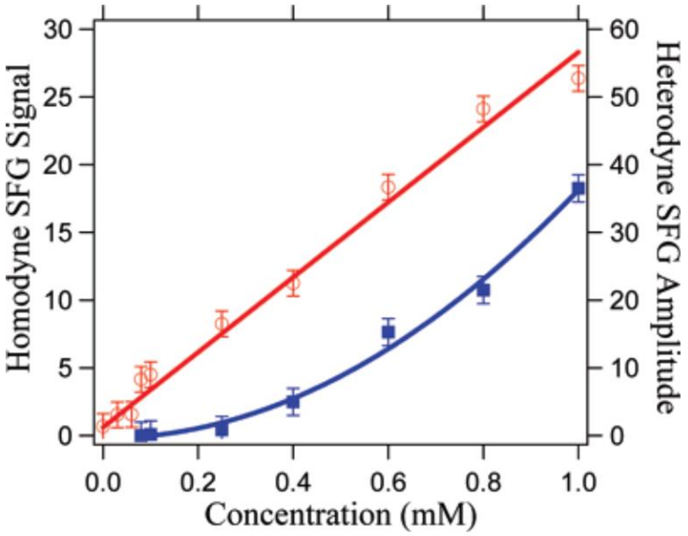

Figure 103: The VSFG intensity in a homodyne experiment (blue) decreases quadratically with concentration, while the HD-VSFG intensity decreases linearly with concentration, reproduced with permission from Stiopkin et al.[4]

Detailed descriptions of the theory of HD-VSFG can be found elsewhere,[4–6] and will only briefly be summarised here. HD-VSFG spectroscopy relies on measuring an interference pattern between the electric field of the sample SFG signal (E_{sample}) and that of a reference beam known as the local oscillator (E_{LO}). The intensity of HD-VSFG signal is given by:

$$I_{HD-VSFG} = |E_{LO}|^2 + |E_{sample}|^2 + E_{LO}E_{sample}\exp(i\omega t) + E_{LO}E_{sample}\exp(-i\omega t) \qquad \text{Eq. B.i.}$$

The crucial difference between homodyne and heterodyne SFG spectroscopy is that the cross terms in HD-VSFG (blue terms in Eq. B.i.) retain phase information of E_{sample}, while this information is lost in homodyne SFG spectroscopy, where only the square of E_{sample} is detected.

The setup developed in this project is based on the design of Vanselous and Petersen[6] and was constructed and tested during a 3-week visit to the CLF using the ULTRA-B experiment. A diagram of the final setup is shown in Figure 104. In this setup the IR and Vis are spatially and temporally overlapped before the sample within a 100 nm layer of ZnO deposited on a 1 mm CaF_2 window to generate the LO. The Wurtzite crystal structure of the ZnO is non-centrosymmetric, so this 100 nm layer produces a strong SFG signal not just from its interfaces, but also from its bulk. The IR, Vis and LO are transmitted through this ZnO sample and refocussed onto the sample position using a set of gold parabolic mirrors. In order to generate a spectral interferogram that is adequately separated in the time domain (to enable the data analysis discussed later), a relative time delay between the LO and the sample SFG signal is introduced by passing only the LO beam through a 2 mm fused silica plate. The IR and Vis are also transmitted through different thicknesses of CaF_2 and Ge to account for the relative time delay between them introduced by transmission through the 1 mm CaF_2 substrate used in LO generation. Both the sample SFG signal and the LO are collected after the sample and focussed through the slits of the spectrograph and the spectral interference between them is detected on the CCD camera.

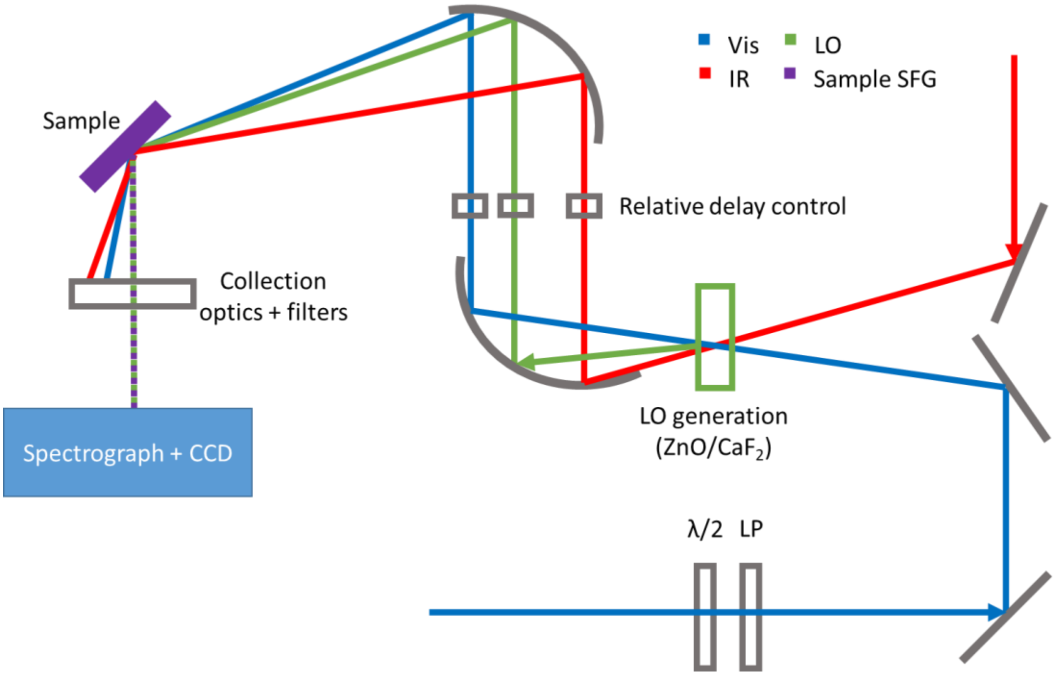

Figure 104: Diagram showing the HD-VSFG experiment developed at the CLF during this project. The IR and Vis beams are spatially and temporally overlapped at two different points within this setup to generate the LO and the sample SFG signals. The LO is passed through a 2 mm piece of fused silica to introduce a relative time delay between the LO and sample SFG signals, resulting in a spectral interferogram. Additional pieces of CaF_2 and Ge are placed in the IR and Vis beams prior to the

sample to account for the relative delay introduced between the IR and Vis by transmission through the ZnO/CaF$_2$ for LO generation.

The analysis of the spectral interferogram involves a few extra steps compared to conventional homodyne SFG spectroscopy. Here the example of a [Mo(bpy)(CO)$_4$] CO$_2$ reduction catalyst at a gold electrode will be used as a model system to showcase the data analysis procedure for an *in situ* electrochemical HD-VSFG experiment. This system has been studied previously in the group using a homodyne electrochemical SFG experiment,[7] which will be used as a basis for comparison. The electrochemical response of this [Mo(bpy)(CO)$_4$] complex is characterised by two reversible reductions prior to the onset of catalytic CO$_2$ reduction. Initially, a one electron reduction produces the singly reduced radical anion, [Mo(bpy)(CO)$_4$]$^{\bullet-}$, which undergoes a further one-electron reduction and loss of a CO ligand to form the active catalyst [Mo(bpy)(CO)$_3$]$^{2-}$. In the presence of CO$_2$ and a proton source, this doubly reduced species carries out catalytic CO$_2$ reduction. The model experiments used here to test the HD-VSFG system were all carried out in the absence of CO$_2$, in an argon purged solution, so the two reductions will be monitored, without any catalytic CO$_2$ reduction processes occurring. A representative voltammogram recorded during an SFG experiment is shown in Figure 105, displaying the two reductions of the [Mo(bpy)(CO)$_4$] complex.

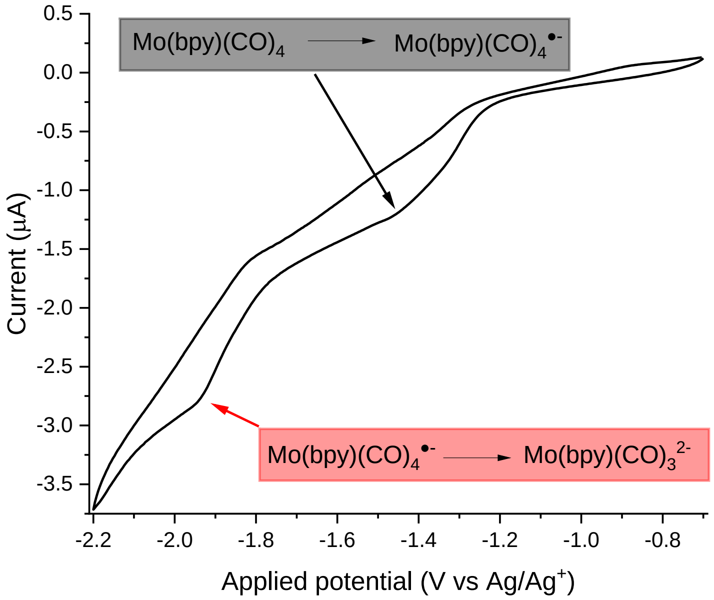

Figure 105: Representative cyclic voltammogram of 1 mM [Mo(bpy)(CO)$_4$] in 0.1 M TBAPF$_6$ in argon-purged acetonitrile with the cell inside the spectrometer. The start potential is at -0.7 V and is scanned to -2.2 V and then back to -0.7 V vs Ag/Ag$^+$ at 10 mV s^{-1}.

A representative spectral interferogram is shown in Figure 106, displaying the characteristic interference fringes. The signal size in counts is very large, close to the saturation limit of the camera (the CCD saturates at 60000 counts), as the bulk SFG signal from the LO is so strong. However, the spectral information of interest is encoded within the interference fringes and requires further analysis.

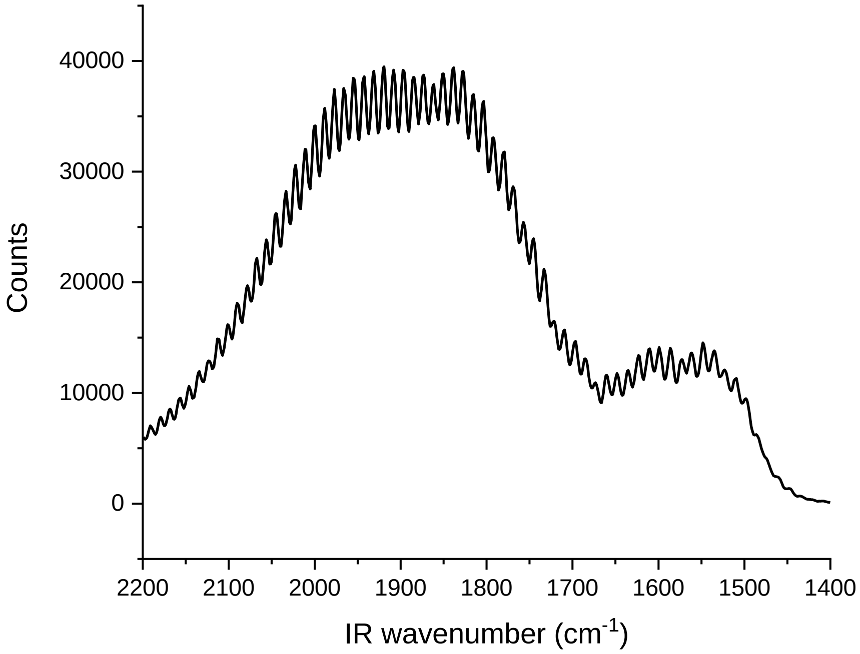

Figure 106: Spectral interferogram detected from a gold electrode surface immersed in a solution of [Mo(Bpy)(CO)$_4$] (1 mM) in argon-purged acetonitrile containing 0.1 M TBAPF$_6$ electrolyte, held at 1.5 V vs Ag/Ag$^+$.

The first step in the analysis is to apply a Fourier transform to convert the data from the frequency domain to the time domain, resulting in the interferogram shown in Figure 107. Three distinct regions can be seen within this representation, a large centre-burst corresponding to the distinct sample SFG and LO terms (black terms in Eq. B.i.), and two smaller bursts to positive and negative times, corresponding to the real and imaginary cross terms (blue terms in Eq. B.i.). The major component of these smaller bursts corresponds to the nonresonant signal, and the resonant vibrations are represented by a free induction decay (FID) extending towards the large centre-burst. The signal can be gated (in this case using a Hanning window function over the region shown in red in Figure 107) to only select one of these cross-terms and the appropriate FID before applying an inverse Fourier transform to extract the frequency dependence of Im[χ^2].

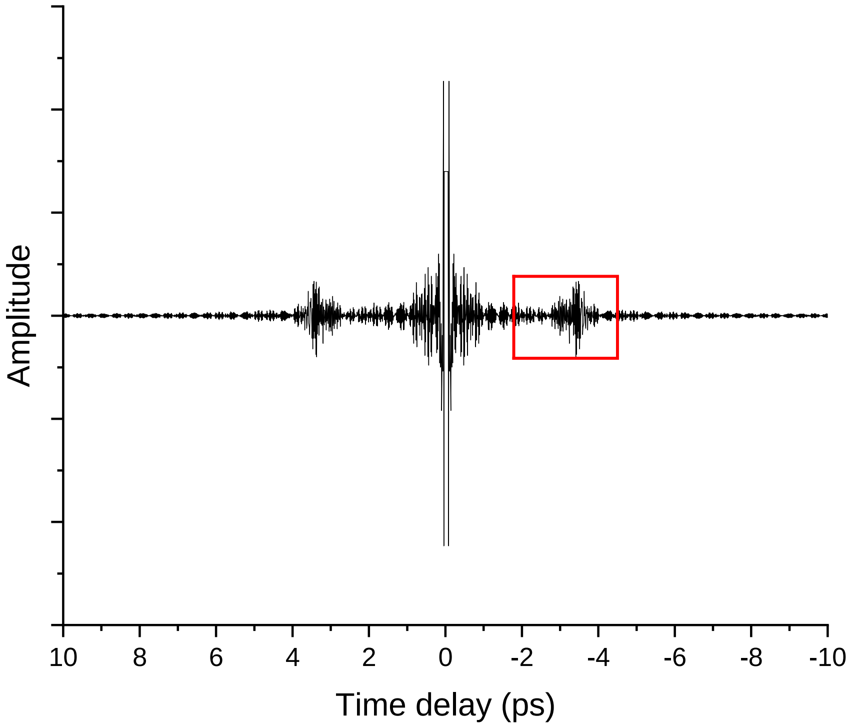

Figure 107: Time-domain representation of the interferogram from Figure 106 after carrying out a Fourier transform. The centre-burst region represents the static E_{sample} and E_{LO} terms, while the two features to the left and right correspond to the cross terms in Eq. B.i. The region highlighted in a red rectangle was chosen using a Hanning window function before carrying out further analysis.

There are several issues with this implementation of the experiment that could be improved in future experiments. Firstly, the level of noise in the time-domain interferogram is very large. While the signal counts are almost saturating the detector in Figure 106, it is the interference pattern itself that encodes the signal. The spectrograph and CCD used in these experiments was the same as that used previous homodyne experiments, where the whole signal only occupies around half of the horizontal pixels on the camera. This was not a problem for the homodyne experiments as the spectral resolution is limited by bandwidth of the etalon-derived visible pulse. In the case of HD-VSFG greater resolution is required to better sample the interference fringe pattern. A simple modification for future HD-VSFG experiments using the same components could be to move the CCD camera further away from the grating in the spectrograph. This would allow the dispersed light from the spectrograph grating to further diverge before impinging on the camera, allowing more of the horizontal pixels to be used to capture the signal. This would increase the number of points sampled in the interferogram and thus reduce some of the noise seen in the time domain signal. Secondly, the two cross-terms are not sufficiently separated in time from the centre-burst corresponding to the individual terms, making it difficult to fully separate the terms of interest without the FID clipping the centre-burst. A thicker piece of fused silica in the LO beam-path could be used to increase the time delay between the LO and sample SFG, resulting in greater temporal separation of the square and cross terms.

The inverse Fourier transform of the example data is shown Figure 108, representing both the resonant and nonresonant components of Im$[\chi^2]$. This signal can be divided by an appropriate reference signal containing only the nonresonant component to give the resonant Im$[\chi^2]$ spectrum. Since the sample spectrum is directly divided by the reference spectrum, a shift in phase between the sample and reference spectra can very easily ruin the resulting Im$[\chi^2]$ spectrum. Ideally the sample chosen for the nonresonant reference signal would be placed at exactly the same position as the sample. Furthermore, the sample position and optic mounts should be sufficiently stable to avoid a gradual drift in phase over the course of an experiment. The transparent electrodes used later in the project had a small gold spot evaporated onto the bottom part of the electrodes for this reason, to allow a nonresonant reference spectrum to be recorded by simply translating the sample in the z-direction using the micrometre translation stage.

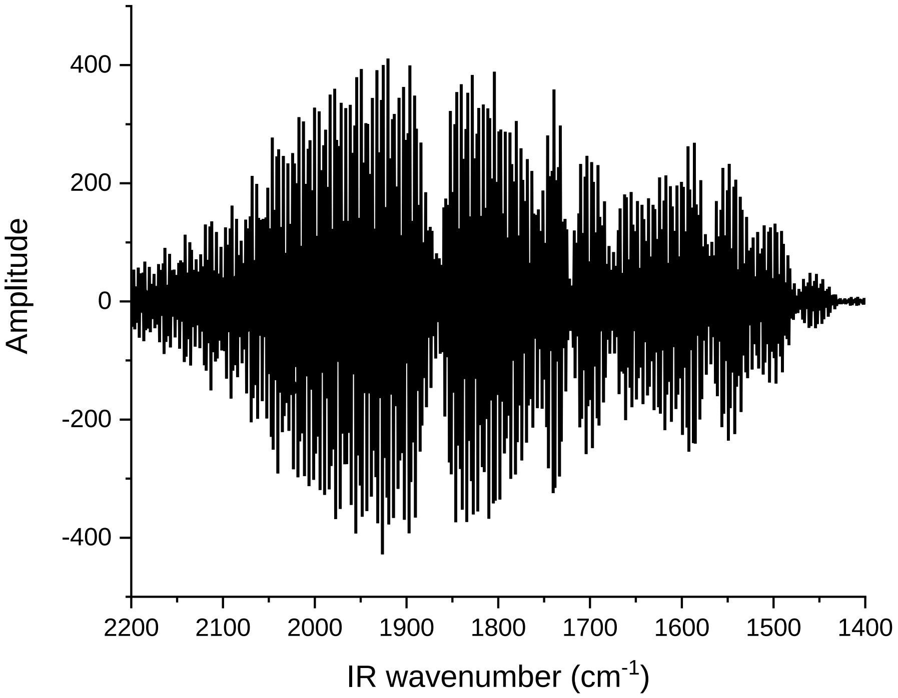

Figure 108: Inverse Fourier transform of the interferogram in Figure 107 after it is multiplied by a Hanning window function to isolate one of the cross terms.

However, for these initial experiments using gold disk electrodes it was not possible to get a clean reference spectrum at exactly the same position as the sample. Instead, the spectrum of the gold electrode itself, at close to the open circuit potential, was used as the nonresonant reference spectrum. This is not ideal as the gold electrode spectrum may contain resonant modes from molecular species from solution orienting themselves at the electrode surface even without a strong applied potential. Despite this possible issue, the referenced spectrum in Figure 109 clearly shows both positive and negative (here negative refers to values below the baseline, *i.e.* <1 due to the referencing method used) resonant modes around 1900 cm^{-1} corresponding to C=O stretching vibrations at the electrode surface. Assignment to a specific ν(CO) mode of [Mo(bpy)(CO)$_4$] is complicated by the presence of directly adsorbed free CO on the gold surface, which is a degradation product from the numerous repeated experiments on the same cell during this instrument development time.

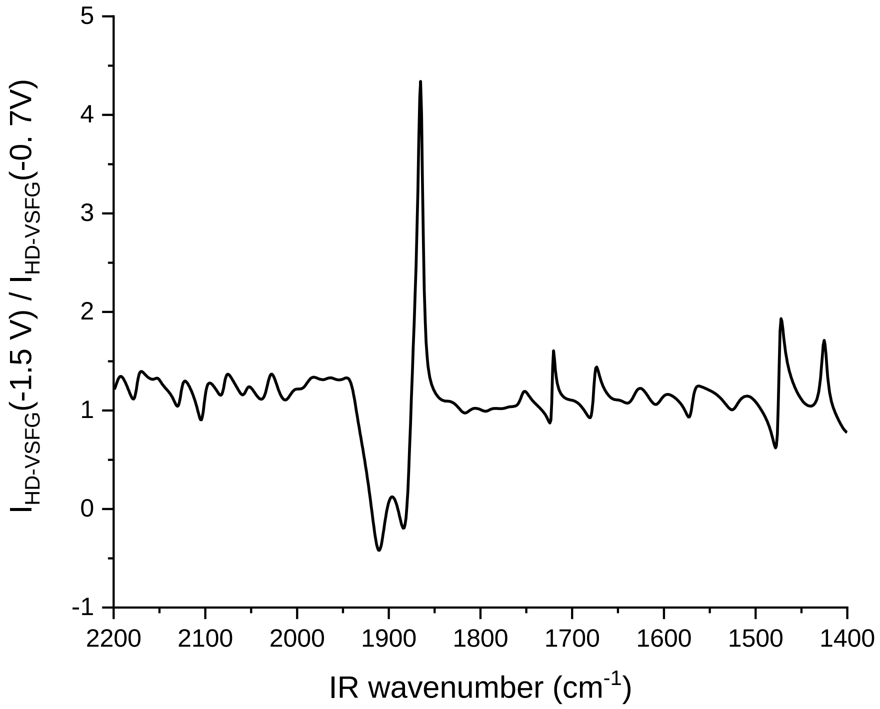

Figure 109: Interferogram from Figure 108 after being divided by a reference spectrum at -0.7 V vs Ag/Ag⁺. This would correspond solely to the resonant Im[χ^2] spectrum if the reference spectrum was a solely nonresonant spectrum, however there were likely resonant modes in the reference spectrum too, complicating analysis.

So far all of the analysis has focused on a single static spectrum, while typical electrochemical SFG experiments involve recording many spectra as the applied potential to the electrode is varied. The spectrum analysed so far in this section represents a single potential value during multiple CV cycles. The additional spectra for all other potentials are presented in the contour plots in Figure 110b, which also contains comparative homodyne SFG spectra from the same setup in Figure 110a. The HD-VSFG setup can record homodyne spectra by simply blocking the LO beam before the sample. In this case the acquisition times for the HD-VSFG spectra were limited to 0.4 s per spectrum as any higher would saturate the CCD, while the homodyne spectra were recorded at 2 s per spectrum to have an appreciable signal. Since both experiments were carried out at the same electrochemical scan rate, the HD-VSFG spectra were co-added in adjacent groups of 5 spectra to improve signal-to-noise and enable direct comparison to the homodyne experiments.

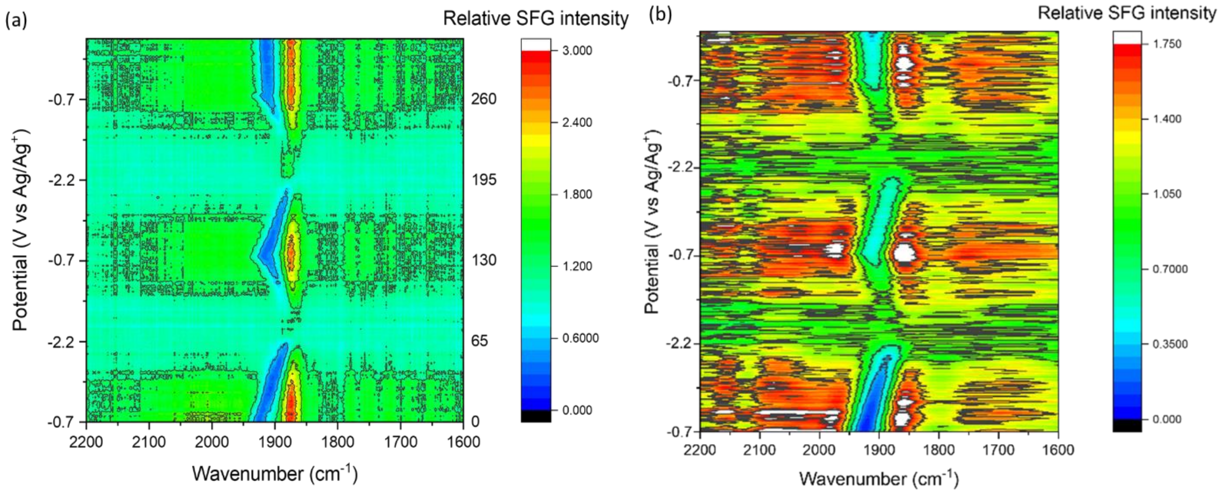

Figure 110: (a) Homodyne VSFG spectra (2 s per spectrum) and (b) HD-VSFG spectra (0.4 s per spectrum) recorded as the potential of the Au working electrode is modulated between -0.7 and -2.2 V in the presence of 1 mM [Mo(bpy)(CO)$_4$] at 10 mV s^{-1} in an argon-purged electrolyte of 0.1 M TBAPF$_6$ in acetonitrile. Note that both sets of spectra are normalised to the initial spectrum for comparison and the homodyne spectra include a 0.2 ps delay between the IR and Vis to suppress the nonresonant.

Both sets of spectra in Figure 110 display shifting of the v(CO) bands with applied potential. This is due the Stark tuning effect, where the frequency of the vibrational modes shifts linearly with applied potential.[8] The observance of this effect confirms that the Au electrode/electrolyte interface is successfully being probed in both sets of spectra. However, the aforementioned complications with adsorption of free CO complicating the assignments of these band and the markedly worse signal-to-noise in the HD-VSFG spectra complicates further analysis in these experiments. Despite these drawbacks, this proof-of-principle study demonstrates that electrochemical VSFG experiments can be carried out with relatively minor adjustments to existing homodyne spectrometers. With some of the suggested improvements, such as extending the time delay between the LO and sample SFG, as well as improving the sampling of the fringes, this HD-VSFG experiment could readily provide more detailed spectral information in our electrochemical experiments. This includes all of the benefits of HD-VSFG mentioned previously, including lower detection limits, orientational information and directly accessing the molecular vibrational information in Im[χ^2].

iii. References:

1 A. Lagutchev, S. A. Hambir and D. D. Dlott, *J. Phys. Chem. C*, 2007, **111**, 13645–13647.

2 R. W. Field, in *Spectra and Dynamics of Small Molecules: Alexander von Humboldt Lectures*, Springer International Publishing, Cham, 2015, pp. 85–111.

3 G. Neri, P. M. Donaldson and A. J. Cowan, *J. Am. Chem. Soc.*, 2017, **139**, 13791–13797.

4 I. V. Stiopkin, H. D. Jayathilake, A. N. Bordenyuk and A. V. Benderskii, *J. Am. Chem. Soc.*, 2008, **130**, 2271–2275.

5 R. E. Pool, J. Versluis, E. H. G. Backus and M. Bonn, *J. Phys. Chem. B*, 2011, **115**, 15362–15369.

6 H. Vanselous and P. B. Petersen, *J. Phys. Chem. C*, 2016, **120**, 8175–8184.

7 G. Neri, P. M. Donaldson and A. J. Cowan, *J. Am. Chem. Soc.*, 2017, **139**, 13791–13797.

8 G. Q. Lu, A. Lagutchev, D. D. Dlott and A. Wieckowski, *Surf. Sci.*, 2005, **585**, 3–16.

Appendix C

PIA supplementary information

i. Hole extinction coefficient determination:

This Appendix describes experiments that were carried out during my undergraduate project to calibrate the PIA amplitude and photocurrents following the procedures outlined by Le Formal *et al.*[1] Inaccuracies in these calibrations gave impossibly high values for surface hole densities, so these methods were not attempted on the electrodes used in this PhD project and the ratio between the two calculated reaction orders was used instead, as discussed in Chapter 4.2.1.

This first section describes the method for calibration of the PIA signal of hematite electrodes at 625 nm to an accurate surface hole concentration (*i.e.* determining the extinction coefficient of surface holes). This is achieved by simultaneous PIA and photocurrent measurements while the electrode is held at a potential prior to the OER onset. Under such conditions irradiation of the hematite electrodes with photon energies greater than its bandgap generates excited electrons and holes, but there is not a sufficient overpotential to give an OER photocurrent. Instead, the photogenerated charges are initially separated, but quickly recombine giving a transient spike in current as seen in Figure 111. Integrating the area of these transient peaks gives a value for the accumulation of charge. Dividing this charge by the charge of an electron yields the electron density and by extension the hole density. Combining this with a simultaneous PIA measurement can relate a change in optical density to a corresponding build-up of holes.

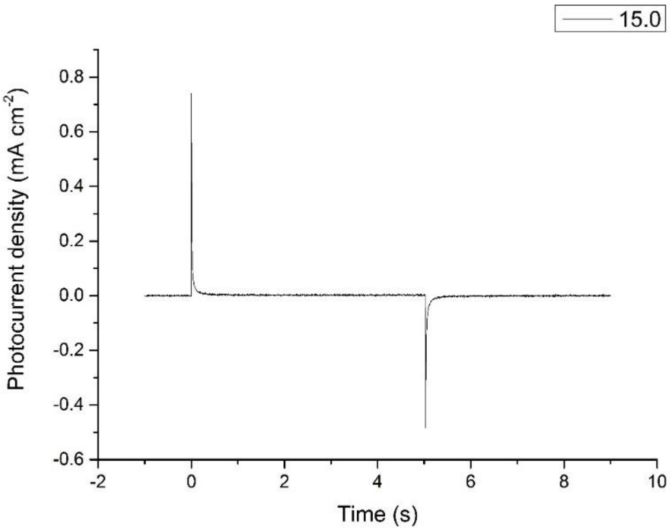

Figure 111: Transient photocurrent of an oxygen-deficient hematite electrode, under an external bias of -0.2V vs Ag/AgCl, under LED illumination with a light intensity of 15.0 mW cm^{-2}

This charge calculation was computed at several light intensities and plotted against the simultaneous PIA amplitude. The gradient of this line (Figure 112) corresponds to the extinction coefficient of the proposed surface hole species at 625 nm. This value of the extinction coefficient gives implausibly high values for the surface hole density in the thousands per square nanometre.

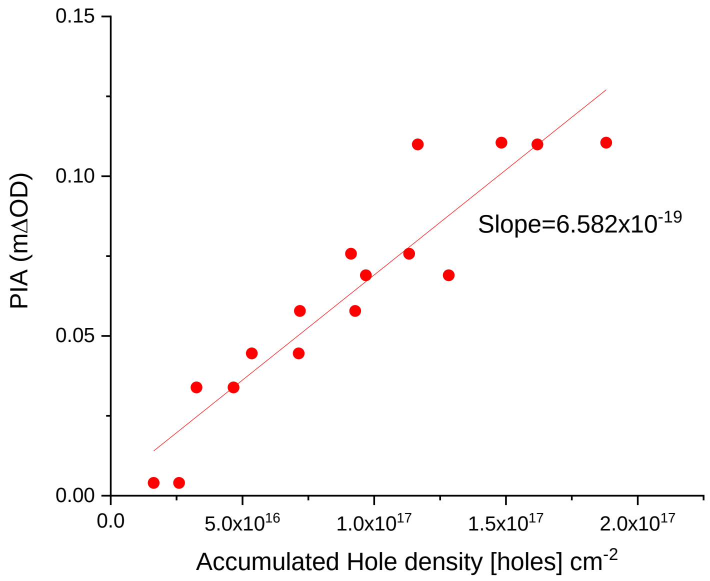

Figure 112: Relationship between change in PIA amplitude with surface hole concentration for an oxygen deficient hematite electrode. The gradient of this line contains the extinction coefficient, which allow the PIA signals from the main data to be converted to surface hole densities.

ii. Surface area determination at hematite electrodes with dyes:

This section describes experiments to determine the true surface area of the hematite electrodes studied above, which can be many times greater than the measured geometric surface area due to surface roughness. The ratio between the true surface area and geometric surface area is known as the roughness factor, which was estimated for these electrodes from a dye adsorption experiment. The general principle is that a monolayer of dye can be adsorbed on the nanostructured surface (Figure 113); the amount of dye molecules and the size of each dye molecule is proportional to the true surface area. These dyes can then be desorbed by submerging the films in a solution, where they dissolve or are cleaved from the surface, and the concentration of dye that dissolves can be determined by UV-vis spectrometry, using known molar absorption coefficients. Multiplying the number of dye molecules that were adsorbed by their adsorbed area gives the true surface area.

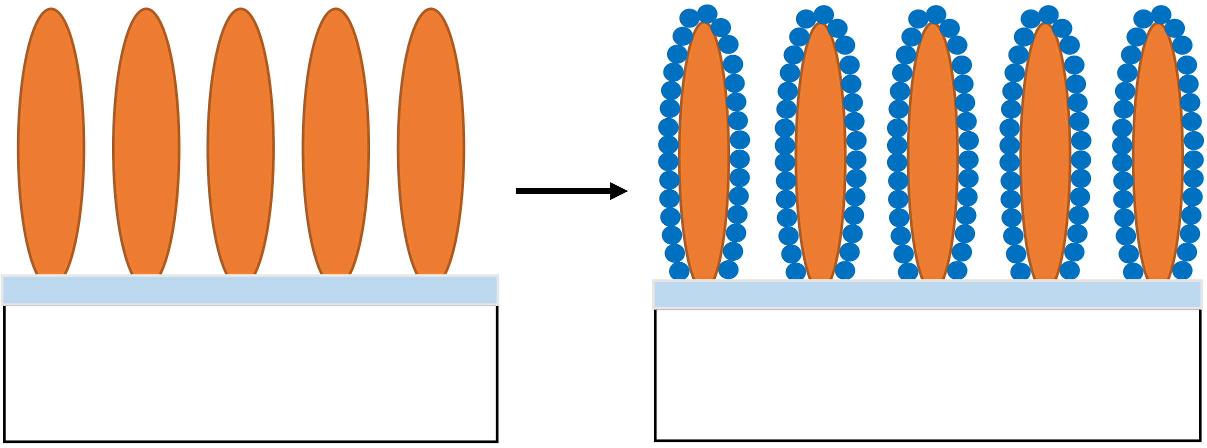

Figure 113: Schematic showing monolayer adsorption of dye molecules (blue circles) onto hematite nanorods (orange ovals) on an FTO coated (light blue layer) glass film. True surface area can be determined by multiplying the number of adsorbed dye molecules by the adsorbed area of each molecule.

The film in question was cut in half, with one half being soaked in Methylene Blue (in ethanol) and the other half in Ruthenium Phosphonate (in water) over 36 hours. Once soaked, the dyes were removed by 1M NaOH for Methylene Blue and acetonitrile for Ruthenium Phosphonate. The concentration of the dyes in these solutions was determined by UV-vis spectrometry in a 1cm glass cuvette; the absorption coefficient (ε) of both dyes is known (ε_{656nm}=73230 cm^{-1} M^{-1} for Methylene Blue and ε_{456nm}=14000 cm^{-1} M^{-1} for $[Ru(bpy)_2(bpy\text{-}PO_3H_2)]Cl_2$).[2,3] The adsorbing area of both dyes is also known ($[Ru(bpy)_2(bpy\text{-}PO_3H_2)]Cl_2$ = 1.65×10^{-18} m^2 and Methylene Blue = 1.298×10^{-18} m^2),[4,5] allowing the roughness factor to be calculated. Methylene Blue dye gave a roughness factor of 10.8, while a ruthenium phosphonate dye ($[Ru(bpy)_2(bpy\text{-}PO_3H_2)]Cl_2$) gave a roughness factor of 52.8. The discrepancy between these two measurements was probably due to non-monolayer adsorption of one of the dyes.

iii. References:

1 F. Le Formal, E. Pastor, S. D. Tilley, C. A. Mesa, S. R. Pendlebury, M. Grätzel and J. R. Durrant, *J. Am. Chem. Soc.*, 2015, **137**, 6629–6637.

2 J. Cenens and R. A. Schoonheydt, *Clays Clay Miner.*, 1988, **36**, 214–224.

3 S. A. Trammell, J. A. Moss, J. C. Yang, B. M. Nakhle, C. A. Slate, F. Odobel, M. Sykora, B. W. Erickson and T. J. Meyer, *Inorg. Chem.*, 1999, **38**, 3665–3669.

4 A. Kay, I. Cesar and M. Grätzel, *J. Am. Chem. Soc.*, 2006, **128**, 15714–15721.

5 M. A. Gross, A. Reynal, J. R. Durrant and E. Reisner, *J. Am. Chem. Soc.*, 2014, **136**, 356–366.

Concluding remarks

This thesis has explored several surface-sensitive spectroscopies as probes of the OER mechanism at electrode surfaces. Several new experimental setups have been built over the course of the project, including SHG, PIA and homodyne VSFG spectrometers at The University of Liverpool as well as a heterodyne VSFG spectrometer at the CLF.

Chapter 2 applied the SHINERS technique to study the OER mechanism at state-of-the-art hydrous iridium oxide electrodes, confirming the formation of an iridium oxo intermediate under catalytic OER currents. Changes in oxidation state of the iridium centres could also be followed in the *in situ* electrochemical SHINER spectra. The technique and spectroelectrochemical cells were then adapted to study thin film photoelectrodes including hematite and TiO_2. While there was no significant evidence of OER intermediates in the SHINER spectra, changes in the bulk crystalline Raman modes were observed, possibly related to changes in the plasmon resonance of the gold nanoparticles. An alternative data analysis procedure using correlational analysis was also investigated, using the iridium oxide SHINERS data as a starting point. Similar results were obtained from the automated correlational analysis compared to the detailed fitting previously carried out on this dataset. The combination of the sensitivity of the SHINERS experiment and this automated correlational analysis procedure is a powerful tool in studying electrochemical interfaces and could be applied to countless other systems. The ease of synthesis of SHINs and relative ubiquity of Raman spectrometers at research institutes make the technique highly accessible. The speed of acquisition and strong signals also make the technique suitable for future time-resolved experiments to better understand faster (photo)-electrochemical processes

Chapter 3 describes attempts at developing an *in situ* electrochemical VSFG experiment to study local water structure in photoelectrodes. An alternative, through-electrode geometry was explored to avoid attenuation of IR light through aqueous electrolytes using ultrathin TCO layers. Several possible resonant modes corresponding to O-D stretching vibrations were observed on both TiO_2 and hematite electrodes. In particular, a high frequency mode (around 2700 cm^{-1}) assigned to the O-D stretch of a non-hydrogen bonded D_2O molecule was observed under OER conditions. Attempts to address some of the deficiencies of the homodyne VSFG experiment motivated the development of an *in situ* electrochemical heterodyne-detected VSG experiment at the CLF. A proof-of-concept HD-VSFG spectrometer was built and used to record a potential-dependent HD-VSFG spectrum of a molecular CO_2 reduction catalyst. While analysis of data was complicated in this Chapter, the use of a HD-VSFG spectrometer and alternative experimental geometries can address many of these concerns. With some further developments, *in situ* electrochemical VSFG spectroscopy can be an incredibly powerful tool for probing electrode interfaces with inherent surface-sensitivity. There is also the possibility of improving this already sensitive technique by combining with the SHINERS concept discussed above. This combination of SHINERS and SFG has recently been reported by He *et al.*[1]

Chapter 4 details the development of two experiments, a PIA spectrometer to study slow hole kinetics at hematite electrodes and an EFISHG experiment to investigate interfacial electric fields in the same electrodes. PIA spectroscopy was used confirm an apparent change in OER mechanism between low and high light intensities. The same electrodes were then used to test the EFISHG experiment. The shape (linear or parabolic) of the potential-dependent SHG response was used to determine which nonlinear susceptibility (2nd or 3rd order) was dominating the system. Deviations from these linear and parabolic shapes were correlated to oxidation and reduction of known surface trap states in hematite, enabling visualisation of field changes due to Fermi level pinning. Further systematic experiments are required to confirm these proposed assignments, though the technique appears to be useful in understanding surface trap state populations and could be applied to the interaction of other semiconductor photoelectrodes and co-catalysts.

At the time of these experiments there were no reports (to my knowledge) of utilising any of the three main techniques (SHINERS, SFG and EFISHG) to study the OER at photoelectrode surfaces. This thesis details the application of these techniques to the *in situ* study of such electrodes, demonstrating the variety of mechanistic insights that can be gained from these surface-sensitive spectroscopies.

References:

1 Y. He, H. Ren, E. M. You, P. M. Radjenovic, S. G. Sun, Z. Q. Tian, J. F. Li and Z. Wang, *Phys. Rev. Lett.*, 2020, **125**, 47401.